Mathematical Modelling of The Liver Microcirculation

by

Kritsada Leungchavaphongse

A thesis submitted for the degree of Doctor of Philosophy

and for the Diploma of Imperial College London

Department of Bioengineering, Imperial College London

January 2013

Author's Declaration of Originality

I here by declare that this thesis is solely composed and originated by me and no part of the thesis has been presented for a degree by any institution or has been published in any publication except where the acknowledgement is made.

Abstract

The models of the microcirculation of blood and interstitial fluid in the human liver lobule are developed based on the classical hexagon model of Kiernan. Both blood and interstitial flows in the lobule are treated as flows in porous medium connected via the fenestrated membrane of sinusoids. Several important physiological components are developed and included in the models. The lobule with tissue elasticity shows that the pressure-flux relationship is non-linear and the poroelastic model has more compliance than the solid elastic model. Models of the interstitial flow in both a single lobule and the whole liver are also developed. The results show that our models can predict the amount of interstitial fluid drainage including the ascites. From the parameter studies, we find that the permeabilities of the sinusoids and the interstitial space, and the portal pressure are the most important factors on ascites production.

We further investigate the oxygen transportation and uptake by liver cells using the advection–diffusion equations and Michaelis-Menten kinetics. The studies show that the main mechanism of oxygen transportation within the sinusoids is advection; however, the transportations within the interstitial space and across the fenestrated endothelial cells are mainly from diffusion process.

The effect of the arrangement of the vessels and the geometry of the lobule on blood perfusion and oxygen distribution is also studied. The results show that the classical hexagonal lobule with the vascular septa provides the optimal perfusion compared to other geometries of the lobule.

In summary, this thesis contributes to the development of mathematical models of several important features in the liver microcirculation such as the tissue elasticity, the interstitial flow, the oxygen distribution, and the arrangement of the vessels in the lobule.

This thesis is dedicated to my mom and dad, my brother, my aunts, my uncles,

and my grandmother who are my beloved family.

Acknowledgements

First of all, I wish to express my gratitude to my supervisors, Dr.Jennifer Siggers and Dr.Rodolfo Repetto for their guidance and support throughout the years of my research. I would also like to thank the Royal Thai Government for the funding throughout the course. Furthermore, I would like to thank every staff at office of educational affairs, the Royal Thai Embassy, London, for their help and advice during my study in UK. Moreover, I would like to thank Professor Charles Michel for his helpful advice in liver physiology and Professor Kim Parker for his useful comment on my research especially in the mathematical point of view. I also would like to thank my colleague: Sevil, Chris, Ani, Andrea, Julia, Saadia, Eugene, Olga, and Caroline for their knowledge, help, and useful opinions on my work.

I wish to give my gratitude to every scientist, engineer, doctor, and researcher who have discovered and developed every element of the scientific knowledge. As a human, I am really appreciated their works as when I look around myself, almost every little thing seems to be originated from their intelligence and hard works. Their works make the world be as it is today and I proud to be one of them. Hopefully, my works will be useful for the others some day in the future. Furthermore, I owe my gratitude and appreciation to all of my teachers who have taught me and make me the person I am today. I would also like to acknowledge my current workplace, department of anatomy,

faculty of medicine, Chulalongkorn university and every staff there who gave me a chance to show my potential in the job and understand every circumstance on my research.

During my stay in UK, I really have wonderful times and lots of good memories here so I would like to thank all British people who are really nice and kind to me everywhere I go. I would also like to thank my senior friends here: P'Toh, P'Annie, and P'Sirus who always give me some good advice and encouragement every time we met, and; importantly, thank all of my friends who always stay beside me. It is my pleasure to know everyone. I also want to give special thanks to previous and current members of the No.3 House including P'Meng, P'Au, P'Sunee and her family, Mac, Dao, Orr, Tar, and Ping who are my friends, family, brothers, and sisters during the wonderful years at Canada Water. They all help me get through my toughest years and I am really appreciated it.

Finally, I would like to thank my parents, my brother, my aunts, my uncles, and my grandma for all kinds of support throughout my life. Their love and support is the most important encouragement for me on this long long road. I would like to say thank you, I love them all, now and forever.

Kritsada Leungchavaphongse

Imperial College London

December 2012

Contents

Chapter 1

Introduction

1.1 Biology of the liver

1.1.1 Anatomy and functions of the liver

The liver is located below the right diaphragm, under the rib cage, and in the abdominal cavity (figure 1.1.1). It has a wedge shape with dimensions 20-23 cm in the lateral direction, 15-17.5 cm in the superior-inferior direction, and 10-12.5 cm in the anteroposterior direction. Its weight is about 1.5 kg in a normal adult. It is the largest internal organ and the largest gland in the body [1].

The liver receives its blood supply from two sources: the hepatic artery and the portal vein. Around a third of the blood supply is oxygenated blood from the hepatic artery. The hepatic artery is an arterial branch arising from the coeliac artery, a branch of the abdominal aorta. The remaining two thirds of the blood supply is from the portal vein

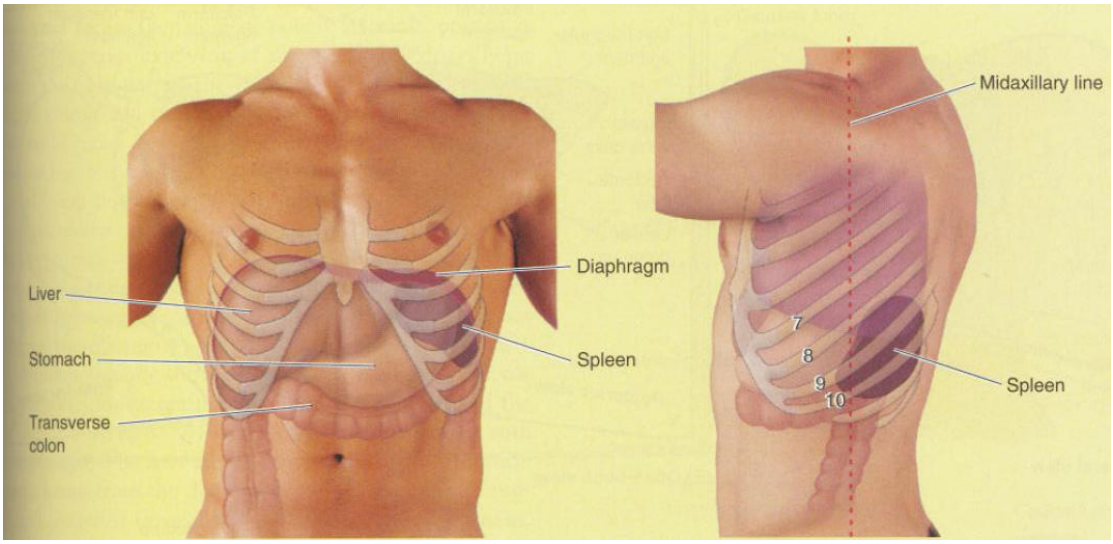

Figure 1.1.1: The liver is located in the abdominal cavity and below the right diaphragm [2].

which carries partially deoxygenated blood. The portal vein receives blood from the mesenteric vein, which contains nutrients from the alimentary tract. In total, the liver receives around 1.4 l/min of blood. Under normal physiological conditions, the liver contains 450 ml of blood, but it can expand its capacity up to one litre [3].

The liver is covered by two layers of tissues: the inner layer is a fibrous tissue called Glisson's capsule that covers the entire liver, and the outer layer is serous fibres [4]. Glisson's capsule covers almost the entire surface of the liver except the area beneath the diaphragm, called the bare area, the porta hepatis, and the area that is attached to the gall bladder (figure 1.1.2).

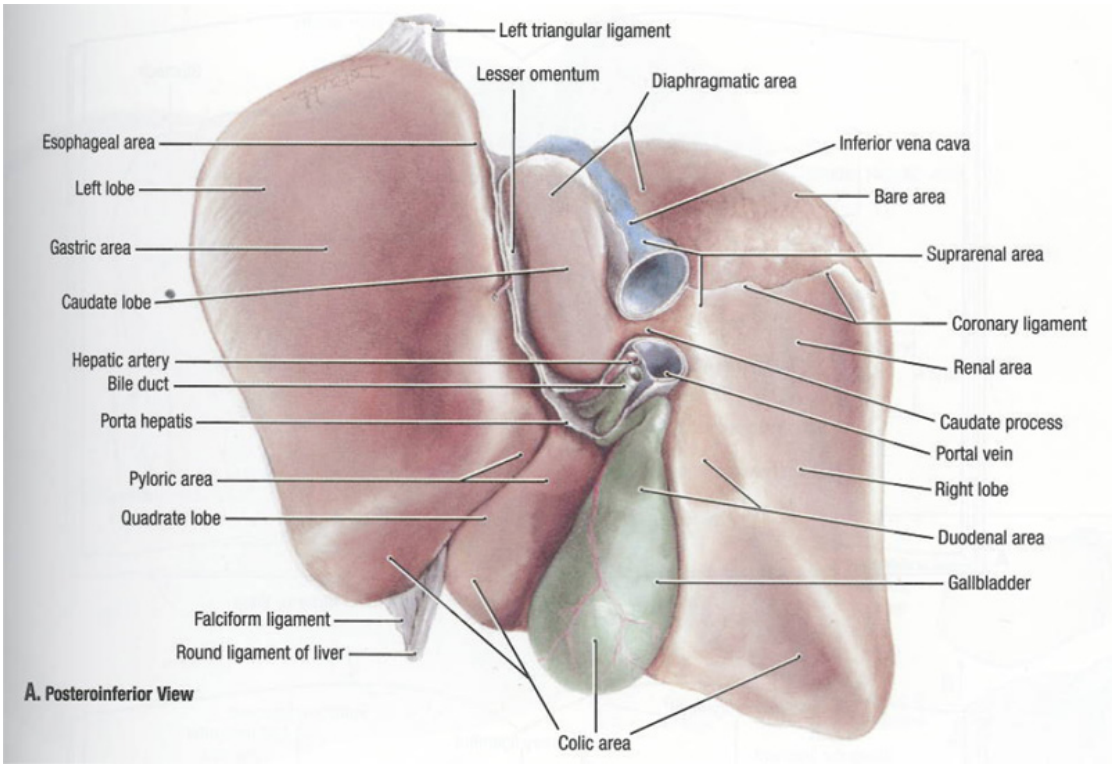

Figure 1.1.2: Posterior view of the liver shows the location of the hepatic artery, the portal vein, porta hepatis, the area attached to the diaphragm (the bare area), and the gall bladder [5].

The liver is often divided into four lobes corresponding to superficial anatomical landmarks. However, it is more useful for us to divide the liver according to functionality. The lobes defined in this way are not the same as the anatomical lobes defined according to the anatomical landmarks. With functional subdivision, the liver is divided into eight segments based on the vascular supply (figure 1.1.3). This subdivision method is very useful in liver surgery. In partial hepatectomy or liver transplantation, surgeons can resect regions of the liver by cutting boundaries between each functional segment to minimize bleeding [2], [3].

The liver performs many important tasks for the body. Some of the major functions are [3]:

- storing vitamins, iron, and other nutrients
- combatting infection
- neutralising and/or eliminating toxic particles
- synthesizing, metabolizing, and storing carbohydrates, proteins, and fats
- forming and secreting bile into bile canaliculi, which merge to form bile ducts. Bile is stored in the gallbladder.

1.1.2 Structure of the hepatic lobule

The microstructure of the liver is divided into functional units called 'liver lobules'. In general, each lobule contains one hepatic centrilobular vein and a number of portal

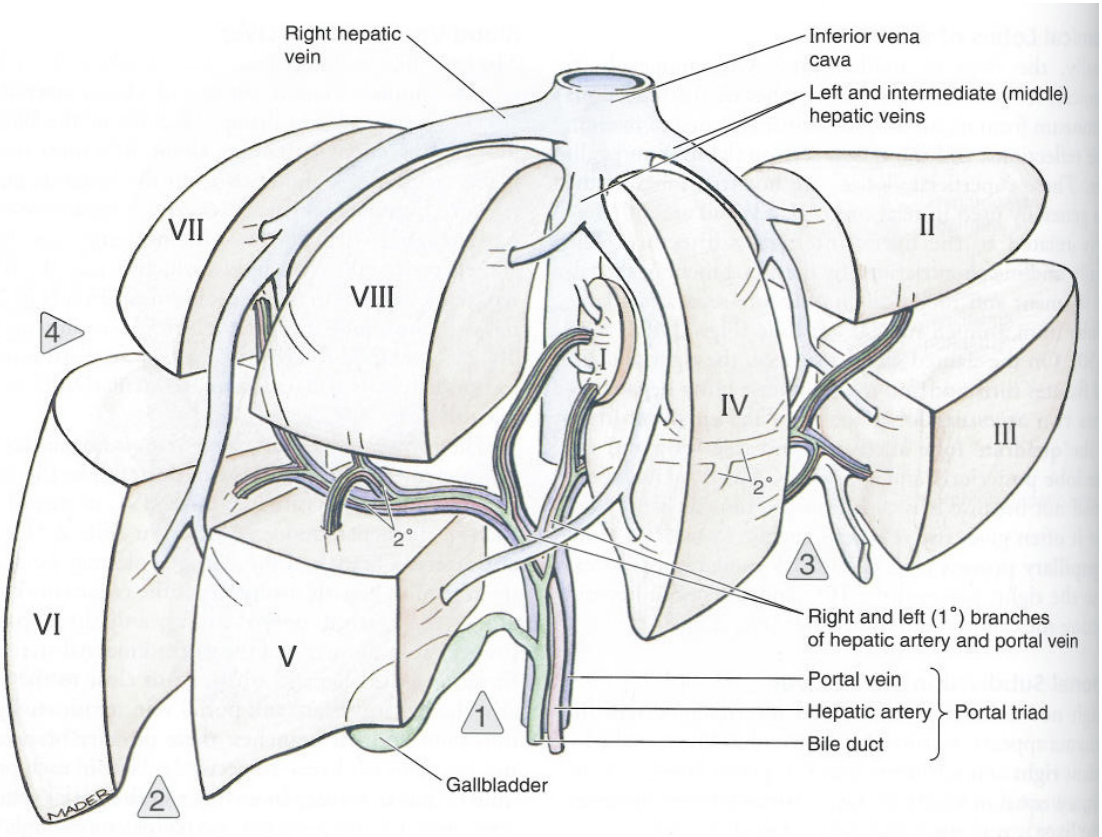

Figure 1.1.3: Segmentation of the liver according to functionality [2].

tracts. The hepatic portal tract is composed of a hepatic artery, a portal vein, and a bile duct. Both hepatic artery and portal vein distribute blood to the liver lobule via an irregular capillary network called the 'liver sinusoids' (figure 1.1.4). Each sinusoid is lined with fenestrated endothelial cells that allow exchange of fluid and some metabolic substances between the sinusoids and the liver cells, or called the 'hepatocytes'. The hepatocytes and endothelial cells of sinusoids are separated by the perisinusoidal space, or 'the space of Disse'. Blood flow from the portal tract and through the sinusoids into the hepatic centrilobular vein undergoes repeated anastomoses with other hepatic centrilobular veins from different lobules to form a sublobular vein, and these veins merge together to form the hepatic vein, draining blood back to the heart via the inferior vena cava [3].

However, the number and the arrangement of the lobular vessels (centrilobular veins and portal tracts) in the histological sections are often irregular, and so simplified models of the lobule have been proposed. The first one is proposed by Kiernan in 1833, known as the 'classical lobule' having the shape of a cylinder with hexagonal cross-section [6]. The portal tracts are along the vertices of the cylinder and the centrilobular vein is along the axis (figure 1.1.5).

The second model was proposed by Mall (1906) [7], who described the portal tract at the centre surrounded by hepatic portal veins. The last model is the acinus described by Rappaport in 1954 [8]. He described that the functional lobule called the 'liver acinus'

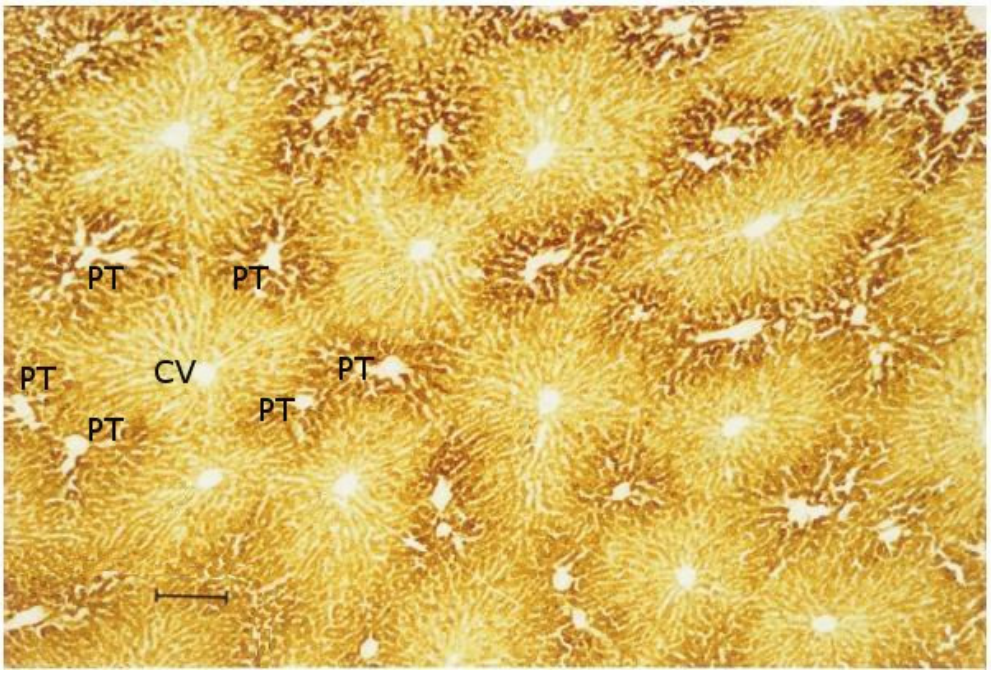

Figure 1.1.4: Histological image of the liver lobule in rat, where PT is a portal tract and CV is a centrilobular vein [9].

is the area between the centrilobular vein and the line between two portal tracts (figure 1.1.6). This area can be divided into three zones with no certain boundaries between them. The area located near the line between two portal tracts is 'zone 1', the area near the centrilobular vein is 'zone 3', and the area between zone 1 and zone 3 is 'zone 2'. Each zone is characterized by a different alignment of the sinusoids and activitity rate of the hepatocytes [8].

In 1979, Matsumoto et al reconstructed a 3D model from serial sections of the human liver. He highlighted the existence of vascular branches connecting vessels between two portal tracts called 'vascular septa', which agrees with the observation of Rappaport [10]. These branches distribute blood directly into zone 1 of the acinus model.

In 2010, Bonfiglio et al. [11] described the classical hexagonal lobule with the edges length 500 μm, the portal tract has a diameter of 50 μm, the centrilobular vein has diameter of 80 μm, while the length of the third dimension is unknown but assumed to be long compared to the diameter of the lobule.

1.1.3 Anatomy and physiology of interstitial fluid pathway in the liver

Although most of the blood entering the capillary network is drained out via the efferent vessels, a small fraction of the plasma that flow into the liver via the hepatic artery and portal vein leaves through the fenestrated membrane of the sinusoids and becomes interstitial fluid. The fluid surrounds the cells and acts as a medium for nutrients, oxygen,

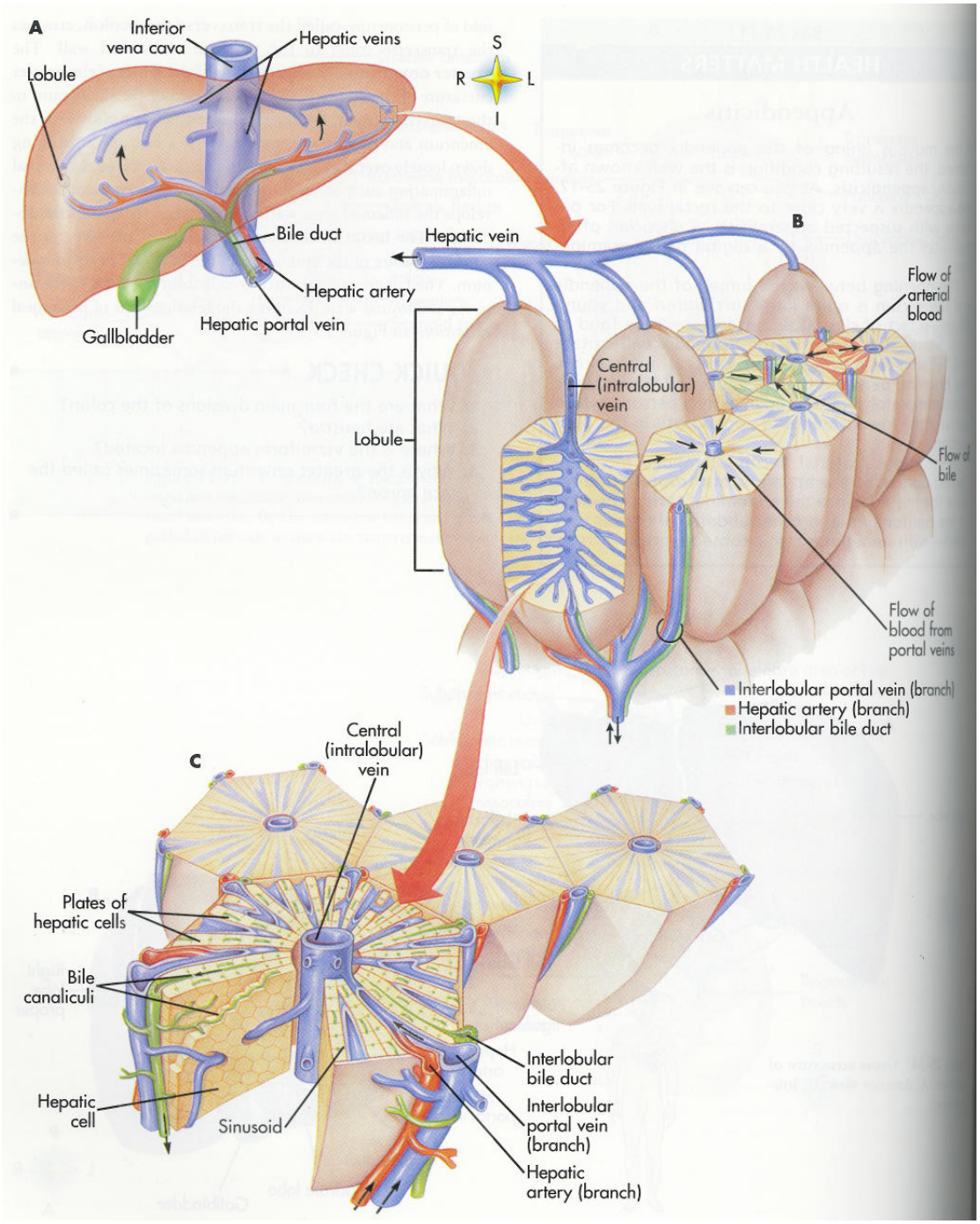

Figure 1.1.5: Schematic diagram of liver showing the blood supply. A) Whole liver B) Hypothesized arrangement of the classical lobules C) Cross-sections of lobules [3].

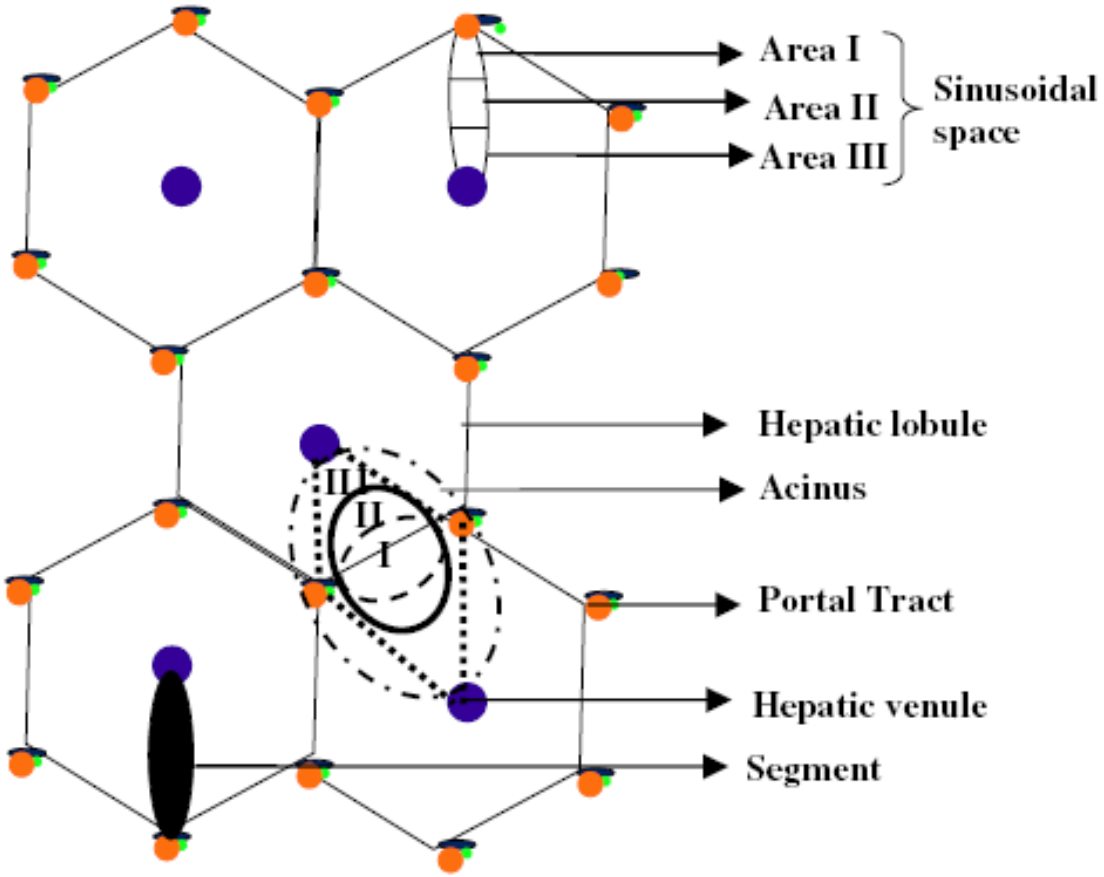

Figure 1.1.6: Diagram of acinus model, which can be divided into three zones (I-III) [47].

and waste products transportation [12].

The interstitial fluid flow drains plasma out of the liver out by three pathways: via the lymphatic ducts, via the bare are, and via the Glissonian-peritoneal membrane [61].

Interstitial fluid pathway via the lymphatic ducts

The liver sinusoids constitute a vascular network covered by fenestrated endothelial cells. The fenestrations in these cells allow the exchange of plasma and proteins contained in the plasma between the sinusoids and the space immediately outside the sinusoids, which is called the perisinusoidal space or the space of Disse. Lymphatic vessels in the interstitial space remove fluid, draining it to the space around portal tracts and the centrilobular vein of each lobule (figure 1.1.7) [14]. From there the vessels in the lymphatic tree coalesce, eventually leaving the liver. The fluid drains into the venous system at the junction of the left subclavian vein and left jugular vein via the thoracic duct [15].

Interstitial fluid pathway via the bare area

Another pathway to drain the interstitial fluid out of the liver is via the bare area under the right diaphragm. The are does not have a layer of peritoneal membrane cover, unlike the Glissonian-peritoneal membrane, allowing fluid to flow pass easier. The fluid from this pathway will merge with the interstitial fluid from the lymphatic ducts in the thoracic duct [56].

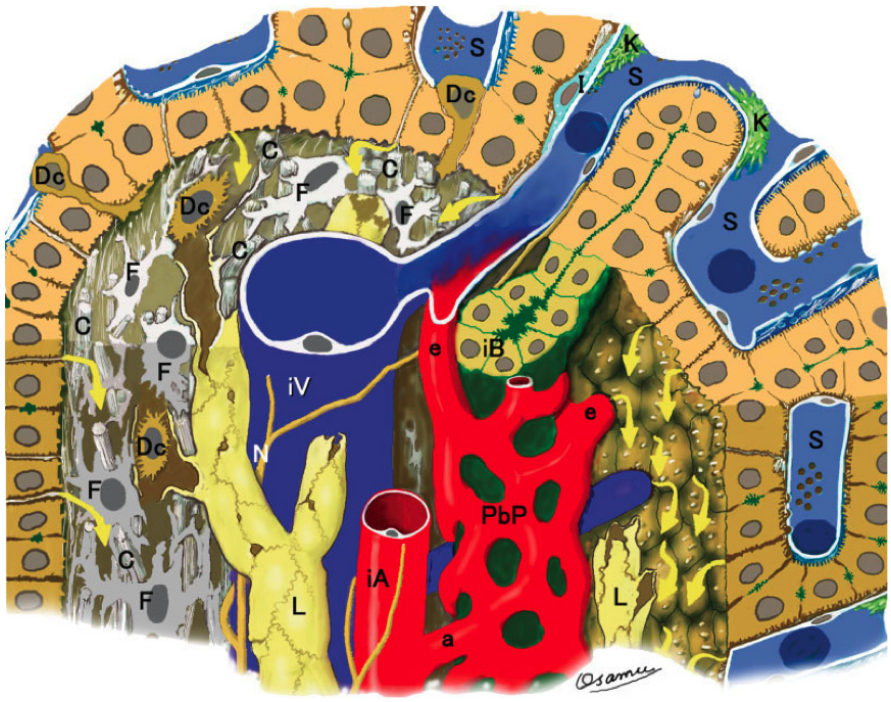

Figure 1.1.7: Diagram shows the lymphatic ducts (L) which receive interstitial fluid from the interstitial space nearby (yellow arrows) [14].

Interstitial fluid pathway via the Glissonian-peritoneal membrane

The last pathway of plasma fluid drainage is via the Glissonian-peritoneal membrane. The membrane is composed of two components: Glisson's collagenous capsule and the peritoneal membrane. The Glissonian-peritoneal membrane separates the liver from the peritoneal cavity, which contains serous fluid that lubricates the internal organs, containing around 50 ml in normal adults [16].

Usually the fluid exchange is in balance so the volume of the fluid in the peritoneal cavity is static. However, if there is a net flow, for example, from fluid leakage due to the raised pressure inside the liver then the volume of fluid in the peritoneal cavity could increase, leading to ascites, a condition in which there is an excess of fluid in the abdominal cavity [17]. The condition is found common in some liver diseases such as cirrhosis.

1.2 Mathematical modelling of cardiovascular physiology

In this section, we describe the basic principles of haemodynamics in blood vessels, beginning with flow in large vessels and then continue to the microcirculation, which is our main focus in this project.

1.2.1 Flow in large artery

There are several mathematical principles and approaches used in modelling of flow in the large arteries such as the aorta, the largest artery in the body. The basic pressure-flow relationship for steady flow in a pipe is described by Poiseuille's equation [18]:

$$Q = \frac{\pi R^4 (P_1 - P_2)}{8\mu L}, \tag{1.2.1}$$

where Q is the flow rate, $P_1 - P_2$ is the pressure difference, R and L are the radius and the length of the pipe, respectively, and μ is the fluid dynamic viscosity.

Poiseuille's equation makes the following assumptions:

- The fluid is a Newtonian incompressible fluid.
- The flow is laminar and fully-developed.
- The flow is steady.
- The flow is axisymmetric.

- The tube is rigid and cylindrical in shape.

Laminar flow of an incompressible fluid can be described by using the Navier-Stokes equation [18]:

$$\rho\left(\frac{\partial \mathbf{v}}{\partial t} + \mathbf{v}\cdot\nabla\mathbf{v}\right) = -\nabla p + \boldsymbol{\nabla}\cdot\mathbf{T} + \mathbf{F}, \tag{1.2.2}$$

where ρ is the density of the fluid, $\mathbf{v}$ is the velocity of the fluid, t is time, p is fluid pressure, $\mathbf{T}$ is the stress tensor, and $\mathbf{F}$ is the force acting on fluid.

However, flow in large arteries such as the aorta is usually more complicated and; therefore, does not follow Poiseuille's law. Firstly, the arterial wall consists of smooth muscle which means the wall has an elastic property. Secondly, the flow is not steady. The pumping of the heart generates pulsatile pressure and flow profiles in the arteries, and leads to a wave of pressure travelling along the vessels [18].

In general, one of the parameters characterising the flow behaviour is the Reynolds number (Re), which is a dimensionless number determined by fluid velocity, diameter of the pipe, viscosity, and density of the fluid:

$$Re = \frac{\rho v D}{\mu} \tag{1.2.3}$$

where ρ is fluid density, v is the average velocity of the fluid, D is hydraulic diameter of

the pipe, and μ is the dynamic viscosity.

Flow in large vessels such as the aorta ($Re \approx 4000$ [19]) and its major branches has a high Reynolds number, while flow in small vessels has low Reynolds number. At low Reynolds numbers, the flow is laminar and the relationship between flow rate and pressure gradient is linear. However, when Reynolds number is high, the pressure-flow relationship turns into non-linear relationship and turbulent flow may occur (figure 1.2.1) [20].

Another factor that affect the flow is the curvature of the vessels, δ, which is determined as the ratio between radius of artery, r, and radius of curvature, R (see figure 1.2.2a):

$$\delta = \frac{r}{R}. \tag{1.2.4}$$

The centrifugal force due to the curvature generates a secondary flow in the plane of cross-section (see figure 1.2.2b) [21].

Moreover, the cross-section of most arteries is not constant as the arteries taper along the length, and also have bifurcations and/or smaller side branches.

Furthermore, blood is composed of several proteins and cells. In some circumstances, it can be modelled as a non-Newtonian fluid whose viscosity is not constant but depends

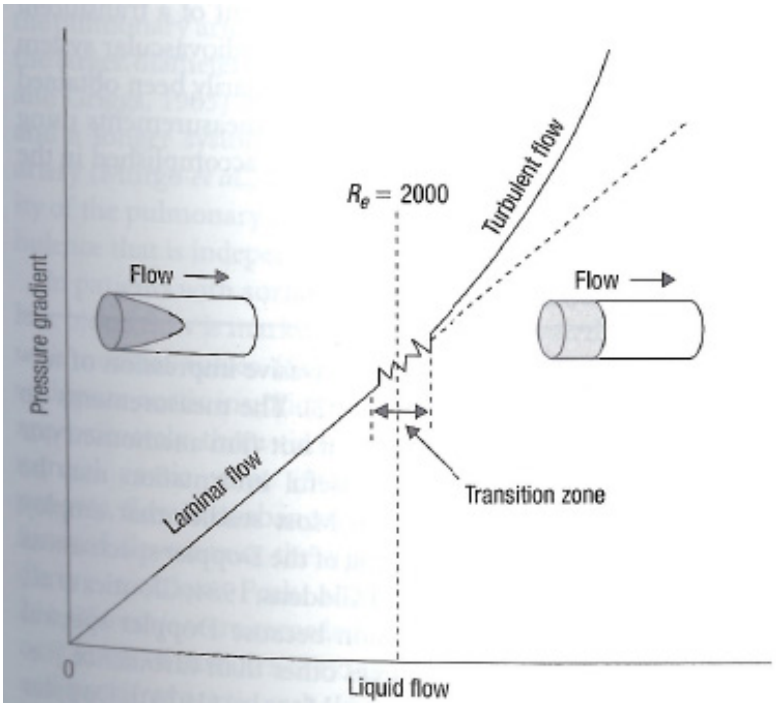

Figure 1.2.1: Laminar flow vs Turbulent flow. The relationship between pressure gradient and flow rate in laminar flow is linear while the velocity is parabolic when Reynolds number is above 2000 [20].

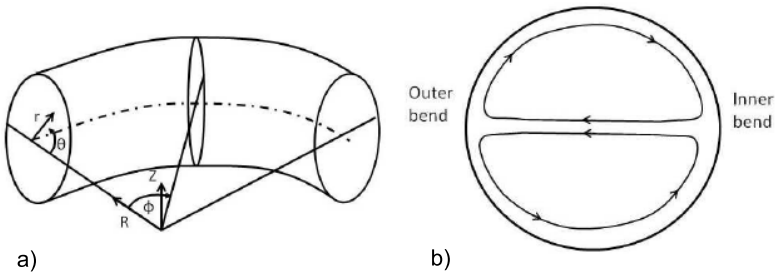

Figure 1.2.2: a) Diagram of a curved artery. b) Typical secondary flow in the vessel [21].

on shear stress [22]. One of the most important components of blood is red blood cells (RBCs). When blood flows slowly, RBCs distribute uniformly across the cross-sectional area of the vessels and cause high viscosity. However, when flow increases, RBCs tend to move to the centre of the vessels, causing less viscosity. This effect is called shear-thinning effect (see figure 1.2.3) [20].

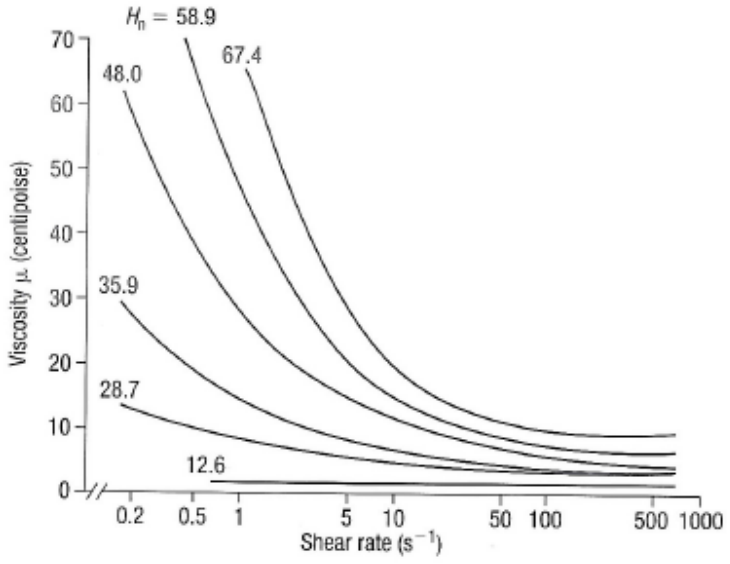

Figure 1.2.3: The relationship between shear rate of human RBCs in plasma in various concentrations against viscosity, demonstrates the effect of shear thinning [20]

.

Flow in the cardiovascular system as a whole can be modelled using an electrical analogue, such as the Windkessel model shown in figure 1.2.4 [23]. The model was developed by Otto Frank in 1899 [24] and later translated to English by Sagawa in 1990 [25]. It includes some important physical properties of the vessels such as the distensibility and

the resistance. However, the model is not accurate as it does not include wave propagation within the vessels. The travelling of pressure waveform can be analysed using wave intensity analysis (WIA), developed by Kim H. Parker in 1990 [26]. The method is based on the one dimensional flow model, tube law, solution of conservation of mass and momentum principles [27]. The measured waveforms of pressure and velocity are visualised as a sum of successive wavefronts propagating along the vessels.

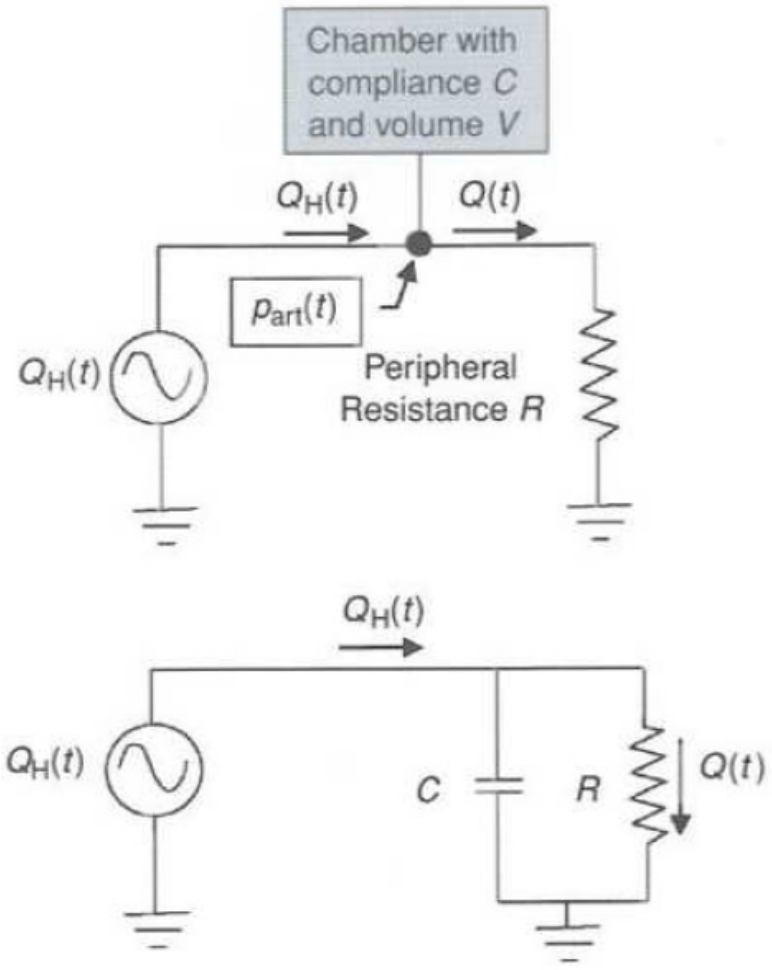

Figure 1.2.4: Top: Diagram of Windkessel model. Bottom: Equivalent electrical analogue. The variable $Q_H(t)$ is the flow rate from the heart, $Q(t)$ is the peripheal bloow flow, $p_{art}(t)$ is the potential difference representing arterial blood pressure, C is the capacitance representing the distensible arteries, R is the resistance of the peripheral vessels, and earth represents zero pressure in veins. [23]

1.2.2 Flow in small vessels

In the cardiovascular system, there are several generations of small vessels: arterioles, capillaries, venules, lymphatics, and interstitial space. The arterioles have a similar wall structure to the artery, having a thin layer of circular and tangential smooth muscles [18].

The capillaries are the bridge connecting the arterial and venous system. They act as terminal branches of the arterioles and consist of a layer of endothelial cells. The structure of the capillaries is different from the other types of vessels, since it has a fenestrated membrane to allow fluid, nutrients, oxygen, and waste products to pass through for exchange between capillaries and interstitial space. Flow in capillaries is not pulsatile, unlike that in either the arteries or arterioles [18].

The venules are the larger vessels linked between capillaries and veins. The wall of both venules and veins also have a layer of smooth muscle, but unlike that of the arteries, its arrangement is irregular and has alignment in helix shape. The lymphatic vessels drain excessive fluid out of the interstitial space. Similar to the capillaries, they do not have smooth muscle in the wall. However, the vessels have valves that prevent backward flow and help an extrinsic pumping mechanism to push fluid forward [28].

For the flow in these small vessels, especially in the capillaries, the viscosity of the blood is different to the one in large arteries as it is a function of the diameter of the vessel and the flow does not follow Poiseuille's equation. This effect is called the

'Fahraeus-Lindqvist effect' which is a result of RBCs moving towards the centre of the vessel (figure 1.2.5) [20].

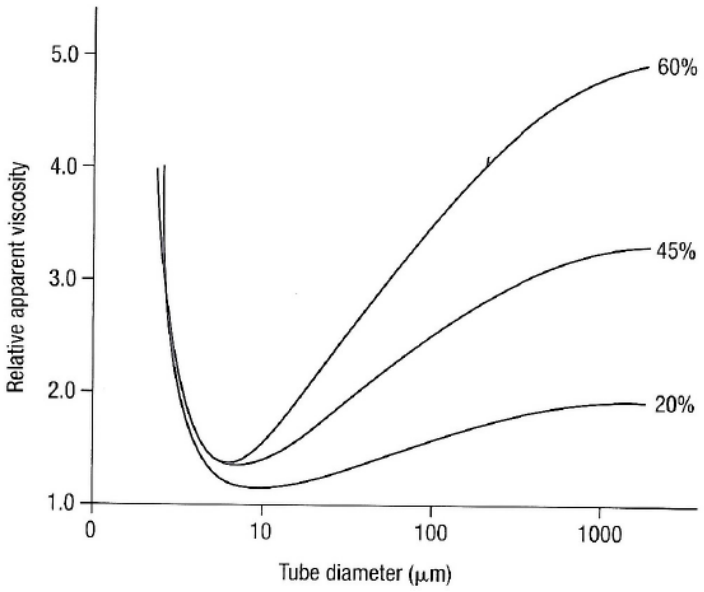

Figure 1.2.5: The relationship between blood viscosity and the vessel diameter with various hematocrit. The graph shows the Fahraeus-Linquist effect in which the apparent viscosity depends on the vessel diameter [20].

1.2.3 Mechanics of fluid flow in porous medium

Much of mathematical modelling of the flow in the vessels of the cardiovascular system treats the vessels as individual pipes. However, for flow in the microcirculation, due to the complexity of the network of interconnected vessels, the concept of flow in porous medium is used in some areas of biological-related haemodynamics such as [29]:

- Flow in placenta [30].
- Flow in scaffolds in tissue engineering [31].
- Flow in brain tissue [32].

For the microcirculation in the liver tissue, there are only a few studies in this area. Ricken et al [50] and Bonfiglio et al [11] used the concept of the flow in a porous medium to mimic the flow in the sinusoids (to be reviewed in the next chapter).

A porous medium is a material that has interconnected pores, which allow fluid to flow pass through them [33]. We therefore can describe the porous medium containing fluid as a system with two phases: solid and liquid phases. The porous property of the medium is described by the porosity (ϕ) which is the ratio of the pore volume over the total volume of a small volume about the point of interest:

$$\phi = \frac{V - V_0}{V}, \tag{1.2.5}$$

where V is the total volume (solid volume + pore volume) and V_0 is the solid volume.

Flow in a porous medium is described by Darcy's law:

$$\mathbf{v} = -\frac{k}{\mu}\boldsymbol{\nabla} p, \tag{1.2.6}$$

where $\mathbf{v}$ is Darcy velocity, k is permeability, μ is dynamic viscosity.

The Darcy velocity is a volume-average velocity over the volume V. If the porous medium is isotropic then k is a scalar, but if the medium is anisotropic then it is a tensor. The hydraulic conductivity, K, is defined as

$$K = \frac{k}{\mu}. \tag{1.2.7}$$

In some types of porous medium, the geometry of the system can be deformed by the effect of pore pressure, resulting from the elasticity of the solid component. The concept of poroelasticity can be described using the Biot model [34], in which the solid and the fluid phases are connected together. In linear elasticity, the solid strain tensor (ϵ_{ij}) can be written in terms of the solid displacement (u_i) as

$$\epsilon_{ij} = \frac{1}{2}(u_{i,j} + u_{j,i}), \tag{1.2.8}$$

where u_i and u_j are the components of the incremental displacements of the tissue in the x and y directions, respectively, and commas denote partial derivatives in those directions.

For the fluid component, its motion relative to the solid is described using the discharge vector, q_i. It can be written as the change of fluid volume per unit volume of the porous material (ζ) over time (t) as

$$\frac{\partial \zeta}{\partial t} = -q_{i,i}. \tag{1.2.9}$$

The dynamic of solid component is determined by the total stress tensor, σ_{ij}, whilst the dynamic of fluid component is determined by the pore pressure, p. The work increment, dW, can be written in terms of the stated variables as

$$dW = \sigma_{ij} d\epsilon_{ij} + p d\zeta. \tag{1.2.10}$$

The mechanisms of poroelastic materials will be discussed further in Chapter 3.

1.2.4 The effect of haemoglobin on oxygen transportation

Another important feature related to the microcirculation in the human physiology is oxygen transportation, as cells need oxygen for respiration. Oxygen is transported to the cells via blood, which contains plasma and two types of cell: red blood cells (RBCs), and white blood cells. Under normal physiological condition, RBCs carry the majority of oxygen in the blood, whilst a smaller amount of oxygen is dissolved in plasma [35].

In general, haemoglobin in adult human has four subunits which means that each haemoglobin can carry up to four oxygen molecules. This binding mechanism between oxygen and haemoglobin is reversible. Oxygen molecules can be dissolved into plasma after being released from haemoglobin and vice versa.

The solubility of oxygen in plasma is determined by the level of oxygen partial pressure (P_{O_2}). Elevated P_{O_2} such in the hyperbaric environment can increase the amount of dissolved oxygen in the plasma [35]. Figure 1.2.6 shows the haemoglobin dissociation curve which represents the affinity of oxygen binding to the haemoglobin. The curve is described by Hill's equation which predicts the percentage of oxygen saturation (S_{O_2}) in plasma,

$$S_{O_2} = \frac{(P_{O_2}/P_{50})^n}{1 + (P_{O_2}/P_{50})^n} \tag{1.2.11}$$

where n is Hill's coefficient (≈ 2.7 in adult human) and is related to the cooperativity degree of oxygen-haemoglobin binding, and P_{50} is the oxygen partial pressure when the haemoglobin is 50 percent oxygenated. The curve shows that when the partial pressure of the oxygen increases, the percentage of oxygen saturation also increases.

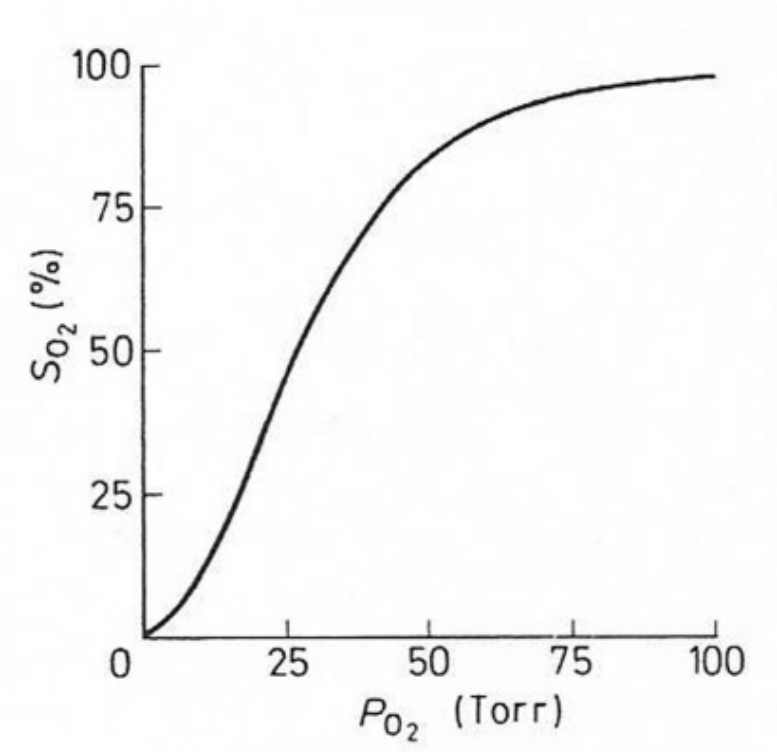

Figure 1.2.6: The oxygen dissociation curve. S_{O_2} is the percentage of oxygen saturation and P_{O_2} is the partial oxygen pressure [35].

There are two ways of changing the oxygen affinity to haemoglobin that caused by changing level of several factors such as blood temperature, blood pH, 2,3-Diphosphoglyceric

acid concentration etc. (figure 1.2.7) [35]:

- Shift to the left (oxygen will bind more to the Hb), which happens when pH increases, temperature decreases, or the level of 2,3 DPG decreases.
- Shift to the right (oxygen will be released from Hb), which happens when pH drops, temperature increases, or the level of 2,3 DPG increases.

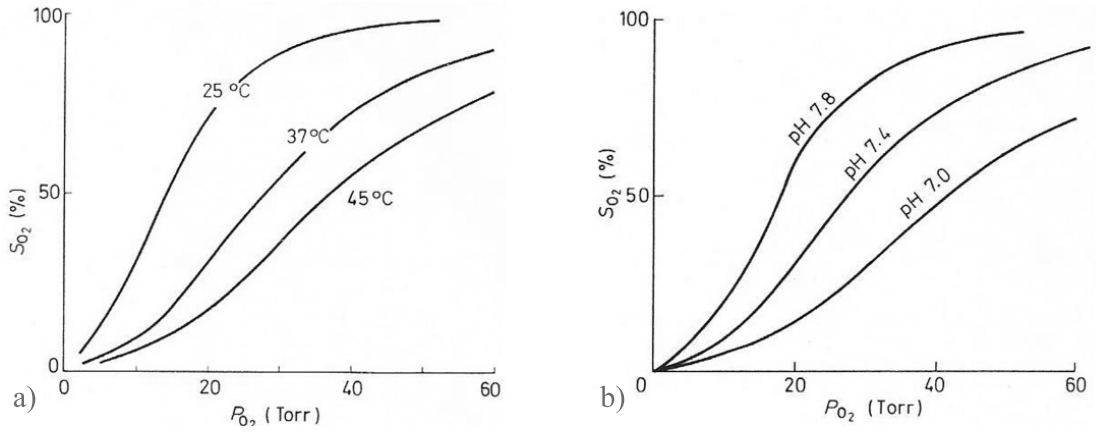

Figure 1.2.7: The oxygen dissociation curve when a) temperature changes and b) pH changes. The curve shifts to the left when temperature drops, pH increases. The curve shifts to the right when temperature rise, pH decreases [35].

When the oxygen dissociation curve shifts to the right, oxygen will be released more into plasma and then delivered into interstitial fluid and uptaken by cells for the metabolic process. On the other hand, when the oxygen dissociation curve shifts to the left, oxygen will bind more to the haemoglobin and the amount of oxygen delivered to the cells via plasma will decrease.

1.3 Motivation for research

In this work, we aim to investigate the behaviour of flow in the liver lobule treated as a porous medium of Bonfiglio et al [11] by adding some important physiological features that were not considered in previous studies. Another objective is to investigate the effect of several parameters used in the model on the flows of fluid by varying the values from the normal physiological value, which can represent some clinical conditions.

In general, changing a lot of flow rate in physiological condition is not common since the system has a feedback mechanism to control the flow dynamic [36]. However, in some special circumstances, the relative flow rate can change dramatically such as after a transplantation of a small-size liver or post-partial hepatectomy condition, when some part of the liver is resected and the remaining tissue has to expose the same amount of blood as before the resection [37].

Partial hepatectomy is required in segmental liver transplantation or some liver diseases such as hepatic cancer, intrahepatic gall stone etc. In segmental liver transplantation, healthy liver tissue of the donor is partially resected and transplanted into the recipient's body, whilst the remainder tissue of the donor still functions [38][39]. The other purpose of partial hepatectomy is to resect the pathological parts, that caused by some liver diseases, and preserve as much as possible of the healthy part in order to maintain the physiological functions.

In both cases, after resection, if the amount of functional liver tissue in the patient is significantly lower than normal, it can cause a post-hepatectomy effect, which can cause liver injury due to a smaller liver receiving a greater blood flow per unit mass of tissue. This condition is known as small-for-size syndrome. Therefore, there is a limitation on the volume of the liver that can be resected [38].

Hence, in this study, we aim to find the relationship between input pressure and change of haemodynamic of the liver. The results can be used further to evaluate how much pressure and flow volume a liver can withstand after partial resection.

As stated previously, there are only a few mathematical models of the liver microcirculation and some important features are yet explored. In this work, we therefore aim to study these significant physiological properties such as the effect of tissue elasticity, flow in the interstitial space, and oxygen distribution.

Tissue elasticity is thought to play an important role in the mechanics of liver due to two experimental studies carried out by the groups of Dahmen and Condon. Dahmen et al carried out in vivo experiments on the hepatic microcirculation in the pig liver [40]. They measured the portal flow and the mean portal pressure when the liver was partially resected from 0 percent (control) to 97 percent of the total liver volume.

We rescale the data from their work to generate the relationship between flow through

the liver and blood pressure drop across the liver. The portal flow was rescaled by dividing by the remaining proportion of liver. The resulting graph is shown in figure 1.3.1 and it shows a nonlinear relationship between flow and pressure, which could be explained by the compliance of the tissue. Normally, the relationship of pressure and flow in a straight rigid pipe is linear. However, if the vascular wall is elastic, higher sinusoidal pressure is expected to stretch the wall out, giving volumetric expansion of the sinusoidal space. As a result, the amount of blood flowing through the liver is expected to increase faster than linearly, when the pressure rises, which agrees with Dahmen et al's results.

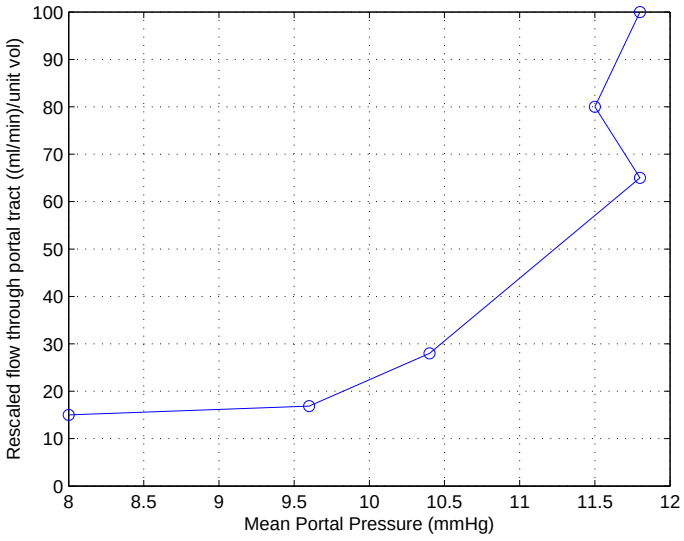

Figure 1.3.1: Rescaled flow-pressure relationship in the portal vein (Data from the experiment of Dahmen et al [40]).

Condon et al measured pressure and flow of the portal vein in an isolated, perfused calf liver. They found that when the flow rate increases, the resistance of the sinusoids also increases. The graph between the two parameters is shown in figure 1.3.2. However, the curvature is opposite to Dahmen's experiment and cannot be explained by the elastic property of the tissue of the liver lobules. They suggested that the behaviour could result from the role of endothelin-1 and stellate cells, both of which work as constrictors of the liver sinusoids. When the constrictors detect high blood pressure, they constrict to reduce the diameter of the inlet vessels in order to decrease the amount of blood flow. This would cause increased resistance at higher pressures, explaining the curvature of the graph. [41][42][43][44][45].

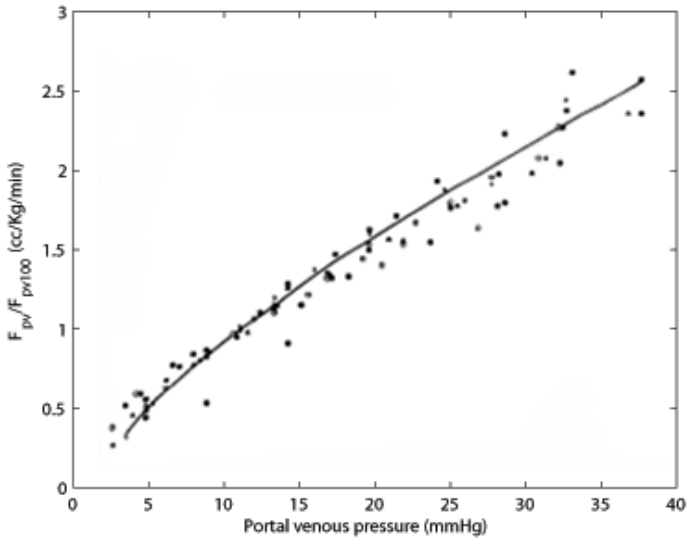

Figure 1.3.2: Pressure-flow relationship in portal vein from the experiment of Condon et al [41].

In summary, the two studies provide different patterns of the relationship between pressure and flux in the liver. Hence, we aim to study this pressure-flux relationship by investigating the effect of tissue elasticity. For the purposes of the project, we take a purely mechanical viewpoint and neglect the effect of endothelin-1 and stellate cells.

Furthermore, flow of interstitial fluid might be important in some situations. There are some common clinical conditions related to the excess interstitial fluid of the liver, such as ascites, and this is a common feature in severe cirrhosis or liver cancer. The ascitic fluid comes mainly from the interstitial space within the liver, and is produced more rapidly when the liver pressure increases [46]. Here we are interested in the production of interstitial fluid resulted from changing of parameters including the portal tract pressure. The result could give us an insight of the importance of interstitial fluid and lead to the estimation of the amount of ascitic fluid by the measurement of portal pressure, and vice versa.

Another important feature of the haemodynamics is the oxygen transportation as hepatocytes need oxygen for the metabolic process. Insufficient oxygen supply could lead to ischaemia, and ultimately to cell death. The study of the oxygen transportation could give a prediction of how much oxygen the liver cells receive in some conditions, such as high pressure or low flow. Moreover, the study of the effect of relevant parameters could give us information that which physiological parameter that affect the oxygen distribution most.

Furthermore, since every cell requires an adequate supply of oxygen, we expect the geometry of the blood vessels to be optimised to ensure as even a distribution as possible. As mentioned previously, histological sections of the liver show that the shape of liver lobules is an irregular unsymmetrical polygon rather than a regular symmetrical hexagon like the classical model described. This motivates an investigation to compare between the classical hexagonal geometry and other geometries by using the effectiveness of blood and oxygen distribution as the criteria. This should include the study of the effect of vascular septa, the interconnecting vessels between the portal tracts, on the oxygen supply. The result could tell us what is the optimal arrangement of the vessels of the lobule and answer the question of whether the classical lobule is the most appropriate model to represent the liver lobule in physiological modelling.

Chapter 2

Previous literatures on modeling of the liver lobule

There are only a few studies on mathematical modelling of the haemodymamics in the microcirculation of the liver lobule. Each work uses different approach to describe the model of liver lobule and we review each study here.

2.1 3D model of Rani et al.

Rani et al (2006) [47] worked on a rigid 3D model, based on the acinar model, consisting of two portal veins, two hepatic arteries, two sinusoids, and one centrilobular vein. Each portal vein and hepatic artery distribute blood to a sinusoid, which has a certain number of uniformly-distributed fenestrations on its wall. Blood is drained out via the

centrilobular vein at the end of the sinosoids.

They assume that the fluid is incompressible and governed by the Navier-Stokes equation:

$$\rho\left(\frac{\partial \mathbf{V}}{\partial t} + (\mathbf{V}\cdot\nabla\mathbf{V})\right) = -\nabla P + \boldsymbol{\nabla}\cdot\mathbf{T}, \tag{2.1.1}$$

$$\nabla\cdot\mathbf{V} = 0, \tag{2.1.2}$$

where $\mathbf{V}$, P, t, and $\mathbf{T}$ are the dimensionless velocity vector, pressure, time, and stress tensor, respectively.

The portal venous and hepatic arterial blood, driven by pressure boundary conditions, have different density and viscosity. The behaviours of blood as Newtonian and non-Newtonian fluid are investigated numerically using the finite volume software from CFDRC (CFD Research Corporation, Huntsville, AL), and the results are compared.

The velocity of blood across the cross-section are shown in figure 2.1.1 showing that the non-Newtonian model has flatten velocity profile at the middle, whilst the Newtonian model has a parabolic shape. This effect is due to the shear thinning effect included in the model.

For the non-Newtonian fluid, in which the density is a function of shear rate, the velocity

decreases from the inlets to the outlet which imply that the hepatocytes located near the centrilobular vein will receive less blood compared to the cells located nearer to the portal tracts. The simulation is shown in figure 2.1.2 that the flow is mainly driven by the hepatic artery pressure without mixing with portal venous blood. They also found secondary flows and eddy currents around the fenestrations in the sinusoids.

The model gives an insight of the flow within the sinusoids of the acinar model. However, the components of the model is specific to the certain numbers of vessels, especially the fenestrations of the sinusoids. There is also no potential connection between the sinusoids and between the sets of portal veins and hepatic arteries.

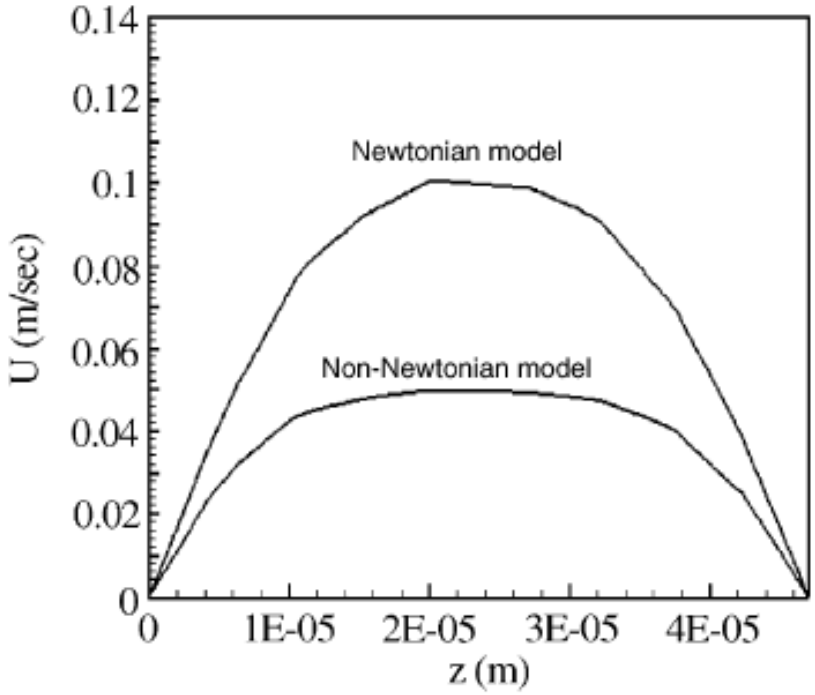

Figure 2.1.1: The comparison of axial velocity profiles across the cross-section of the vessel for the Newtonian and non-Newtonian blood flows [47].

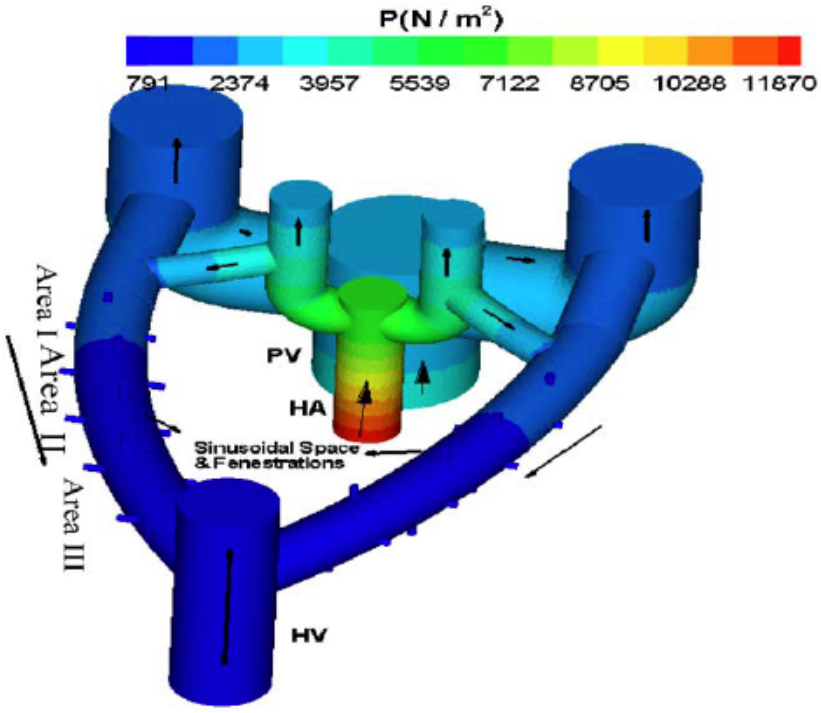

Figure 2.1.2: 3D model of blood flow in liver sinusoids. Each hepatic artery (HA) and hepatic portal vein (PV) provide blood into a sinusoid that has fenestrations along the length. Two sinusoids drain the blood out via the hepatic vein (HV) [47].

2.2 Electrical analogue Models of van der Plaats et al. / Debbaut et al.

Van der Plaats et al simulated the hepatic circulation numerically by treating the vascular components of the liver (portal vein, hepactic artery, and hepatic vein) and their branches as a cascade of electrical components [48] (see equivalent model in figure 2.2.2). The Navier-Stokes equations are translated into four electrical components of resistance, inertia of the blood, compliance, and viscoelasticity of the vessels. All electrical analogues are implemented in Orcad Pspice 9.2 for the simulation, and all parameters values, including pulsatile boundary pressures, were from the data collected from $10 - 15$ kg dogs used in the experiment by Mall in the early 1900's [7].

The results show that there is a large pressure drop along the branching generation of the hepatic artery. The largest pressure drop is at the $7th$ generation and; for subsequent generations, the pressures of hepatic artery and centrilobular vein are similar (figure 2.2.1). The total flow was calculated and compared to the data from Mall's study. However, the flow rate of their work is much higher than Mall's work. Van der Plaats et al suggested that the discrepancy could result from low-pressure perfusion in Mall's casting process causing less expansion in diameters of the vessels.

Debbaut et al used the same principle as Van der Plaats et al, but used the data from a human liver [49]. The anatomical parameters were collected by using a vascular corro-

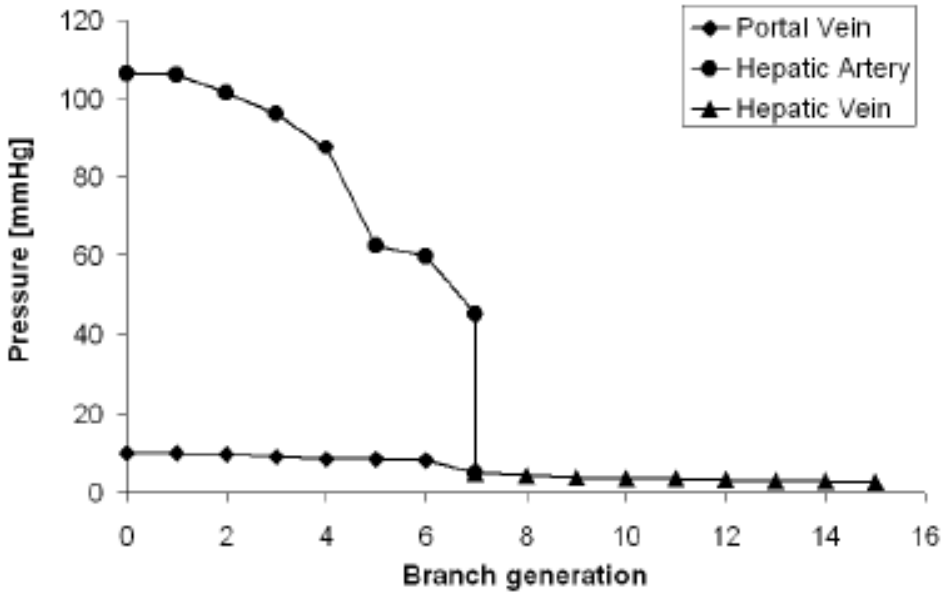

Figure 2.2.1: The pressure profile in each branching generation of portal vein, hepatic artery, and hepatic vein [48].

sion casting technique, micro-CT imaging, and image processing (figure 2.2.3). However, parameters from only first 5-6 generations of each of the three trees of vessels (hepatic artery, hepatic portal vein, and hepatic vein) were collected due to the limitations of the computational resolution. As a result, they estimated the higher generations by using extrapolation of the trend lines of the lower generations (figure 2.2.2).

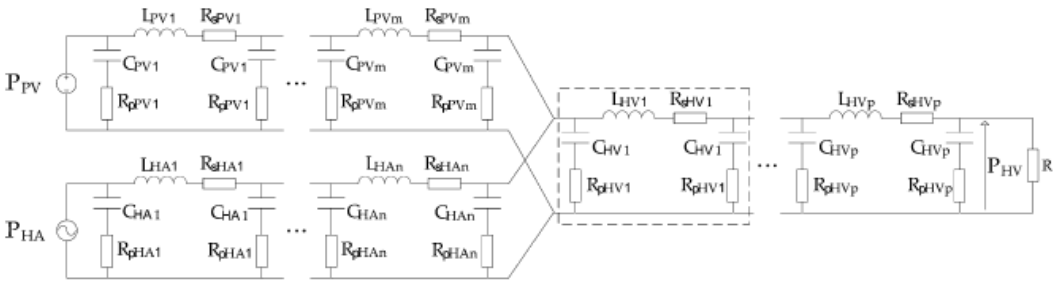

Figure 2.2.2: Electrical analogue model of the liver used by Debbaut et al (2011). Each branch of the hepatic artery (HA), hepatic portal vein (PV), and hepatic vein consists of four components: the vascular resistance (R_S), the vascular compliance (L), the elasticity (C), and the viscoelasticity (R_p) [49].

Both models are based on the casting technique and the availability of data collected at the higher generations of vessels is limited. Moreover, the models are only specific to certain livers from the experiments. Different livers may have different branching pattern in each generations. Further data collection maybe needed.

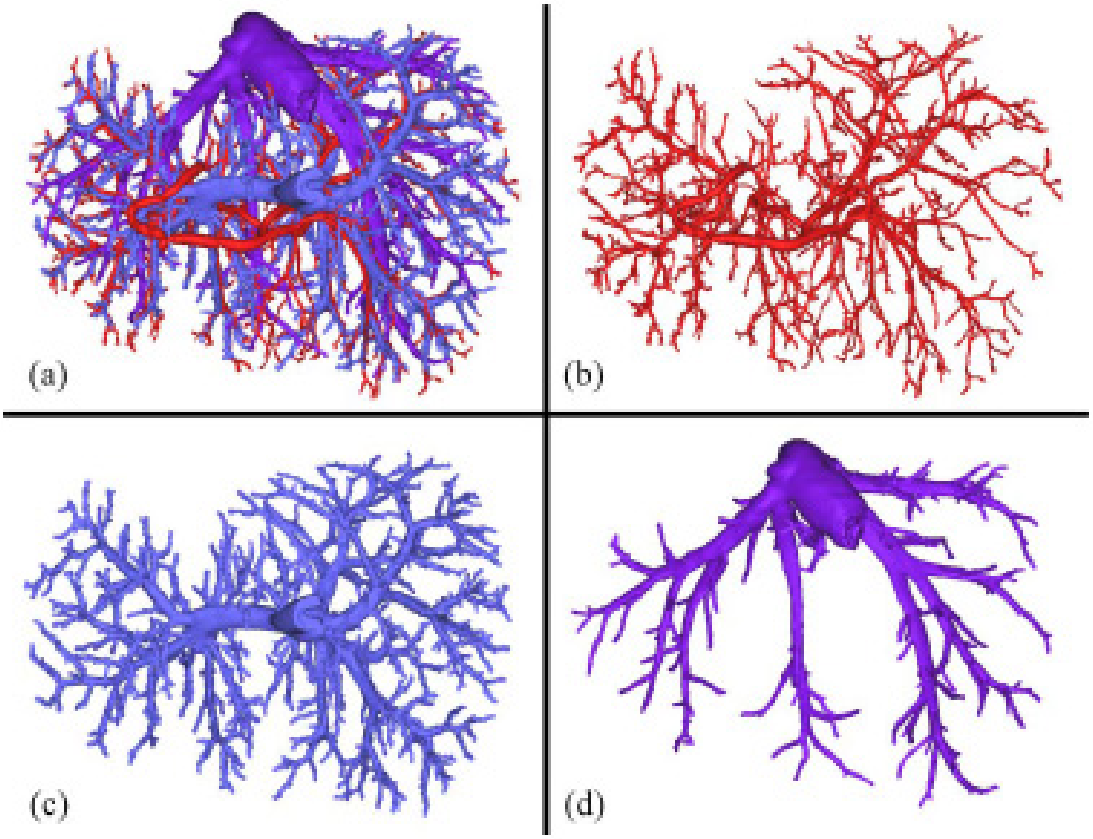

Figure 2.2.3: The 3D reconstruction of a) all three vascular trees, b) the hepatic arteries, c) the portal veins, and d) the hepatic veins. The images are from the work of Debbaut et al.) [49].

2.3 Biphasic Model of Ricken et al.

Ricken et al studied remodelling of the sinusoids, which occurs after outflow obstruction as a result of liver resection, using a biphasic model [50]. The model is based on three assumptions. Firstly, they assumed that the liver tissue consists of two phases: a porous solid phase and a fluid phase. Secondly, there is no mass exchanges between the solid and fluid phases. Finally, the temperature and energy interchanges during the remodelling process is negligible.

The process of remodelling is driven by the blood pressure gradient and the deformation of the solid phase and the motion of the fluid phase are naturally described by Lagrangian and Eulerian kinematics, respectively (see figure 2.3.1). The motion of both phases are connected together by the interaction force $\hat{\mathbf{p}}^{\mathbf{F}} = -\hat{\mathbf{p}}^{\mathbf{S}}$. The base permeability in the model can be described by using the solid permeability k_S and the effective shear viscosity μ_F:

$$\frac{n_F^2}{\alpha_F} = \left(\frac{n_F}{1 - n_S}\right)_m \frac{k_S}{\mu_F}, \tag{2.3.1}$$

where n_F and n_S are the fluid and solid volume fractions, respectively, α_F is a constant, the subscript S and F denote the solid and fluid phases, respectively, and m denotes that the parameters ardimensionless parameters.

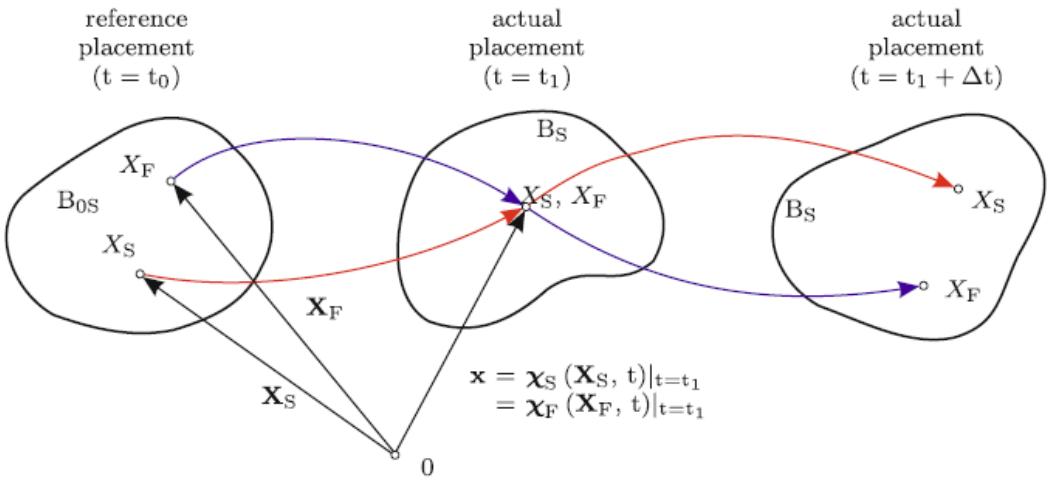

Figure 2.3.1: Kinematics of the rearrangement of solid (S) and fluid (F) components over time [50].

The mass and momentum conservation of both phases is also included. Moreover, in the remodelling process, the concept of entropy inequality is taken into account. The model is simulated numerically using the Galerkin procedure in the finite element method. The results in figure 2.3.2 show the remodelling process of the sinusoidal vessels over time in the healthy case. Initially the vessels are assumed to be aligned perpendicular to the portal tracts and centrilobular veins, and the model should show how this orientation changes over time. The orientation of the sinusoidal tract is driven by pressure gradient from the portal tract to the centrilobular vein.

Figure 2.3.3 shows the remodelling process of the sinusoids over time in the focal obstruction case. The model shows sinusoids reorientate towards the nearest centrilobular

vein.

The model includes solid and fluid parts, and describe the interaction between both components governed by pressure gradient. However, the model do not include the interstitial space, which is the channel for excess fluid to drain out.

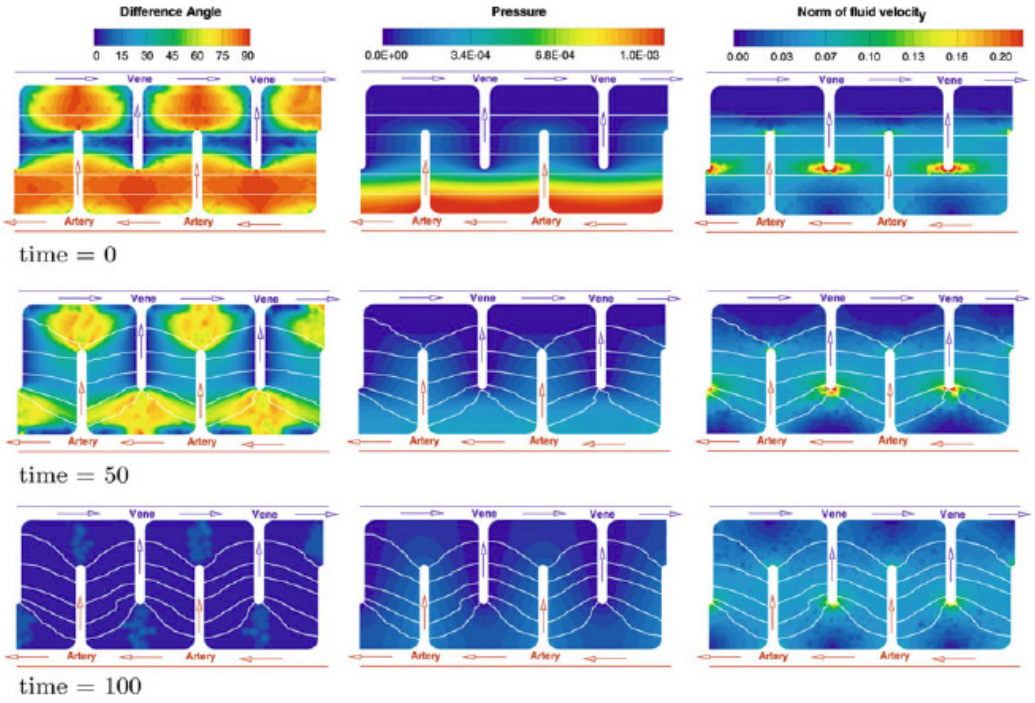

Figure 2.3.2: Biphasic model of the liver perfusion shows the rearrangement of the sinusoids in physiological condition after at the start [50].

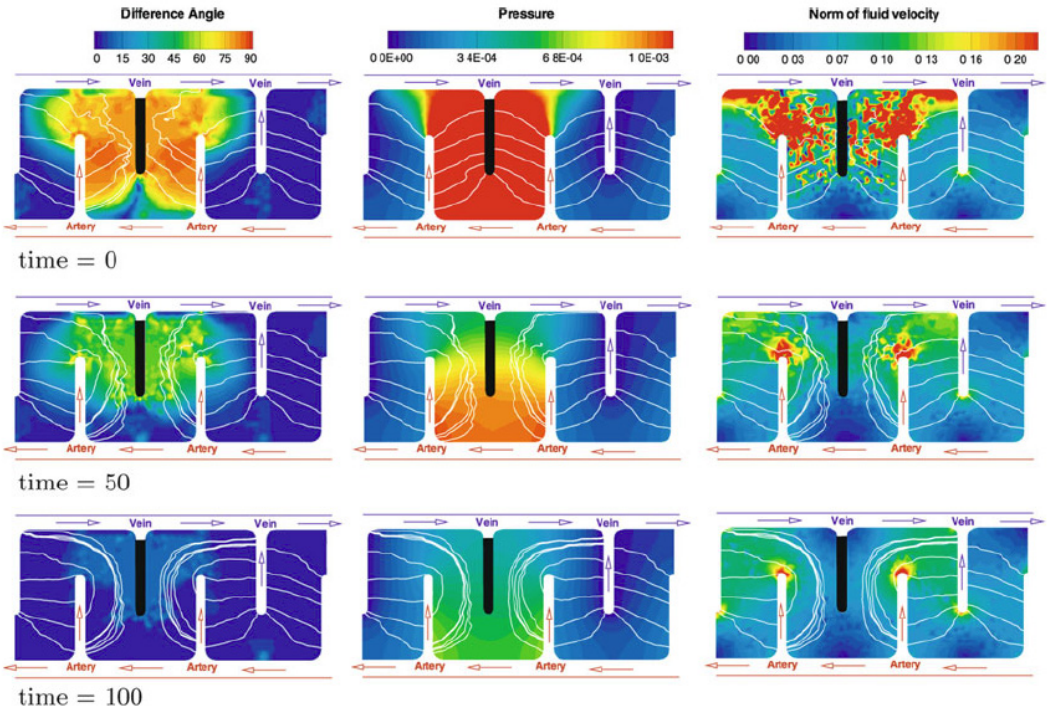

Figure 2.3.3: Biphasic model of the liver perfusion shows the remodelling process of the sinusoids after an ouflow obstruction at the centrilobular vein (black rod) [50].

2.4 Porous medium model of Bonfiglio et al.

The author of this thesis was involved in the porous medium model of Bonfiglio et al. Moreover, the preliminary model used in this thesis is heavily based on the model of Bonfiglio et al; therefore, we describe it here in more detail than the other models.

Bonfiglio et al [11] worked on a rigid 2D model of liver lobule with hexagonal cross-section based on the geometry of the classical lobule. In the model, a portal tract is located at each vertex and a centrilobular vein is located at the centre of the hexagon (figure 2.4.1). Only sinusoidal flow is considered in this model. The axial length is assumed to be long compared to the diameter of the lobule; therefore, the end effects are negligible and the flow is then considered as two dimensional across the cross-section.

Two types of lobule are considered: treating lobule as an isotropic medium or an anisotropic medium in which the blood flow follows Darcy's law. In the anisotropic model, we have

$$v = -\mathbf{K} \cdot \boldsymbol{\nabla} p, \tag{2.4.1}$$

where v is blood velocity, p is blood pressure in the portal tract, and $\mathbf{K}$ is the hydraulic conductivity tensor of the lobule. Note that $\mathbf{K} = \mathbf{k}/\mu$ where $\mathbf{k}$ is the permeability tensor of the lobule and μ is dynamic blood viscocity. In Cartesian coordinates, the

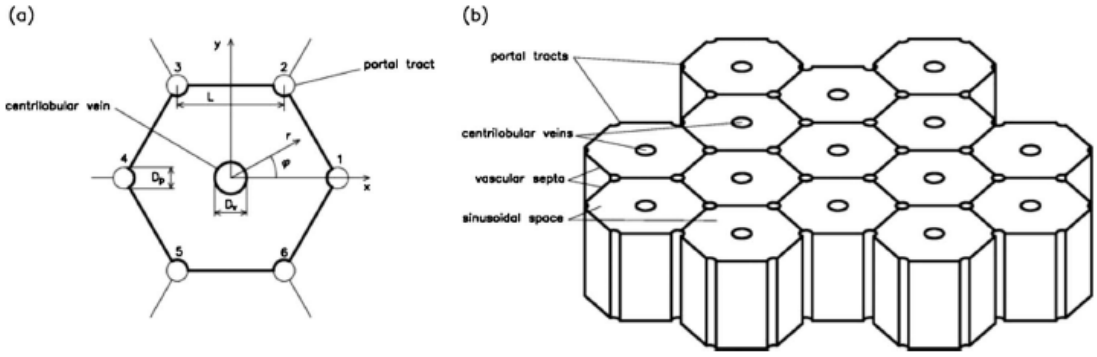

Figure 2.4.1: a) Cross-section of the classical lobule. b) A lattice of classial lobules [11].

permeability tensor $\mathbf{k}$ can be written in terms of the radial permeability k_r and the azimuthal permeability k_θ. The medium is assumed to be homogenous; therefore, k_r and k_θ are constants and typically $k_r > k_\theta$. By transforming to Cartesian coordinates, we obtain

$$\mathbf{k} = \begin{pmatrix} \frac{k_r x^2 + k_\theta y^2}{x^2+y^2} & \frac{(k_r - k_\theta)(xy)}{x^2+y^2} \\ \\ \frac{(k_r - k_\theta)(xy)}{x^2+y^2} & \frac{k_r y^2 + k_\theta x^2}{x^2+y^2} \end{pmatrix}. \tag{2.4.2}$$

Note that, in the isotropic model, k is a scalar quantity, also K. Blood is assumed to be a Newtonian fluid and incompressible; giving

$$\boldsymbol{\nabla} \cdot \mathbf{v} = 0. \tag{2.4.3}$$

For the boundary conditions, pressures are prescribed at the portal tracts and cen-

trilobular vein. There is no flux across the edges of the lobule. The whole system is nondimensionalised and the solution is found numerically using the commercial software COMSOL Multiphysics. This software solves differential equations using a finite element method and the equations used in COMSOL can be provided in either differential form or in weak form.

Figure 2.4.2 a) and b) show the pressure and velocity contours, respectively, when the lobule is treated as an isotropic medium. The pressure is highest near the portal tracts and lowest near the centrilobular vein. The result also shows that the velocity of the blood is high near the portal tracts and the centrilobular vein but very low near the middle part of the edges.

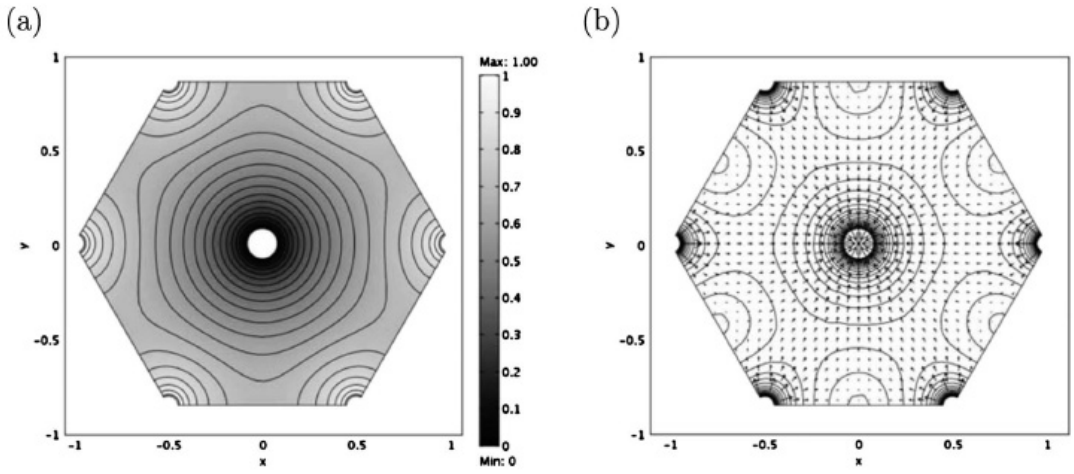

Figure 2.4.2: The sinusoidal pressure (a) and velocity profile (b) of the isotropic lobule [11].

The difference between pressure in the isotropic and anisotropic cases is shown in figure 2.4.3. It shows that, when changing the ratio k_r/k_θ from 2/1 to 3/1, the difference of the pressure distribution pattern is very small. It also shows that the area that has the largest pressure difference is near the edges of the vessels whilst the area along the line connecting portal tracts and the centrilobular vein has smaller pressure difference. The authors suggested this may result from the non-existence of the vascular septa in the model.

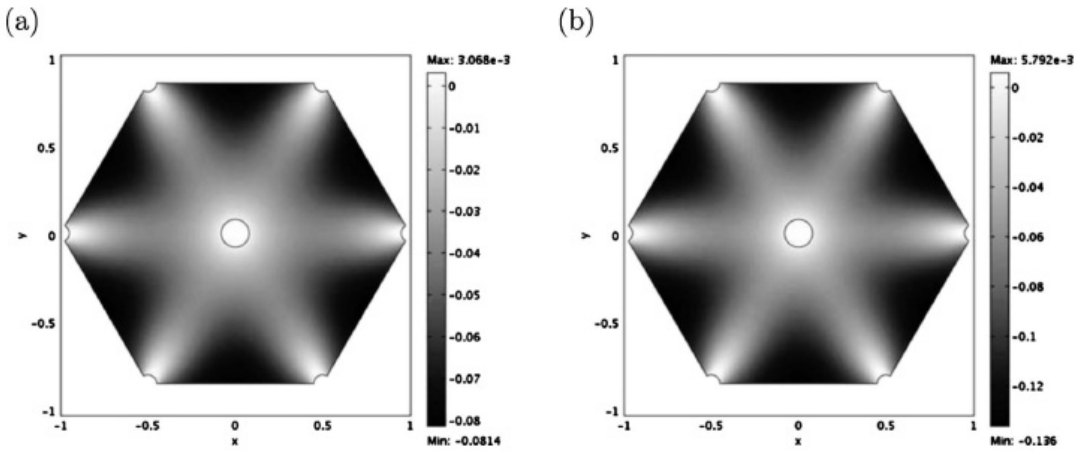

Figure 2.4.3: The pressure difference between isotropic and anisotropic cases when: (a) $k_r/k_\theta = 2/1$ and (b) $k_r/k_\theta = 3/1$ [11].

The deformable lobule due to poroelasticity was also investigated using the Biot formulation. The work was extended from the primary model done by the author of this thesis (will be described later in the next chapter). The anisotropic and the shear thinning properties were not included in this part since they were proved to have only a small

effect. However, the permeability of the sinusoids has changed due to the deformation with the following relationship:

$$K^* = \left(\frac{3}{\phi} - 1\right) \boldsymbol{\nabla}^* \cdot \mathbf{u}^* K_0^*, \tag{2.4.4}$$

where K^* and K_0^* are the dimensionless permeability of the deformed and undeformed lobule, respectively, ϕ is the porosity of the undeformed lobule, and $\mathbf{u}^*$ is the dimensionless displacement. Figure 2.4.4a shows the pattern of the deformation when the portal tract pressure is increased, while figure 2.4.4b shows the contour lines K^*/K_0^* when the lobule is deformed.

This liver lobule model will be further extended in the next chapters of this thesis. Several additional features are incorporated to the model, including flow of the interstitial fluid, oxygen transportation, and the effect of vascular septa.

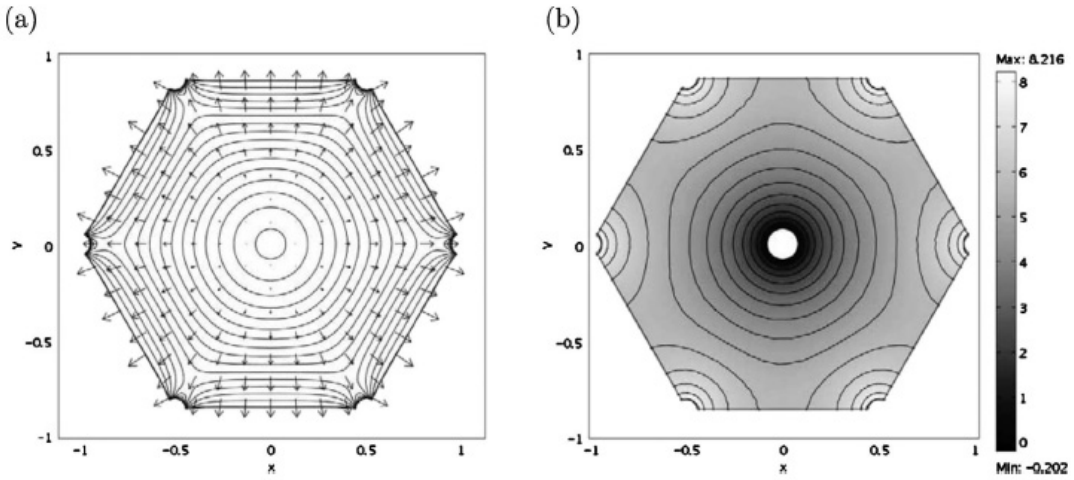

Figure 2.4.4: a) Displacement (arrows) and the countour lines of the lobule when the portal tract pressure is increased by 15from the normal value. b) Contour lines of the ratio K^*/K_0^* in the deformed lobule [11].

Chapter 3

Elastic model of the liver lobule

Soft tissues have elastic properties, which means they deform if there is a force applied. In the liver, tissue elasticity might be significant in the case of partial resection, in which the pressure in the portal venous tree is expected to be high. In this chapter, we aim to study the elastic behaviour of the liver tissue by developing two different elastic models: a linear elastic model and a poroelastic model.

3.1 Linear elastic model

3.1.1 Working hypothesis

Since the problem is complicated, we make several simplifying assumptions to the hexagonal model, used by Bonfigio et al, described previously:

- The deformation of the liver is caused by the pressure difference between high pressure inside the liver and low pressure outside the liver, leading to volumetric

expansion.

- The tissue of the liver is assumed to be a solid with linear elastic properties.
- The liver is assumed to be spherical and packed with many much smaller circular cylindrical lobules.
- We make simplifying assumptions about the geometry of the individual lobules:
  - Each lobule has a centrilobular vein along its axis that does not expand radially.
  - The lobule deforms axisymmetrically.
  - The axial expansion is assumed to be uniform and in proportion to the radial expansion at the outside of the lobule.

3.1.2 Cylindrical elastic lobule model

In normal physiological pressure conditions, the lobule has radius R_{l0} and length L_z while the centrilobular vein has radius R_{CV} (see figure 3.1.1). The value of radius R_{l0} is calculated by conserving the cross-sectional area of the hexagonal lobule from the work of Bonfiglio et al [11]; therefore, $\pi R_{l0}^2 = \frac{3\sqrt{3}L^2}{2}$, where L is the length of the edge of the lobule ($L = 500\mu m$). For the radius of the spherical liver, R_L, the normal volume is conserved ($\approx 1520\ cm^3$) from the literature [51]; thus, we can find R_L from $\frac{4}{3}\pi R_L^3 = 1520\ cm^3$. The parameter values using in this chapter are shown in table 3.1.

Table 3.1: Physiological parameter values used in the elastic model

Symbol	Description	Typical Value	Reference
R_{l0}	Radius of the lobule	455×10^{-6} m	see section 3.1.2
R_{CV}	Radius of the centrilobular vein	40×10^{-6} m	[51]
R_L	Radius of the liver	0.07 m	see section 3.1.2
E	Young's modulus of the liver	6 kPa	[82]
ν	Poisson's ratio of the liver	0.431	[52]
$P_0 = P_{PT} - P_{CV}$	The difference of portal tract and centrilobular venous pressure	2.95 mmHg	[11]

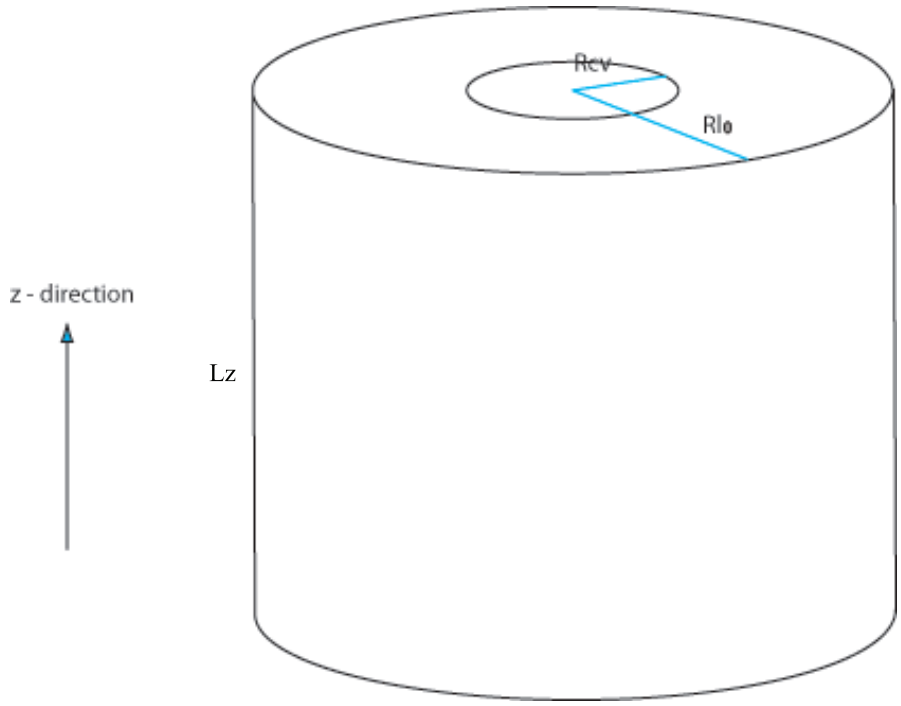

Figure 3.1.1: Cylindrical model of the elastic liver lobule with radius R_{l0} and length L_z. The centrilobular vein has a radius of R_{CV}.

Derivation of model equation

Since we assume uniform expansion in the z–direction, we neglect the third dimension and consider a 2D model of stress and strain by using the Biot model of stress. In this model, stress is related to strain by [53]

$$\boldsymbol{\sigma} = 2\mu\boldsymbol{\epsilon} + \lambda(Tr(\boldsymbol{\epsilon}))\mathbf{I}, \tag{3.1.1}$$

where $\boldsymbol{\sigma}$ is the stress tensor, μ and λ are the *Lamé* first and second parameters, respectively, and $\boldsymbol{\epsilon}$ is the strain tensor, given in Cartesian coordinates by

$$\epsilon_{ij} = \frac{1}{2}(u_{i,j} + u_{j,i}), \tag{3.1.2}$$

where u_i and u_j are the components of the incremental displacements of the tissue in the x and y directions, respectively, and commas denote partial derivatives in those directions.

The *Lamé* parameters can be written in terms of Young's modulus, E, and Poisson's ratio, ν, of the liver as

$$\mu = \frac{E}{2(1+\nu)} \quad , \quad \lambda = \frac{E\nu}{(1+\nu)(1-2\nu)}. \tag{3.1.3}$$

Assuming mechanical equilibrium,

$$\boldsymbol{\nabla} \cdot \boldsymbol{\sigma} = 0. \tag{3.1.4}$$

Combining (3.1.1) – (3.1.4), we obtain

$$\mu \nabla^2 \mathbf{u} + (\mu + \lambda) \boldsymbol{\nabla} (\boldsymbol{\nabla} \cdot \mathbf{u}) = 0. \tag{3.1.5}$$

Derivation of boundary conditions

We assume the centrilobular vein is rigid and cannot expand; thus,

$$\mathbf{u} = 0, \quad \text{at} \quad r = R_{CV}, \tag{3.1.6}$$

and that the lobule expands by a factor $1+C$ (to be determined) at the outer boundary:

$$\mathbf{u} = C R_{l0} \boldsymbol{e_r}, \quad \text{at} \quad r = R_{l0}, \tag{3.1.7}$$

where $\boldsymbol{e_r}$ is the unit vector in radial direction.

Thus the expansion in the z-direction has ratio $1 + C$,

$$u_z = Cz. \tag{3.1.8}$$

Nondimensionalisation of variables and parameters

We nondimensionalise the system, using *'s to denote nondimensional variables:

$$\mathbf{u}^* = \frac{\mathbf{u}}{R_{l0}}, \tag{3.1.9}$$

$$\nabla^* = R_{l0}\nabla, \tag{3.1.10}$$

$$E^* = \frac{E}{P_0} \quad , \quad \nu^* = \nu, \tag{3.1.11}$$

where P_0 is the pressure difference across the lobule between the portal tract pressure, P_{PT}, and the centrilobular vein pressure, P_{CV}, ($P_0 = P_{PT} - P_{CV}$).

Thus, equation (3.1.5) becomes

$$\frac{\mu}{R_{l0}^2}\nabla^{*2}(R_{l0}\mathbf{u}^*) + \frac{(\mu+\lambda)}{R_{l0}}\boldsymbol{\nabla}^*(\boldsymbol{\nabla}^*\cdot\mathbf{u}^*) = 0. \tag{3.1.12}$$

Substituting (3.1.3) into (3.1.12) gives

$$\nabla^{*2}\mathbf{u}^* + \frac{1}{1-2\nu^*}\boldsymbol{\nabla}^*(\boldsymbol{\nabla}^*\cdot\mathbf{u}^*) = 0. \tag{3.1.13}$$

Since we assume an axisymmetric solution, in cylindrical polar coordinates, we have $\mathbf{u}^* = u_r^*(r^*)\boldsymbol{e_r}$, where u_r^* is the displacement in the radial direction and $\boldsymbol{e_r}$ is the radial unit vector.

We can then derive

$$\nabla^{*2}\mathbf{u}^* = \left(\nabla^{*2}u_r^* - \frac{u_r^*}{r^{*2}}\right)\mathbf{e_r}, \tag{3.1.14}$$

$$\boldsymbol{\nabla}^*\cdot\mathbf{u}^* = \frac{1}{r^*}\frac{\partial}{\partial r^*}(r^*u_r^*), \tag{3.1.15}$$

$$\boldsymbol{\nabla}^*(\boldsymbol{\nabla}^*\cdot\mathbf{u}^*) = \frac{\partial}{\partial r^*}\left(\frac{1}{r^*}\frac{\partial}{\partial r^*}(r^*u_r^*)\right)\mathbf{e_r}. \tag{3.1.16}$$

Then, equation (3.1.13) becomes

$$\frac{\partial^2 u_r^*}{\partial r^{*2}} + \frac{1}{r^*}\frac{\partial u_r^*}{\partial r^*} - \frac{u_r^*}{r^{*2}} = 0, \tag{3.1.17}$$

which has general solution

$$u_r^* = \frac{c_1}{r^*} + c_2 r^*. \tag{3.1.18}$$

We can find the constants c_1 and c_2 from the boundary conditions.

Nondimensionalisation of boundary conditions

The nondimensionalised boundary conditions are

$$u_r^* = 0 \quad , \quad at \quad r^* = R_{CV}^*, \tag{3.1.19}$$

$$u_r^* = CR_{l0}^* \quad , \quad at \quad r^* = 1. \tag{3.1.20}$$

Solution for u_r^*

Using the boundary conditions above to find c_1 and c_2, we find

$$c_1 = -\frac{CR_{l0}^{*2}R_{CV}^{*2}}{R_{l0}^{*2} - R_{CV}^{*2}}, \tag{3.1.21}$$

$$c_2 = \frac{CR_{l0}^{*2}}{R_{l0}^{*2} - R_{CV}^{*2}}. \tag{3.1.22}$$

Therefore, the solution for u_r^* is

$$u_r^* = \frac{CR_{l0}^{*2}}{R_{l0}^{*2} - R_{CV}^{*2}} \left(r^* - \frac{R_{CV}^{*2}}{r^*} \right). \tag{3.1.23}$$

The unknown constant C will be found later by considering a model of the whole liver.

3.1.3 Spherical model of the whole liver

In order to find the value of C, for simplicity, we consider an idealised geometry of the whole liver as a perfect sphere of radius R_L with spherical symmetry. We work in spherical polar coordinates with R being the radial coordinate centred on the liver.

Derivation of model equation

We assume deformation of the liver is driven by the normal stress at the liver surface, which is given by the difference between pressure inside the liver (P_{liver}) and the external pressure in the body (P_{body}):

$$\boldsymbol{\sigma}\mathbf{n} = (P_{liver} - P_{body})\mathbf{n}. \tag{3.1.24}$$

Using (3.1.1), this becomes

$$2\mu\epsilon\mathbf{e_R} + \lambda(Tr(\epsilon))\mathbf{e_R} = (P_{liver} - P_{body})\mathbf{e_R}. \tag{3.1.25}$$

As the whole liver model expands in the same manner as the lobules, equation (3.1.5) applies

$$\mu\nabla^2\mathbf{U} + (\mu + \lambda)\boldsymbol{\nabla}(\boldsymbol{\nabla} \cdot \mathbf{U}) = 0, \tag{3.1.26}$$

where U_R is the displacement in spherical polar coordinates, and $\mathbf{U} = U_R\boldsymbol{e_R}$.

Derivation of boundary conditions

For the boundary conditions, regularity implies there is no expansion at the centre of the sphere, whilst the stress at the surface of the liver follows equation (3.1.25). These conditions become

$$U_R = 0, \quad \text{at} \quad R = 0, \tag{3.1.27}$$

$$(\lambda + 2\mu)\frac{\partial U_R}{\partial R} + 2\lambda\frac{U_R}{R} = P_{liver} - P_{body} \quad \text{at} \quad R = R_L. \tag{3.1.28}$$

Nondimensionalisation of variables and parameters

We nondimensionalise the system, using *'s to denote nondimensional variables

$$\mathbf{U}^* = \frac{\mathbf{U}}{R_L}, \tag{3.1.29}$$

$$\nabla^* = R_L \nabla, \tag{3.1.30}$$

$$P^* = \frac{P}{P_{00}} \tag{3.1.31}$$

$$E^* = \frac{E}{P_{00}}, \quad \nu^* = \nu, \tag{3.1.32}$$

where P is pressure, P_{00} is the pressure difference between inside and outside of the liver ($P_{00} = P_{liver} - P_{body}$).

The governing equation (3.1.13) becomes

$$\nabla^{*2}\mathbf{U}^* + \frac{1}{1-2\nu^*}\nabla^*(\nabla^* \cdot \mathbf{U}^*) = 0. \tag{3.1.33}$$

Using spherical polar coordinates (R^*, θ^*, ϕ^*) and assuming spherical symmetry ($\mathbf{U}^* = U_R^*(R^*)\mathbf{e_R}$), where $\mathbf{e_R}$ is the radial unit vector, we obtain

$$\nabla^{*2}\mathbf{U}^* = \left(\frac{1}{R^{*2}}\frac{\partial}{\partial R^*}(R^{*2}\frac{\partial U_R^*}{\partial R^*}) - \frac{2U_R^*}{R^{*2}}\right)\mathbf{e_R}, \tag{3.1.34}$$

$$\boldsymbol{\nabla}^* \cdot \mathbf{U}^* = \frac{1}{R^{*2}}\frac{\partial}{\partial R^*}(R^{*2}U_R^*), \tag{3.1.35}$$

$$\boldsymbol{\nabla}^*(\boldsymbol{\nabla}^* \cdot \mathbf{U}^*) = \frac{\partial}{\partial R^*}\left(\frac{1}{R^{*2}}\frac{\partial}{\partial R^*}(R^{*2}U_R^*)\right)\mathbf{e_R}. \tag{3.1.36}$$

Then we can rewrite equation (3.1.33) as

$$\left(\frac{1}{R^{*2}}\frac{\partial}{\partial R^*}(R^{*2}\frac{\partial U_R^*}{\partial R^*}) - \frac{2U_R^*}{R^{*2}}\right) + (\frac{1}{1-2\nu^*})\frac{\partial}{\partial R^*}\left(\frac{1}{R^{*2}}\frac{\partial}{\partial R^*}(R^{*2}U_R^*)\right) = 0$$
$$, \quad \text{for} \quad 0 < R^* < R^*_{liver}, \tag{3.1.37}$$

which is our governing equation for the nondimensionalised displacement of the internal part of the liver U_R^*.

Nondimensionalisation of boundary conditions

The boundary conditions are

$$U_R^* = 0, \quad \text{at} \quad R^* = 0, \tag{3.1.38}$$

$$(\lambda + 2\mu)\frac{\partial U_R^*}{\partial R^*} + 2\lambda\frac{U_R^*}{R^*} = 1, \quad \text{at} \quad R^* = R_{liver}^*. \tag{3.1.39}$$

Solution for U_R^*

Using the above boundary conditions, equation (3.1.37) can be simplified into

$$\frac{\partial^2 U_R^*}{\partial R^{*2}} + \frac{2}{R^*}\frac{\partial U_R^*}{\partial R^*} - \frac{2U_R^*}{R^{*2}} = 0, \tag{3.1.40}$$

which has general solution

$$U_R^* = \frac{c_1}{R^{*2}} + c_2 R^*. \tag{3.1.41}$$

Since $U_R^* = 0$ at $R^* = 0$ we must have $c_1 = 0$. Then,

$$c_2 = \frac{1 - 2\nu^*}{E^*}, \tag{3.1.42}$$

and note that $c_2 = C$ in equation (3.1.23). And so

$$U_R^* = \frac{1 - 2\nu^*}{E^*} R^*. \tag{3.1.43}$$

Thus the liver expands uniformly by the ratio $C = \frac{1-2\nu^*}{E^*}$.

3.1.4 Results

Calculation of C. Since elastic properties of porcine liver tissue are easier to obtain than those of human liver tissue, we use the Young's modulus and Poisson's ratio of porcine liver which have values of 6 kPa and 0.431, respectively [82] [52]. From equation (3.1.42), we redimensionalise it into

$$C = \frac{(1 - 2\nu)(P_{liver} - P_{body})}{E}, \tag{3.1.44}$$

For the linear elasticity to be valid, we apply a small pressure difference $(P_{liver} - P_{body})$ of 1 mmHg, and substitute those values of the Young's modulus and Poisson's ratio, from equation (3.1.44), we obtain

$$C = 0.003. \tag{3.1.45}$$

Since the value of C is small ($\approx 0.3\%$), this calculation suggests that the volumetric expansion of the solid part of the tissue is not great. Therefore, if we only take the solid elasticity of the tissue into account, the lobules do not deform dramatically. In the last section of this chapter, we will further investigate behaviour of the deformation if the lobules are treated as poroelastic material.

3.2 Elastodynamic model

In this section, we explore the dynamic behaviour of the model described in the previous section. We consider the effect of time variation in abdominal pressure, $P(t)$, which occurs due to respiration. For simplicity, we assume the forcing pressure $P(t)$ is sinusoidal, that is

$$P(t) = P_0 \sin kt \tag{3.2.1}$$

where P_0 is the maximum amplitude of the pressure and k is the angular frequency.

The elastodynamic equation is applied to both the single lobule model and the whole liver model. Similar to the previous section, we assume that, in normal physiological condition, the lobule is an axisymmetric cylinder with radius R_{l0} and a centrilobular vein with radius R_{CV} located along the axis, whilst the liver is a spherical symmetric sphere with radius R_L. The working hypothesis used in this model is the same as in section 3.1.1. The relevant parameter values used in the model are listed in table 3.1.

3.2.1 Whole liver model

We first investigate the elastodynamic behaviour of the whole liver. The elastodynamic equation, described by Wang in 1993, for a sphere is [54]

$$\frac{E(1-\nu)}{(1+\nu)(1-2\nu)}\left(U_{RR}+\frac{2}{R}U_R-\frac{2}{R^2}U\right)=\rho U_{tt}, \tag{3.2.2}$$

where U is the radial displacement of the liver tissue, R is the distance from the centre of the liver, ρ is the tissue density (assumed to be the same as the lobule density), E is Young's modulus, ν is Poissons' ratio, and t is time.

We use the method of the separation of variables to solve the equation. Thus, we set

$$U(R,t)=X(R)G(t), \tag{3.2.3}$$

where $X(R)$ is the space-only dependent variable and $G(t)$ is the time-only dependent variable.

From the two above equations, we obtain

$$\frac{X''}{X}+\frac{2}{R}\frac{X'}{X}-\frac{2}{R^2}=\frac{\rho(1+\nu)(1-2\nu)}{E(1-\nu)}\frac{G''}{G}=-\gamma, \tag{3.2.4}$$

where γ is a constant. We then solve for X and G separately using equation (3.2.4).

Function of R

From equation (3.2.4), we obtain

$$R^2X'' + 2RX' + (\gamma R^2 - 2)X = 0. \tag{3.2.5}$$

In order to solve this equation, we define

$$X(R) = R^{-\frac{1}{2}}F(R). \tag{3.2.6}$$

Substituing the value of $X(R)$ into equation (3.2.5), we have

$$R^2(R^{-\frac{1}{2}}F'' - R^{-\frac{3}{2}}F' + \frac{3}{4}R^{-\frac{5}{2}}F) + 2R(R^{-\frac{1}{2}}F' - \frac{1}{2}R^{-\frac{3}{2}}F) + (\gamma R^2 - 2)R^{-\frac{1}{2}}F = 0. \tag{3.2.7}$$

Rearranging, we get

$$R^2F'' + RF' + (\gamma R^2 - \frac{9}{4})F = 0, \tag{3.2.8}$$

which we can rewrite in the form of the standard Bessel function as

$$Z^2\frac{\partial^2 F}{\partial Z^2} + Z\frac{\partial F}{\partial Z} + \left(Z^2 - \frac{9}{4}\right)F = 0, \tag{3.2.9}$$

where $Z = \sqrt{\gamma}R$.

The general solution of the Bessel equation above is

$$F = A_1 J_{\frac{3}{2}}(Z) + A_2 Y_{\frac{3}{2}}(Z), \tag{3.2.10}$$

where A_1 and A_2 are arbitrary constants, $J_{\frac{3}{2}}$ and $Y_{\frac{3}{2}}$ are Bessels functions of the first and second kinds of order $\frac{3}{2}$, respectivly.

Hence, from equation (3.2.9), we get

$$X(R) = \frac{A_1}{\sqrt{R}} J_{\frac{3}{2}}(Z) + \frac{A_2}{\sqrt{R}} Y_{\frac{3}{2}}(Z). \tag{3.2.11}$$

Regularity at the centre implies

$$X(0) = 0 \qquad \text{at} \quad R = 0. \tag{3.2.12}$$

Hence, from equation (3.2.11), we obtain

$$A_2 = 0, \tag{3.2.13}$$

since the Bessel function of the second kind tends to $-\infty$ as $r \to 0$. The solution for $X(R)$ in the equation (3.2.11) is then reduced to

$$X(R) = \frac{A_1}{\sqrt{R}} J_{\frac{3}{2}}(\sqrt{\gamma}R). \tag{3.2.14}$$

Function of t

The equation for G from (3.2.4) is

$$G'' + \frac{\gamma E(1-\nu)}{\rho(1+\nu)(1-2\nu)} G = 0, \tag{3.2.15}$$

which has the general solution

$$G(t) = C_1 \cos\left(\sqrt{\frac{\gamma E(1-\nu)}{\rho(1+\nu)(1-2\nu)}}t\right) + C_2 \sin\left(\sqrt{\frac{\gamma E(1-\nu)}{\rho(1+\nu)(1-2\nu)}}t\right). \tag{3.2.16}$$

where C_1 and C_2 are arbitrary constants.

General solution of $U(R,t)$

Thus U is a sum of the above terms and can be written as

$$U(R,t) = \frac{1}{\sqrt{R}} J_{3/2}(\sqrt{\gamma}R)\left(C_1 \cos\left(\sqrt{\frac{\gamma E(1-\nu)}{\rho(1+\nu)(1-2\nu)}}t\right) + C_2 \sin\left(\sqrt{\frac{\gamma E(1-\nu)}{\rho(1+\nu)(1-2\nu)}}t\right)\right) \tag{3.2.17}$$

for different values γ and different constants C_1, C_2 for each value of γ, where the constant A_1 has been absorbed into the definition of C_1 and C_2. Need to apply boundary conditions to determine C_1, C_2, and possible values of γ.

Periodic solution of $U(R,t)$

A general periodic external pressure can be written as a sum of harmonics of different frequencies. Since the equations and the boundary conditions are linear, the general solution will be a sum of different harmonics by superposition. For simplicity, here we consider only the fundamental harmonic of the external pressure $P(t) = P_0 \sin(kt)$

The stress at the surface of the liver is given by

$$\begin{aligned} \boldsymbol{\sigma e_R} \mid_{R=R_{liver}} &= (2\mu\boldsymbol{\epsilon} + \lambda Tr(\boldsymbol{\epsilon})I)\boldsymbol{e_R} \mid_{R=R_{liver}} \\ &= \left(2\mu\frac{\partial U}{\partial R} + \frac{\lambda}{R^2}\frac{\partial R^2 U}{\partial R}\right)\boldsymbol{e_R} \mid_{R=R_{liver}} \end{aligned} \tag{3.2.18}$$

which must equal $P_0 \sin kt$. Thus, the only possible value of γ is the one for which $k =$

$\sqrt{\frac{\gamma E(1-\nu)}{\rho(1+\nu)(1-2\nu)}}$ or any values of γ for which $2\mu\frac{\partial}{\partial R}\left(\frac{1}{\sqrt{R}}J_{\frac{3}{2}}(\sqrt{\gamma}R)\right)+\frac{\lambda}{R^2}\frac{\partial}{\partial R}\left(R^{\frac{3}{2}}J_{\frac{3}{2}}(\sqrt{\gamma}R)\right)=$ 0. The latter are the natural frequencies of oscillation and the relevant γ is denoted as γ_n, which will be considered later.

Thus, we have

$$U=\frac{C_2}{\sqrt{R}}J_{\frac{3}{2}}(\sqrt{\gamma}R)\sin kt \tag{3.2.19}$$

The relevant value of γ corresponding to this frequency is denoted as γ^*, given by

$$k=\sqrt{\frac{\gamma^* E(1-\nu)}{\rho(1+\nu)(1-2\nu)}}, \tag{3.2.20}$$

which gives

$$\gamma^*=\frac{k^2\rho(1+\nu)(1-2\nu)}{E(1-\nu)}. \tag{3.2.21}$$

Thus, equation (3.2.1) becomes

$$P(t)=P_0\sin\left(\sqrt{\frac{\gamma^* E(1-\nu)}{\rho(1+\nu)(1-2\nu)}}t\right). \tag{3.2.22}$$

To find C_2 in equation (3.2.19), we solve equation (3.1.28):

$$(\lambda + 2\mu)\frac{\partial U(R,t)}{\partial R} + 2\lambda\frac{U(R,t)}{R} = P(t) \quad at \quad R = R_L, \tag{3.2.23}$$

Using the identity

$$\begin{aligned}\frac{\partial}{\partial R}\left(\frac{J_{\frac{3}{2}}(\sqrt{\gamma^*}R)}{\sqrt{R}}\right) &= \sqrt{R}\frac{\partial J_{\frac{3}{2}}(\sqrt{\gamma^*}R)}{\partial R} - \frac{J_{\frac{3}{2}}(\sqrt{\gamma^*}R)}{2R\sqrt{R}} \\ &= \sqrt{\gamma^*}\frac{J_{\frac{1}{2}}(\sqrt{\gamma^*}R)}{\sqrt{R}} - 2\frac{J_{\frac{3}{2}}(\sqrt{\gamma^*}R)}{R\sqrt{R}},\end{aligned} \tag{3.2.24}$$

equation (3.2.23) becomes,

$$\begin{aligned}P(t) \quad = \quad & \left((\lambda + 2\mu)\left(\sqrt{\gamma^*}\frac{J_{\frac{1}{2}}(\sqrt{\gamma^*}R)}{\sqrt{R}} - 2\frac{J_{\frac{3}{2}}(\sqrt{\gamma^*}R)}{R\sqrt{R}}\right) + 2\lambda\frac{J_{\frac{3}{2}}(\sqrt{\gamma^*}R)}{R\sqrt{R}}\right) \\ & \times \sin\left(\sqrt{\frac{\gamma^* E(1-\nu)}{\rho(1+\nu)(1-2\nu)}}t\right) \quad \text{at} \quad R = R_L.\end{aligned} \tag{3.2.25}$$

Comparison of similar terms between equation (3.2.22) and equation (3.2.25) gives

$$C_2\left((\lambda + 2\mu)\left(\sqrt{\gamma^*}\frac{J_{\frac{1}{2}}(\sqrt{\gamma^*}R_L)}{\sqrt{R_L}} - 2\frac{J_{\frac{3}{2}}(\sqrt{\gamma^*}R_L)}{R_L\sqrt{R_L}}\right) + 2\lambda\frac{J_{\frac{3}{2}}(\sqrt{\gamma^*}R_L)}{R_L\sqrt{R_L}}\right) = P_0; \tag{3.2.26}$$

then,

$$C_2 = \frac{P_0}{\left((\lambda+2\mu)\left(\sqrt{\gamma^*}\frac{J_{\frac{1}{2}}(\sqrt{\gamma^*}R_L)}{\sqrt{R_L}} - 2\frac{J_{\frac{3}{2}}(\sqrt{\gamma^*}R_L)}{R_L\sqrt{R_L}}\right) + 2\lambda\frac{J_{\frac{3}{2}}(\sqrt{\gamma^*}R_L)}{R_L\sqrt{R_L}}\right)}. \tag{3.2.27}$$

Therefore, the solution for the displacement in the sphere is

$$U(R,t) = \frac{J_{\frac{3}{2}}(\sqrt{\gamma^*}R)P_0}{\left((\lambda+2\mu)\left(\sqrt{\gamma^*}\frac{J_{\frac{1}{2}}(\sqrt{\gamma^*}R_L)}{\sqrt{R_L}} - 2\frac{J_{\frac{3}{2}}(\sqrt{\gamma^*}R_L)}{R_L\sqrt{R_L}}\right) + 2\lambda\frac{J_{\frac{3}{2}}(\sqrt{\gamma^*}R_L)}{R_L\sqrt{R_L}}\right)\sqrt{R}} \times \sin\left(\sqrt{\frac{\gamma^* E(1-\nu)}{\rho(1+\nu)(1-2\nu)}}t\right). \tag{3.2.28}$$

From equation (3.2.28), we can plot the displacement pattern of the whole liver when we apply a pressure $P_0 = 1$ mmHg to the model (figure 3.2.1). The result shows a linear pattern of displacement at each points in the liver related to the respiratory cycle. The maximum displacement occurs at the outer surface of the liver with the value of 0.22 mm, which is about 0.3% of the radius of the liver.

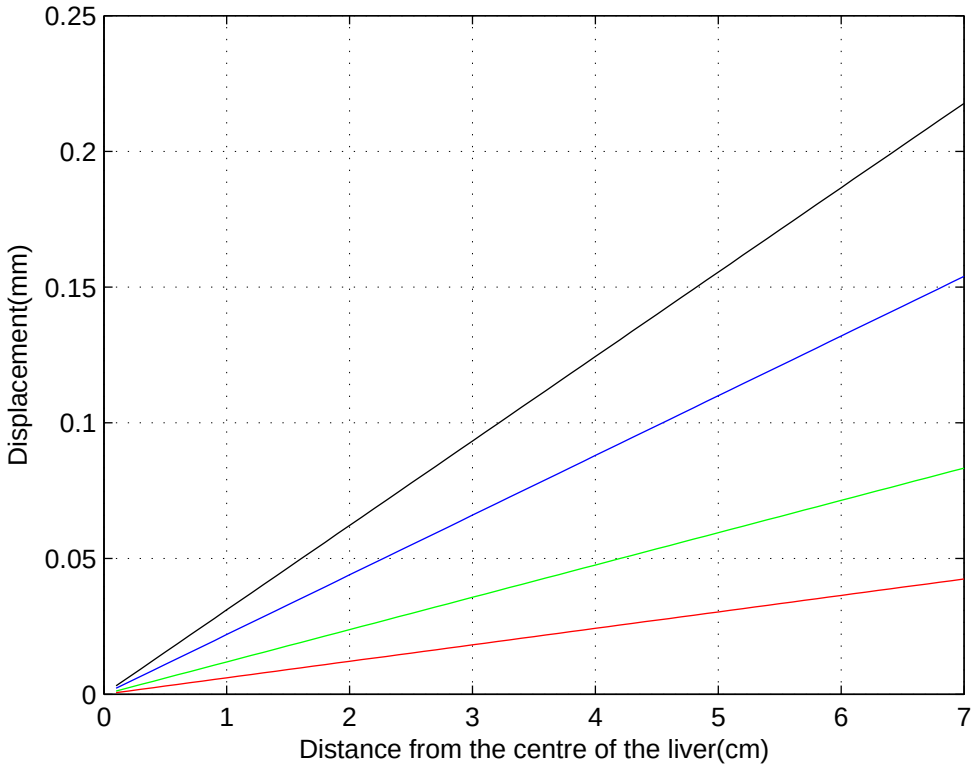

Figure 3.2.1: Displacement pattern of the liver at different times: $t = \frac{\pi}{16k}$ (red), $t = \frac{\pi}{8k}$ (green), $t = \frac{\pi}{4k}$ (blue), and $t = \frac{\pi}{2k}$ (black) when the pressure of 1 mmHg is applied at the surface of the liver.

Solution for γ_n

We consider the case of natural frequencies, in which the liver continues to oscillate at these frequencies if excited. The relevant γ from the general solution of $U(R,t)$ is denoted as γ_n. To find γ_n, from equation (3.2.19) we can write

$$(\lambda+2\mu)\left(\sqrt{\gamma_n}\frac{J_{\frac{1}{2}}(\sqrt{\gamma_n}R)}{\sqrt{R}}-2\frac{J_{\frac{3}{2}}(\sqrt{\gamma_n}R)}{R\sqrt{R}}\right)+2\lambda\frac{J_{\frac{3}{2}}(\sqrt{\gamma_n}R)}{R\sqrt{R}}=0; \tag{3.2.29}$$

thus

$$S=(\lambda+2\mu)\sqrt{\gamma_n}J_{\frac{1}{2}}(\sqrt{\gamma_n}R)-\left(\frac{4\mu}{R}\right)J_{\frac{3}{2}}(\sqrt{\gamma_n}R)=0. \tag{3.2.30}$$

The solution for γ_n can be considered as complex number. We can check whether it has an imaginary part by plotting contours of real and imaginary components of S. The result is shown in figure 3.2.2. The real part and the imaginary part intersect with each other only on the positive real axis. Since S will be zero only when its real and imaginary parts are both zero; therefore, from figure 3.2.2, we see that every γ_n is a real number. Using equation (3.2.30) to plot the graph of $\sqrt{\gamma}R$, we can find γ_n's in figure 3.2.3 as points intersected on the x-axis.

However, in this case, we are interested only in the forced frequency, in which the periodic force is applied. Therefore, only the solution with γ^* will be considered and

investigated further in the single lobule model.

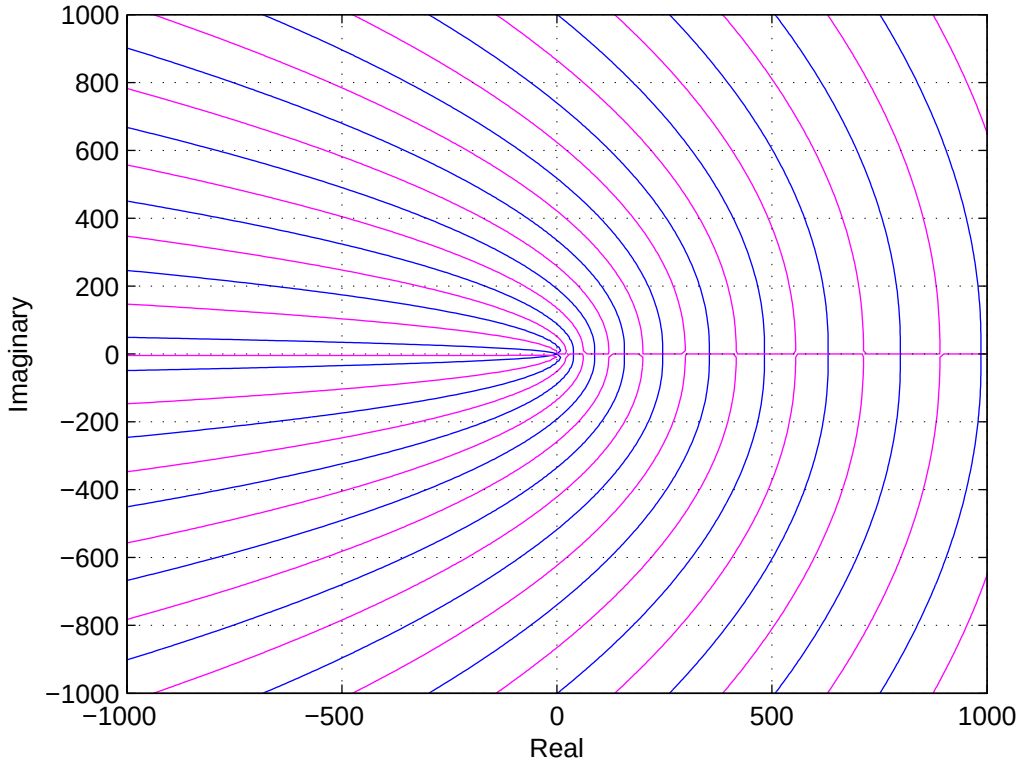

Figure 3.2.2: Contours of the real zeros of the real (blue) and imaginary (pink) parts of S inthe complex plane given by (3.2.30).

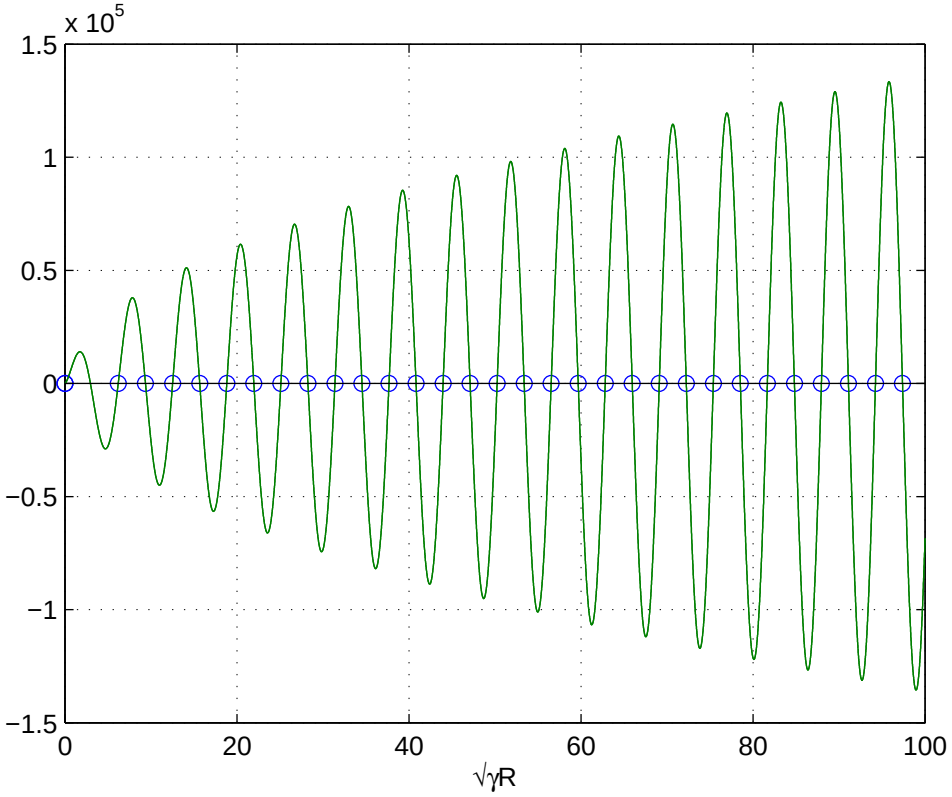

Figure 3.2.3: Real (green) and imaginary (blue) parts of S for the real value of γ_n.

3.2.2 Single lobule model

We are now look back to the dynamics of the lobule. For simplicity, we assume that expansion of the lobule in the axial direction is the same as that in the radial direction. Wang (1991) described the elastodynamic equation for the radial component in a circular cylindrical lobule as [55]

$$\frac{E(1-\nu)}{(1+\nu)(1-2\nu)}\left(u_{rr}+\frac{1}{r}u_r-\frac{1}{r^2}u\right)=\rho u_{tt}, \tag{3.2.31}$$

where u is the displacement, r is the distance from the centre of the lobule in the radial direction, ρ is the tissue density, E is Young's modulus, and t is time.

To solve the equation, we use the method of separation of variables, and set

$$u(r,t)=\phi(r)\psi(t) \tag{3.2.32}$$

where $\phi(r)$ is the space-only dependent variable and $\psi(t)$ is the time-only dependent variable.

From the two above equations, we obtain

$$\frac{\phi''}{\phi}+\frac{1}{r}\frac{\phi'}{\phi}-\frac{1}{r^2}=\frac{\rho(1+\nu)(1-2\nu)}{E(1-\nu)}\frac{\psi''}{\psi}=-\gamma \ , \ \ \gamma>0, \tag{3.2.33}$$

where γ is a constant. We then solve two components from equation (3.2.33) separately.

Function of r

The equation for ϕ from equation (3.2.33) is

$$r^2\phi'' + r\phi' + (\gamma r^2 - 1)\phi = 0. \tag{3.2.34}$$

We convert this to the standard form of Bessel's equation function as follows:

$$z^2\frac{\partial^2\phi}{\partial z^2} + z\frac{\partial\phi}{\partial z} + (z^2 - 1)\phi = 0, \tag{3.2.35}$$

where $z = \sqrt{\gamma}r$, and hence the general solution is

$$\phi(r) = a_1 J_1(\sqrt{\gamma}r) + a_2 Y_1(\sqrt{\gamma}r). \tag{3.2.36}$$

where a_1 and a_2 are arbitrary constants, J_1 and Y_1 are Bessel functions of the first and second kinds of order 1, respectivly.

As before, we assume that the centrilobular vein cannot deform, so the boundary condition is

$$\phi(R_{CV}) = 0 \qquad\qquad at \quad r = R_{CV}; \tag{3.2.37}$$

hence,

$$0 = a_1 J_1(\sqrt{\gamma} R_{CV}) + a_2 Y_1(\sqrt{\gamma} R_{CV}). \tag{3.2.38}$$

Substituting the value of a_2 from equation (3.2.38) into equation (3.2.36), we then obtain

$$\phi(r) = a_1 \left(J_1(\sqrt{\gamma} r) - \frac{J_1(\sqrt{\gamma} R_{CV})}{Y_1(\sqrt{\gamma} R_{CV})} Y_1(\sqrt{\gamma} r) \right). \tag{3.2.39}$$

Function of t

Considering only the time-dependent component from equation (3.2.33), we obtain

$$\psi'' + \frac{\gamma E(1-\nu)}{\rho(1+\nu)(1-2\nu)} \psi = 0, \tag{3.2.40}$$

which has the general solution of

$$\psi(t) = c_1 \cos\left(\sqrt{\frac{\gamma E(1-\nu)}{\rho(1+\nu)(1-2\nu)}} t \right) + c_2 \sin\left(\sqrt{\frac{\gamma E(1-\nu)}{\rho(1+\nu)(1-2\nu)}} t \right). \tag{3.2.41}$$

where c_1 and c_2 are arbitrary constants.

Since the lobules located at the surface of the liver will receive the similar stress as the liver; thus, the stress applied to the outermost lobules must equal $P_0 \sin kt$. Therefore, from equation (3.2.41), $c_1 = 0$ and the solution is then reduced to

$$\psi(t) = c_2 \sin\left(\sqrt{\frac{\gamma E(1-\nu)}{\rho(1+\nu)(1-2\nu)}}t\right). \tag{3.2.42}$$

This means that the lobule oscillates in time with period $2\pi\sqrt{\frac{\rho(1+\nu)(1-2\nu)}{\gamma E(1-\nu)}}$.

General solution of $u(r,t)$

From equation (3.2.32), $u(r,t)$ can be written in terms of $\phi(r)$ and $\psi(t)$ terms. Thus, we obtain the general solution of

$$u(r,t) = \left(J_1(\sqrt{\gamma}r) - \frac{J_1(\sqrt{\gamma}R_{CV})}{Y_1(\sqrt{\gamma}R_{CV})}Y_1(\sqrt{\gamma}r)\right) c_2 \sin\left(\sqrt{\frac{\gamma E(1-\nu)}{\rho(1+\nu)(1-2\nu)}}t\right). \tag{3.2.43}$$

To find the constants γ and c_2, we need to solve for the length expansion ratio from a model of the whole liver, which will be explained in the next part.

3.2.3 Analysis of the volume expansion

In this section, we aim to find the final solution for the displacement of the lobule $u(r,t)$ in equation (3.2.43) by using the volume expansion analysis. As now, we have solutions of the displacement for both single lobule and the whole liver models. The two solutions are related by the fact that, at any certain position in the liver, the expansion ratio of the lobule is the same as the expansion ratio of the element of the liver at the same position. We now aim to find the length expansion ratio at any certain position R in the spherical model of the whole liver.

The whole liver model

We can translate a sphere with the displacement function $U(R,t)$ from the spherical polar coordinates (R,θ,ϕ) into the Cartesian coordinates (X,Y,Z) as below

$$X = R\cos\phi\sin\theta + U(R,t)\cos\phi\sin\theta, \tag{3.2.44}$$

$$Y = R\sin\phi\sin\theta + U(R,t)\sin\phi\sin\theta, \tag{3.2.45}$$

$$Z = R\cos\theta + U(R,t)\cos\theta. \tag{3.2.46}$$

From the above relationships, we can write an infinitesimal volume of the sphere with displacement as

$$
\begin{aligned}
V_{new} &= dRd\theta d\phi \begin{vmatrix} \frac{\partial X}{\partial R} & \frac{\partial Y}{\partial R} & \frac{\partial W}{\partial R} \\ \frac{\partial X}{\partial \theta} & \frac{\partial Y}{\partial \theta} & \frac{\partial Z}{\partial \theta} \\ \frac{\partial X}{\partial \phi} & \frac{\partial Y}{\partial \phi} & \frac{\partial Z}{\partial \phi} \end{vmatrix} \\
&= dRd\theta d\phi (R + U(R,t))^2 \sin\theta \left(1 + \frac{\partial U(R,t)}{\partial R}\right). \qquad (3.2.47)
\end{aligned}
$$

The default (undeformed) volume of the sphere (V_{old}) can be written as

$$V_{old} = R^2 dRd\theta d\phi \sin\theta. \qquad (3.2.48)$$

Therefore, the volume ratio of the deformed ($V_{new} = V_{old} + dV$) and the undeformed spheres (V_{old}) is

$$\frac{V_{new}}{V_{old}} = \left(1 + \frac{U(R,t)}{R}\right)^2 \left(1 + \frac{\partial U(R,t)}{\partial R}\right). \qquad (3.2.49)$$

Substituting the value of $U(R,t)$ from equation (3.2.28), we then have

$$
\begin{aligned}
\frac{V_{new}}{V_{old}} &= \left(1 + \left(C_2 \frac{J_{\frac{3}{2}}(\sqrt{\gamma^*}R)}{R\sqrt{R}} \sin\left(\sqrt{\frac{\gamma^* E(1-\nu)}{\rho(1+\nu)(1-2\nu)}}t\right)\right)\right)^2 \\
&\quad \times \left(1 + C_2 \left(\sqrt{\gamma^*} \frac{J_{\frac{1}{2}}(\sqrt{\gamma^*}R)}{\sqrt{R}} - 2\frac{J_{\frac{3}{2}}(\sqrt{\gamma^*}R)}{R\sqrt{R}}\right) \sin kt\right). \qquad (3.2.50)
\end{aligned}
$$

We assume that the displacement is very small; therefore,

$$\left|C_2\frac{J_{\frac{3}{2}}(\sqrt{\gamma^*}R)}{R\sqrt{R}}\right|, \left|C_2\left(\sqrt{\gamma^*}\frac{J_{\frac{1}{2}}(\sqrt{\gamma^*}R)}{\sqrt{R}} - 2\frac{J_{\frac{3}{2}}(\sqrt{\gamma^*}R)}{R\sqrt{R}}\right)\right| \ll 1.$$

Thus, we can rewrite equation (3.2.50) as

$$\begin{aligned}\frac{V_{new}}{V_{old}} &\approx 1 + \left(2C_2\frac{J_{\frac{3}{2}}(\sqrt{\gamma^*}R)}{R\sqrt{R}} + C_2\left(\sqrt{\gamma^*}\frac{J_{\frac{1}{2}}(\sqrt{\gamma^*}R)}{\sqrt{R}} - 2\frac{J_{\frac{3}{2}}(\sqrt{\gamma^*}R)}{R\sqrt{R}}\right)\right) \\ &\quad \times \sin\left(\sqrt{\frac{\gamma^* E(1-\nu)}{\rho(1+\nu)(1-2\nu)}}t\right) \\ &\approx 1 + C_2\sqrt{\gamma^*}\frac{J_{\frac{1}{2}}(\sqrt{\gamma^*}R)}{\sqrt{R}}\sin\left(\sqrt{\frac{\gamma^* E(1-\nu)}{\rho(1+\nu)(1-2\nu)}}t\right). \qquad (3.2.51)\end{aligned}$$

We can now solve for the length ratio of the deformed and the undeformed spheres as

$$\frac{L_{new}}{L_{old}} = \sqrt[3]{\frac{V_{new}}{V_{old}}} \approx \left(1 + C_2\sqrt{\gamma^*}\frac{J_{\frac{1}{2}}(\sqrt{\gamma^*}R)}{\sqrt{R}}\sin\left(\sqrt{\frac{\gamma^* E(1-\nu)}{\rho(1+\nu)(1-2\nu)}}t\right)\right)^{\frac{1}{3}}, \quad (3.2.52)$$

where L_{new} is the radius of the deformed spherical liver and L_{old} is the radius of the undeformed liver.

Using a Taylor expansion, we obtain

$$\frac{L_{new}}{L_{old}} \approx 1 + \frac{C_2}{3}\sqrt{\gamma^*}\frac{J_{\frac{1}{2}}(\sqrt{\gamma^*}R)}{\sqrt{R}}\sin\left(\sqrt{\frac{\gamma^* E(1-\nu)}{\rho(1+\nu)(1-2\nu)}}t\right). \tag{3.2.53}$$

We define the length expansion ratio as $L_E = \frac{L_{new}-L_{old}}{L_{old}}$ and its value is

$$L_E(R,t) = \frac{C_2}{3}\sqrt{\gamma^*}\frac{J_{\frac{1}{2}}(\sqrt{\gamma^*}R)}{\sqrt{R}}\sin\left(\sqrt{\frac{\gamma^* E(1-\nu)}{\rho(1+\nu)(1-2\nu)}}t\right). \tag{3.2.54}$$

The single lobule model

Since the outer surface of the single lobule model at the distance R from the centre of the liver must have the same length expansion ratio to the element of the liver at the same position; therefore, we can write

$$u(R_{l0},t) = L_E(R,t)R_{l0} \quad \text{at} \quad r = R_{l0}. \tag{3.2.55}$$

From equation (3.2.43) and the above equation, we then obtain

$$\begin{aligned}\frac{C_2}{3}\sqrt{\gamma^*}\frac{J_{\frac{1}{2}}(\sqrt{\gamma^*}R)}{\sqrt{R}}\sin\left(\sqrt{\frac{\gamma^* E(1-\nu)}{\rho(1+\nu)(1-2\nu)}}t\right)R_{l0} &= \left(J_1(\sqrt{\gamma^*}R_{l0}) - \frac{J_1(\sqrt{\gamma^*}R_{CV})}{Y_1(\sqrt{\gamma^*}R_{CV})}Y_1(\sqrt{\gamma^*}R_{l0})\right) \\ &\quad \times c_2\sin\left(\sqrt{\frac{\gamma^* E(1-\nu)}{\rho(1+\nu)(1-2\nu)}}t\right). \end{aligned} \tag{3.2.56}$$

Owing to the time dependence and assumption of periodicity, we are left only with the term proportional to $\sin\left(\sqrt{\frac{\gamma^* E(1-\nu)}{\rho(1+\nu)(1-2\nu)}}\right)$

Now, we can solve for the unknown c_2:

$$c_2 = \frac{C_2 R_{l0}\sqrt{\gamma^*} J_{\frac{1}{2}}(\sqrt{\gamma^*}R)}{3\sqrt{R}\left(J_1(\sqrt{\gamma^*}R_{l0}) - \frac{J_1(\sqrt{\gamma^*}R_{CV})}{Y_1(\sqrt{\gamma^*}R_{CV})}\right)}. \tag{3.2.57}$$

Finally, we can rewrite equation (3.2.43)

$$u(r,R,t) = \frac{C_2 R_{l0}\sqrt{\gamma^*} J_{\frac{1}{2}}(\sqrt{\gamma^*}R)\left(J_1(\sqrt{\gamma^*}r) - \frac{J_1(\sqrt{\gamma^*}R_{CV})}{Y_1(\sqrt{\gamma^*}R_{CV})}Y_1(\sqrt{\gamma^*}r\right)}{3\sqrt{R}\left(J_1(\sqrt{\gamma^*}R_{l0}) - \frac{J_1(\sqrt{\gamma^*}R_{CV})}{Y_1(\sqrt{\gamma^*}R_{CV})}Y_1(\sqrt{\gamma^*}R_{l0}\right)} \times \sin\left(\sqrt{\frac{\gamma^* E(1-\nu)}{\rho(1+\nu)(1-2\nu)}}t\right) \tag{3.2.58}$$

This means that the displacement of each lobule also depends on its position R in the liver. However, since the term $\frac{J_{\frac{1}{2}}(\sqrt{\gamma}R)}{\sqrt{R}} \approx 0.45$ for any $0 < R < 0.07$, we therefore can rewrite (3.2.58) as

$$u(r,t) = \frac{0.15 C_2 R_{l0}\sqrt{\gamma^*}\left(J_1(\sqrt{\gamma^*}r) - \frac{J_1(\sqrt{\gamma^*}R_{CV})}{Y_1(\sqrt{\gamma^*}R_{CV})}Y_1(\sqrt{\gamma^*}r\right)}{\left(J_1(\sqrt{\gamma^*}R_{l0}) - \frac{J_1(\sqrt{\gamma^*}R_{CV})}{Y_1(\sqrt{\gamma^*}R_{CV})}Y_1(\sqrt{\gamma^*}R_{l0}\right)} \times \sin\left(\sqrt{\frac{\gamma^* E(1-\nu)}{\rho(1+\nu)(1-2\nu)}}t\right) \tag{3.2.59}$$

We now can find the dynamic of the displacement within of a lobule when the pressue $P_0 = 1$ mmHg is applied to the model (figure 3.2.4). At each time point, the graph shows that the displacement grows approximately linear when it is far from the centrilobular vein. The maximum displacement occurs at the outer surface of the lobule with the value of 1.4 μm, which is about 0.3% of the radius of the lobule.

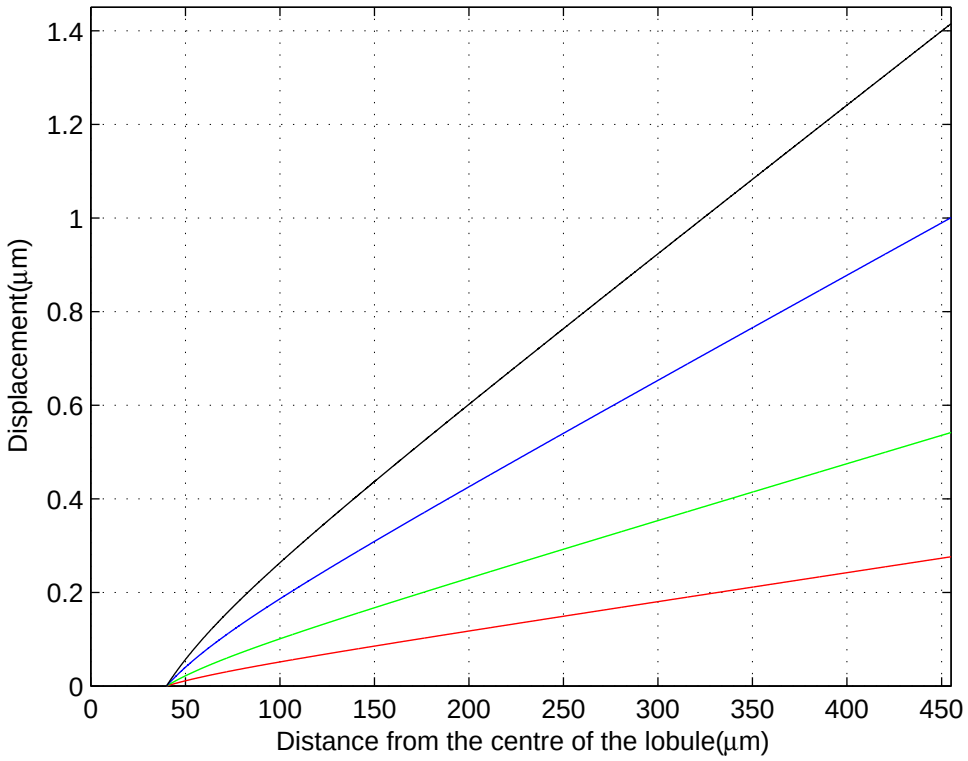

Figure 3.2.4: Displacement vs distance from the centre of the lobule at different times: $t = \frac{\pi}{16k}$ (red), $t = \frac{\pi}{8k}$ (green), $t = \frac{\pi}{4k}$ (blue), and $t = \frac{\pi}{2k}$ (black) when the pressure of 1 mmHg is applied at the surface of the liver.

3.3 Poroelastic Model

In the previous sections, we explored the deformation of the liver tissue assuming it is an elastic solid. However, in reality, the liver lobule has sinusoidal space, which is perfused by blood, so to account for this, we model the liver tissue as a poroelastic material. In this case, pressure boundary conditions are applied at the boundary of the lobule itself, so there is no need for considering a model of the whole liver.

3.3.1 Working hypothesis

We assume that both solid and fluid parts are incompressible, and if the fluid pressure varies, the lobule deforms due to changing of volume in the porous space. For simplicity, we study an idealised model of a lobule as an axisymmetric circular cylinder with radius R_{l0}. The fluid flow within the lobule is also assumed to be axisymmetric and have no flow in the axial direction. For the deformation in the axial direction, we assume linear expansion similar to the elastic model stated previously.

We assume the portal tracts to be uniformly distributed around the outer surface of the lobule and the centrilobular vein with radius R_{CV} is at the centre. Under normal physiological state, in which the lobule is undeformed, the portal pressure is prescribed as P_{PT} and the centrilobular vein pressure is P_{CV}. We also assume that the pressure at the centrilobular vein is constant and the vessel itself is rigid and cannot change the configuration. The linear poroelasticity is used in the model and the lobule is deformed

due to a small strain applied to the solid part. The relevant parameters used in the model is listed in table 3.2.

Table 3.2: Physiological parameter values used in the poroelastic model

Symbol	Description	Typical Value	Reference
R_{l0}	Radius of the lobule	455×10^{-6} m	see section 3.1.2
R_{CV}	Radius of the centrilobular vein	40×10^{-6} m	[51]
E	Young's modulus of the liver	6 kPa	[82]
ν	Poisson's ratio of the liver	0.431	[52]
K	Sinusoidal hydraulic conductivity	1.1×10^{-8} m^2/mmHg/s	[11]
P_{PT}	Portal tract pressure	4.4 mmHg	[11]
P_{CV}	Centrilobular venous pressure	1.45 mmHg	[11]

3.3.2 Derivation of model equations

We use the Biot formulation to prescribe the linear poroelasticity of the lobule; therefore,

$$\boldsymbol{\sigma} = \frac{E\nu}{(1+\nu)(1-2\nu)}(\boldsymbol{\nabla} \cdot \mathbf{u})\mathbf{I} + \frac{E}{1+\nu}\boldsymbol{\epsilon} - (p - p_0)\mathbf{I}, \tag{3.3.1}$$

where $\boldsymbol{\sigma}$ is the stress tensor, $\mathbf{u}$ is the displacement of the lobule, E is the Young modulus, ν is the Poisson ratio, p is the applied fluid pressure, p_0 is the fluid pressure of the undeformed lobule, and $\boldsymbol{\epsilon}$ is the strain tensor, which can be written in terms of the solid displacement (u_i) as

$$\epsilon_{ij} = \frac{1}{2}(u_{i,j} + u_{j,i}), \tag{3.3.2}$$

where u_i and u_j are the components of the incremental displacements of the tissue in the x and y directions, respectively, and commas denote partial derivatives in those directions.

In mechanical equilibrium, we have

$$\boldsymbol{\nabla} \cdot \boldsymbol{\sigma} = 0. \tag{3.3.3}$$

We also use Darcy's equation to prescribe the flow within the lobule; thus,

$$\mathbf{v} = -K\boldsymbol{\nabla} p = -\frac{k}{\mu}\boldsymbol{\nabla} p, \tag{3.3.4}$$

where $\mathbf{v}$ is Darcy's velocity, K is the hydraulic conductivity, k is the permeability of the lobule, and μ is the dynamic viscosity of blood.

Moreover, since we assume that blood is incompressible; therefore,

$$\boldsymbol{\nabla} \cdot \mathbf{v} = 0. \tag{3.3.5}$$

From equation (3.3.1) - (3.3.3), we obtain

$$\frac{\nu}{(1+\nu)(1-2\nu)}\boldsymbol{\nabla}(\boldsymbol{\nabla}\cdot\mathbf{u})+\frac{1}{2(1+\nu)}(\boldsymbol{\nabla}(\boldsymbol{\nabla}\cdot\mathbf{u})+\nabla^2\mathbf{u})-\boldsymbol{\nabla}(p-p_0)=0. \tag{3.3.6}$$

From equation (3.3.4) and (3.3.5), we obtain

$$\nabla^2 p = 0 \tag{3.3.7}$$

3.3.3 Boundary conditions

We apply the physiological pressure boundary conditions P_{PT} at the outer surface and P_{CV} at the centrilobular vein for the Darcy's flow in the undeformed lobule. For the solid part of the lobule to be deformed, the stress, σ_a, is applied by increasing the pressure, $P_a = 1\ mmHg$ or about 133 Pa, at the outer surface. At the centrilobular vein, the pressure and the displacement do not change.

- At the outer wall of the lobule

$$p = P_{PT}. \tag{3.3.8}$$

$$\boldsymbol{\sigma_a}\cdot\mathbf{n} = P_a. \tag{3.3.9}$$

- At the centrilobular vein

$$p = P_{CV}. \tag{3.3.10}$$

$$\boldsymbol{\sigma_a} \cdot \mathbf{n} = 0. \tag{3.3.11}$$

$$u = 0. \tag{3.3.12}$$

3.3.4 Results

We solve equations (3.3.6) and (3.3.7) numerically by using the boundary conditions from (3.3.8) - (3.3.12) for the solution of displacement and pressure profiles. The model is computed by using the finite element method in COMSOL Multiphysics software version 4.2.

The result in figure 3.3.1 shows the displacement profile of the lobule with the maximum displacement at the outer wall of the lobule and no displacement at the centrilobular vein. When we increase 1 mmHg or about 23% of the physiological pressure at the portal tract, the maximum displacement is about 9.7 μm or 2.1% of the radius of the lobule, which is more than the 0.3% displacement of the solid elastic lobule.

The pressure gradient along the radius of the lobule is plotted in figure 3.3.2. It shows a nonlinear relationship, in which the pressure gradient is higher near the centrilobular

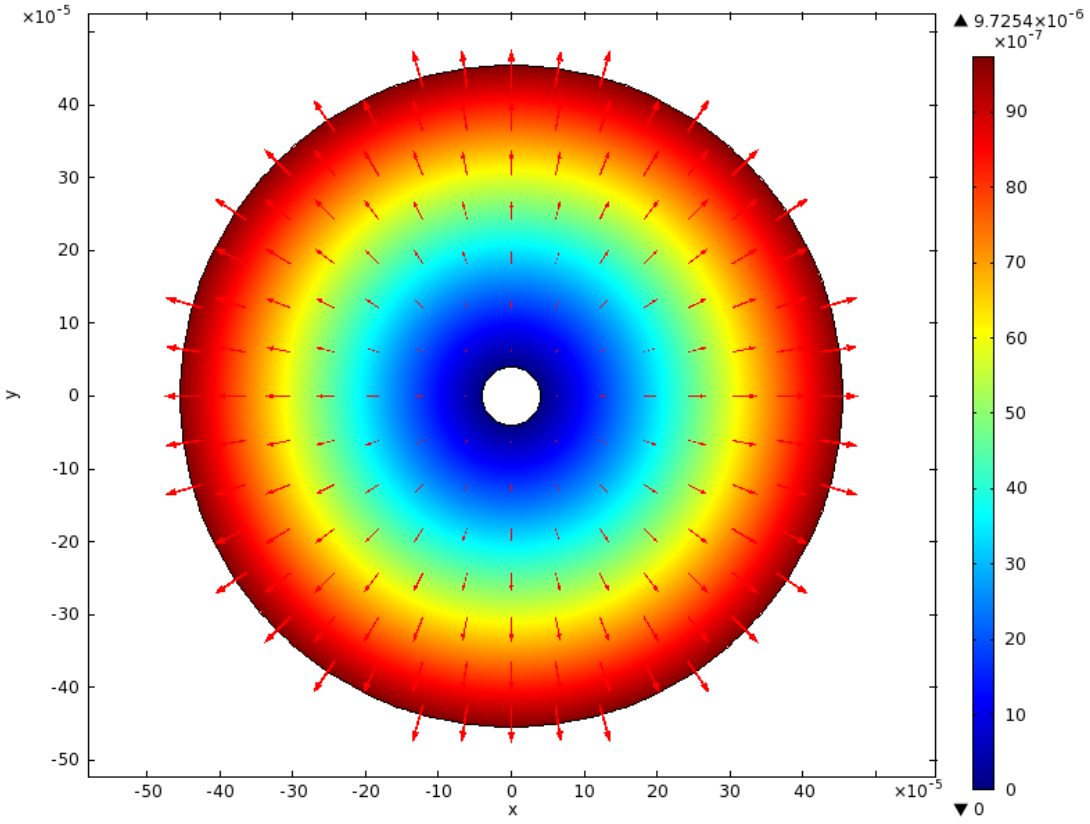

Figure 3.3.1: Displacement profile of the lobule in the poroelastic model when the stress of 1 $mmHg$ is applied at the outer surface. The arrows show the magnitude and direction of the displacement. The relevant parameter values used in the model is listed in table 3.2.

vein than the outer edge of the lobule.

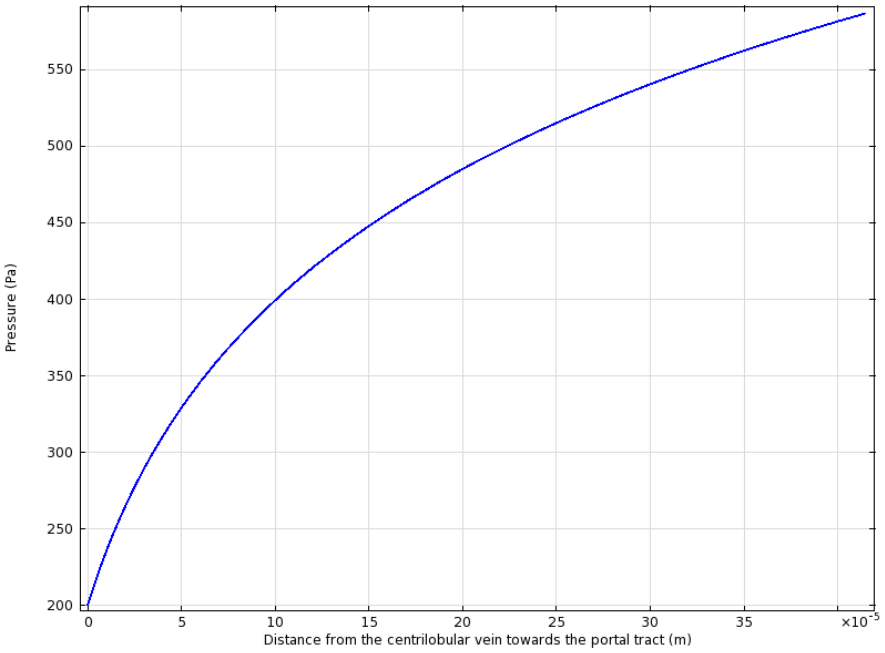

Figure 3.3.2: Pressure distribution within the lobule in the poroelastic model.

3.4 Summary and discussion

In this chapter, we investigated the effect of tissue elasticity on the deformation of the liver lobule. Firstly, as an initial model, the lobules are treated as elastic solid circular cylinders packed in a spherical liver. The lobule is assumed to expand linearly in radial direction with the pressure boundary condition applied at the surface of the liver. The result shows that the expansion ratio is small ($\approx 0.3\%$) under a change of 1 mmHg of pressure, which suggests that the elasticity has a small effect in the model. The elastodynamic change of the lobule is also analysed by applying the periodic pressure boundary condition related to the respiratory cycle. The solution shows the dynamic behaviour of the liver lobule, which deforms linearly when it is far from the centrilobular vein. As a result, the liver tissue also deforms linearly from its centre of mass.

We further investigated the tissue deformation by treating the lobule as a poroelastic material. Similar to the first model, the lobule is treated as a circular cylinder and assumed to expand in radial direction from the pressure boundary condition applied at the surface of the lobule. The Biot formulation and the Darcy equation are used as the governing equations of the solid and fluid component, respectively. The pressure boundary condition is applied to the lobule in order to deform. The numerical result shows that the pressure distribution within the lobule is nonlinear with the highest gradient located near the centrilobular vein. This suggests that the fluid velocity must be faster near the centrilobular vein than the outside of the lobule.

Moreover, the poroelastic model shows that it has more compliance compared to the solid elastic model as it deforms more when the equal pressure is applied. This suggests that the poroelasticity might be important on the haemodynamics of blood in the liver under very high pressure conditions.

The in-depth analysis and the extension of this poroelastic model are further studied by Bonfiglio et al, a group of colleage of the author of this thesis. The model is further implemented in the hexagonal geometry. However, in their model, the liver is described as a hyperelastic material and the strain-energy function is also applied. This causes a different value of Young's modulus, E, which is calculated as ≈ 1230 Pa, lower than the value used in this thesis. They later calculated the change of flux with different pressure input. The pressure-flux relationship is finally achieved and compared to the rigid model and the experimental data from Dahmen et al. In their results, when the pressure increases, the flow grows more than linearly. This can be explained by the increase of permeability when the lobule expands (see figure 3.4.1).

In summary, the model in this thesis and the model of Bonfiglio et al show that the permeability of the liver sinusoids increases when the portal pressure increases; as a result, blood flow into the lobules increases more than linearly. This indicates that the liver will receive an overwhelm amount of blood under very high pressure conditions. The compliance of the liver is likely to be important after a partial resection of the liver or after a small size liver transplant as the liver will expose higher pressure and higher

blood flow per unit volume.

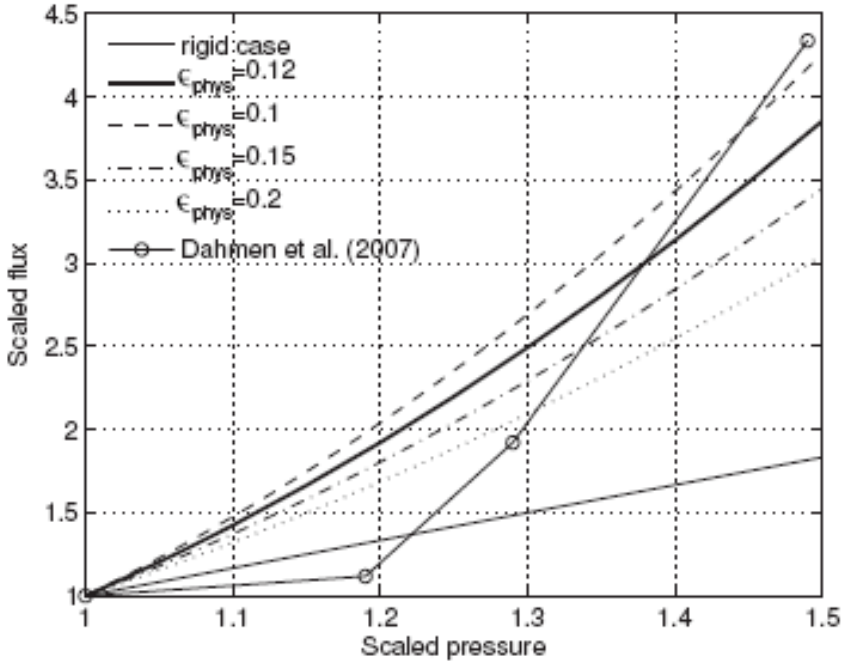

Figure 3.4.1: Comparison of pressure-flux relationship between the rigid model and the deformable model. The scaled flux is the ratio of the total flux under the deformed lobule to the total flux under the undeformed lobule, in which the porosity ϵ_{phy} is applied. [11]

Chapter 4

Model of interstitial fluid flow in the liver

In this chapter, we investigate behaviours of the interstitial fluid flow within the liver. Two scales of flow are considered: flow within a single lobule and flow in the entire liver. In the first section, a mathematical model of the interstitial fluid pathway is added to the model of Bonfiglio et al [11], described previously in section 2.4. Both numerical and analytical solutions are investigated and compared.

In the second section of this chapter, we investigate both blood and interstitial flows in the whole liver by adding drainage pathways of the interstitial fluid that was described in section 1.1.3 (see also figure 4.1.1 and 4.1.2).

4.1 Model of the interstitial fluid pathway in a single lobule

We use the same geometry of the lobule as that of Bonfiglio et al [11], which is shown in figure 2.4.1. All parameters value used in the model are shown in table 4.1. Since the effect of the anisotropic medium was shown to be very small in their work, the lobule is considered as an isotropic medium. We also neglect non-Newtonian behaviour and compliance of the tissue.

Moreover, the cross-sectional area of the fenestrations is large enough to allow most of the proteins in the blood to diffuse across the membrane. Therefore, the osmotic pressure difference between blood and interstitial fluid is negligible, and hence the fluid flow through the fenestrations is mostly due to the gradient of the hydrostatic pressure between the two spaces alone [57].

We treat each of the sinusoidal space and the interstitial space as a porous medium with different permeabilities; both spaces occupy the whole interior of the lobule.

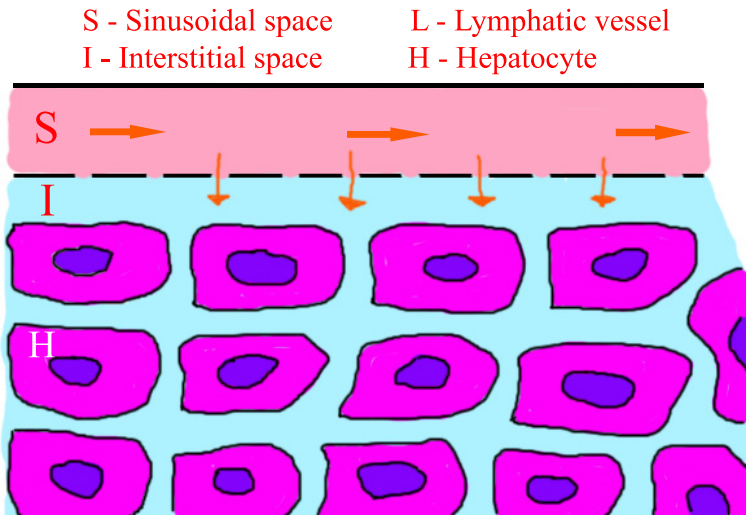

Figure 4.1.1: Pathway of the plasma fluid inside the liver lobule. The fluid flows from the sinusoidal space (S) into the interstitial space (I) via the fenestrations, and later drains into lymphatic vessels (L) (see figure 4.1.2 below).

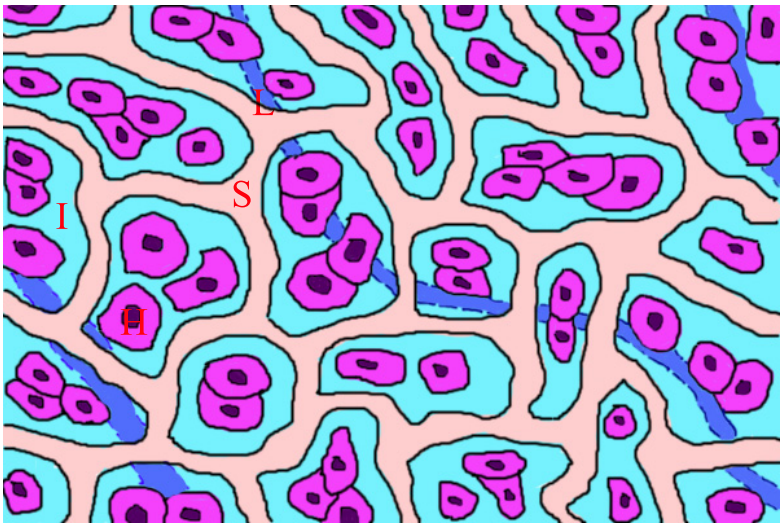

Figure 4.1.2: Diagram of tissue, vessels, and space lining inside the lobule.

Table 4.1: Physiological parameter values used in the single lobule model

Symbol	Description	Typical Value	Reference
L	Typical length of the edge of the lobule	500×10^{-6} m	[51]
R_{PT}	Radius of portal tracts	25×10^{-6} m	[11]
R_{CV}	Radius of centrilobular veins	40×10^{-6} m	[51]
K_S	Sinusoidal hydraulic conductivity	1.1×10^{-8} m^2/mmHg/s	[11]
K_I	Interstitial hydraulic conductivity	$0.0003K_S$	see appendix C
$p_{SPT} - p_{SCV}$	The difference of portal tract and centrilobular venous pressure	2.95 mmHg	[11]
ρ	Liver density	1060 kg/m^3	[58]
F	Hepatic filtration coefficient	0.3 ml/min/mmHg/100 g of tissue $= 5 \times 10^{-8}$ m^3/kg/mmHg/s see Appendix D	[59]

4.1.1 Derivation of model equations

The Darcy velocity of the fluid in the sinusoids and in the interstitial space are denoted as $\mathbf{v_S}$ and $\mathbf{v_I}$, respectively. The Darcy equation for the flow in each space gives

$$\mathbf{v_S} = -K_S \boldsymbol{\nabla} p_S, \tag{4.1.1}$$

$$\mathbf{v_I} = -K_I \boldsymbol{\nabla} p_I, \tag{4.1.2}$$

for the sinusoidal and interstitial flow, respectively, where K_S and K_I are the hydraulic conductivity of the sinusoids and interstitial space, respectively. Note that $K_S = \frac{k_S}{\mu_S}$ and $K_I = \frac{k_I}{\mu_I}$, where k_S and k_I are the permeability of the sinusoidal and interstitial space, respectively, and μ_S and μ_I are the dynamic viscosity of blood and interstitial fluid, respectively.

We assume that the flux across the endothelial wall from the sinusoids to the interstitial space per unit length of the vessel, Q_E, is proportional to the pressure difference between the two spaces, that is

$$Q_E = \beta(p_S - p_I), \tag{4.1.3}$$

where β is the filtration coefficient of blood through the sinusoidal endothelial wall, p_S

and p_I are the pressure of fluid in the sinusoids and in the interstitial space, respectively.

Considering the flow in one sinusoid, as shown in figure 4.1.3, we define x as the coordinate along the sinusoid, A_S and U_S as the cross-sectional area and the physical velocity of blood in a single sinusoid, respectively. Using the principle of conservation of mass, we obtain

$$(A_S + dA_S)(U_S + dU_S) + Q_E dx = A_S U_S. \tag{4.1.4}$$

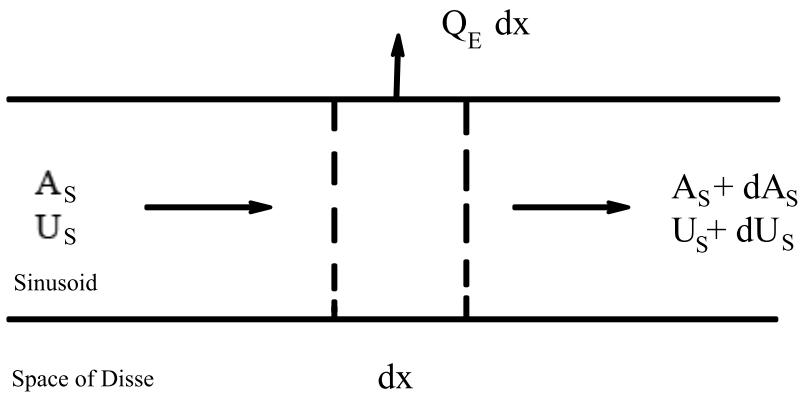

Figure 4.1.3: Diagram of flow in a single sinusoid. In this figure, x is the coordinate along the sinusoid, A is the cross-sectional area of the sinusoid, U is the fluid velocity, and Q_E is the flux flowing across the endothelial wall per unit length of the vessel.

Assuming that the cross-sectional area of the sinusoid is consistent, we can rewrite equation (4.1.4) as

$$\frac{\partial}{\partial x}(A_S U_S) + Q_E = 0, \tag{4.1.5}$$

The Darcy velocities $\mathbf{v_S}$ and $\mathbf{v_I}$ are related to the corresponding physical velocities $\mathbf{U_S}$ and $\mathbf{U_I}$ (that is a typical velocity of the actual flow velocities in the vessels) as

$$\mathbf{U_S} = \frac{\mathbf{v_S}}{\phi_S} \tag{4.1.6}$$

$$\mathbf{U_I} = \frac{\mathbf{v_I}}{\phi_I} \tag{4.1.7}$$

where ϕ_S and ϕ_I are the porosity of sinusoidal and interstitial space, respectively. Now $\frac{\phi_S}{A_S}$ is the number density of sinusoids (number of sinusoids crossing a unit cross-sectional area). Since almost all of the volume of interstitial space is contained in the space of Disse, $\frac{\phi_I}{A_I}$ is the number density of spaces of Disse, and thus, since each space of Disse corresponds to a sinusoid,

$$\frac{\phi_S}{A_S} = \frac{\phi_I}{A_I}. \tag{4.1.8}$$

Thus, we can rewrite equation (4.1.5) as

$$\boldsymbol{\nabla} \cdot \mathbf{v_S} + \frac{\phi_S Q_E}{A_S} = 0. \tag{4.1.9}$$

The same argument applied to the interstitial space leads to

$$\boldsymbol{\nabla} \cdot \mathbf{v_I} - \frac{\phi_I Q_E}{A_I} = 0. \tag{4.1.10}$$

We substitute the value from equation (4.1.1) and (4.1.2) into equation (4.1.9) and (4.1.10) and then obtain,

$$-K_S \nabla^2 p_S + \frac{\phi_S Q_E}{A_S} = 0, \tag{4.1.11}$$

$$-K_I \nabla^2 p_I - \frac{\phi_I Q_E}{A_I} = 0. \tag{4.1.12}$$

Substituting the definition of Q_E into (4.1.11) and (4.1.12), we get the governing equations

$$-K_S \nabla^2 p_S + \frac{\phi_S \beta (p_S - p_I)}{A_S} = 0, \tag{4.1.13}$$

$$-K_I \nabla^2 p_I - \frac{\phi_I \beta (p_S - p_I)}{A_I} = 0. \tag{4.1.14}$$

Since ϕ_S and ϕ_I are unknown, we need to eliminate these variables. From appendix, we have $\beta = \frac{\rho F}{L_S}$, where ρ is the density of the liver, F is the hepatic filtration coefficient,

and L_S is the length of sinusoids per unit volume of liver tissue. Since, $\frac{\phi_S}{A_S} = \frac{\phi_I}{A_I}$; therefore, $\frac{\phi_S \beta}{A_S} = \frac{\phi_I \beta}{A_I} = \frac{\phi_S \rho F}{A_S L_S} = \frac{\phi_I \rho F}{A_I L_S}$.

Since the terms $\frac{\phi_S}{A_S}$ and $\frac{\phi_I}{A_I}$ are equal to L_S; thus, equation 4.1.13 and 4.1.14 become

$$-K_S \nabla^2 p_S + \rho F(p_S - p_I) = 0, \tag{4.1.15}$$

$$-K_I \nabla^2 p_I - \rho F(p_S - p_I) = 0. \tag{4.1.16}$$

4.1.2 Derivation of boundary conditions

In the single lobule, we assume that sinusoidal blood and interstitial fluid cannot flow across the edges of the lobule. For the sinusoidal flow, we prescribe pressure boundary conditions at both portal tracts and centrilobular vein as P_{SPT} and P_{SCV}, respectively. Furthermore, since the data of interstitial pressure is not available (due to the small space occupied), we assume that the interstitial pressure at both portal tract and centrilobular vein ends are the same as the sinusoidal pressure at the centrilobular vein, P_{SCV}. We also assume there is no flow across the boundaries due to symmetry. Therefore, the boundary conditions are:

- At the edges of the lobule

$$-K_S \mathbf{n} \cdot \boldsymbol{\nabla} p_S = 0, \tag{4.1.17}$$

$$-K_I \mathbf{n} \cdot \boldsymbol{\nabla} p_I = 0. \tag{4.1.18}$$

- At the portal tracts

$$p_S = P_{SPT}, \tag{4.1.19}$$

$$p_I = P_{SCV}. \tag{4.1.20}$$

- At the centrilobular vein

$$p_S = P_{SCV}, \tag{4.1.21}$$

$$p_I = P_{SCV}. \tag{4.1.22}$$

Figure 4.1.4 shows diagram of the boundary conditions of the model.

4.1.3 Nondimensionalization

Nondimensionalisation of the variables and parameters

We nondimensionalise the system, using stars to denote nondimensional variables

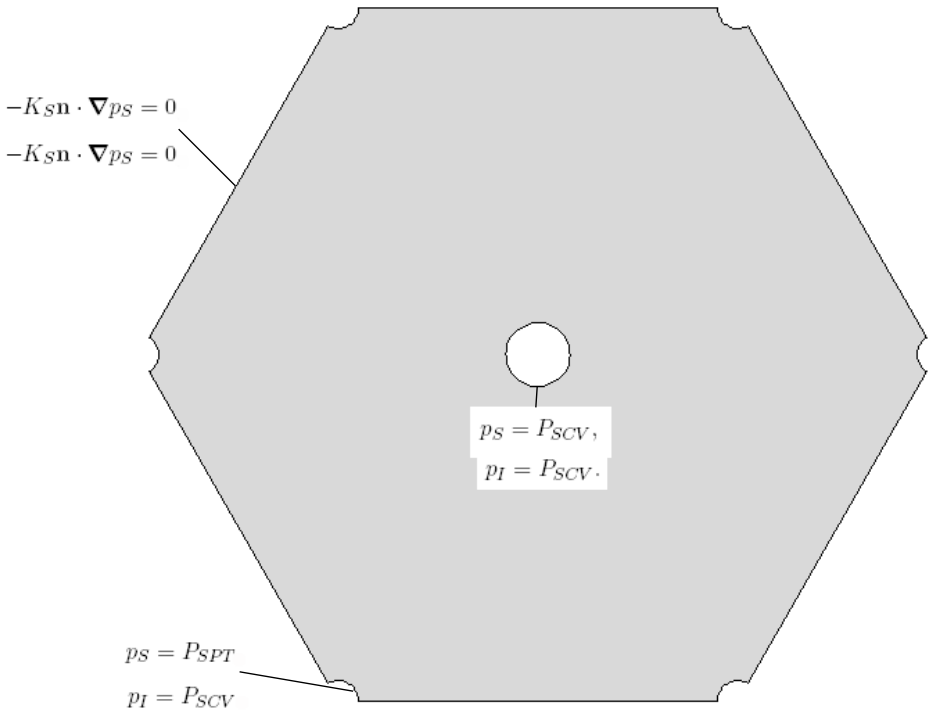

Figure 4.1.4: Diagram of boundary conditions of the single lobule model in section 4.1.

$$\mathbf{x} = L\mathbf{x}^*, \tag{4.1.23}$$

$$p_S = P_{SCV} + (P_{SPT} - P_{SCV})p_S^*, \tag{4.1.24}$$

$$p_I = P_{SCV} + (P_{SPT} - P_{SCV})p_I^*, \tag{4.1.25}$$

where L is the length of the edge of the lobule.

Equations (4.1.15) and (4.1.16) become

$$-\frac{K_S(P_{SPT} - P_{SCV})}{L^2}\nabla^{*2} \cdot p_S^* + \rho F(P_{SPT} - P_{SCV})(p_S^* - p_I^*) = 0, \tag{4.1.26}$$

$$-\frac{K_I(P_{SPT} - P_{SCV})}{L^2}\nabla^{*2} \cdot p_I^* - \rho F(P_{SPT} - P_{SCV})(p_S^* - p_I^*) = 0. \tag{4.1.27}$$

We define $F_S = \frac{L^2\rho F}{K_S}$ and $F_I = \frac{L^2\rho F}{K_I}$. Thus, we substitute the values of F_S and F_I into (4.1.26) and (4.1.27) and obtain the dimensionless governing equations

$$-\nabla^{*2}p_S^* + F_S(p_S^* - p_I^*) = 0, \tag{4.1.28}$$

$$-\nabla^{*2}p_I^* - F_I(p_S^* - p_I^*) = 0. \tag{4.1.29}$$

Nondimensionalised boundary conditions of the lobule

From equation (4.1.17) - (4.1.22), we nondimensionalised all variables and obtain

- At the edges of the lobule

$$-\mathbf{n} \cdot \boldsymbol{\nabla}^* p_S^* = 0, \tag{4.1.30}$$

$$-\mathbf{n} \cdot \boldsymbol{\nabla}^* p_I^* = 0. \tag{4.1.31}$$

- At the portal tracts

$$p_S^* = 1, \tag{4.1.32}$$

$$p_I^* = 0. \tag{4.1.33}$$

- At the centrilobular vein

$$p_S^* = 0, \tag{4.1.34}$$

$$p_I^* = 0. \tag{4.1.35}$$

4.1.4 Numerical solutions

We carry out the numerical simulation using the finite element solver COMSOL Multiphysics version 4.2. We translate the governing equations (4.1.28) and (4.1.29) into the weak formulation. Solving the system we find the pressure contours of the sinusoidal and interstitial spaces throughout the lobule. The results are shown in figures 4.1.5 and 4.1.6.

The sinusoidal pressure profile appears similar to that found by Bonfiglio et al, with the highest pressure at the portal tracts and lowest at the centrilobular vein. For the interstitial pressure profile, the highest pressure is in the middle part between the portal tracts and the centrilobular vein, with a pressure drop to the the edge of the vessels to comply with the boundary conditions.

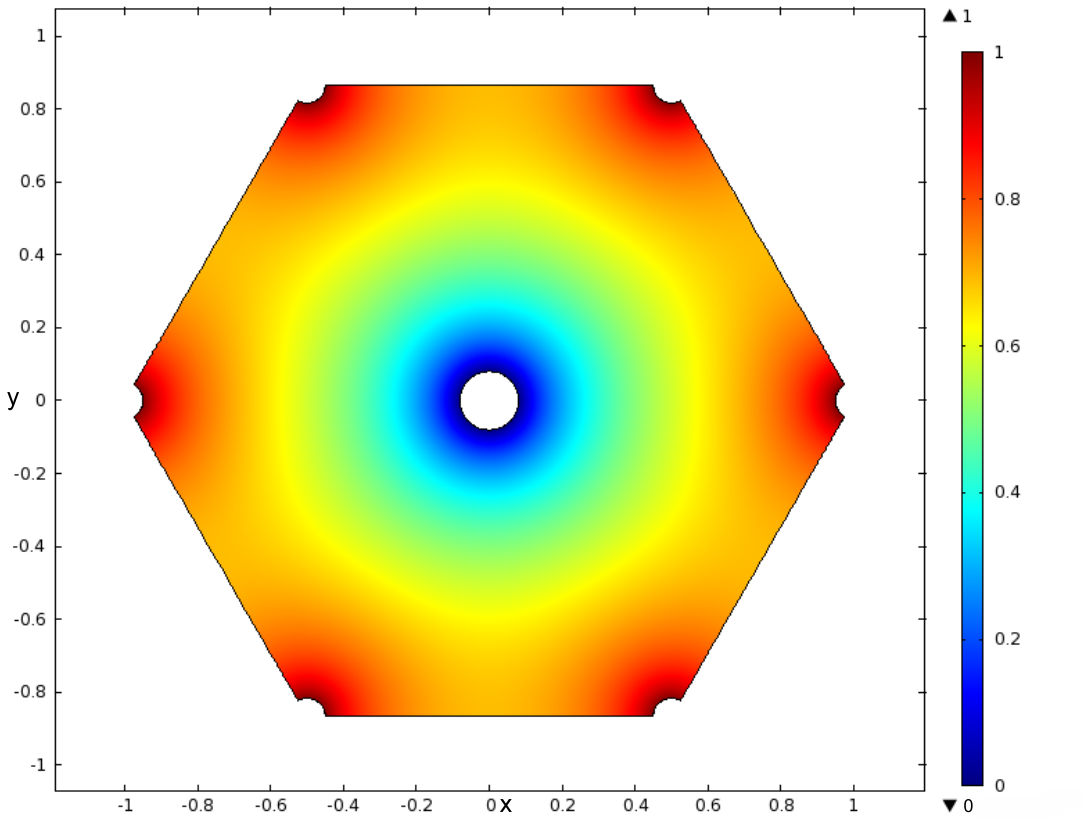

Figure 4.1.5: Dimensionless sinusoidal pressure profile for the model of a single lobule with interstitial flow. The nondimensionalised sinusoidal pressure 1 is applied at the portal tracts while the nondimensionalised zero pressure is applied at the centrilobular vein.

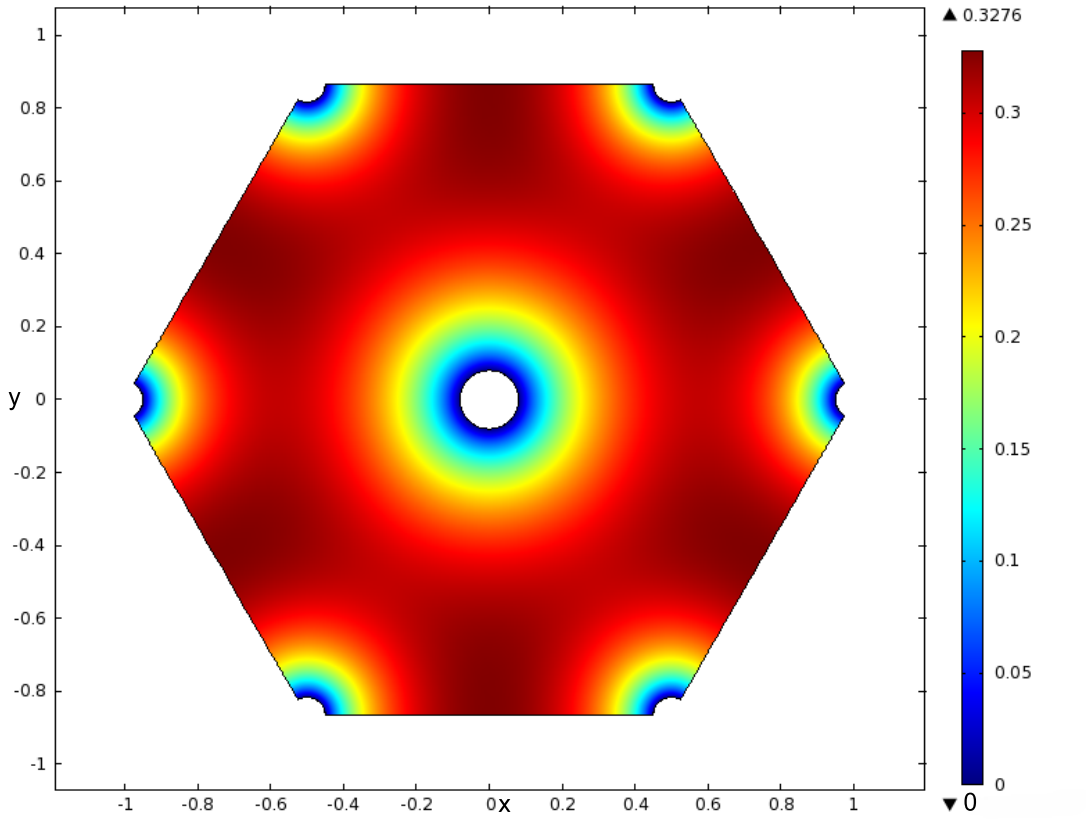

Figure 4.1.6: Dimensionless interstitial pressure profile for the single lobule model. The nondimensionalised zero interstitial pressures are applied at the portal tracts and the centrilobular vein.

4.1.5 Analytical solutions

We now consider solving the equations analytically, and the results will be compared to the numerical solutions. To solve this problem analytically, we assume the portal tracts and the centrilobular veins are point sources and sinks, respectively. The system is modelled as an infinite lattice of hexagonal lobules with portal tracts (PT) as point sources at the vertexes of the hexagons and centrilobular veins (CV) as point sinks at the centres of the hexagons. The ratio of the number of PT to the number of CV is $2:1$.

General solution for a point source / sink

Subtracting equations (4.1.28) and (4.1.29), we obtain

$$\nabla^{*2} p^* - (F_S + F_I) p^* = 0, \tag{4.1.36}$$

where $p^* = p_S^* - p_I^*$.

Since the governing equations are linear, any sum of solutions is also a solution. We therefore solve for the pressure profile with a single point source and sink, and obtain the full solution by superposition.

The Laplacian of the scalar function ψ in 2D polar coordinates is

$$\nabla^2\psi = \frac{1}{r}\frac{\partial}{\partial r}\left(r\frac{\partial\psi}{\partial r}\right) + \frac{1}{r^2}\frac{\partial^2\psi}{\partial\theta^2} + \frac{\partial^2\psi}{\partial z^2}, \tag{4.1.37}$$

Assuming axisymmetry, (4.1.36) becomes

$$\frac{1}{r^*}\frac{\partial}{\partial r^*}\left(r^*\frac{\partial p^*}{\partial r^*}\right) - (F_S + F_I)p^* = 0. \tag{4.1.38}$$

Then,

$$r^{*2}\frac{\partial^2 p^*}{\partial r^{*2}} + r^*\frac{\partial p^*}{\partial r^*} - r^{*2}(F_S + F_I)p^* = 0. \tag{4.1.39}$$

and, substituting $\gamma = F_S + F_I$,

$$r^{*2}\frac{\partial^2 p^*}{\partial r^{*2}} + r^*\frac{\partial p^*}{\partial r^*} - r^{*2}\gamma p^* = 0. \tag{4.1.40}$$

Defining

$$z^* = \sqrt{\gamma}r^*. \tag{4.1.41}$$

Equation (4.1.40) becomes

$$z^{*2}\frac{\partial^2 p^*}{\partial z^{*2}} + z^*\frac{\partial p^*}{\partial z^*} - z^{*2}p^* = 0. \tag{4.1.42}$$

This is a Modified Bessel Equation which has general solution

$$p^* = AI_0(\sqrt{\gamma}r^*) + BK_0(\sqrt{\gamma}r^*), \tag{4.1.43}$$

where A and B are arbitrary constants and I_0 and K_0 are the modified Bessel functions of the first and second kinds, respectively.

Since the function $I_0(\sqrt{\gamma}r^*)$ increases exponentially quickly as $r^* \to \infty$, we must set $A = 0$ in order to eliminate this behaviour. Therefore,

$$p^* = p_s^* - p_I^* = BK_0(\sqrt{\gamma}r^*). \tag{4.1.44}$$

We now have the related p_S and p_I, and can derive them separately.

From equation (4.1.28) and (4.1.44), we can write

$$-\nabla^{*2}p_S^* + F_S BK_0(\sqrt{\gamma}r^*) = 0. \tag{4.1.45}$$

To find the particular integral of this equation, we try

$$p_S^* = HK_0(\sqrt{\gamma}r^*), \tag{4.1.46}$$

where H is a constant. With this,

$$\nabla^{*2} p_S^* = \gamma H K_0(\sqrt{\gamma} r^*). \tag{4.1.47}$$

Comparing equations (4.1.45) and (4.1.47), we then obtain

$$H = \frac{F_S B}{\gamma}. \tag{4.1.48}$$

This means that p_S^* can be written as a modified Bessel function alone as

$$p_S^* = \frac{F_S}{\gamma} B K_0(\sqrt{\gamma} r^*) \tag{4.1.49}$$

The complementary function from solving equation (4.1.47) is given by $D + E \ln r^*$ for arbitrary constants D and E. From equations (4.1.44) and (4.1.49), we now can calculate the sinusoidal pressure (p_S^*) and the interstitial pressure (p_I^*) as

$$p_S^* = \frac{F_S}{\gamma} B K_0(\sqrt{\gamma} r^*) + D + E \ln r^*, \tag{4.1.50}$$

$$p_I^* = \left(\frac{F_S}{\gamma} - 1 \right) B K_0(\sqrt{\gamma} r^*) + D + E \ln r^*. \tag{4.1.51}$$

Application of boundary conditions

We define P^*_{SPTi}, P^*_{IPTi}, P^*_{SCVj}, and P^*_{ICVj} as the nondimensionalised sinusoidal and interstitial pressures at the ith portal tract and at the jth centrilobular vein, respectively. Using the method of superposition, we can write p^*_S and p^*_I as

$$p^*_S = \sum_{PT,i} P^*_{SPTi} + \sum_{CV,j} P^*_{SCVj}, \tag{4.1.52}$$

$$p^*_I = \sum_{PT,i} P^*_{IPTi} + \sum_{CV,j} P^*_{ICVj}, \tag{4.1.53}$$

From equations (4.1.50) and (4.1.51), we can write P^*_{SPTi}, P^*_{IPTi}, P^*_{SCVj}, and P^*_{ICVj} as

$$P^*_{SPTi} = \frac{F_S}{\gamma} B_{PTi} K_0(\sqrt{\gamma} r^*_{PTi}) + D_{PTi} + E_{PTi} \ln r^*_{PTi}, \tag{4.1.54}$$

$$P^*_{SCVj} = \frac{F_S}{\gamma} B_{CVj} K_0(\sqrt{\gamma} r^*_{CVj}) + D_{CVj} + E_{CVj} \ln r^*_{CVj}, \tag{4.1.55}$$

$$P^*_{IPTi} = \left(\frac{F_S}{\gamma} - 1\right) B_{PTi} K_0(\sqrt{\gamma} r^*_{PTi}) + D_{PTi} + E_{PTi} \ln r^*_{PTi}, \tag{4.1.56}$$

$$P^*_{ICVj} = \left(\frac{F_S}{\gamma} - 1\right) B_{CVj} K_0(\sqrt{\gamma} r^*_{CVj}) + D_{CVj} + E_{CVj} \ln r^*_{CVj}. \tag{4.1.57}$$

The constants D_{PTi} and D_{CVj} can be eliminated by choosing a suitable gauge which we set them all to zero. It remains to find B_{PTi}, B_{CVj}, E_{PTi}, and E_{CVj}

Since the model we are using has singularity at all point sources and sinks; therefore, we prescribe all the fluxes at the edges of the portal tracts radius R_{PT} and the centrilobular veins radius R_{CV} instead.

From (4.1.54) - (4.1.57), we may now calculate the total flux flowing out of the portal tract via sinusoidal space (q_S^*) and the total flux flowing into the portal tract via interstitial space (q_I^*) by integrating the radial component of the velocity around a small circle of radius a surrounding the vessels.

$$q_S^* = \int_0^{2\pi} -\frac{dp_S^*}{dr}|_{r=a} a d\theta = -2\pi \left(\frac{F_S a B}{\sqrt{\gamma}} K_0'(\sqrt{\gamma}a) + E \right), \tag{4.1.58}$$

$$q_I^* = \int_0^{2\pi} -\frac{dp_I^*}{dr}|_{r=a} a d\theta = -2\pi \left(\left(\frac{F_S}{\gamma} - 1 \right) \sqrt{\gamma} a B K_0'(\sqrt{\gamma}a) + E \right), \tag{4.1.59}$$

Letting $a \to 0$, we obtain the flux out of the portal tract into the sinusoids and the flux from sinusoids into the centrilobular vein (see Appendix A for the approximation when $a \to 0$):

$$
\begin{aligned}
q^*_{SPTi} &= \lim_{a\to 0}\left(-2\pi\left(\frac{F_S a B_{PTi}}{\sqrt{\gamma}}K_0'(\sqrt{\gamma}a)+E_{PTi}\right)\right)\\
&= 2\pi\left(\frac{F_S B_{PTi}}{\gamma}-E_{PTi}\right), \qquad (4.1.60)
\end{aligned}
$$

$$
\begin{aligned}
q^*_{SCVj} &= \lim_{a\to 0}\left(-2\pi\left(\frac{F_S a B_{CVj}}{\sqrt{\gamma}}K_0'(\sqrt{\gamma}a)+E_{CVj}\right)\right)\\
&= 2\pi\left(\frac{F_S B_{CVj}}{\gamma}-E_{CVj}\right), \qquad (4.1.61)
\end{aligned}
$$

Similar formulas also apply respectivly to the interstitial parts of both portal tract and centrilobular vein:

$$
\begin{aligned}
q^*_{IPTi} &= \lim_{a\to 0}\left(-2\pi\left(\left(\frac{F_S}{\gamma}-1\right)\sqrt{\gamma}a B_{PTi}K_0'(\sqrt{\gamma}a)+E_{PTi}\right)\right)\\
&= 2\pi\left(\left(\frac{F_S}{\gamma}-1\right)B_{PTi}-E_{PTi}\right), \qquad (4.1.62)
\end{aligned}
$$

$$
\begin{aligned}
q^*_{ICVj} &= \lim_{a\to 0}\left(-2\pi\left(\left(\frac{F_S}{\gamma}-1\right)\sqrt{\gamma}a B_{CVj}K_0'(\sqrt{\gamma}a)+E_{CVj}\right)\right)\\
&= 2\pi\left(\left(\frac{F_S}{\gamma}-1\right)B_{CVj}-E_{CVj}\right). \qquad (4.1.63)
\end{aligned}
$$

We assume that all portal tracts are the same so all the B_{PTi} are equal and, similarly for the E_{PTi}, B_{CVj}, and E_{CVj}. We now denote these parameters as B_{PT}, E_{PT}, B_{CV}, and E_{CV} only and their values solved from equations (4.1.60) - (4.1.63) are:

$$B_{PT} = \frac{1}{2\pi}(q^*_{SPT} - q^*_{IPT}), \tag{4.1.64}$$

$$E_{PT} = \frac{1}{2\pi}\left(q^*_{SPT}\left(\frac{F_S}{\gamma} - 1\right) - q^*_{IPT}\left(\frac{F_S}{\gamma}\right)\right), \tag{4.1.65}$$

$$B_{CV} = \frac{1}{2\pi}(q^*_{SCV} - q^*_{ICV}), \tag{4.1.66}$$

$$E_{CV} = \frac{1}{2\pi}\left(q^*_{SCV}\left(\frac{F_S}{\gamma} - 1\right) - q^*_{ICV}\left(\frac{F_S}{\gamma}\right)\right). \tag{4.1.67}$$

These parameters are then replaced back into equations 4.1.54 - 4.1.57 for the calculation. The results, plotted using MATLAB, are shown in figure 4.1.7 and 4.1.8. The results show similar pattern of both sinusoidal and interstitial pressure profiles to the numerical results.

4.1.6 Comparison of Analytical and Numerical Model

We compare both sinusoidal and interstitial pressure profiles of the analytical solutions from MATLAB and the numerical solutions from COMSOL. The comparisons are shown in figure 4.1.9 and the results show good agreement.

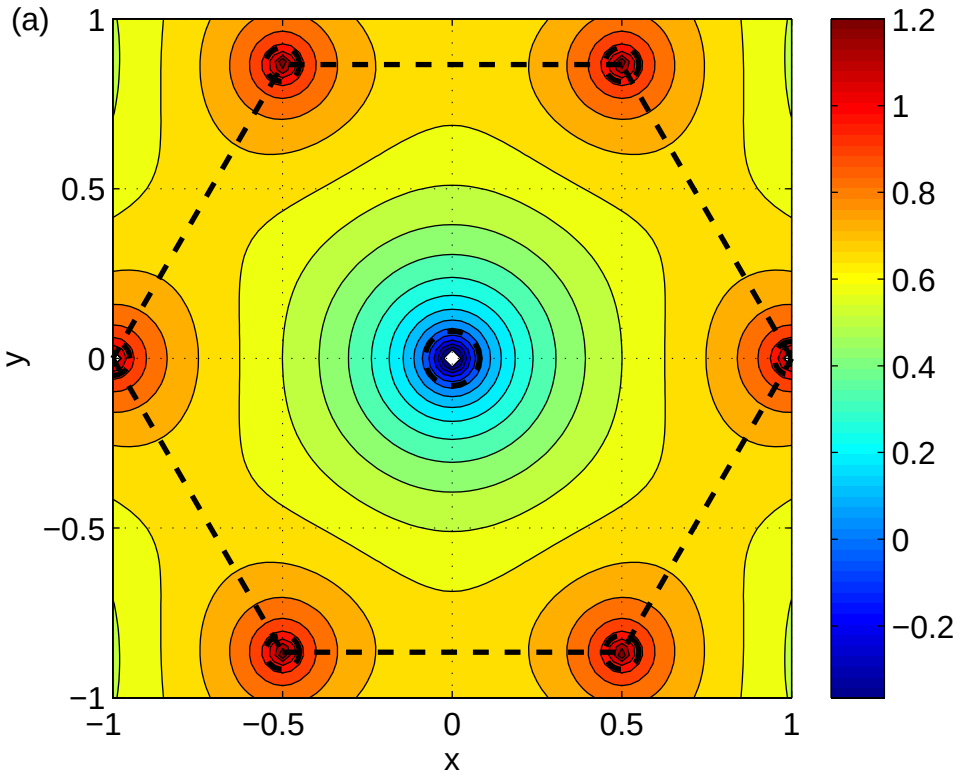

Figure 4.1.7: Dimensionless sinusoidal pressure contour using analytical method.

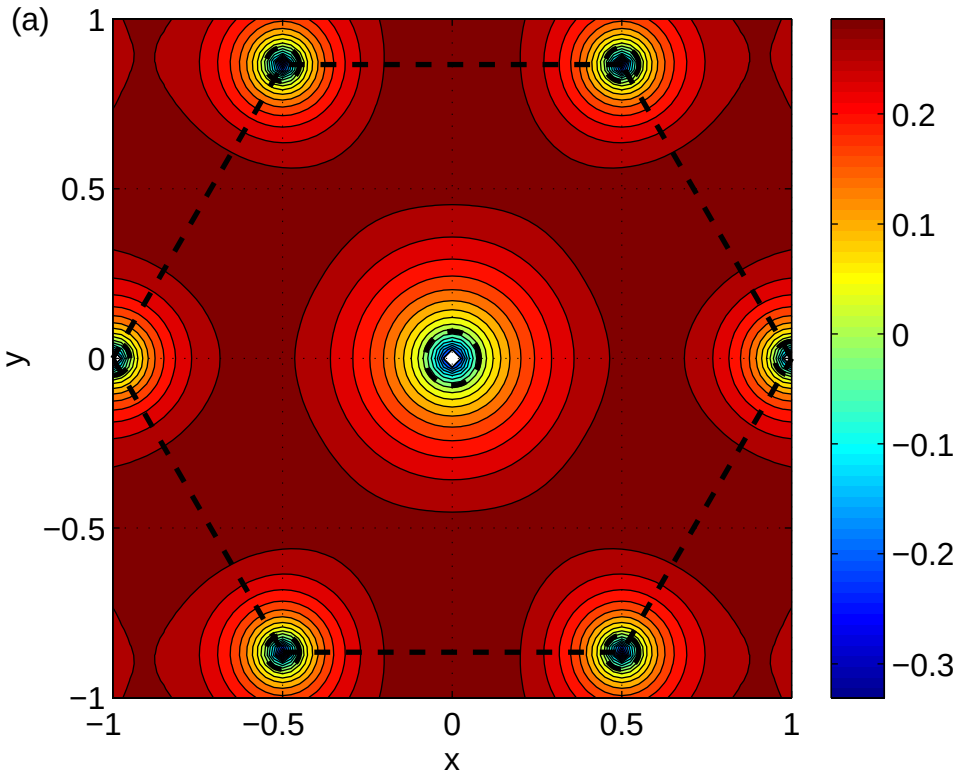

Figure 4.1.8: Dimensionless interstitial pressure contour using analytical method.

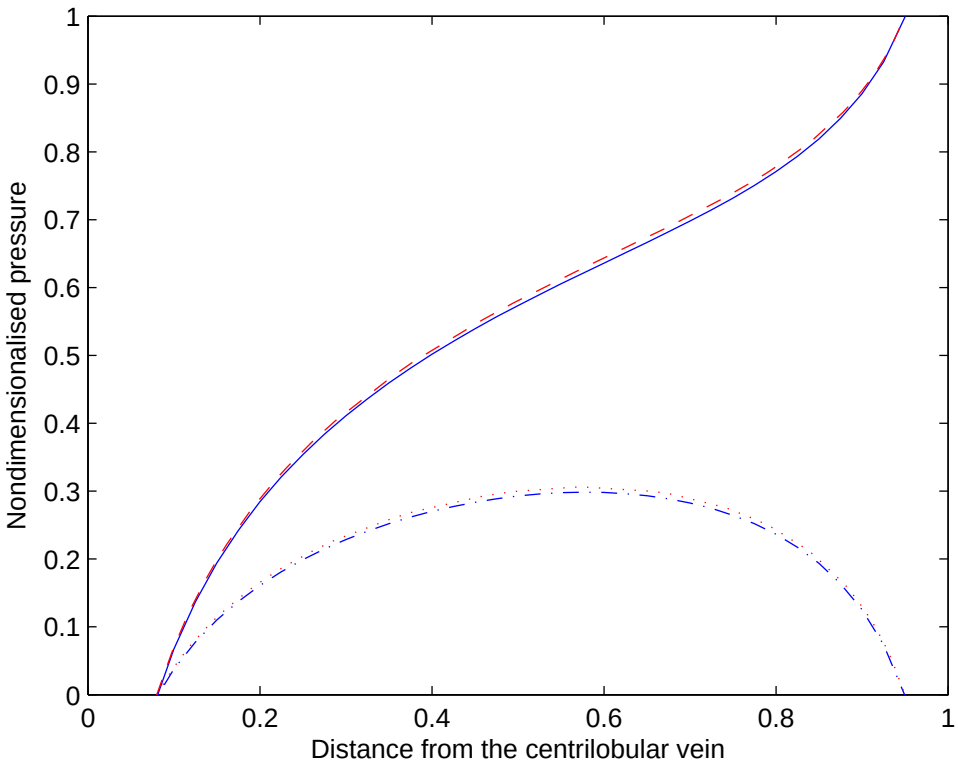

Figure 4.1.9: Comparison of analytical and numerical results of dimensionless sinusoidal and interstitial pressure across the lobule. [analytical/sinusoid (blue $-$), analytical/interstitial (blue $.-$), numerical/sinusoid (red $--$), numerical/interstitial(red $\ldots$)]

4.2 Model of the interstitial fluid pathway in the whole liver

In this section, we investigate the interstitial flow within the entire liver, in which the effect of uptake of lymphatic ducts and the leakage via surfaces of the liver are included.

For the flow within the lobules, the model is extended from the previous section by adding up the mathematical term of the lymphatic duct uptake. The sinusoidal blood flow cannot flow across the lobular boundaries. In contrast, the interstitial fluid can flow freely between lobules and can leak out via the boundaries of the liver.

In order to be able to apply the boundary conditions at the surface of the liver, we must solve the equations numerically. We use parameters from experiments in the literature. However, since we do not include the third dimension in our model, we must make an assumption in order to apply the parameters to our 2D model.

We simplify the liver geometry by treating it as a cuboid with a square cross-section of side L_L and the length L_z (see figure 4.2.1). The lobules also have cuboid shape with a length of L_z similar to the liver but they have square cross-sections of side $L_l = \frac{L_L}{n}$ where n is the number of lobules along each side of the liver. Therefore, the total number of the lobules is equal to n^2.

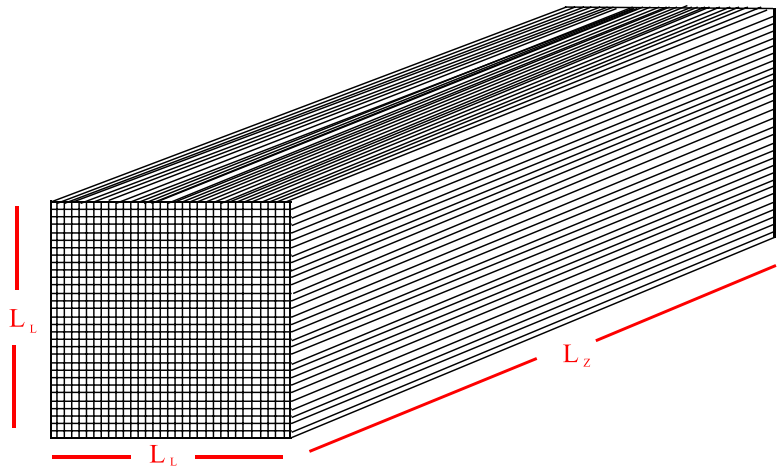

Figure 4.2.1: Diagram of the cuboid liver model.

Since our calculation is based on 2D flow, parallel to the cross-sectional surface of the cuboid, we have to neglect the cross-sectional area of both side of square surface of the cuboid. Therefore, we obtain the surface area of the liver, $A_L = 4L_L L_z$. Alternatively, we can write A_L in terms of the volume of the liver, $V_L = L_L^2 L_z$, as

$$A_L = \frac{4V_L}{L_L}. \tag{4.2.1}$$

Replacing $L_L = nL_l$, we obtain

$$n = \frac{4V_L}{A_L L_l}. \tag{4.2.2}$$

In order to find the number of lobules in our cuboid liver, the values of V_L, A_L, and L_l must be sorted. From the real data, an average volume of human liver is 1520 cm^3 [60].

We use this number as V_L. The normal size of the liver is $20 \times 15 \times 10$ $cm.$, and it has the shape of a triangular prism. Thus, the surface area is $\approx 20 * 15 + 15 * 10 + 20 * 10 + 10\sqrt{20^2 + 15^2} = 900$ cm^2.

From the previous data (done by Bonfiglio et al [11]), the side length of the hexagonal lobule is about 500 μm. By conserving the lobule area, we calculate the side length of our square lobule (L_l) as 800 μm. Substituting these values into equation 4.2.2, we obtain $n \approx 84$ which means the total number of the lobules (n^2) is ≈ 7000. We set $n_0 = 84$, the realistic number of lobules along an edge. All parameter values used in this section are listed in table 4.2

Table 4.2: Physiological parameter values used in the whole liver model

Symbol	Description	Typical Value	Reference
V_L	Liver volume	1.52×10^{-3} m^3	[51]
A_L	Surface area of the liver	9×10^{-2} m^2	[1] see equation 4.2.1
L_l	Side length of the square lobule	8×10^{-4} m	converted from hexagonal lobule
M_L	Permeability of the lower surface of the liver	2.15×10^{-8} m/s/mmHg	[61]
M_U	Permeability of the upper surface of the liver	assumed to be $100M_L$	
R_l	Resistance of the lymphatic duct	1.22×10^6 mmHg·s	[63]
p_0	Pressure at the hilus of the liver	assumed to be zero	

4.2.1 Derivation of model equations

As before, in both sinusoidal and interstitial spaces, Darcy's equation governs the flow in each space:

$$\mathbf{v_S} = -K_S \boldsymbol{\nabla} p_S, \tag{4.2.3}$$

$$\mathbf{v_I} = -K_I \boldsymbol{\nabla} p_I, \tag{4.2.4}$$

where $\mathbf{v_S}$ and $\mathbf{v_I}$ are the Darcy velocities of the fluid in the sinusoidal and interstitial space, respectively, K_S and K_I are the hydraulic conductivity of the sinusoidal space and interstitial space, respectively, and p_S and p_I are the sinusoidal pressure and interstitial pressure, respectively.

We define

$$Q_W = \rho F(p_S - p_I), \tag{4.2.5}$$

to be the volume of the interstitial fluid flow from the sinusoids into the interstitial space per unit time per unit volume of tissue, F is the hepatic filtration coefficient, and ρ is the density of the liver. Assuming the fluids are incompressible and using volume conservation in each space, we can write

$$\nabla \cdot \mathbf{v_S} + Q_W = 0, \tag{4.2.6}$$

$$\nabla \cdot \mathbf{v_I} - Q_W + Q_L = 0, \tag{4.2.7}$$

where Q_L is the volume of interstitial fluid removed from the interstitial space into the lymphatic system per unit time per unit volume of tissue.

Laine et al.(1988) [13] experimentally found the relationship between Q_L and p_I to be the following linear relationship:

$$Q_L = \frac{p_I - p_0}{R_l}, \tag{4.2.8}$$

where R_I is the resistance of the interstitial outflow pathway and p_0 is the pressure in the lymphatic network at the hilus of the liver (a reference point, see figure(4.2.2)).
From equations (4.2.6) - (4.2.7), we can rewrite the system in terms of the pressures as

$$-K_S \nabla^2 p_S + \rho F(p_S - p_I) = 0, \tag{4.2.9}$$

$$-K_I \nabla^2 p_I - \rho F(p_S - p_I) + \frac{p_I - p_0}{R_l} = 0. \tag{4.2.10}$$

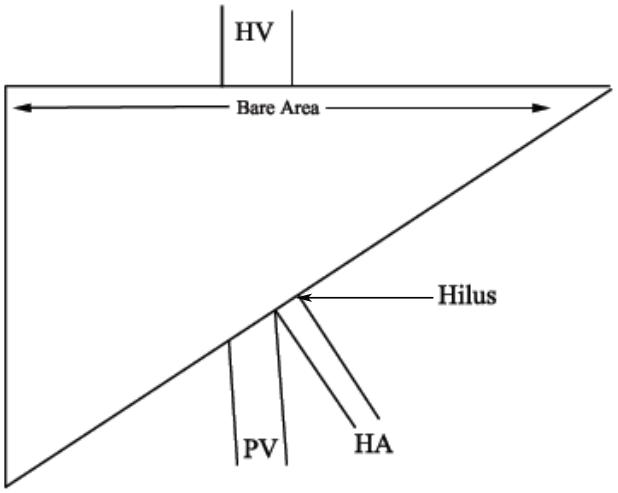

Figure 4.2.2: Diagram of liver and its blood supplies and boundaries.

4.2.2 Derivation of boundary conditions

We treat the lobules as a regular lattice tessellating the cross-section. We assume that sinusoidal blood cannot flow across the edges of the lobule, whilst the interstitial fluid can flow freely across the boundaries. Therefore, the boundary condition is:

- at the edges of the lobule

$$-K_S \mathbf{n} \cdot \boldsymbol{\nabla} p_S = 0, \tag{4.2.11}$$

whilst the continuous boundary condition is applied to the interstitial flow.

For the boundary of the vessels; however, we consider two different models of portal tracts and centrilobular veins: treating them as points and treating them as finite size vessels.

Point model of vessels

We treat each portal tract and each centrilobular vein as a point in the plane where the nth portal tract each produces a flux q_{SPTn} per unit length and the nth centrilobular vein receives a flux q_{SCVn} per unit length, and all fluxes are distributed evenly in all directions. Each lymphatic duct at the portal tract and the centrilobular vein receives a flux q_{IPTn} per unit length and q_{ICVn} per unit length, respectively. Note that all q_{SCVn}, q_{IPTn}, and q_{ICVn} are negative. Thus, we integrate the flux crossing an arc of a small circle around the portal tract and the centrilobular vein because they have zero area in the model, and the boundary conditions are:

- At the portal tracts,

$$\int_{arc} \mathbf{v_S} \cdot \mathbf{n} dl = \lim_{\epsilon \to 0} \int_{\theta_0}^{\theta_1} -K_S \frac{\partial p_S}{\partial r} \mid_{r=\epsilon} \epsilon d\theta = \frac{\theta_1 - \theta_0}{2\pi} q_{SPTn}, \tag{4.2.12}$$

$$\int_{arc} \mathbf{v_I} \cdot \mathbf{n} dl = \lim_{\epsilon \to 0} \int_{\theta_0}^{\theta_1} -K_I \frac{\partial p_I}{\partial r} \mid_{r=\epsilon} \epsilon d\theta = \frac{\theta_1 - \theta_0}{2\pi} q_{IPTn}, \tag{4.2.13}$$

for any angles θ_0, θ_1.

- Similarly, at the centrilobular veins,

$$\int_{arc} \mathbf{v_S} \cdot \mathbf{n} dl = \lim_{\epsilon \to 0} \int_{\theta_0}^{\theta_1} -K_S \frac{\partial p_S}{\partial r} \mid_{r=\epsilon} \epsilon d\theta = \frac{\theta_1 - \theta_0}{2\pi} q_{SCVn}, \tag{4.2.14}$$

$$\int_{arc} \mathbf{v_I} \cdot \mathbf{n} dl = \lim_{\epsilon \to 0} \int_{\theta_0}^{\theta_1} -K_I \frac{\partial p_I}{\partial r} \mid_{r=\epsilon} \epsilon d\theta = \frac{\theta_1 - \theta_0}{2\pi} q_{ICVn}, \tag{4.2.15}$$

In these equations, $\mathbf{n}$ is the normal unit vector to the boundary and ϵ is the radius from the centre of the vessels. However, in this model, we cannot prescribe the pressure as there is a singularity at the points. We then consider a finite size model to be able to prescribe the pressures.

Finite size model of vessels

In this model, we can prescribe either the sinusoidal pressure or the fluxes at the vessels:

- at the portal tracts,

  Pressure

$$p_S = p_{SPTn}, \tag{4.2.16}$$

  or

Flux

$$\mathbf{n} \cdot \mathbf{v}_S = -K_S \mathbf{n} \cdot \boldsymbol{\nabla} p_S = \frac{q_{SPTn}}{2\pi r_{PTn}} \tag{4.2.17}$$

- at the centrilobular veins,

  Pressure

$$p_S = p_{SCVn}, \tag{4.2.18}$$

  or

  Flux

$$\mathbf{n} \cdot \mathbf{v}_S = -K_S \mathbf{n} \cdot \boldsymbol{\nabla} p_S = \frac{q_{SCVn}}{2\pi r_{CVn}}. \tag{4.2.19}$$

For the interstitial part, we set the boundary conditions as

- at the portal tracts,

  Pressure

$$p_I = p_{IPTn}, \tag{4.2.20}$$

  or

  Flux

$$\mathbf{n} \cdot \mathbf{v}_I = -K_I \mathbf{n} \cdot \boldsymbol{\nabla} p_I = \frac{q_{IPTn}}{2\pi r_{PTn}}. \tag{4.2.21}$$

- at the centrilobular veins,

  Pressure

$$p_I = p_{ICVn}, \tag{4.2.22}$$

or

Flux

$$\mathbf{n} \cdot \mathbf{v}_I = -K_I \mathbf{n} \cdot \boldsymbol{\nabla} p_I = \frac{q_{ICVn}}{2\pi r_{CVn}}. \tag{4.2.23}$$

where p_{SPTn} and p_{SCVn} are the prescribed sinusoidal pressure at the nth portal tract and nth centrilobular vein , respectively, p_{IPTn} and p_{ICVn} are the prescribed interstitial pressure at the nth portal tract and nth centrilobular vein, respectively, while r_{PTn} and r_{CVn} are the radius of the nth portal tract and nth centrilobular vein, respectively (we assume that all portal tracts and all centrilobular veins are circular).

For the boundary conditions of the liver, we use a no flux condition for sinusoidal flow since the blood cannot leak out from the liver. For the interstitial flow,we assume the surface can be modelled by membranes of permeability M_U and M_L at the bare area and at the rest of the surface (see figure 4.2.2), respectively. We assume that the permeability of the bare area is much more higher than the rest of the surface; therefore, $M_U \gg M_L$.

Thus, at the surfaces of the liver, we use the following boundary conditions:

- at all surfaces of the liver

$$\mathbf{n} \cdot \boldsymbol{\nabla} p_S = 0 \tag{4.2.24}$$

- at the bare area (upper boundary)

$$-K_I \mathbf{n} \cdot \boldsymbol{\nabla} p_I = M_U (p_I - p_{VC}) \tag{4.2.25}$$

- at the rest of the surfaces (lower boundary)

$$-K_I \mathbf{n} \cdot \boldsymbol{\nabla} p_I = M_L (p_I - p_{abd}) \tag{4.2.26}$$

where p_{VC} is the vena cava pressure and p_{abd} is the intraabdominal pressure; both are assumed to be zero.

4.2.3 Nondimensionalisation

Nondimensionalsation of the variables and parameters

We nondimensionalise the system, using *s to denote nondimensional variables:

$$\mathbf{x} = L\mathbf{x}^*, \tag{4.2.27}$$

$$\mathbf{v_S} = V\mathbf{v_S^*}, \tag{4.2.28}$$

$$\mathbf{v_I} = V\mathbf{v_I^*}, \tag{4.2.29}$$

$$p_S = p_0 + (p_{SPT} - p_0)p_S^*, \tag{4.2.30}$$

$$p_I = p_0 + (p_{SPT} - p_0)p_I^*, \tag{4.2.31}$$

$$Q_L = \frac{K_I(p_{SPT} - p_0)}{L^2} Q_L^* \tag{4.2.32}$$

where L is the length of the edge of the lobule, the velocity scale V is defined as $\frac{K_S(p_{SPT}-p_0)}{L}$ so that all parameters can be vanished, p_{SPT} is an average sinusoidal pressure at the portal tracts, p_0 is the pressure at the hilus of the liver, q_{SPT} is the flux per unit length of circumference of the portal tract, and Q is the flux per unit length of circumference of the portal tract that gives $p = p_{SPT}$ at the portal tract.

We can rewrite (4.2.3)-(4.2.4) $\mathbf{v_S}$ and $\mathbf{v_I}$ in terms of the nondimensionalised variables as

$$\mathbf{v_S} = -\frac{K_S(p_{SPT} - p_0)}{L} \boldsymbol{\nabla}^* p_S^* \Rightarrow \mathbf{v_S^*} = -\boldsymbol{\nabla}^* p_S^*, \tag{4.2.33}$$

$$\mathbf{v_I} = -\frac{K_I(P_{SPT} - p_0)}{L} \boldsymbol{\nabla}^* p_I^* \Rightarrow \mathbf{v_I^*} = -K_R \boldsymbol{\nabla}^* p_I^*, \tag{4.2.34}$$

where $K_R = \frac{K_I}{K_S}$.

We can rewrite (4.2.9)-(4.2.10) in nondimensionalised form as

$$\nabla^{*2} p_S^* - F_S^*(p_S^* - p_I^*) = 0, \tag{4.2.35}$$

$$\nabla^{*2} p_I^* + F_I^*(p_S^* - p_I^*) - \frac{p_I^*}{R_l^*} = 0, \tag{4.2.36}$$

where $F_S^* = \frac{L^2 \rho F}{K_S}$, $F_I^* = \frac{L^2 \rho F}{K_I}$, $F_I^* = \frac{F_S^*}{K_R}$, and $R_l^* = \frac{K_I}{L^2} R_l$.

Nondimensionalised boundary conditions of the lobules and the liver

The nondimensionalised boundary conditions of the lobules are:

- at the edge of the portal tract

$$-\mathbf{n} \cdot \boldsymbol{\nabla}^* p_S^* = \frac{q_{SPTn}}{2\pi K_S (p_{SPT} - p_0) r_{PTn}^*} = q_{SPTn}^*, \tag{4.2.37}$$

$$-\mathbf{n} \cdot \boldsymbol{\nabla}^* p_I^* = \frac{q_{IPTn}}{2\pi K_I (p_{SPT} - p_0) r_{PTn}^*} = q_{IPTn}^*, \tag{4.2.38}$$

- at the edge of the centrilobular vein

$$-\mathbf{n} \cdot \boldsymbol{\nabla}^* p_S^* = \frac{q_{SCVn}}{2\pi K_S (p_{SPT} - p_0) r_{CVn}^*} = q_{SCVn}^*, \tag{4.2.39}$$

$$-\mathbf{n} \cdot \boldsymbol{\nabla}^* p_I^* = \frac{q_{ICVn}}{2\pi K_I (p_{SPT} - p_0) r_{CVn}^*} = q_{ICVn}^*, \tag{4.2.40}$$

where q^*_{SPTn} and q^*_{SCVn} are the nondimensionalised sinusoidal flux at the portal tract and centrilobular vein, respectively, q^*_{IPTn} and q^*_{ICVn} are the nondimensionalised interstitial flux at the portal tract and centrilobular vein, respectively, r^*_{PTn} and r^*_{CVn} are nondimensionalised radii of the portal tract and the centrilobular vein, respectively.

- at the boundary between lobules

$$\mathbf{n} \cdot \boldsymbol{\nabla}^* p^*_S = 0, \tag{4.2.41}$$

The Nondimensionalised boundary conditions of the liver are:

- at all boundaries/surfaces of the liver

$$\mathbf{n} \cdot \boldsymbol{\nabla}^* p^*_S = 0, \tag{4.2.42}$$

- at the bare area (upper boundary)

$$-\mathbf{n} \cdot \boldsymbol{\nabla}^* p^*_I = \frac{M_U L}{K_I} \left(p^*_I - p^*_{VC} \right), \tag{4.2.43}$$

- at the rest of the surfaces (lower boundary)

$$-\mathbf{n} \cdot \boldsymbol{\nabla}^* p^*_I = \frac{M_L L}{K_I} \left(p^*_I - p^*_{abd} \right), \tag{4.2.44}$$

where $p^*_{VC} = \frac{p_{VC}-p_0}{p_{SPT}-p_0}$ and $p^*_{abd} = \frac{p_{abd}-p_0}{p_{SPT}-p_0}$.

4.2.4 Analytical solution in the case of small vessels

To make analytical progress and simplify the model, we consider an idealised case, in which the model consists of an infinite regular hexagonal lattice of lobules, with each lobule having a centrilobular vein in the centre and a portal tract at each vertex.

From (4.2.35), we get

$$p^*_I = -\frac{1}{F^*_S}\nabla^{*2}p^*_S + p^*_S. \tag{4.2.45}$$

substituting p^*_I from (4.2.45) into (4.2.36), we get the single 4th order differential equation

$$\nabla^{*4}p^*_S - (F^*_S + F^*_I + \frac{1}{R^*_I})\nabla^{*2}p^*_S + \frac{F^*_S p^*_S}{R^*_I} = 0, \tag{4.2.46}$$

To solve the equation (4.2.46), we write it as

$$(\nabla^{*2} - C_1^2)(\nabla^{*2} - C_2^2)p^*_S = 0, \tag{4.2.47}$$

and then C_1 and C_2 are given by

$$C_{1,2} = \left(\frac{(F_S^* + F_I^* + \frac{1}{R_I^*}) \pm \sqrt{(F_S^* + F_I^* + \frac{1}{R_I^*})^2 - \frac{4F_S^*}{R_I^*}}}{2} \right)^{\frac{1}{2}}. \tag{4.2.48}$$

Equation (4.2.47) implies that $\nabla^{*2} p_S^* - C_1^2 p_S^* = 0$ or $\nabla^{*2} p_S^* - C_2^2 p_S^* = 0$.

We now find the general solution for an infinite plane containing a single portal tract or centrilobular vein; the solution of a plane with multiple vessels can be obtained by superposition.

Using cylindrical coordinates centred on the portal tract or centrilobular vein and assuming an axisymmetric solution, we get

$$\frac{\partial^2 p_S^*}{\partial r^{*2}} + \frac{1}{r^*} \frac{\partial p_S^*}{\partial r^*} - C_{1,2}^2 p_S^* = 0, \tag{4.2.49}$$

which has a solution in terms of modified Bessel functions. Hence, using the principle of linear superposition, the general solution is

$$p_S^* = a_1 I_0(C_1 r^*) + b_1 K_0(C_1 r^*) + a_2 I_0(C_2 r^*) + b_2 K_0(C_2 r^*), \tag{4.2.50}$$

where a_1, a_2, b_1, and b_2 are constants.

Since p_S^* cannot rise exponentially away from the portal tracts, the terms involving I_0 are not allowed and so $a_1 = a_2 = 0$.

Hence for a plane with multiple portal tracts and centrilobular veins, the general solution for p_S^* is

$$p_S^* = \sum_{n=1}^{N_{PT}} \sum_{j=1}^{2} b_{PTnj} K_0(C_j r_{PTn}^*) + \sum_{n=1}^{N_{CV}} \sum_{j=1}^{2} b_{CVnj} K_0(C_j r_{CVn}^*), \tag{4.2.51}$$

and using (4.2.45),

$$\begin{aligned} p_I^* &= -\frac{1}{F_S}\nabla^2 p_S^* + p_S^* \\ &= \sum_{n=1}^{N_{PT}} \sum_{j=1}^{2} b_{PTnj} \left(1 - \frac{C_j^2}{F_S^*}\right) K_0(C_j r_{PTn}^*) + \\ &\quad \sum_{n=1}^{N_{CV}} \sum_{j=1}^{2} b_{CVnj} \left(1 - \frac{C_j^2}{F_S^*}\right) K_0(C_j r_{CVn}^*), \end{aligned} \tag{4.2.52}$$

where N_{PT} and N_{CV} are the numbers of portal tracts and centrilobular veins, respectively, r_{PTn}^* and r_{CVn}^* are the radial distance from the centre of nth portal tract and nth centrilobular vein, respectively, b_{PTnj} and b_{CVnj} are unknown constants to be determined from the boundary conditions.

Finding the total fluid flux across a small circle of radius ϵ surrounding a given portal

tract or centrilobular vein and letting $\epsilon \to 0$, we obtain the flux given by the boundary conditions (see Appendix A for details). Thus, we obtain the following equations:

$$\begin{aligned}
\tilde{q}^*_{SPTn} &= \lim_{\epsilon\to 0}\int_0^{2\pi} -\left.\frac{dp^*_S}{dr^*}\right|_{r^*=\epsilon} \epsilon d\theta \\
&= \lim_{\epsilon\to 0}(-2\pi b_{PTn1} C_1 \epsilon K_0'(C_1\epsilon) - 2\pi b_{PTn2} C_2 \epsilon K_0'(C_2\epsilon)) \\
&= 2\pi(b_{PTn1} + b_{PTn2}), \qquad (4.2.53)
\end{aligned}$$

$$\begin{aligned}
\tilde{q}^*_{SCVn} &= \lim_{\epsilon\to 0}\int_0^{2\pi} -\left.\frac{dp^*_S}{dr^*}\right|_{r^*=\epsilon} \epsilon d\theta \\
&= \lim_{\epsilon\to 0}(-2\pi b_{CVn1} C_1 \epsilon K_0'(C_1\epsilon) - 2\pi b_{CVn2} C_2 \epsilon K_0'(C_2\epsilon)) \\
&= 2\pi(b_{CVn1} + b_{CVn2}), \qquad (4.2.54)
\end{aligned}$$

$$\begin{aligned}
\tilde{q}^*_{IPTn} &= \lim_{\epsilon\to 0}\int_0^{2\pi} -\left.\frac{dp^*_I}{dr^*}\right|_{r^*=\epsilon} \epsilon d\theta \\
&= \lim_{\epsilon\to 0}\left(-2\pi b_{PTn1} C_1 \epsilon \left(1 - \frac{C_1^2}{F_S^*}\right) K'(C_1\epsilon) - 2\pi b_{PTn2} C_2 \epsilon \left(1 - \frac{C_2^2}{F_S^*}\right) K'(C_2\epsilon)\right) \\
&= 2\pi\left(b_{PTn1}\left(1 - \frac{C_1^2}{F_S^*}\right) + b_{PTn2}\left(1 - \frac{C_2^2}{F_S^*}\right)\right), \qquad (4.2.55)
\end{aligned}$$

$$\begin{aligned}\tilde{q}^*_{ICVn} &= \lim_{\epsilon\to 0}\int_0^{2\pi} -\left.\frac{dp^*_I}{dr^*}\right|_{r^*=\epsilon}\epsilon d\theta \\ &= \lim_{\epsilon\to 0}\left(-2\pi b_{CVn1}\epsilon C_1\left(1-\frac{C_1^2}{F^*_S}\right)K'(C_1\epsilon) - 2\pi b_{CVn2}\epsilon C_2\left(1-\frac{C_2^2}{F^*_S}\right)K'(C_2\epsilon)\right) \\ &= 2\pi\left(b_{CVn1}\left(1-\frac{C_1^2}{F^*_S}\right)+b_{CVn2}\left(1-\frac{C_2^2}{F^*_S}\right)\right). \qquad (4.2.56)\end{aligned}$$

From the above set of equations, we can solve for b^{pt}_{n1}, b^{pt}_{n2}, b^{cv}_{n1}, and b^{cv}_{n2} as

$$b_{PTn1} = \frac{\tilde{q}^*_{SPTn}}{2\pi} - \frac{F^*_S}{2\pi(C_1^2-C_2^2)}\left(\tilde{q}^*_{IPTn} - \tilde{q}^*_{SPTn}\left(1-\frac{C_1^2}{F^*_S}\right)\right), \qquad (4.2.57)$$

$$b_{PTn2} = \frac{F^*_S}{2\pi(C_1^2-C_2^2)}\left(\tilde{q}^*_{IPTn} - \tilde{q}^*_{SPTn}\left(1-\frac{C_1^2}{F^*_S}\right)\right), \qquad (4.2.58)$$

$$b_{CVn1} = \frac{\tilde{q}^*_{SCVn}}{2\pi} - \frac{F^*_S}{2\pi(C_1^2-C_2^2)}\left(\tilde{q}^*_{ICVn} - \tilde{q}^*_{SCVn}\left(1-\frac{C_1^2}{F^*_S}\right)\right), \qquad (4.2.59)$$

$$b_{CVn2} = \frac{F^*_S}{2\pi(C_1^2-C_2^2)}\left(\tilde{q}^*_{ICVn} - \tilde{q}^*_{SCVn}\left(1-\frac{C_1^2}{F^*_S}\right)\right). \qquad (4.2.60)$$

These can be substituted into (4.2.51)-(4.2.52) to give p^*_S and p^*_I.

In the previous section, we treated the vessels as points; however, we need to satisfy the boundary conditions at the edges of the lobules. The continuity boundary condition is satisfied (since the solutions (4.2.51) and (4.2.52) are analytic everywhere except at the

portal tracts and the centrilobular veins). However, to satisfy (4.2.11) approximately, we consider a very large regular hexagonal lattice, and assume $\tilde{q}^*_{SPTn}$ and $\tilde{q}^*_{SCVn}$ are equal for all n, which means that (4.2.11) is approximately satisfied by symmetry in the lobules far from the boundaries.

This approach can only be used to model flow far from the surfaces of the liver and of interstitial fluid over the large scale, owing to the assumption of symmetry.

4.2.5 Numerical solution for finite size vessels

We aim to find the amount of total interstitial fluid leakage via the surfaces of the liver from the model, $Q_{sf}^{n_0}$. However, since the value of n_0 is too large for our computer to simulate, we choose smaller values of n instead and expect that the results can predict the value of $Q_{sf}^{n_0}$.

Boundary conditions of the lobule

Similar to the previous, we assume that blood cannot flow across the edges of the lobule whilst the interstitial fluid can flow freely. We apply either pressure or flux boundary conditions at the portal tracts. For the pressure boundary condition, for simplicity, we assume that every portal tract is prescribed with the same pressure P_{SPT}. For the flux boundary condition, we assume that every lobule receive blood supply equally from the total blood entry, which means that each lobule receive blood of $\frac{1.4}{n^2}$ l/min. In both cases, every centrilobular vein is prescribed with pressure P_{SCV}, whilst there is no flow of the interstitial fluid across all the vessels.

- At the edges of the lobule

$$-K_S \mathbf{n} \cdot \boldsymbol{\nabla} p_S = 0, \tag{4.2.61}$$

- At portal tracts

$$p_S = P_{SPT} \quad \text{or} \quad \frac{q_{SPT}}{2\pi r_{PT}} = 6.25 \times 10^{-5}, \tag{4.2.62}$$

$$-K_I \mathbf{n} \cdot \boldsymbol{\nabla} p_I = 0, \tag{4.2.63}$$

- At centrilobular vein

$$p_S = P_{SCV}, \tag{4.2.64}$$

$$-K_I \mathbf{n} \cdot \boldsymbol{\nabla} p_I = 0. \tag{4.2.65}$$

Boundary conditions at the surface of the liver

As before, we assume that blood cannot leak pass the liver surface whilst the interstitial fluid can flow across both upper and lower surfaces which have different permeabilities, give the conditions in 4.2.24 - 4.2.26. Note that we do not know how much of the surface is covered by the bare area. Here, we have arbitrarily chosen one face of the model liver, the upper surface, to be the bare area, meaning the proportion is $\frac{1}{4}$. Figure 4.2.3 shows diagram of the boundary conditions of the model.

Nondimensionalised boundary conditions of the lobule

Equations (4.2.61) - (4.2.65) can be nondimensionalised as

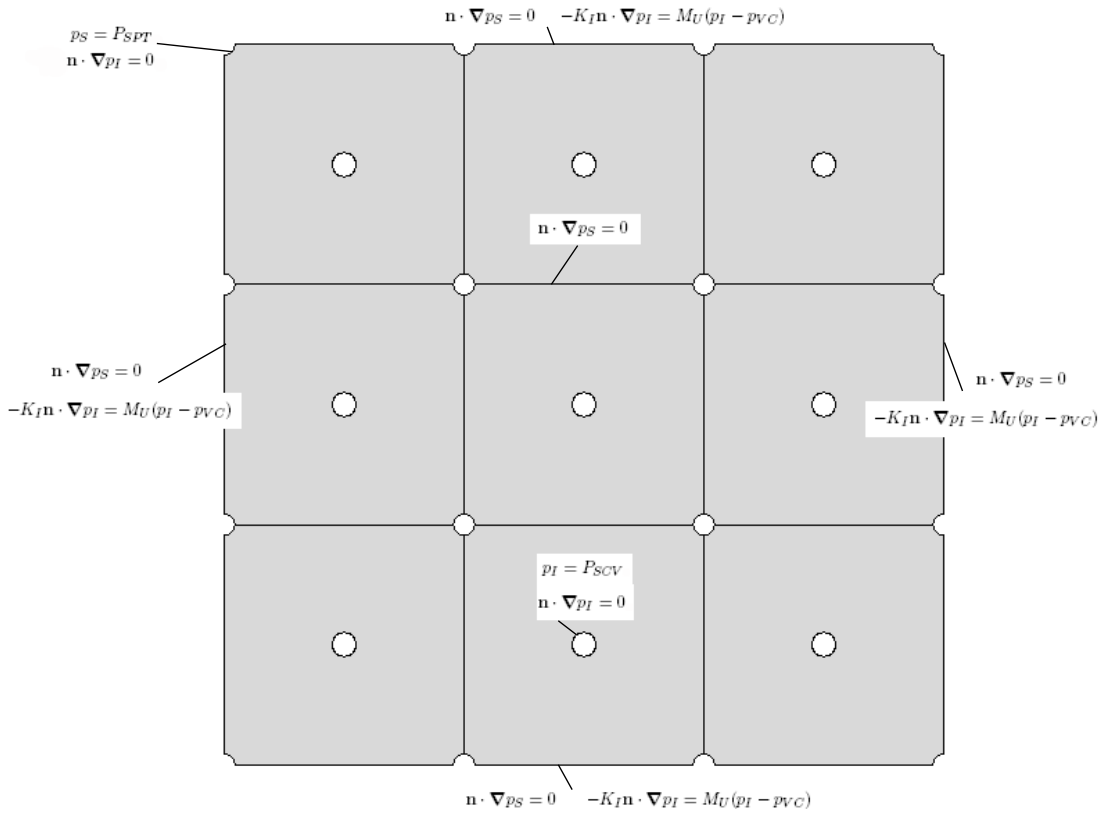

Figure 4.2.3: Diagram of pressure boundary conditions of the 3×3 liver model.

- At the edges of the lobule

$$\mathbf{n} \cdot \boldsymbol{\nabla}^* p_S^* = 0 \quad \text{or} \quad q_{SPT}^* = 1.04, \tag{4.2.66}$$

- At portal tracts

$$p_S^* = 1 \tag{4.2.67}$$

$$\mathbf{n} \cdot \boldsymbol{\nabla}^* p_I^* = 0, \tag{4.2.68}$$

- At centrilobular vein

$$p_S^* = \frac{P_{SCV} - p_0}{P_{SPT} - p_0}, \tag{4.2.69}$$

$$\mathbf{n} \cdot \boldsymbol{\nabla}^* p_I^* = 0. \tag{4.2.70}$$

Nondimensionalised boundary conditions at the surface of the liver

The nondimensionalised boundary conditions are given by equations 4.2.42 - 4.2.44

Numerical results

The numerical analysis is done using a finite element method in COMSOL Multiphysics software version 4.2. Using the governing equations and the boundary conditions stated previously, we can simulate the pressure profiles of both sinusoidal and interstitial flows with different n. However, the value $n = 84$ in the real liver is too large for computing; we found that $n = 6$ is the maximum value we can achieve.

We simulated the models using $n = 2, 3, 4, 5$, and 6 in order to check whether the flux crossing the liver surfaces depends on n. Here we choose the results from $n = 3$ and $n = 6$ as examples. Figure 4.2.4 and 4.2.6 show that the pressure gradient in the sinusoids of each lobule is similar throughout the whole liver. For the interstitial space, as shown in figure 4.2.5 and 4.2.7, the fluid pressures in lobules that are away from the surfaces of the liver are very close to each other. Thus, the pressure drop seems to be confined to the lobules that are located at the surfaces.

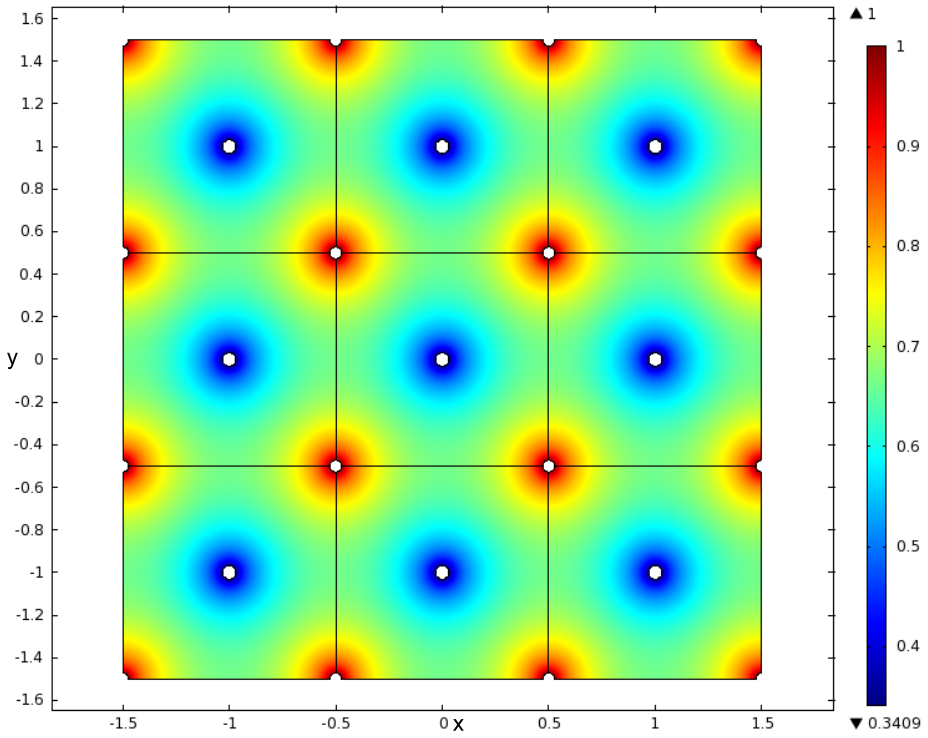

Figure 4.2.4: Dimensionless sinusoidal pressure profile ($n = 3$) when the dimensionless pressure boundary condition is applied at the portal tracts.

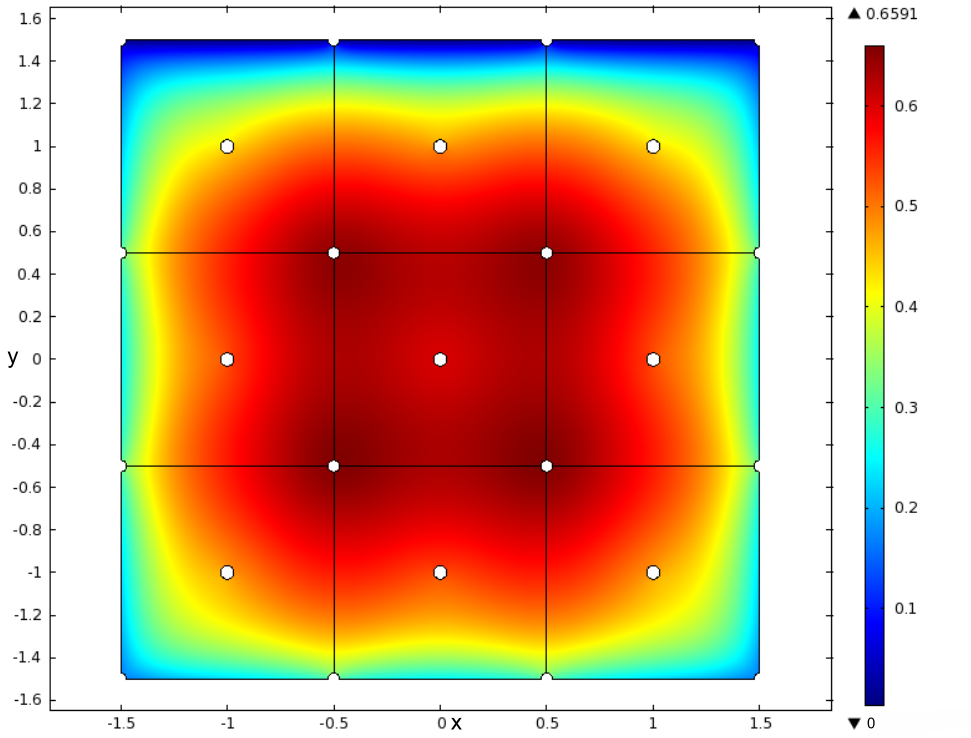

Figure 4.2.5: Dimensionless interstitial pressure profile ($n = 3$) when the dimensionless pressure boundary condition is applied at the portal tracts.

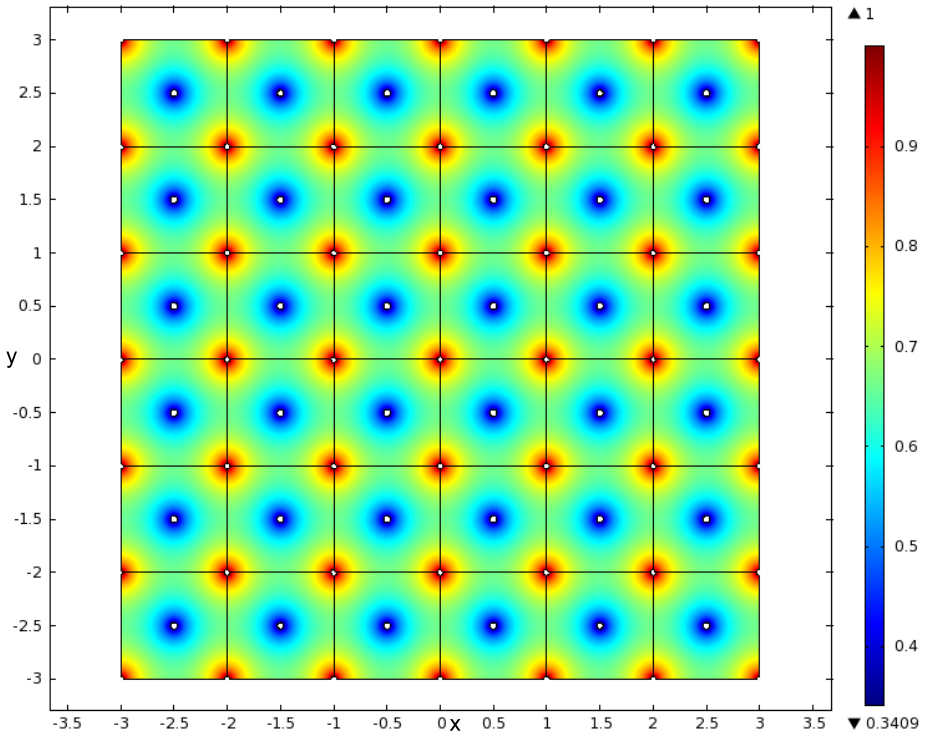

Figure 4.2.6: Dimensionless sinusoidal pressure profile ($n = 6$) when the dimensionless pressure boundary condition is applied at the portal tracts.

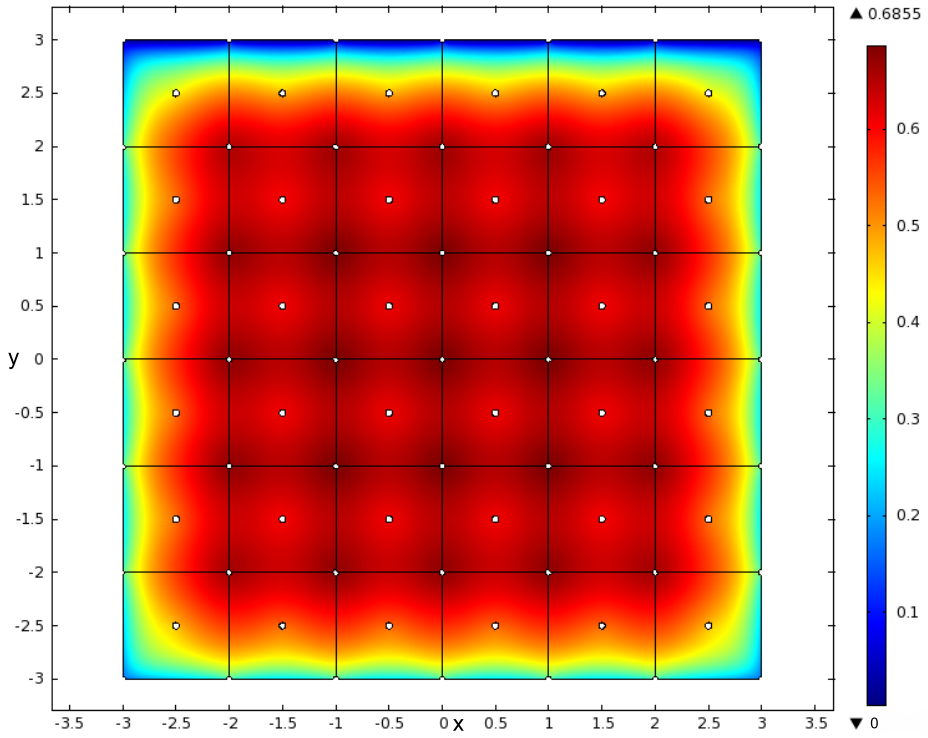

Figure 4.2.7: Dimensionless interstitial pressure profile ($n = 6$) when the dimensionless pressure boundary condition is applied at the portal tracts.

Calculation of fluid flow in both interstitial pathways

For any $n \times n$ lobule, the total amount of blood supply, Q_{bl}^n, can be calculated from:

$$\begin{aligned} Q_{bl}^n &= \frac{V_L}{n^2 L_l^2} \int -\mathbf{n} \cdot \mathbf{v_S} dl \\ &= \frac{V_L K_S}{n^2 L_l^2} \int \mathbf{n} \cdot \boldsymbol{\nabla} p_S dl, \end{aligned} \tag{4.2.71}$$

which can be written in terms of dimensionless variables as

$$Q_{bl}^n = \frac{V_L K_S (p_{PT} - p_0)}{n^2 L_l^2} \int \mathbf{n} \cdot \boldsymbol{\nabla}^* p_S^* dl^*. \tag{4.2.72}$$

From the models, when we prescribe the pressure boundary condition at the portal tracts, we find that the value of Q_{bl}^n is independent of n; therefore, $Q_{bl}^n = Q_{bl}$ with the average value of 5.4 l/min, and is independent of n. The value has the same order of magnitude as the physiological value, which is about 1.4 l/min [3].

The total flux of fluid leaving the liver via the lower surface of the liver, Q_{sf}^n, can be calculated using the following relationship:

$$\begin{aligned} Q_{sf}^n &= \frac{A_L}{4nL_l} \oint -\mathbf{n} \cdot \mathbf{v}_I dl \\ &= \frac{A_L K_I}{4nL_l} \oint \mathbf{n} \cdot \boldsymbol{\nabla} p_I dl, \end{aligned} \tag{4.2.73}$$

which can be written in terms of dimensionless variables as

$$\begin{aligned} Q^n_{sf} &= \frac{A_L K_I (p_{PT} - p_0)}{4nL_l} \oint \mathbf{n} \cdot \boldsymbol{\nabla}^* p^*_I dl^* \\ &= \frac{A_L K_I (p_{PT} - p_0)}{4nL_l} \oint M^*_L p^*_I dl^*. \end{aligned} \tag{4.2.74}$$

The flux of the interstitial fluid leaving the liver via the bare area, Q^n_{ba}, can be calculated by using the similar terms; therefore,

$$Q^n_{ba} = \frac{A_L K_I (p_{PT} - p_0)}{4nL_l} \oint M^*_U p^*_I dl^*. \tag{4.2.75}$$

The values of Q^n_{sf} and Q^n_{ba} are found to be dependent of n as shown in figure 4.2.8a. The extrapolation shows that when the number of lobules is very high, both Q^n_{sf} and Q^n_{ba} reach the certain values. From the graph, the values of flux calculated from the '$n = 6$' model are very close to the maximum values of the '$n = 84$' model. This suggests that the model is a good representative of the whole liver. From now, we will use Q_{sf} and Q_{ba} to represent Q^n_{sf} and Q^n_{ba}, respectively, when $n \geq 6$.

We therefore can predict that when $n \to 84$, Q_{sf} is about 5.4 ml/hr or 130 ml/day, which is about 0.0017% of the total liver blood flow whilst Q_{ba} is about 3 ml/hr or 72 ml/day, which is about 0.0009% of the total blood flow. We also calculate the average

sinusoidal pressure in the model, $P_{av}^{p} \approx 2.91$ mmHg.

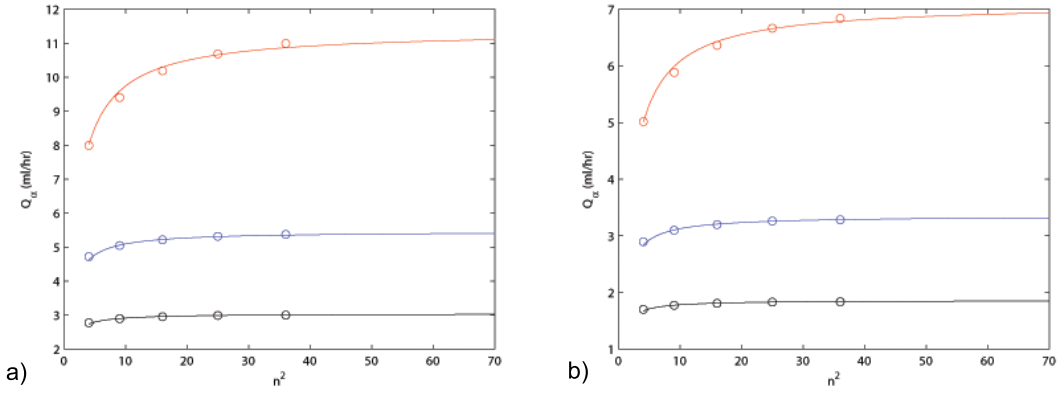

Figure 4.2.8: The relationship between the number of lobules, n^2, and Q_α which represents one of Q_{sf} (blue), Q_{ba} (black), or Q_{ld} (red) when a) the pressure boundary condition is applied, or b) the flux boundary condition is applied at the portal tracts.

The amount of the interstitial fluid leaving the liver via the lymphatic ducts, Q_{ld}^{n}, equals the average flux per unit volume, Q_L, integrated over the volume of the liver:

$$\begin{aligned} Q_{ld}^{n} &= \frac{V_L}{n^2 L_l^2} \int Q_L dA \\ &= \frac{V_L}{n^2 L_l^2 R_l} \int (p_I - p_0) dA, \end{aligned} \tag{4.2.76}$$

which can be written in terms of dimensionless variables as

$$Q_{ld}^{n} = \frac{V_L (p_{PT} - p_0)}{n^2 R_l} \int p_I^* dA^*. \tag{4.2.77}$$

From the COMSOL model, Q_{ld}^n is also depend on n and the extrapolation shows that when $n \to 84$, $Q_{ld}^n \approx 11.3$ ml/hr. From the graph in figure 4.2.8a, Q_{ld}^6 is very close to the limit when n is very large. This suggests that the 6×6 model can fairly represent the whole liver model. From now, we will use Q_{ld} to represent Q_{ld}^n when $n \geq 6$.

Since the interstitial fluid leaving the liver via the bare area and the interstitial fluid from the lymphatic ducts will accumulate in the thoracic duct; therefore, the amount of fluid draining into the thoracic duct from the liver is about 14.3 ml/hr or 343 ml/day. The value is about 0.0044% of the total blood flow.

There is a limitation of data of the lymphatic flow rate from the liver; however, there is an approximation that the amount of liver lymphatic flow is about 1/3 of the total lymph flow in the thoracic duct [86], which is about 49 ml/hr or 0.06% of the total blood flow in normal physiology [85]. Therefore, the lymphatic flow from the liver is approximately 0.02% of the total blood flow. The calculated value from our model is about 4.5 times lower than the physiological value.

However, when we prescribed the flux boundary condition at the portal tract that give the total flux into the liver of 1.4 l/min, the normal physiological value, and prescribe the pressure boundary condition at the centrilobular veins, the results give $Q_{sf} \approx 3.3$ ml/hr or 0.004% of the total blood flow, $Q_{ba} \approx 1.85$ ml/hr, and $Q_{ld} \approx 7$ ml/hr (see figure

4.2.8b). Therefore, the total lymph flow from the liver is about 8.85 ml/hr or 0.011% of the total blood flow. The number is about half of the physiological value, showing a better estimation than prescribing pressure boundary condition. We also calculate the average sinusoidal pressure from the model, $P_{av}^{f} = 1.86\ mmHg$.

From the work of Negrini et al [61], who measured the amount of fluid leakage from the rabbit livers after the perfusion of whole plasma, the average volume of interstitial fluid leakage via the Glisson's capsule, Q_{exp}, is about 1.86 ml/hr/mmHg. If we multiply the number by the average sinusoidal pressure calculated from our model when the pressure boundary condition is applied (P_{av}^{p}), we obtain $Q_{exp} \approx 5.4$ ml/hr. Moreover, if we multiply Q_{exp} by the average sinusoidal pressure calculated from our model when the flux boundary condition is applied (P_{av}^{f}), we obtain $Q_{exp} \approx 3.46$ ml/hr. Both results show good estimations of the amount of ascitic fluid when compared to the Q_{sf}'s calculated previously.

4.3 Effect of parameters on the development of ascites

In some pathological livers, the amount of interstitial fluid increases dramatically due to either higher production rate or drainage blockage. The excessive fluid leaked from the liver into the abdomen leads to ascites. It is one of the common conditions secondary to liver disease. The condition causes abdominal discomfort to patients due to the collection of fluid in the abdominal cavity. In this section, we aim to find the relationships between related parameters and the amount of the interstitial fluid leakage via the lower surface of the liver, Q_{sf}. The cuboid liver model is used for analyses with the applied pressure boundary conditions from (4.2.66) - (4.2.70).

4.3.1 Hepatic filtration coefficient, sinusoidal, and interstitial hydraulic conductivity

In some physiological and pathological conditions such as liver cirrhosis, the permeability of the sinusoidal and interstitial spaces can change; also the permeability of the fenestrations in the endothelial cells of the sinusoids, F, can change. We therefore investigate the dependence of the amount of the interstitial fluid production on these parameters.

We aim find which parameter has the most influence on the amount of interstitial fluid leakage via the lower surface of the liver. We vary the parameters by scaling from 0.1 to 5 times the normal values. Figure 4.3.1 shows that the hydraulic conductivities of the sinusoids (K_S) and the interstitial space (K_I) are the most influential factors among

the three parameters. When either of both parameters decreases, the amount of interstitial fluid draining into the peritoneal cavity increases dramatically. This means that the amount of ascitic fluid production depends on the physiological alteration in the sinusoids and the interstitial space more than that in the fenestrated endothelium.

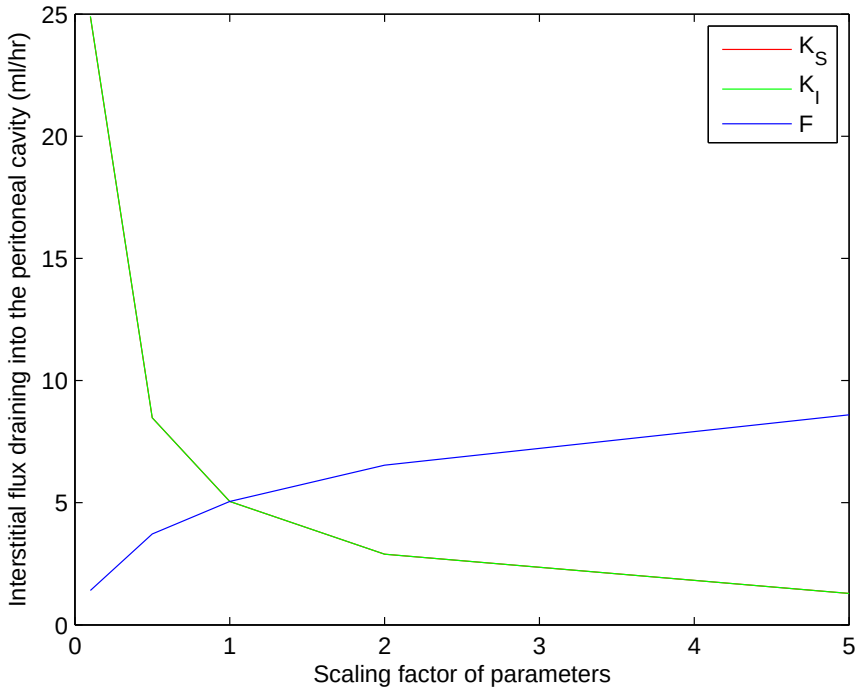

Figure 4.3.1: Sensitivity analysis of K_S, K_I, and F. Red (very close to the green line), green, and blue lines represent the value of interstitial flux flowing across the liver surface by varying the value of K_S, K_I, and F, respectively.

4.3.2 Other parameters

Permeabilities of the Glisson's capsule

We vary value of the permeabilities of the Glisson's capsule, M_L and M_U, using the scaling factor from 0.1 to 5 times the normal values to find the total amount of the ascitic fluid. Figure 4.3.2 shows that when the permeabilities of the Glisson's capsule increase, the interstitial fluid leaks more to the abdominal cavity. However, when the permeabilities are very high, the rate of the fluid leakage is dropped. This maybe from the limitation of the interstitial fluid production as the amount of the interstitial fluid leakage reaches the total amount of the interstitial fluid production.

Resistance of the lymphatic duct

We vary value of the resistance of the lymphatic duct, R_l, using the scaling factor from 0.1 to 5 times the normal value. The result (figure 4.3.3) shows that when the resistance of the lymphatic duct increases, the amount of the interstitial fluid leakage increases but tends to reach the plateau phase. This could imply that when the resistance of the lymphatic duct is very high, the interstitial fluid cannot leave the liver via the lymphatic duct anymore. Most of the interstitial fluid is then leave the liver via its surface to the abdominal cavity. The value of changed total flux leaving the liver surface is less than 10%, meaning that changing of the lymphatic duct resistance does not have a dramatic effect on the ascitic fluid development.

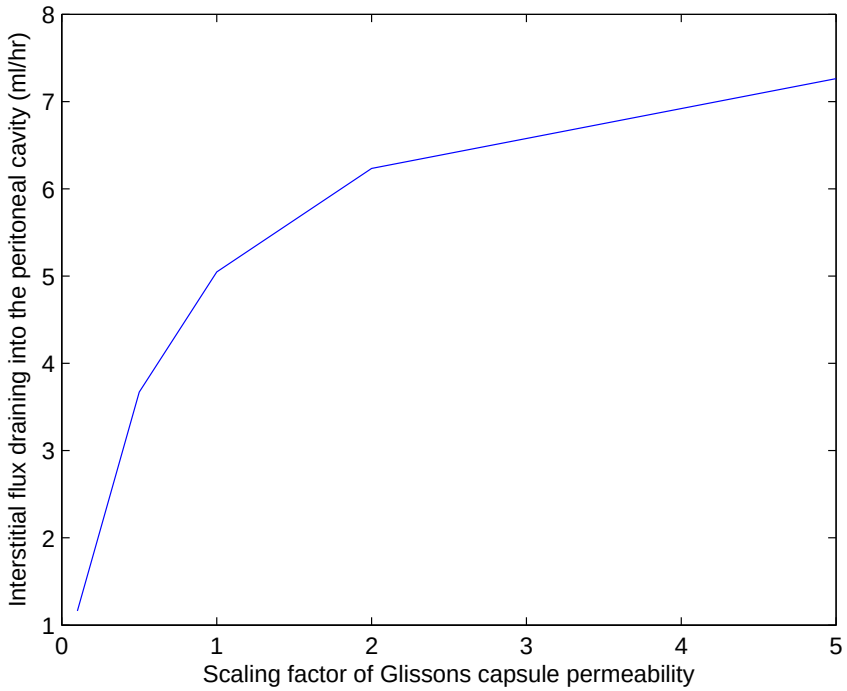

Figure 4.3.2: The interstitial fluid flux leaving the liver into the peritoneal cavity vs permeability of the Glisson's capsule.

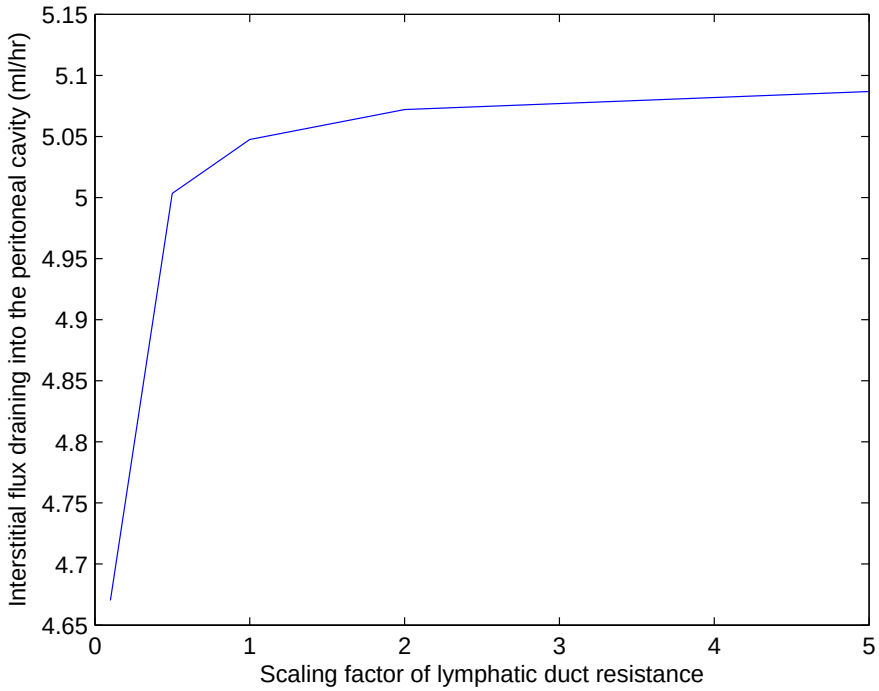

Figure 4.3.3: The interstitial fluid flux leaving the liver into the peritoneal cavity vs resistance of the lymphatic duct.

Lymphatic duct pressure

We vary value of dimensionless lymphatic duct pressure, p_0, from zero to 0.4 times the normal value. Figure 4.3.4 shows the linear relationship between the lymphatic duct pressure and the amount of the interstitial leakage via the liver surface. High lymphatic duct presssure means it is harder for the interstitial fluid to leave the liver via the pathway. As a result, the interstitial fluid instead tends to flow out of the liver via the liver surface. However, changing value of p_0 does not change the total flux leaving the liver surface dramatically, similar to the resistance of the lymphatic duct.

Portal tract pressure

We vary value of the portal tract pressures using the scaling factor from 0.4 to 5. The result shows that the relationship between the portal tract pressure and the amount of the interstitial leakage via the liver surface is linear, as expected, given that the model is linear. The range of the amount of fluid produced is also high, suggesting that the portal pressure is an important factor on the production of ascitic fluid.

4.3.3 Effect of the liver size on the interstitial fluid leakage

In some clinical conditions such as liver cancer, surgeon needs to resect the pathological regions. One of the common postoperative complications is high ascitic fluid production from changing of haemodynamics during and after surgery. The operation decreases

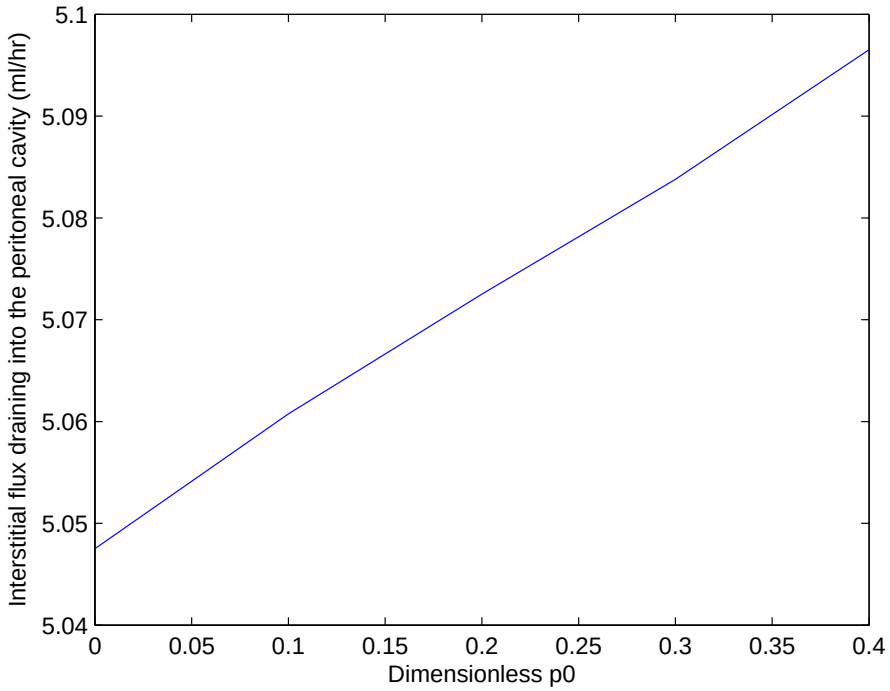

Figure 4.3.4: The interstitial fluid flux leaving the liver into the peritoneal cavity vs lymphatic duct pressure.

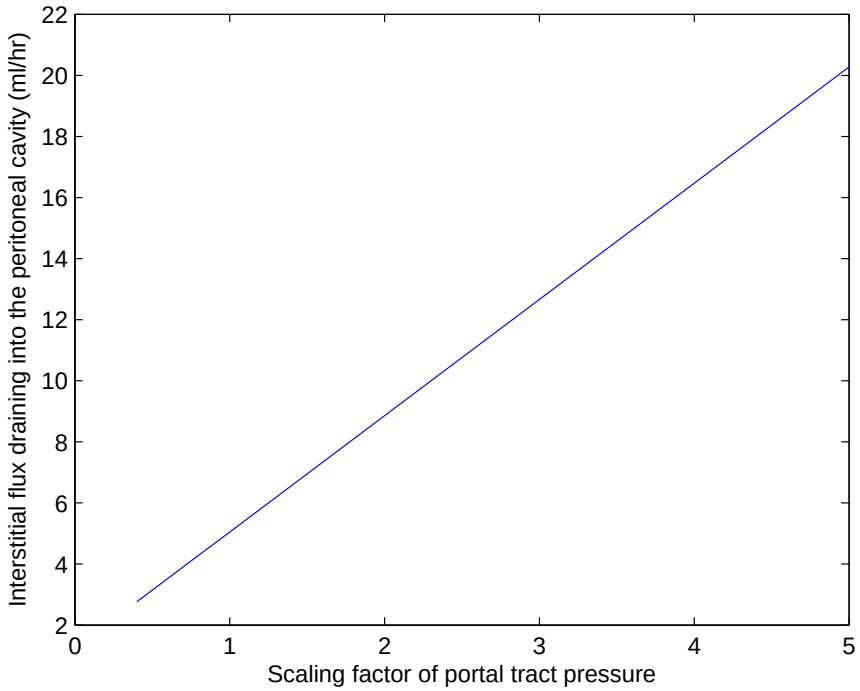

Figure 4.3.5: The interstitial fluid flux leaving the liver into the peritoneal cavity vs portal tract pressure.

liver volume whilst the liver itself still receives the same amount of blood supply; hence, the procedure also affects the flow of blood and interstitial fluid. Therefore, in this part, we aim to find the relationship between liver size and the amount of the leakage of the interstitial fluid via the surface of the liver, Q_{sf}, per unit volume of liver. We simulate the resected liver using our cuboid model as the geometry is simple to investigate. Two simple methods of resection are considered as we hope they provide estimates of the effect on flux. The first one is to preserve the number of lobules but shorten the length of third dimension (as shown in figure 4.3.6a). The second one, in figure 4.3.6b, is to reduce the number of the lobules but preserve the length of the third dimension. The 6×6 lobules model is used as an unresected liver. Furthermore, the total amount of input flux is conserved in each case. In the unresected liver, we use the flux boundary condition that satisfies the pressure boundary condition in (4.2.66).

In figure 4.3.7, the red line represents the first method of resection that the number of lobules is preserved but the length is varied. The blue line represents the second method of resection that the length of the lobule is preserved but the number of lobules is varied. The result shows the nonlinear relationship between Q_{sf} per unit volume of liver and the volume percentage in both cases. This means that liver resection increases the proportion of ascitic fluid production to the liver volume. It also shows that the flux of ascitic fluid in the second method is more sensitive to the volumetric change than the first method. This is because the ratio of surface area to liver volume is affected more in the second method than the first one. As a result, the surface area to volume ratio from

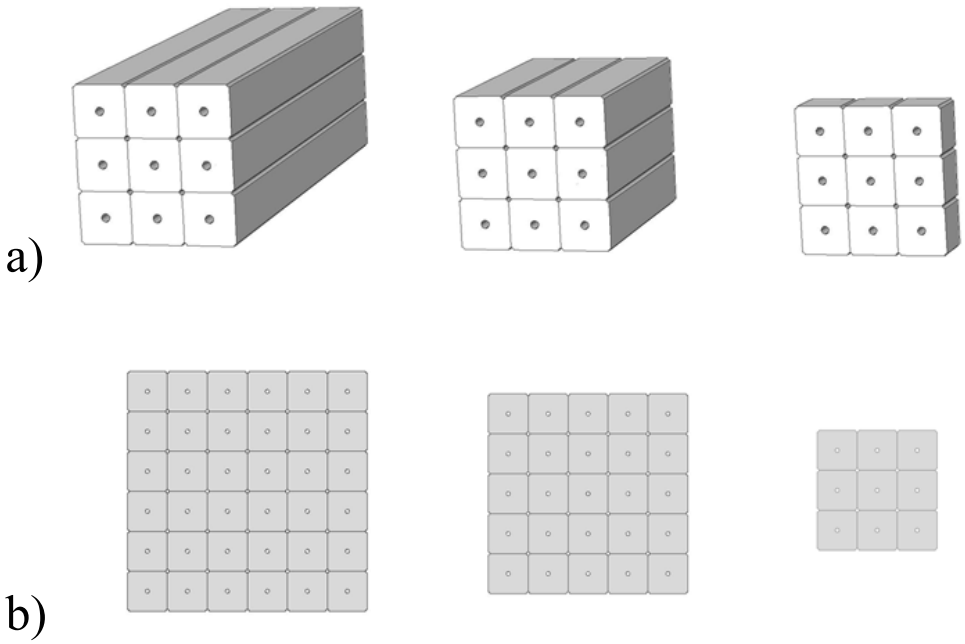

Figure 4.3.6: Two Methods of resection: a) shorten the length b) reduce the number of lobules.

the second method of resection is always higher than the first method, producing more flow of the interstitial fluid leakage. This could be applied to the surgical techniques in the liver resection. The less liver surface area to volume ratio left after resection, the less ascitic fluid is produced.

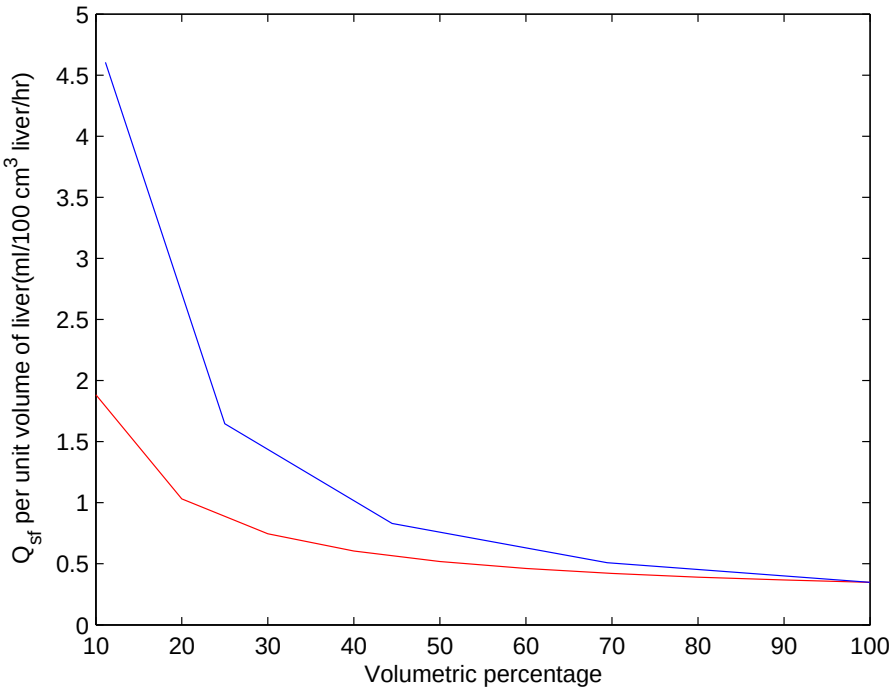

Figure 4.3.7: The interstitial fluid flux leaving the lower surface (Q_{sf}) per unit volume of liver vs remaining liver volume after resection. The red line represents the method that the number of lobules is preserved but the length is varied. The blue line represents the method that the length of the lobule is preserved but the number of lobules is varied.

4.4 Summary and discussion

In this chapter, we investigated the mechanics of interstitial fluid flow, which is an important pathway of the haemodynamics in the liver. Firstly, we developed the interstitial fluid model in a single lobule using the principle of flow in a porous medium, similar to the sinusoidal flow developed by Bonfiglio et al [11]. The sinusoids and the interstitial space are connected together and the conservation of mass law is applied. The model is calculated using both numerical and analytical methods and the results show that both approaches agree with each other. We later extended the investigation to the whole liver scale, considering all pathways of the fluid, which include the drainage via lymphatic duct, drainage via the bare area, and the leakage via the Glissons' capsule into the peritoneal cavity. Either of pressure or flux boundary condition is prescribed at the portal tracts and the numerical result shows there is no difference of the sinusoidal flow pattern among the regions of the liver. In contrast, there is a gradient of the interstitial flow, dropping down from middle part of the liver to the edges. This suggests that the fluid leakage via the liver surface comes mainly from the lobules located near the liver surface. Furthermore, the calculations show that our model gives a good estimation of the amount of interstitial fluid via both lymphatic duct and the Glisson's capsule compared to the values from the literature. The calculation also shows that the production of interstitial fluid in all pathways is small under normal physiological condition ($< 1\%$ of total blood flow).

Moreover, since the ascites is an important feature that related to pathological livers,

several parameters were investigated in order to find which ones have a significant effect on the ascitic fluid development. The results show that the permeabilities of sinusoids (related to K_S) and the interstitial space (related to K_I) are more important than the permeability of the fenestrations (F). When either of K_S or K_I decreases, the amount of ascites increases dramatically. This suggests that reduction of either parameters may cause a high amount of ascitic fluid production. The result agrees with the experimental findings that the sinusoidal diameter decreases in some pathological conditions, in which ascites usually occurs, such as cirrhosis. [83] [84].

Additionally, the rate of the ascites production is high when the permeabilities of the Glissons' capsule is low but it is lower when the permeabilities is very high. This phenomenon also happens to the lymphatic duct resistance, showing nonlinear relationship between the parameter and the rate of ascites production. However, the effect of the lymphatic duct resistance is less than the effect of the permeability of Glissons' capsule, suggesting that the later parameter is more significant. Meanwhile, the relationship between either portal tract pressure or lymphatic duct pressure and the interstitial fluid leakage is linear; however, the former parameter shows that it has more impact on the ascites production.

The effect of size of the liver is also investigated. Two methods of resection are considered: shorten the length or reduce the number of lobules. The later method shows more significant impact on the interstitial fluid leakage since its surface area to volume

ratio is affected more than the former. Therefore, the surgical techniques that leaves less surface area to volume ratio of the liver could reduces an amount of ascites.

Nonetheless, some properties such as the value of Glissons' capsule permeability on the upper surface (the bare area), the cuboid liver model, and the resection method are heavily based on assumptions that may not follow the in-vivo physiology. However, the results give us an insight of the importance of interstitial fluid flow on the haemodynamics in the liver, especially when some parameters are changed from their normal physiological values, which occurs in several clinical conditions. In conclusion, the permeability of the sinusoids, the permeability of the interstitial space, and the portal pressure are the most important factors on the production of ascitic fluid.

Chapter 5

Oxygen transportation model

Cellular metabolism depends on an adequate supply of oxygen from the blood. Therefore, an effective oxygen distribution is important for cell survival. In the liver lobule, oxygen is distributed from the blood into the interstitial space via the fenestrated endothelial cells and is then consumed by hepatocytes. In this chapter, we investigate the oxygen distribution in the sinusoids and interstitial space using the advection–diffusion equation and Michaelis–Menten kinetics for the cellular uptake. We then investigate the effect of related parameters on the oxygen distribution in order to find the importance of each parameter on the oxygen supply to the cells. The relevant parameters used in the model are listed in table 5.1.

5.1 Derivation of model equations

As before, we consider a single lobule with hexagonal geometry and treat it as a porous medium. We also assume that both blood and interstitial fluid are Newtonian fluids,

Table 5.1: Physiological parameter values used in the oxygen transportation model

Symbol	Description	Typical Value	Reference
C_0	Inlet oxygen concentration	0.21 mol/m^3	[62] see appendix D
$p_{SPT} - p_{SCV}$	The difference of portal tract and centrilobular venous pressure	2.95 mmHg	[11]
D_S	Diffusion coefficient of oxygen in blood	2×10^{-9} m^2/s	[63]
D_I	Diffusion coefficient of oxygen in interstitial fluid	$1.12D_S$	see equation 5.1.5
G_W	Filtration coefficient of oxygen through the endothelial wall via diffusion process	2200 s^{-1}	[64] see appendix D
F_W	Filtration coefficient of oxygen through the endothelial wall via advection process	5.3×10^{-5} m^3/s/kg/mmHg	see appendix D
Q_m	Maximum oxygen uptake rate by hepatocytes	7.9×10^{-3} mol/m^3/s	[65] see appendix D
K_m	Michaelis-Menten constant	5.9×10^{-3} mol/m^3	[65] see appendix D

and neglect the presence of red and white blood cells. We use Darcy's equation for flows in the sinusoidal and interstitial spaces. Considering the flow via the fenestrations and the lymphatic uptake using the mass conservation principle, we obtain equation (4.2.9) and (4.2.10):

$$-K_S \nabla^2 p_S + \rho F(p_S - p_I) = 0, \tag{5.1.1}$$

$$-K_I \nabla^2 p_I - \rho F(p_S - p_I) + \frac{p_I - p_0}{R_l} = 0. \tag{5.1.2}$$

For the distribution of oxygen in the lobule, we define C_S and C_I as the oxygen concentrations in the sinusoidal and interstitial spaces, respectively, and the advection–diffusion

equations of the oxygen in both spaces are

$$\frac{\partial C_S}{\partial t} = -\mathbf{v_S} \cdot \boldsymbol{\nabla} C_S + D_S \nabla^2 C_S, \tag{5.1.3}$$

$$\frac{\partial C_I}{\partial t} = -\mathbf{v_I} \cdot \boldsymbol{\nabla} C_I + D_I \nabla^2 C_I - \phi, \tag{5.1.4}$$

where D_S and D_I are the diffusion coefficients of oxygen in the sinusoids and the interstitial space, respectively, and ϕ is the oxygen uptake rate by hepatocytes. Note that the diffusion coefficient is a function of the dynamic viscosity, μ, such that

$$\frac{D_S}{D_I} = \frac{\mu_I}{\mu_S}. \tag{5.1.5}$$

The oxygen is transported between two spaces via the fenestrations by diffusion and advection processes. Thus, the rate of transport is

$$\frac{\partial C}{\partial t} = G_W(C_S - C_I) + F_W(p_S - p_I)(C_S - C_I), \tag{5.1.6}$$

where G_W is the filtration coefficient of oxygen through the sinusoidal endothelial wall via diffusion process and F_W is the filtration coefficient of oxygen through the sinusoidal endothelial wall via advection process. The first term on the right-hand side of equation 5.1.6 represents the diffusion process, whilst the second term represents the advection

process.

We couple this with the advection–diffusion equation in both spaces; thus,

$$\frac{\partial C_S}{\partial t} = -\mathbf{v_S} \cdot \boldsymbol{\nabla} C_S + D_S \nabla^2 C_S - G_W(C_S - C_I) - F_W(p_S - p_I)(C_S - C_I), \quad (5.1.7)$$

$$\frac{\partial C_I}{\partial t} = -\mathbf{v_I} \cdot \boldsymbol{\nabla} C_I + D_I \nabla^2 C_I + G_W(C_S - C_I) + F_W(p_S - p_I)(C_S - C_I) - \phi. \quad (5.1.8)$$

We seek a steady solution and set

$$\frac{\partial C_S}{\partial t} = \frac{\partial C_I}{\partial t} = 0. \quad (5.1.9)$$

Equation (5.1.7) and (5.1.8) then becomes

$$-K_S \boldsymbol{\nabla} p_S \cdot \boldsymbol{\nabla} C_S - D_S \nabla^2 C_S + G_W(C_S - C_I) + F_W(p_S - p_I)(C_S - C_I) = 0, \quad (5.1.10)$$

$$-K_I \boldsymbol{\nabla} p_I \cdot \boldsymbol{\nabla} C_I - D_I \nabla^2 C_I - G_W(C_S - C_I) - F_W(p_S - p_I)(C_S - C_I) + \phi = 0. \quad (5.1.11)$$

We use Michaelis-Menten kinetics for the oxygen uptake rate (ϕ),

$$\phi = -\frac{Q_m C_I}{C_I + K_m}, \quad (5.1.12)$$

where Q_m is the maximum oxygen uptake rate, C_I is the oxygen concentration in the interstitial space, and $K_m = \frac{k_{-1}+k_2}{k_1}$, a reaction constant. The derivation of ϕ can be seen in appendix E.

5.2 Derivation of boundary conditions

We assume there is no flow across the edges of the lobule in both the sinusoidal and the interstitial spaces. We prescribe the sinusoidal pressures at both the portal tracts and the centrilobular vein. We also assume there is no interstitial flow across the edges of all the vessels. For the oxygen distribution in the sinusoidal space, we assume that each portal tract provides a constant concentration of oxygen, C_0, and there is no change of oxygen concentration at the centrilobular vein. In the interstitial space, there are no changes of oxygen flux at both portal tracts and centrilobular vein. Diagrams showing the boundary conditions in both spaces are shown in figure 5.2.1 and 5.2.2.

The boundary conditions are:

- At the edges of the lobule

$$-K_S \mathbf{n} \cdot \boldsymbol{\nabla} p_S = 0, \tag{5.2.1}$$

$$-K_I \mathbf{n} \cdot \boldsymbol{\nabla} p_I = 0, \tag{5.2.2}$$

$$\mathbf{n} \cdot \boldsymbol{\nabla} C_S = 0, \tag{5.2.3}$$

$$\mathbf{n} \cdot \boldsymbol{\nabla} C_I = 0. \tag{5.2.4}$$

- At the portal tracts

$$p_S = P_{SPT}, \tag{5.2.5}$$

$$-K_I \mathbf{n} \cdot \boldsymbol{\nabla} p_I = 0, \tag{5.2.6}$$

$$C_S = C_0, \tag{5.2.7}$$

$$\mathbf{n} \cdot \boldsymbol{\nabla} C_I = 0. \tag{5.2.8}$$

- At centrilobular vein

$$p_S = P_{SCV}, \tag{5.2.9}$$

$$-K_I \mathbf{n} \cdot \boldsymbol{\nabla} p_I = 0, \tag{5.2.10}$$

$$\mathbf{n} \cdot \boldsymbol{\nabla} C_S = 0, \tag{5.2.11}$$

$$\mathbf{n} \cdot \boldsymbol{\nabla} C_I = 0. \tag{5.2.12}$$

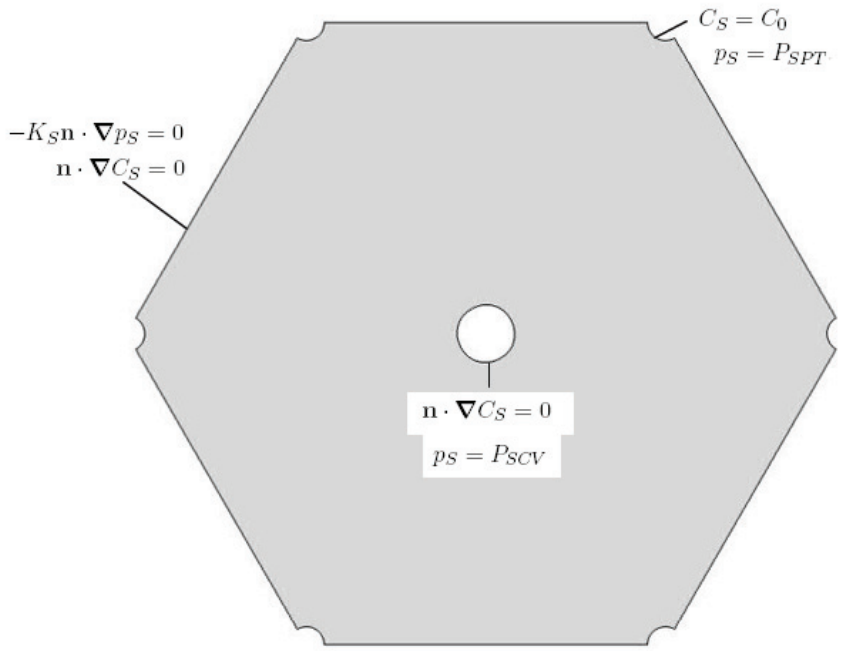

Figure 5.2.1: Diagram of boundary conditions of the sinusoids.

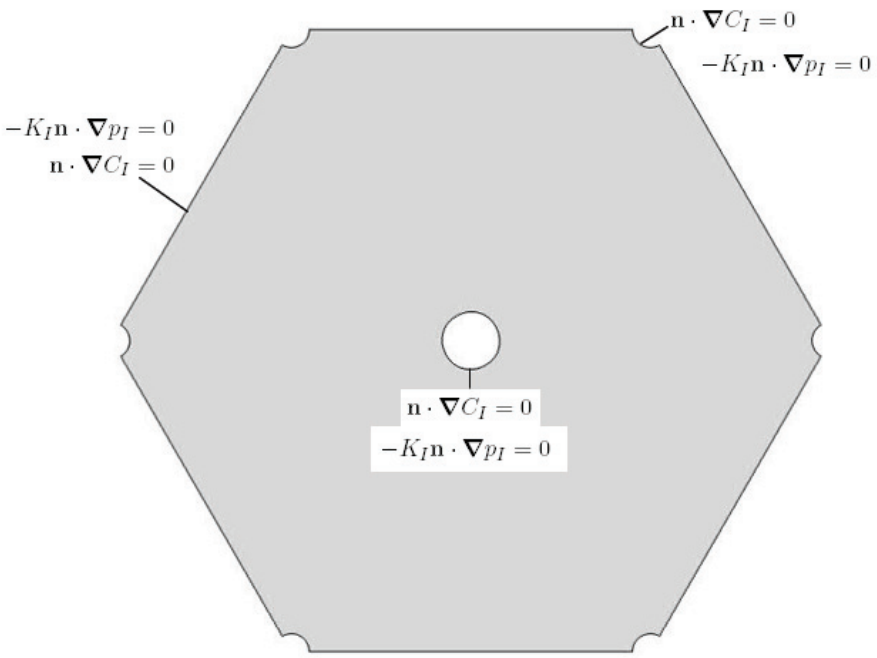

Figure 5.2.2: Diagram of boundary conditions of the interstitial space.

5.3 Nondimensionalisation

5.3.1 Nondimensionalisation of parameters and variables

We nondimensionalised the parameters and variables as follows:

$$\mathbf{x} = L\boldsymbol{x}^{*}, \tag{5.3.1}$$

$$p_S = P_{SCV} + (P_{SPT} - P_{SCV})p_S^*, \tag{5.3.2}$$

$$p_I = P_{SCV} + (P_{SPT} - P_{SCV})p_I^*, \tag{5.3.3}$$

$$C = C_0 C^*, \tag{5.3.4}$$

where C is either C_S or C_I, P_{SPT} is the pressure at the portal tracts, and P_{SCV} is the pressure at the centrilobular vein.

Equations (5.1.1) and (5.1.2) then becomes

$$\nabla^{*2} p_S^* - F_S^*(p_S^* - p_I^*) = 0, \tag{5.3.5}$$

$$\nabla^{*2} p_I^* + F_I^*(p_S^* - p_I^*) - \frac{p_I^*}{R_l^*} = 0, \tag{5.3.6}$$

where $F_S^* = \frac{L^2\rho F}{K_S}$, $F_I^* = \frac{L^2\rho F}{K_I}$, $F_I^* = \frac{F_S^*}{K_R}$, , $K_R = \frac{K_I}{K_S}$, and $R_l^* = \frac{K_I}{L^2}R_l$.

Equations (5.1.10) and (5.1.11) also becomes

$$-\boldsymbol{\nabla^*} p_S^* \cdot \boldsymbol{\nabla^*} C_S^* - D_{SS}\nabla^{*2} C_S^* + G_{WS}(C_S^* - C_I^*) + F_S(p_S^* - p_I^*)(C_S^* - C_I^*) = 0, \quad (5.3.7)$$

$$-\boldsymbol{\nabla^*} p_I^* \cdot \boldsymbol{\nabla^*} C_I^* - D_{II}\nabla^{*2} C_I^* - G_{WI}(C_S^* - C_I^*) - F_I(p_S^* - p_I^*)(C_S^* - C_I^*) + \phi^* = 0, \quad (5.3.8)$$

where $D_{SS} = \frac{D_S}{K_S(P_{SPT}-P_{SCV})}$, $D_{II} = \frac{D_I}{K_I(P_{SPT}-P_{SCV})}$, $G_{WS} = \frac{G_W L^2}{K_S(P_{SPT}-P_{SCV})}$,

$G_{WI} = \frac{G_W L^2}{K_I(P_{SPT}-P_{SCV})}$, $F_S = \frac{F_W L^2}{K_S}$, $F_I = \frac{F_W L^2}{K_I}$, and $\phi^* = \frac{\phi L^2}{C_0 K_I(P_{SPT}-P_{SCV})}$.

5.3.2 Nondimensionalisation of boundary conditions

- At the edges of the lobule

$$\mathbf{n} \cdot \boldsymbol{\nabla}^* p_S^* = 0, \quad (5.3.9)$$

$$\mathbf{n} \cdot \boldsymbol{\nabla}^* p_I^* = 0, \quad (5.3.10)$$

$$\mathbf{n} \cdot \boldsymbol{\nabla}^* C_S^* = 0, \tag{5.3.11}$$

$$\mathbf{n} \cdot \boldsymbol{\nabla}^* C_I^* = 0. \tag{5.3.12}$$

- At the portal tracts

$$p_S^* = 1, \tag{5.3.13}$$

$$\mathbf{n} \cdot \boldsymbol{\nabla}^* p_I^* = 0, \tag{5.3.14}$$

$$C_S^* = 1, \tag{5.3.15}$$

$$\mathbf{n} \cdot \boldsymbol{\nabla}^* C_I^* = 0. \tag{5.3.16}$$

- At the centrilobular vein

$$p_S^* = 0, \tag{5.3.17}$$

$$\mathbf{n} \cdot \boldsymbol{\nabla}^* p_I^* = 0, \tag{5.3.18}$$

$$\mathbf{n} \cdot \boldsymbol{\nabla}^* C_S^* = 0, \tag{5.3.19}$$

$$\mathbf{n} \cdot \boldsymbol{\nabla}^* C_I^* = 0. \tag{5.3.20}$$

5.4 Numerical results

We calculate the oxygen distribution numerically using finite element method. The nondimensionalised governing equations and boundary conditions are derived in weak formulations as inputs in COMSOL Multiphysics software version 4.2.

Figures 5.4.1 and 5.4.2 show the oxygen distributions in the sinusoidal and the interstitial spaces, respectively. The oxygen level is highest at the portal tracts and lowest at the centrilobular vein. The oxygen distributions in both sinusoids and interstitial space show the similar pattern. Moreover, the levels of oxygen in both spaces are close to each other, showing that the oxygen transport between the sinusoids and the interstitial space is very effective. The results also show that the concentration of oxygen in the interstitial space remaining at the centrilobular vein is about 2/3 or 67% of that delivered at the portal tract, meaning that the hepatocytes consume about 1/3 of the oxygen input.

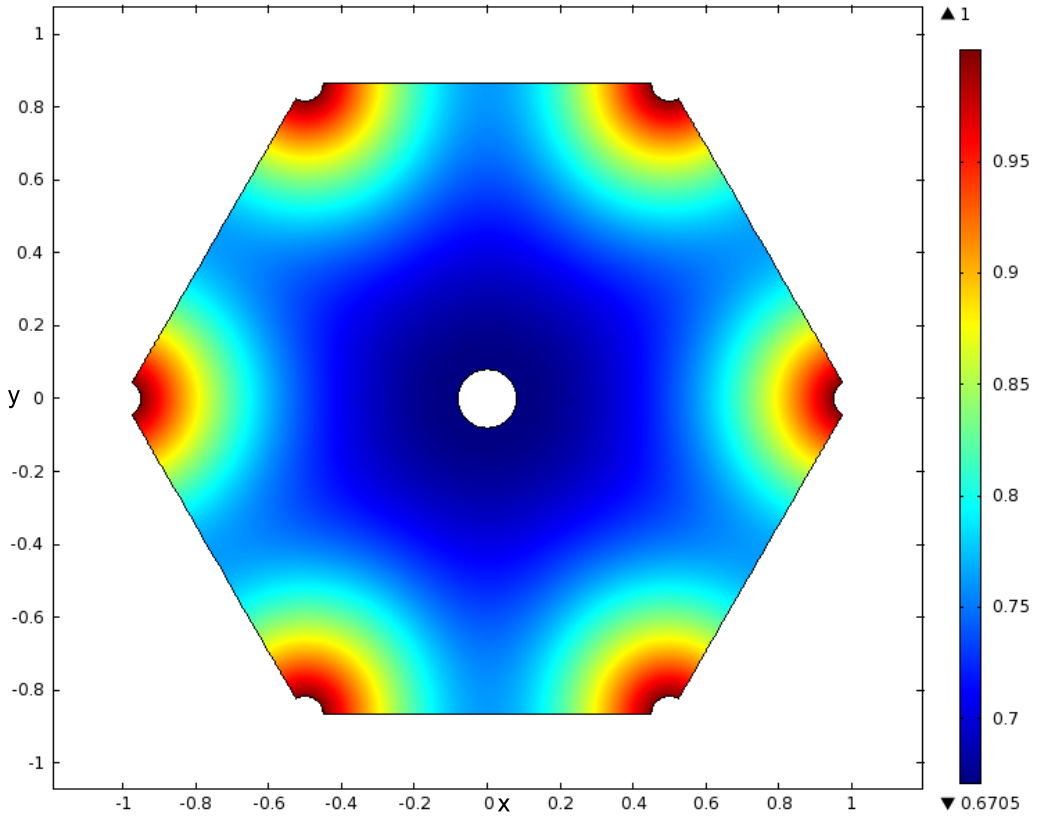

Figure 5.4.1: Dimensionless oxygen concentration in the sinusoidal space.

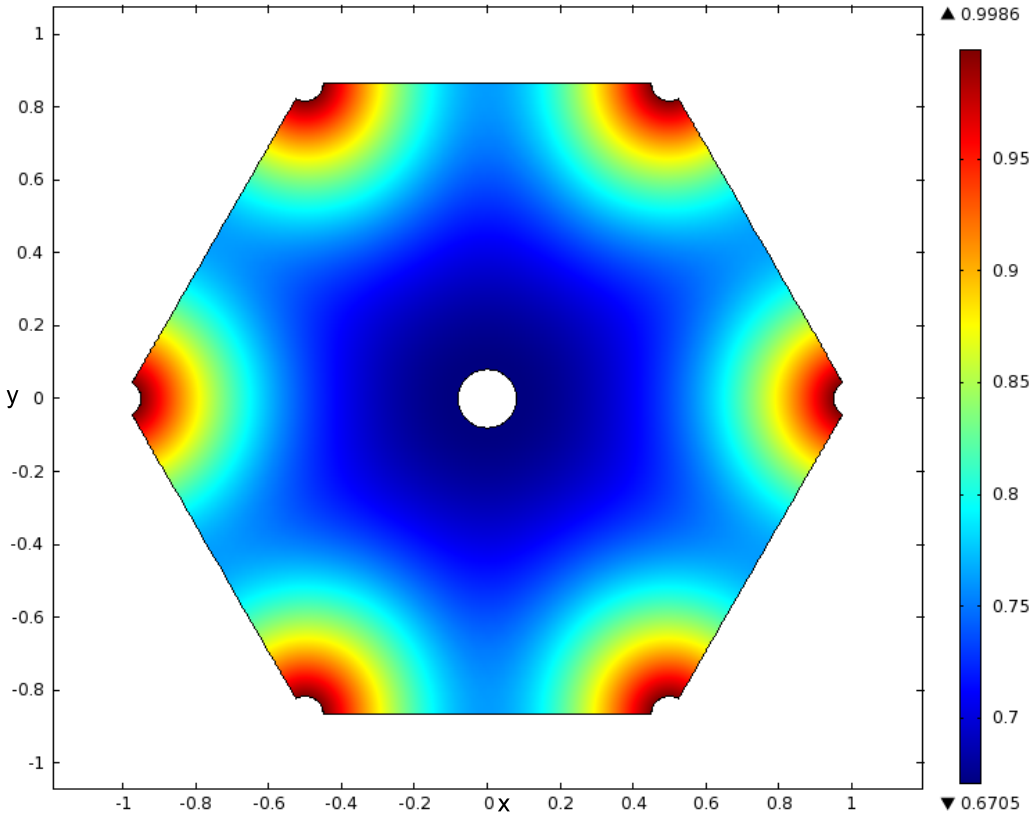

Figure 5.4.2: Dimensionless oxygen concentration in the interstitial space.

5.5 Effect of parameters on the oxygen distribution

In this section, we investigated the relationship between related parameters and the distribution of oxygen within the lobule. Several parameters are chosen and varied from lower to higher level of the normal values, which are listed in table 5.1.

5.5.1 Portal tract pressure

We vary the portal tract pressure from 0.1 to 5 times the normal value. The interstitial oxygen concentration profiles are plotted along the line from one of the portal tracts towards the centrilobular vein. Figure 5.5.1 shows that higher pressure can provide better oxygen supply to the whole area of the lobule, especially the area near the centrilobular vein. This is because high portal tract pressure drains more blood from the sinusoids into the interstitial space. As a result, the interstitial oxygen level increases from the starting point towards the end.

5.5.2 Oxygen concentration

The oxygen concentration at the portal tract is varied from 0.1 to 5 times the normal value. Figure 5.5.2 shows that higher oxygen input gives higher oxygen level towards the centrilobular vein. However, when the oxygen level is high enough, the patterns of oxygen distribution within the lobule seems to be similar. This is because, in each case,

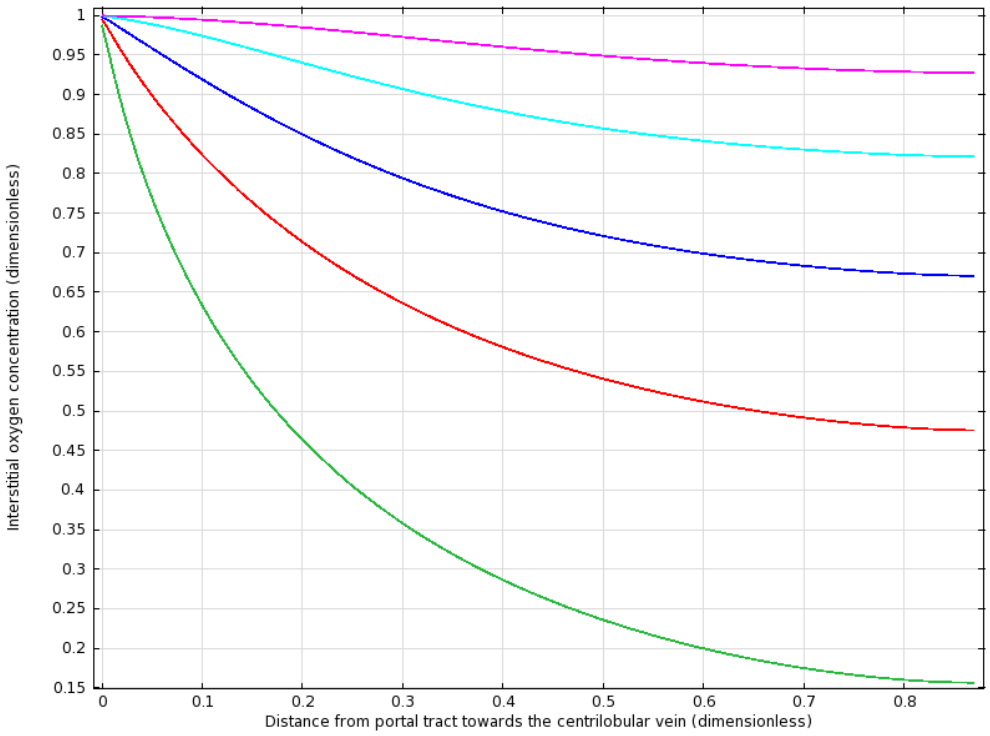

Figure 5.5.1: The dimensionless interstitial oxygen concentration along the line from one of the portal tracts towards the centrilobular vein vs portal tract pressure. The green, red, dark blue, light blue, and pink lines represent portal tract pressures of 0.1, 0.5, 1, 2, and 5 times the normal value, respectively.

the oxygen depletion rate (ϕ in equation 5.1.12) is unchanged due to the high level of C_I. It means that, in certain circumstances, the hepatocytes consume a limited amount of oxygen, and excessive oxygen supply is unnecessary.

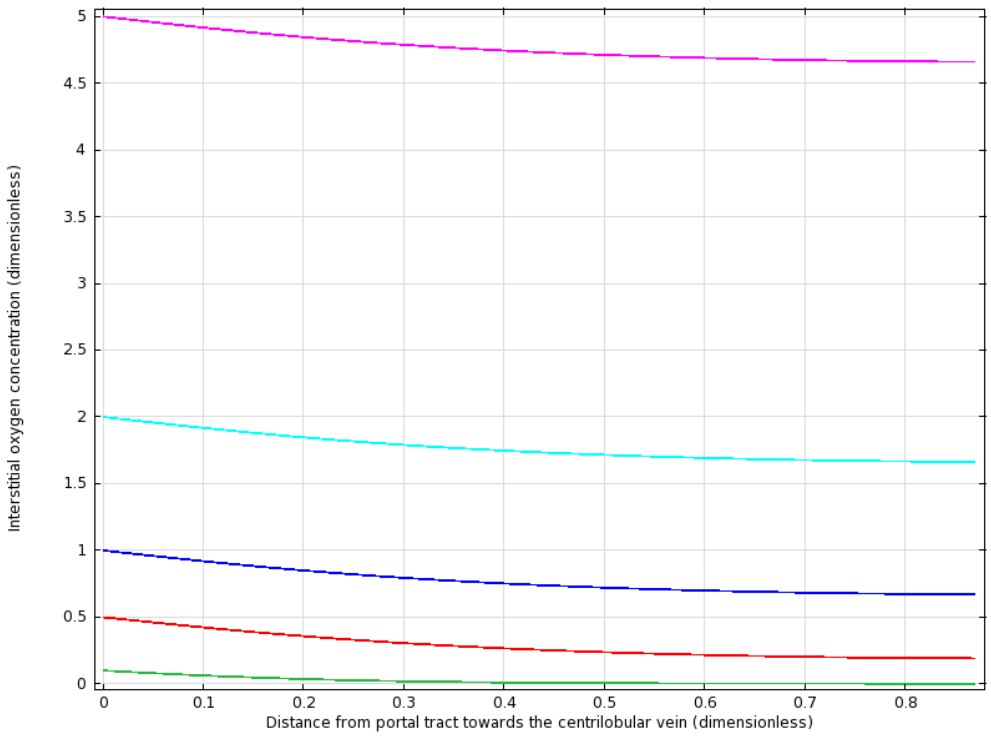

Figure 5.5.2: The dimensionless interstitial oxygen concentration along the line from one of the portal tracts towards the centrilobular vein vs oxygen concentration at the portal tracts. The green, red, dark blue, light blue, and pink lines represent oxygen concentration of 0.1, 0.5, 1, 2, and 5 times the normal value, respectively.

5.5.3 Oxygen uptake rate

The oxygen uptake rate of hepatocytes (ϕ - see equation 5.1.12) is varied from 0.1 to 5 times the normal value. Figure 5.5.3 shows the profiles of the oxygen concentration in the interstitial space along the line from a portal tract towards the centrilobular vein. Low oxygen uptake rate means there is enough oxygen left for the cells living near the centrilobular vein. On the other hand, hepatocytes living in the central area of the lobule with high oxygen uptake rate will lack oxygen since the cells in the proximal part consumes most of the oxygen before it reaches the distal pathway.

5.5.4 Oxygen filtration coefficients, diffusion coefficients, sinusoidal and interstitial permeabilities

The oxygen filtration coefficient via the advection process (F_W), the oxygen filtration coefficient via the diffusion process (G_W), the oxygen diffusion coefficient of the sinusoidal space (D_S), the oxygen diffusion coefficient of the interstitial space (D_I), the sinusoidal hydraulic conductivity (K_S), and the interstitial hydraulic conductivity (K_I) are varied from 0.1 to 5 times the normal values.

Figure 5.5.4a shows that the sinusoidal permeability (related to K_S) has a significant effect on the oxygen distribution within the lobule as the oxygen profile changes dramatically when K_S is varied . Low sinusoidal permeability means low oxygen level is delivered to the hepatocytes living near the pericentral area of the lobule. When we

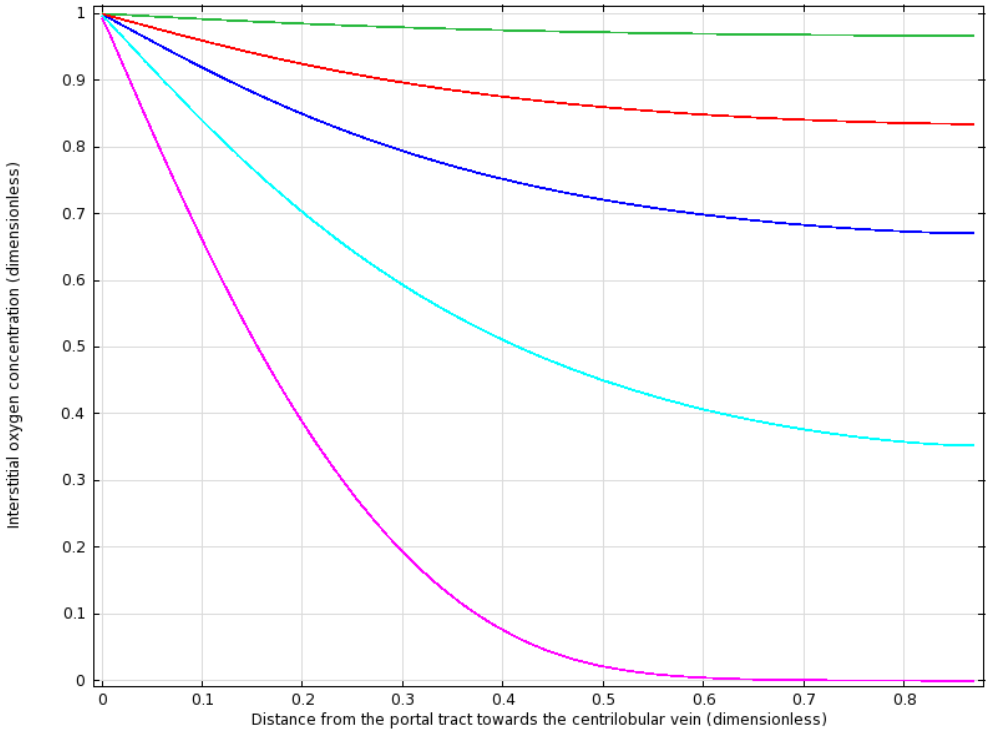

Figure 5.5.3: The dimensionless interstitial oxygen concentration along the line from one of the portal tracts towards the centrilobular vein vs oxygen uptake rate. The green, red, dark blue, light blue, and pink lines represent oxygen uptake rate of 0.1, 0.5, 1, 2, and 5 times of the normal value, respectively.

vary the value of oxygen diffusion coefficient of the sinusoidal space (D_S), as shown in figure 5.5.4b, the oxygen profiles also show that high D_S provides better oxygen level towards the pericentral region; however, the range of the oxygen level is narrower than changing K_S. In the graph, when the lower oxygen diffusion coefficients are applied to the model, the oxygen concentrations in the periportal region are high because that the advection process dominates the distribution; however, the mechanism cannot compensate the ineffective diffusion process; thus, the oxygen level finally drops near the pericentral region. This also explains the result in figure 5.5.5b.

In contrast, interestingly, figure 5.5.5a shows that the interstitial permeability (related to K_I) almost has no effect on the oxygen distribution as there is no difference of the oxygen level when value of the parameter is varied. However, when the value of oxygen diffusion coefficient of the interstitial space (D_I) is varied, the oxygen distribution changes as shown in figure 5.5.5b. Similar to the K_I, figure 5.5.6a shows that the oxygen filtration coefficient via the advection process (F_W) does not have a significant effect on the oxygen distribution as the oxygen level does not change when value of the parameter is varied. However, when we vary the value of the oxygen filtration coefficient via the diffusion process (G_W), figure 5.5.6b shows a slight difference in oxygen level.

These results imply that, among these six parameters, the sinusoidal permeability (related to K_S) is the most influential factor on the oxygen distribution. Moreover, since K_S determines the advection process of the oxygen in the sinusoids, we therefore can

conclude that the advection process is dominant to the diffusion process for the oxygen distribution from the portal tracts towards the centrilobular vein in the sinusoidal space. On the contrary, for the oxygen distribution within the interstitial space, the diffusion process plays a major role compared to the advection process as D_I has more impact on the oxygen transport than K_I. Similarly, G_W dominant to F_W on the oxygen distribution suggests that the majority of the oxygen flow across the endothelial wall due to diffusion rather than advection.

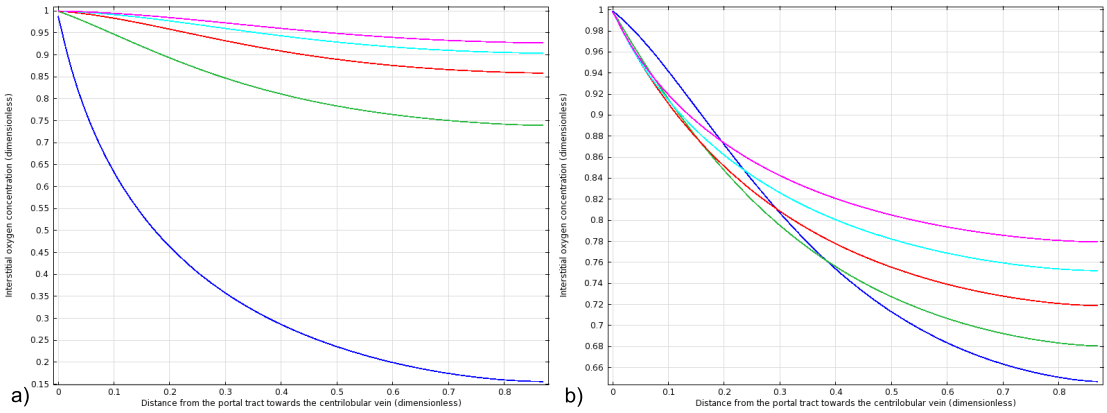

Figure 5.5.4: a) The dimensionless interstitial oxygen concentration profile for different values of sinusoidal hydraulic conductivity (K_S) along the line from one of the portal tracts towards the centrilobular vein. b) The dimensionless interstitial oxygen concentration profile for different values of sinusoidal oxygen diffusion coefficient (D_S) along the line from one of the portal tracts towards the centrilobular vein. The blue, green, red, light blue, and pink lines represent values of 0.1, 1.325, 2.55, 3.775, and 5 times the normal values, respectively.

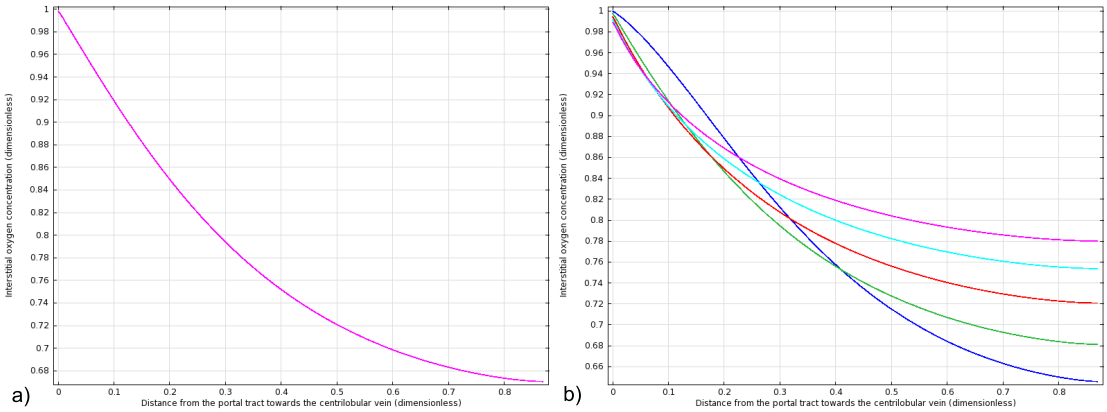

Figure 5.5.5: a) The dimensionless interstitial oxygen concentration profile for different values of interstitial hydraulic conductivity (K_I) along the line from one of the portal tracts towards the centrilobular vein. b) The dimensionless interstitial oxygen concentration profile for different values of interstitial oxygen diffusion coefficient (D_I) along the line from one of the portal tracts towards the centrilobular vein. The blue, green, red, light blue, and pink lines represent values of 0.1, 1.325, 2.55, 3.775, and 5 times the normal values, respectively. In figure a), different values of K_I produce lines almost lie on top of each other and does not make distinctive differences of the interstitial oxygen level.

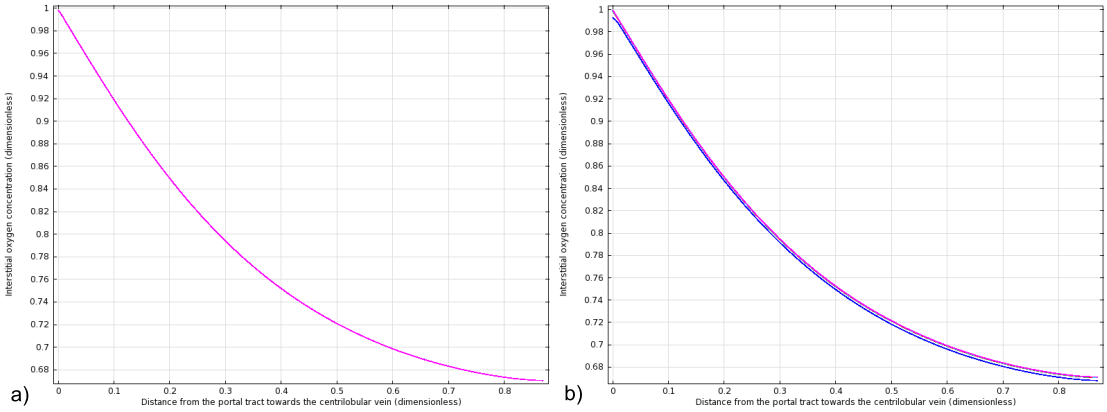

Figure 5.5.6: a) The dimensionless interstitial oxygen concentration profile with different values of hepatic filtration coefficient via advection process (F_W) along the line from one of the portal tracts towards the centrilobular vein. b) The dimensionless interstitial oxygen concentration profile with different values of hepatic filtration coefficient via diffusion process (G_W) along the line from one of the portal tracts towards the centrilobular vein. The blue, green, red, light blue, and pink lines represent values of 0.1, 1.325, 2.55, 3.775, and 5 times the normal values, respectively. In figure a), different values of K_I produce lines almost lie on top of each other and does not make distinctive differences of the interstitial oxygen level. In figure b), the green, red, light blue, and pink are also very close to each other.

5.6 Summary and discussion

In this chapter, we developed a model of oxygen transportation within the liver lobule using the advection–diffusion mechanism for the oxygen distribution and the Michaelis–Menten kinetics for the cellular uptake. The results show that the oxygen level remaining at the centrilobular vein is about 67% of the input at the portal tracts. This ratio is a good estimation compared to the result from the experiments of Matsumura et al [79][80], in which the oxygen concentrations in the periportal and pericentral areas of the rat livers perfused by Krebs-Henseleit bicarbonate buffer were measured. According to the data from two studies of Matsumura et al, the oxygen levels at the pericentral regions are estimated to be about 57% and 63% of those at the periportal regions.

The results from our model also show that the oxygen concentration in the sinusoids and in the interstitial space are close to each other. This agrees with the result from the cardiac model of Beard [81], in which the oxygen levels in capillary, interstitium, and cardiomyocyte compartments are compared. The cardiomyocytes, or cardiac muscles, is supplied by the continuous capillaries, which has less permeability to the molecules compared to the fenestrated capillaries such as the liver sinusoids. His prediction shows that the oxygen levels in the capillary and the interstitium are very close to each other, which means that the oxygen transport between the continuous capillary and the interstitial space is very effective. Since we anticipate that the oxygen transport via the fenestrated endothelial will be more effective, we might conclude that the proximity of the oxygen levels in the sinusoids and the interstitial space in our model is reasonable.

Moreover, we investigated the role of several parameters on the oxygen distribution within the lobule. High level of portal tract pressure and high oxygen concentration at the portal tracts can improve the oxygen supply to the hepatocytes. In contrast, high oxygen uptake rate, which can occur in some clinical conditions such as alcoholic liver disease can cause ischaemia to the hepatocytes living near the central part of the lobule [66], [67]. In this case, the liver itself may have a feedback mechanism to increase portal pressure to compensate the oxygen supply. However, the mechanism is beyond the scope of this project and not included in the model.

The sinusoidal permeability is also an important factor that affects the oxygen distribution to the hepatocytes. The results suggest that the effectiveness of the oxygen distribution depends mainly on sinusoidal flow rather than fluid filtration rate or interstitial flow. The result suggests that conditions that decrease the permeability of the sinusoids can also cause cell ischaemia. On the other hand, the permeabilities of the fenestrated endothelial wall and the interstitial space seem to have less effect on the oxygen distribution. However, these three spaces are connected together and any pathological condition could affect all three spaces at the same time [68], [69], [70]. Future work should involve developing a model of a pathological state.

The domination of K_S over D_S, D_I over K_I, and G_W over F_W on the oxygen distribution suggests that the main mechanism for the oxygen distribution across the lobule via

the sinusoids is advection rather than diffusion; however, the main mechanism for oxygen transportation across the fenestrated endothelial and within the interstitial space is diffusion.

However, in this study, we only consider the oxygen dissolved in plasma and did not account for the presence of the red blood cells (RBCs), which contain haemoglobins, the proteins that have high affinity to oxygen. Haemoglobins can carry and release oxygen into blood plasma via the process described in the first chapter. A model of haemoglobin carrying–releasing oxygen should also be incorporated in future models to provide more precise results.

Chapter 6

Optimal vascular arrangement on blood perfusion of the liver lobule

The classical hexagonal model of Kiernan is widely used to represent the liver lobule in physiological modelling. However, histological images of the liver tissue (see example in figure 1.1.4) show that the lobules vary considerably in shape and size. Blood flow and oxygen should be distributed as evenly as possible, both within the lobule and between different lobules, so that the hepatocytes receive a more equal distribution of oxygen and nutrients.

Therefore, in this study, we compare the efficiency of different geometries of the lobule by comparing the flux and pressure drop across the lobule, and also the homogeneity of the blood distribution. Moreover, we investigate the effect of the vascular septa and the geometry of the lobule on the oxygen distribution. Several geometries are considered

and the results are compared with our basic hexagonal lobule in order to find whether the classical lobule is the optimum model. However, due to time limitations, we consider only sinusoidal flow and neglect the flow in interstitial space in the first section.

6.1 The effect of non-uniformly distributed vessels on blood perfusion in the lobule

In this section we investigate the effect of non-uniformly distributed portal tracts and centrilobular vein on blood velocity and its variance within the lobule as we aim to find whether the positions of the vessels have an effect on the homogeneity of the blood perfusion. The hexagonal lobules with variation of the positions of the portal tracts and centrilobular vein are studied. The models are calculated numerically using the Darcy's equations for the sinusoidal flow in a single lobule and the results are compared to the basic model in which all the vessels are distributed uniformly.

6.1.1 Distribution of the vessels

In order to create irregular hexagonal geometries, we assume that the positions of the portal tracts are distributed randomly around their original positions in a regular hexagon, in a normal distribution with a prescribed standard deviation. Moreover, the displacement of each portal tract is independent of the other. The position of the centrilobular vein is distributed randomly in a normal distribution from the centroid of the new hexagon created with the same standard deviation.

We use the bivariate normal distribution (figure 6.1.1) to determine the positions of each portal tract and centrilobular vein. The standard deviations of the x-component and of the y-component are equal ($\sigma_x = \sigma_y = \sigma$) and the distributions are independent of each other. The diameter of the vessels remains the same as in the original model. Similar to the previous chapters, we nondimensionalise lengths with respect to the lobular side length ($L = 500 \times 10^{-6}$ m., see table 6.1).

For each value of σ ($\sigma = 0.05, 0.10, 0.15, ...$), we generate 10 hexagons at random from the distribution. If a hexagon satisfies one or more of the following criteria then we reject it and generate a replacement. The criteria are:

- A hexagon that has one or more angles of more than 180 degrees (i.e. the hexagon is not convex).
- A hexagon that has one edge across the other.
- A hexagon that has the centrilobular vein located outside the area of the hexagon.

We found that the proportion of hexagons rejected is low (< 10 percent of total) when σ is 0.25 or less, while the number increases significantly (> 40 percent of total) when σ is 0.3 or greater. A lower number of rejections means that the distribution of shape of the hexagon we used is close to the bivariate normal distribution we prescribed. Therefore, in this study, we use only 5 values of σ (0.05, 0.1, 0.15, 0.2, and 0.25). Examples of geometry that are eliminated and examples of valid geometry are shown in figures 6.1.2 and 6.1.3, respectively.

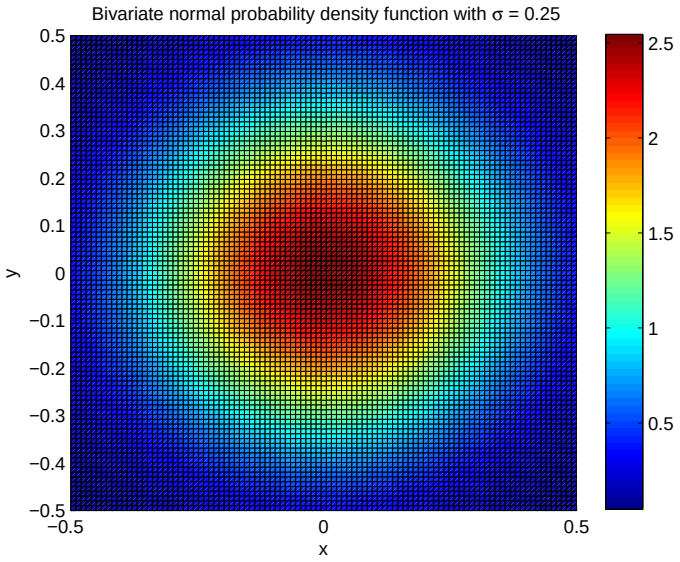

Figure 6.1.1: Bivariate normal probability density function of the position of each vessel with $\sigma = 0.25$.

6.1.2 Derivation of model equations

In this section, only flow in the sinusoids is taken into account. As stated previously in chapter 4, the Darcy equation for the flow is:

$$\mathbf{v_S} = -K_S \boldsymbol{\nabla} p_S, \tag{6.1.1}$$

where $\mathbf{v_S}$ is the Darcy velocity in the sinusoidal space, K_S is the hydraulic conductivity of the sinusoids, and p_S is the sinusoidal pressure. All related parameters used in this

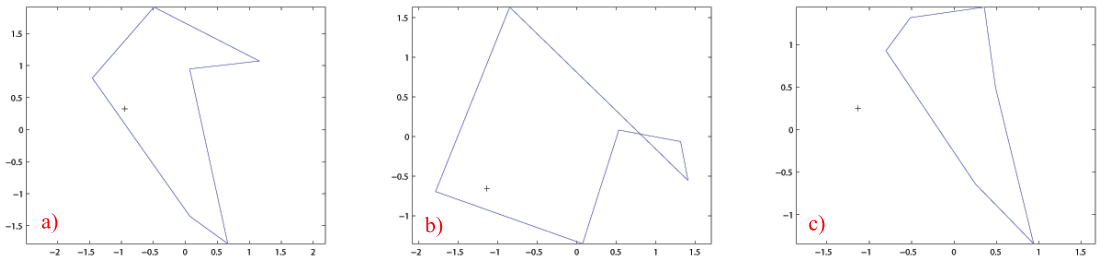

Figure 6.1.2: Examples of geometry that are eliminated. The position of the centrilobular vein is represented by '+'.

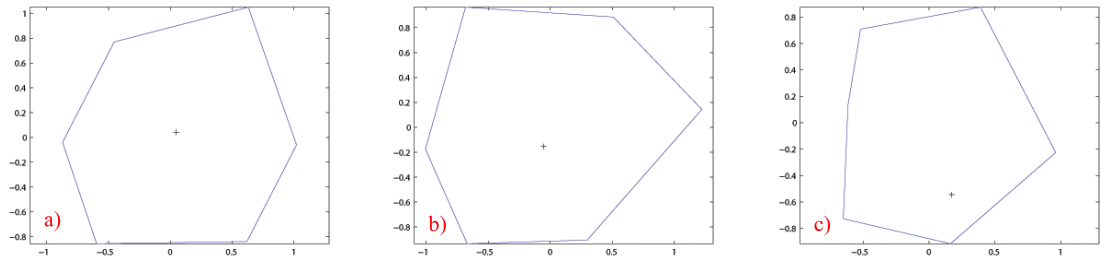

Figure 6.1.3: Examples of valid geometry.

section is listed in table 6.1.

Table 6.1: Physiological parameter values used in section 6.1

Symbol	Description	Typical Value	Reference
L	Typical length of the edge of the lobule	500×10^{-6} m	[51]
R_{PT}	Radius of portal tracts	25×10^{-6} m	[11]
R_{CV}	Radius of centrilobular veins	40×10^{-6} m	[51]
K_S	Sinusoidal hydraulic conductivity	1.1×10^{-8} m^2/mmHg/s	[11] appendix C
$P_{SPT} - P_{SCV}$	The difference of portal tract and centrilobular venous pressure	2.95 mmHg	[11]
Q_{PT}	Flux per unit area of vessels	2.2×10^{-5} m/s	see section 6.1.3

6.1.3 Boundary conditions

We consider two different sets of boundary conditions:

- Prescribed pressures at the portal tracts and the centrilobular vein (a higher pressure P_{SPT} at the portal tracts and a lower pressure P_{SCV} at the centrilobular vein).

- Prescribed input flux per unit area (Q_{PT}). We apply the amount of flux Q_{PT} that maintain the portal tract pressure P_{SPT} at each portal tract.

6.1.4 Nondimensionalisation

All variables are nondimensionalised similar to ones in the single lobule model stated in chapter 4, using stars to denote nondimensional variables:

$$\mathbf{x} = L\mathbf{x}^*, \tag{6.1.2}$$

$$q = Q_{PT}q^*, \tag{6.1.3}$$

$$p_S = P_{SCV} + (P_{SPT} - P_{SCV})p_S^*, \tag{6.1.4}$$

where q is the sinusoidal flux and p_S is the sinusoidal pressure.

6.1.5 Results

We generate a regular hexagon and another 10 shapes of irregular hexagon and the positions of the centrilobular vein for each σ using MATLAB. We then draw the geometry in COMSOL Multiphysics software version 4.2, and solve the governing equation with both pressure and flux boundary conditions stated above numerically in each model. The pressure and the velocity profiles of both sets of boundary conditions are shown in figures 6.1.4, 6.1.5, 6.1.6, and 6.1.7, respectively. We then compare the average flux and pressure at the portal tracts for each σ. We also calculate the total flux per unit area of lobule and its variance. Additionally, we find the maximum, the minimum, and the average velocities and we also find the variance of the velocity distribution within the lobule.

There are differences in the pressure and velocity distributions between the cases of the

prescribed pressure and the prescribed flux boundary conditions (figure 6.1.4 - 6.1.7). However, in both cases, the velocities are highest near the portal tracts and the centrilobular veins, while the minimum velocities occur near the mid-points of the edges.

When we prescribe equal pressure at each portal tract, the total flux flowing through the lobule shows no significant dependence of the value of σ (figure 6.1.8a). In figure 6.1.9a and 6.1.9b (blue lines), the total flux per unit area of lobule is roughly the same when σ increases while its variance increases with σ.

For the velocity profiles, the variance of the spatial velocity distribution increases with σ (figure 6.1.10a-blue line). The minimum velocity seems not to change significantly when σ increases, likewise the average velocity, while the maximum velocity increases with σ (figure 6.1.10b-blue lines).

When we prescribe the fluxes at the portal tracts, on the other hand, the average pressure drop increases only slightly with σ (figure 6.1.8b). The total flux per unit area of lobule also does not increase significantly as the variance increases (figure 6.1.9a-red line). Figure 6.1.9b (red line) shows that the variance of the total flux per unit area of the lobule increases with σ but with a smaller rate than in the case of a prescribed pressure boundary condition.

Figure 6.1.10a (red line) shows that the variance of the spatial distribution of the

sinusoidal velocity does not increase with σ unlike that with the prescribed pressure boundary condition. The minimum and the average velocities also do not change with σ, while the maximum velocity increases only slightly with σ (figure 6.1.10b-red lines).

6.1.6 Statistical analysis

We use one-way ANOVA to test the statistical significance of the findings. From the test, the p-value is 0.9917 which means there is no significant difference at 95% confidence level of q_{PT} when the value of σ is varied. Similar to the first one, ANOVA test shows no significant difference at 95% confidence level of P_{PT} when σ is varied.

There are also no statistical differences at 95% confidence level of the total flux per unit area of the lobule for both prescribed flux and pressure boundary conditions. On the other hand, the variances in both cases increases significantly with the value of σ.

Moreover, there is no statistical difference at 95% confidence level of the variance of the spatial velocity when the prescribed flux boundary conditions are applied. In contrast, the variance increases with the value of σ when the pressure boundary condition is applied.

Furthermore, there are no significant difference of the minimum, the average, and the maximum velocities when σ is varied in the prescribed flux boundary conditions. There

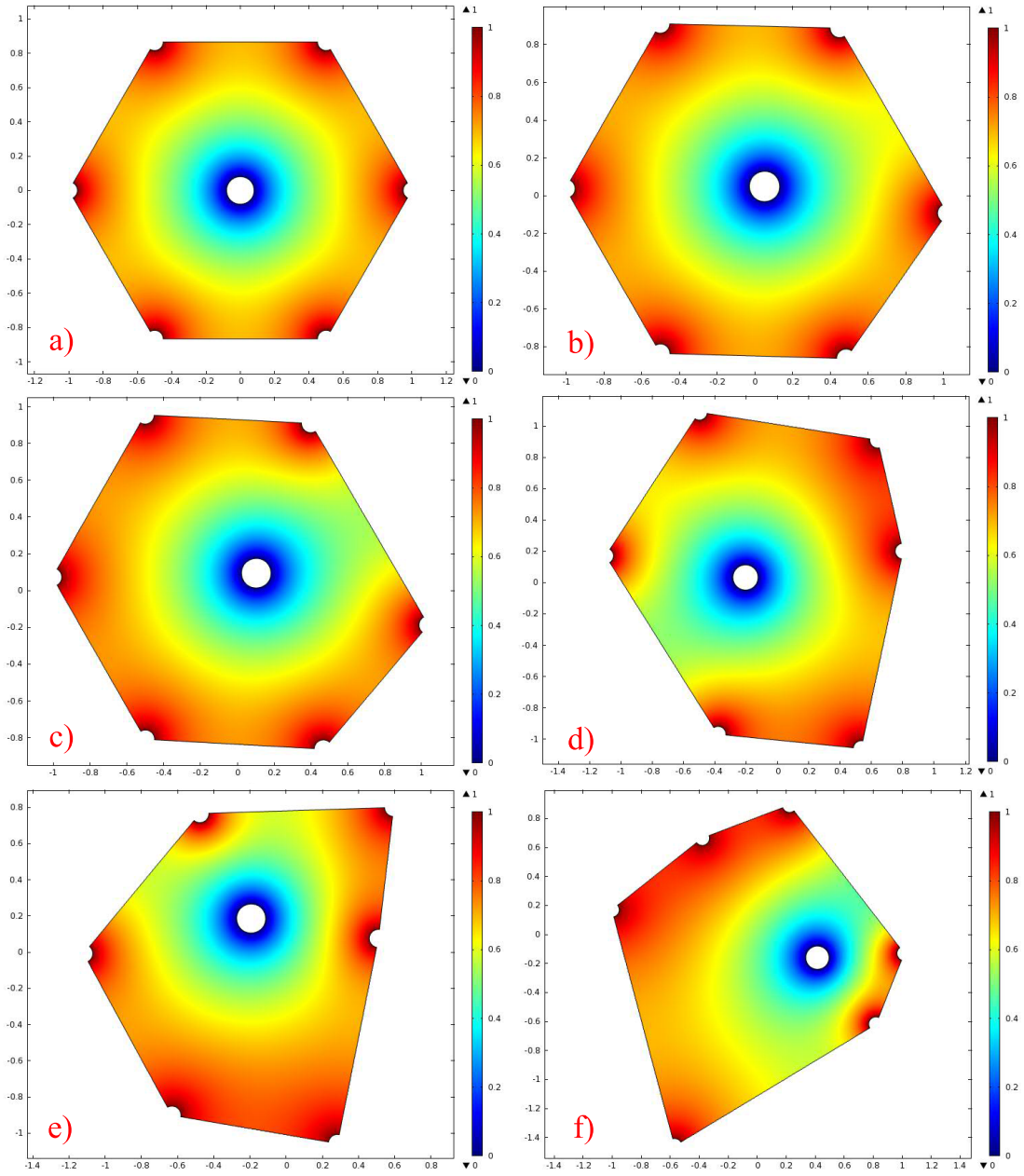

Figure 6.1.4: Examples of sinusoidal pressure profile of the lobule with different σ when prescribe pressure at the portal tracts: a) $\sigma = 0$, b) $\sigma = 0.05$, c) $\sigma = 0.1$, d) $\sigma = 0.15$, e) $\sigma = 0.2$, and f) $\sigma = 0.25$.

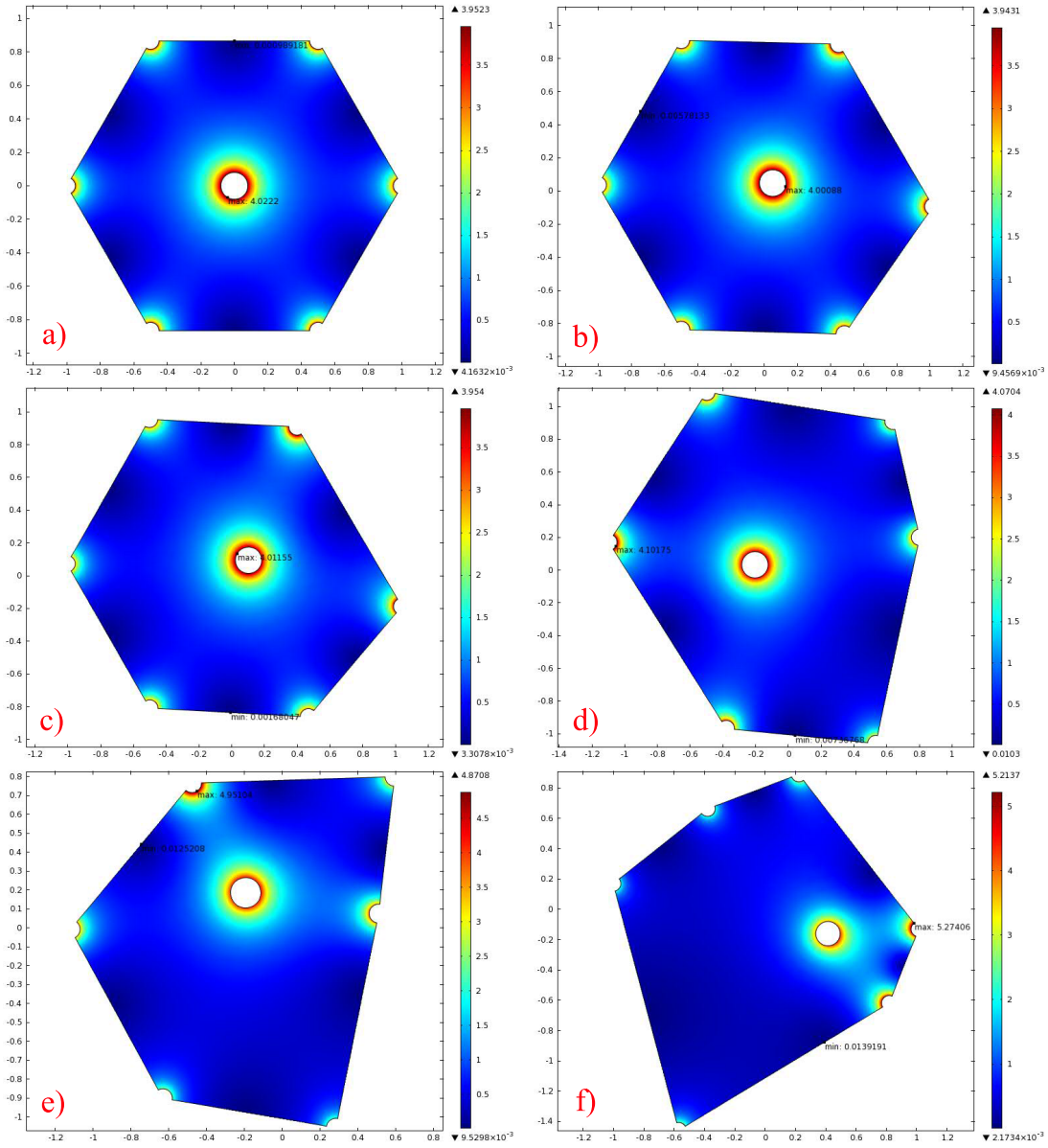

Figure 6.1.5: Magnitudes of sinusoidal velocity of the lobule corresponding to figure 6.1.4.

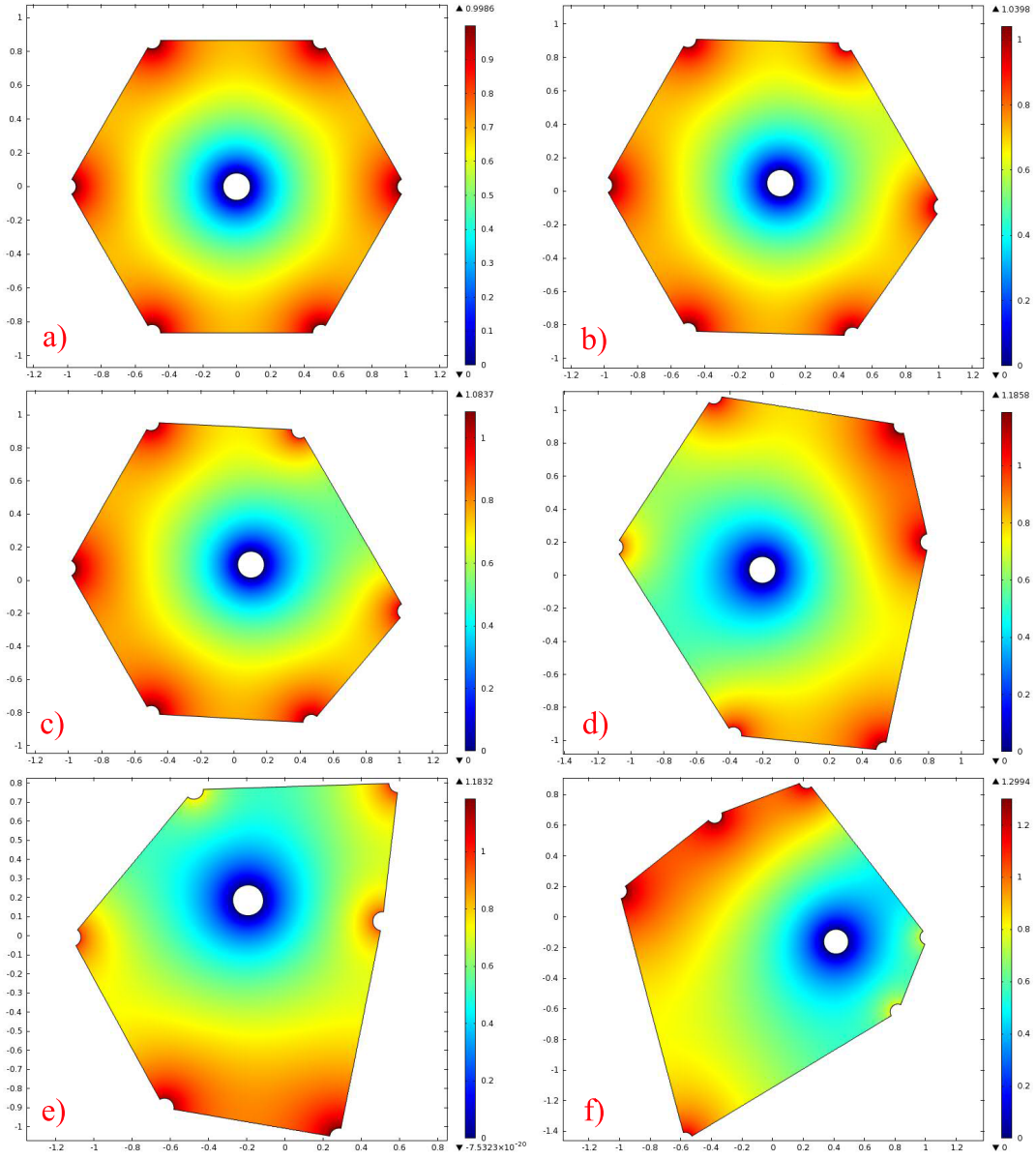

Figure 6.1.6: Examples of sinusoidal pressure profile of the lobule with different σ when prescribe flux at the portal tracts. The same cases as in figure 6.1.4 are considered.

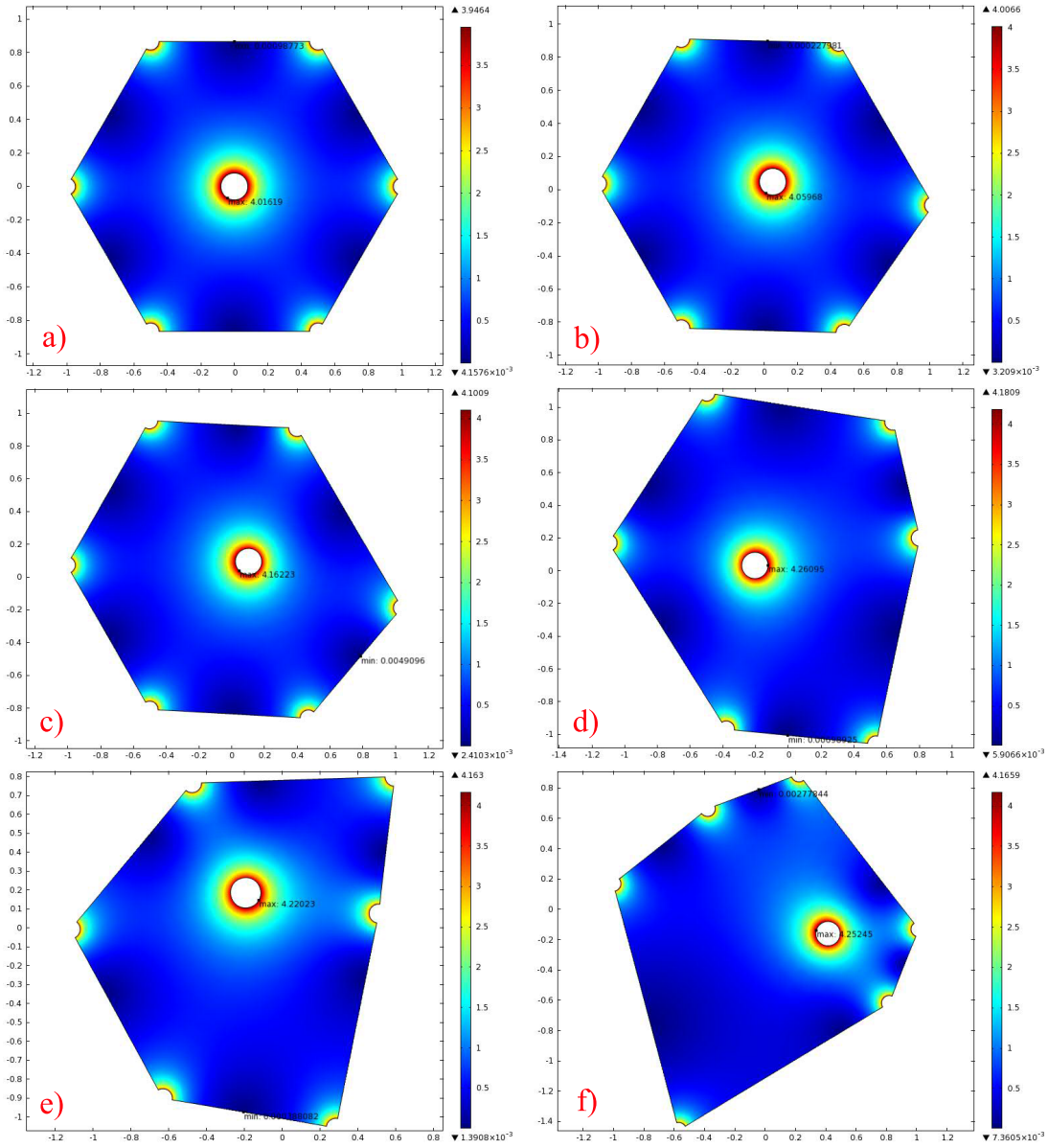

Figure 6.1.7: Magnitudes of sinusoidal velocity of the lobule corresponding to figure 6.1.6.

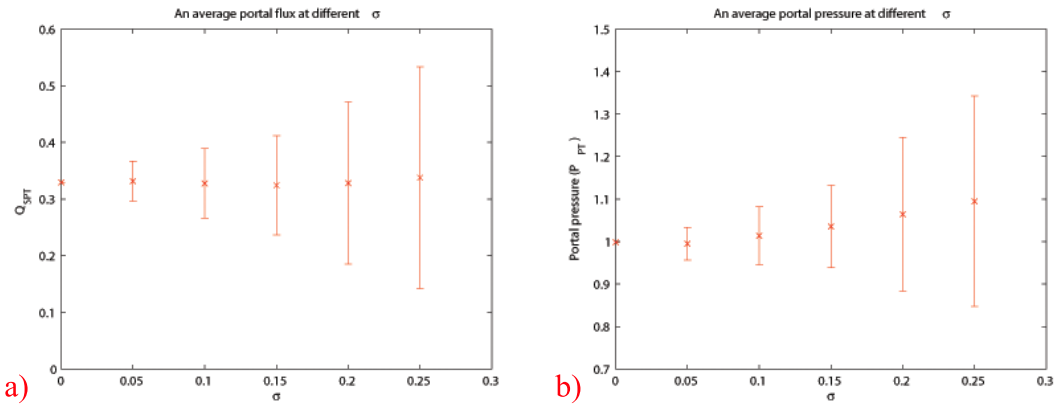

Figure 6.1.8: a) Comparison of the average flux at the portal tract (Q_{SPT}) with different σ when prescribe pressure boundary conditions. b) Comparison of the average portal pressure (P_{PT}) with different σ when prescribe flux boundary condition.

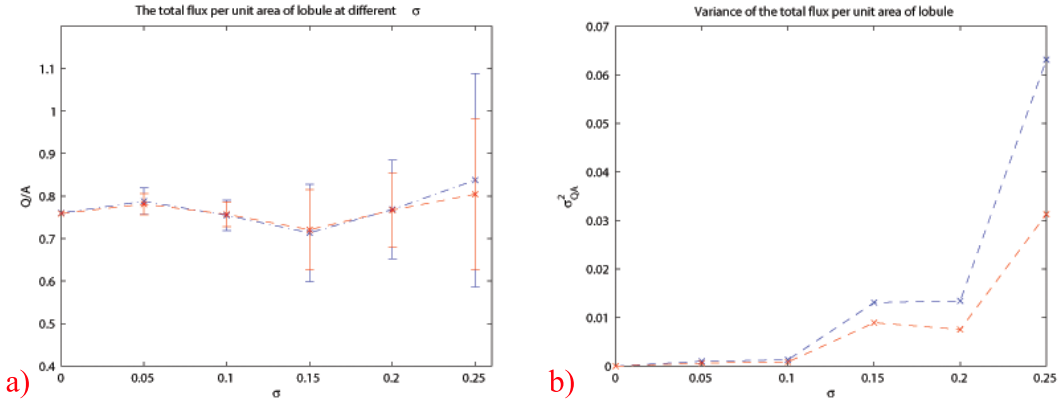

Figure 6.1.9: a) Comparison of the total flux per unit area of the lobule (Q/A) with different σ. b) Comparison of the variance of the total flux per unit area of the lobule (σ^2_{QA}) with different σ. In both graphs, the blue lines represent the data from the prescribed pressure BC while the red lines represent the data from the prescribed flux BC.

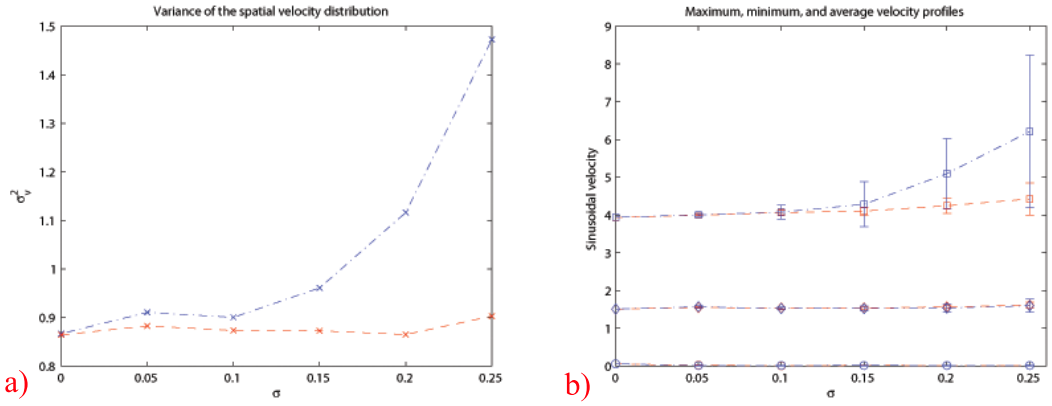

Figure 6.1.10: a) Comparison of the variance of the spatial distribution of the sinusoidal velocity (σ_V^2)with different σ. b) Comparison of the minimum ($\circ$), the average ($\Diamond$), and the maximum sinusoidal velocities ($\square$) with different σ. In both graphs, the blue lines represent the data from the prescribed pressure BC while the red lines represent the data from the prescribed flux BC.

are also no significant difference of the minimum and the average velocities in the prescribed pressure boundary conditions; however, the maximum velocity increases significantly at 95% confidence level when σ increases.

6.1.7 Discussion

We investigate the arrangement of the vessels to find which model gives the optimal perfusion for the lobule among the lobules formed by uniformly distributed vessels and lobule formed by non-uniformly distributed vessels with different variances. When we prescribe pressures at both the portal tracts and the centrilobular vein, the average fluxes (and also the total fluxes) at the portal tract show no significant difference when the geometry changes (figure 6.1.8a). There is a slight fluctuation of the total flux per unit area of the lobule with different σ (figure 6.1.9a-blue line) while its variance increases when σ increases (figure 6.1.9b-blue line). This means that, in a lobular lattice with non-uniform distributed vessels, some lobules receive high perfusion, some receive low perfusion while the lobules formed by uniformly distributed vessels receive more equal perfusion.

The geometry of the lobule receiving the highest perfusion is probably the lobule with smallest area, in which the vessels are packed close to each other. However, this arrangement does not happen in the real liver because the hepatocytes require their own space. Also, the highest perfusion does not always reflect the optimal perfusion for the hepatocytes. In this study, we only consider the sinusoidal space and yet include the interstitial space in which the hepatocytes live. There are factors that related to the health of hepatocytes, such as oxygen distribution or shear stress from the interstitial fluid. Excessive amount of flux can cause injury and also excessive amounts of oxygen delivered to the hepatocytes. In the future, we should include the interstitial component

in the model, and reinvestigate the effect of the vascular arrangement on the oxygen distribution and the shear stress.

Another parameter that can be used to quantify the effectiveness of perfusion is the homogeneity of the blood distribution. The variance of the spatial distribution of the sinusoidal velocity (figure 6.1.10a-blue line) shows that the regular hexagonal lobule gives a more homogeneous perfusion for the flow within the lobule compared to the lobule with more randomly positioned vessels. However, the velocity profile of each model shows large areas of very slow flow near the mid-point of the edges (figure 6.1.5) which leads to a relatively high value of the variance of velocity σ_v^2 even when the variance of position $\sigma = 0$. This may not be very realistic because, in reality, there are small septal branches of two adjacent portal tracts that are connected as an anastomosis along the vascular septa which can distribute blood through the edges of the lobule. The investigation of the effect of the septal branches will be done in section 6.2.

The minimum and the average velocity within the lobule are almost equal with different σ while the maximum velocity increases with σ (figure 6.1.10b-blue lines). This could lead to overperfusion for the certain area of the lobule and have physiological effects, such as excessive shear stress on the hepatocytes.

With prescribed fluxes rather than prescribed pressures, the average pressure drop across the lobule increases slightly with σ (figure 6.1.8b). There is a slight fluctuation of the

total flux per unit area of the lobule with different σ (figure 6.1.9a-red line), while its variance tends to increase with σ but the rate is smaller than the one with the prescribed pressure boundary condition (figure 6.1.9b-red line). Thus the prescribed flux boundary condition produces a more even perfusion in lobules with non-uniformly distributed vessels than the prescribed pressure condition.

Interestingly, the variance of the spatial velocity distribution does not vary significantly with σ (figure 6.1.10a-red line). The minimum and the average velocities are almost the same as those with the prescribed pressure boundary condition, but the maximum velocity is much less and increases only slightly with σ (figure 6.1.10b-red lines).

In conclusion, there is no significant difference in the perfusion between the prescribed pressure and the prescribed flux boundary conditions in the lobule with uniformly distributed vessels. On the other hand, with very irregular geometries, the prescribed flux boundary condition gives a more homogeneous perfusion than the prescribed pressure condition. Moreover, with the prescribed flux boundary condition, the difference in the perfusion between the lobules formed by uniformly and non-uniformly distributed vessels is small compared to the prescribed pressure condition.

These findings suggest that if the rate of distribution of blood is maintained quite uniform across all portal tracts then the spatial non-uniformities in the positioning of portal tracts has relatively minor effect.

6.2 The effect of vascular septa on oxygen distribution in the lobule

Another question of interest is to determine the spatial density of the vessels in the lobule for optimal perfusion to cells. In this section, we compare the minimum oxygen concentrations in the classical lobule as the number of feeding vessels varies until applying the vascular septa which gives blood to the lobule from all directions.

The vascular septa are the surfaces spanning the gap between two neighbouring portal tracts that contain branches of the vessels connected between them. In some animals, such as pigs and rats [9], this structure is obviously visible but it is harder to identify in human liver tissue. Matsumoto et al also mentioned about the existence of this vascular network in their 3D reconstruction of the liver lobule [10].

6.2.1 Geometry description

We count whole numbers of portal tract in the hexagonal lobule; thus for example, a portal tract on a straight edge counts as $\frac{1}{2}$ and a portal tract at the corner of a regular hexagon counts as $\frac{1}{3}$. We consider four cases: $n = 1$, $n = 2$, $n = 5$, where n is the total number of portal tracts, and also the case when flux is uniformly distributed around the whole boundary, which represents vascular septa. In each case, the portal tracts are located uniformly as much as possible around the boundary of the lobule. The relevant

parameters used in the model are listed in table 6.2 and 6.3.

6.2.2 Governing equations

We use the same governing equations for the flow and the oxygen distribution in both sinusoidal and interstitial spaces as stated in the previous chapter: (5.1.1), (5.1.2), (5.1.10), and (5.1.11).

6.2.3 Boundary conditions

To ensure comparability between the different cases, we assume that the total flux flowing into the lobule is the same, which means that the flux per unit area of the vessel is varied between different cases. We apply the amount of input flux that maintain the portal tract pressure P_{SPT}, as used in the previous chapters, at each portal tract. Moreover, we apply no flux boundary condition at the edges and apply P_{SCV} as the pressure boundary condition at the centrilobular vein.

6.2.4 Nondimensionalisation

All variables and parameters are nondimensionalised as done previously in chapter 5. The dimensional and nondimensional parameter values are shown in table 6.2 and 6.3, respectively.

Table 6.2: Table of dimensional parameters used in section 6.2 and the minimum oxygen concentration ($[O_2]$) measured

Number of portal tract per lobule (n)	Flux per unit area of vessels (m/s)	Minimum $[O_2]$ (mol/m^3)
1	13.86×10^{-5}	0.116
2	6.93×10^{-5}	0.141
5	2.78×10^{-5}	0.160
2 + vascular septa	0.73×10^{-5}	0.169

Table 6.3: Table of nonimensionalised parameters used in section 6.2 and the minimum oxygen concentration ($[O_2]$) measured

Number of portal tract per lobule (n)	Flux per unit area of vessels	Minimum $[O_2]$
1	6.3	0.5526
2	3.15	0.6705
5	1.26	0.7638
2 + vascular septa	0.33	0.8054

6.2.5 Numerical results

The governing equations with the boundary conditions are calculated numerically by using weak formulations as inputs in COMSOL Multiphysics software version 4.2. The numerical results are shown in figures 6.2.1 - 6.2.4 and the values of dimensional and nondimensional minimum oxygen concentration in each case are shown in table 6.2 and 6.3, respectively. It shows that the level of minimum oxygen concentration increases with the number of portal tracts in the model, and the lobule with vascular septa, which has a uniform distribution around the boundary, has the highest level. This suggests that the presence of the vascular septa ensures a better optimal oxygen distribution to the cells, and this agrees with several findings of this vascular network in the liver of living

creatures [9].

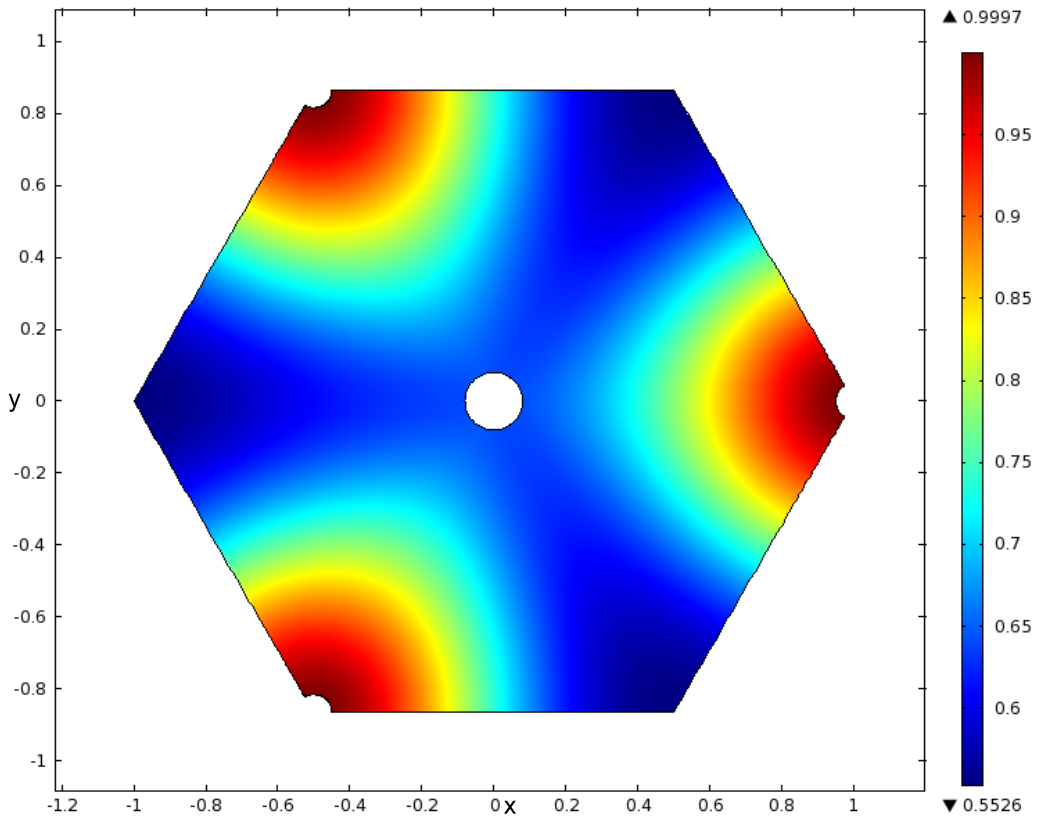

Figure 6.2.1: Interstitial oxygen concentration gradient (dimensionless) when $n = 1$.

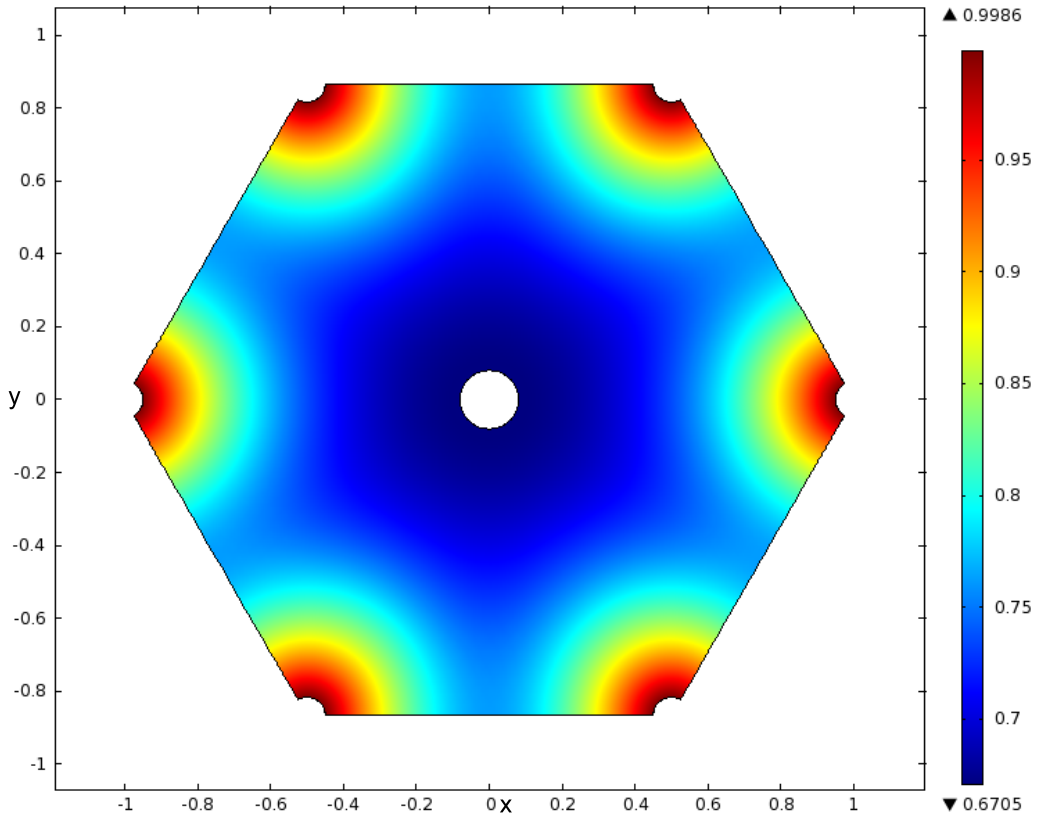

Figure 6.2.2: Interstitial oxygen concentration gradient (dimensionless) when $n = 2$.

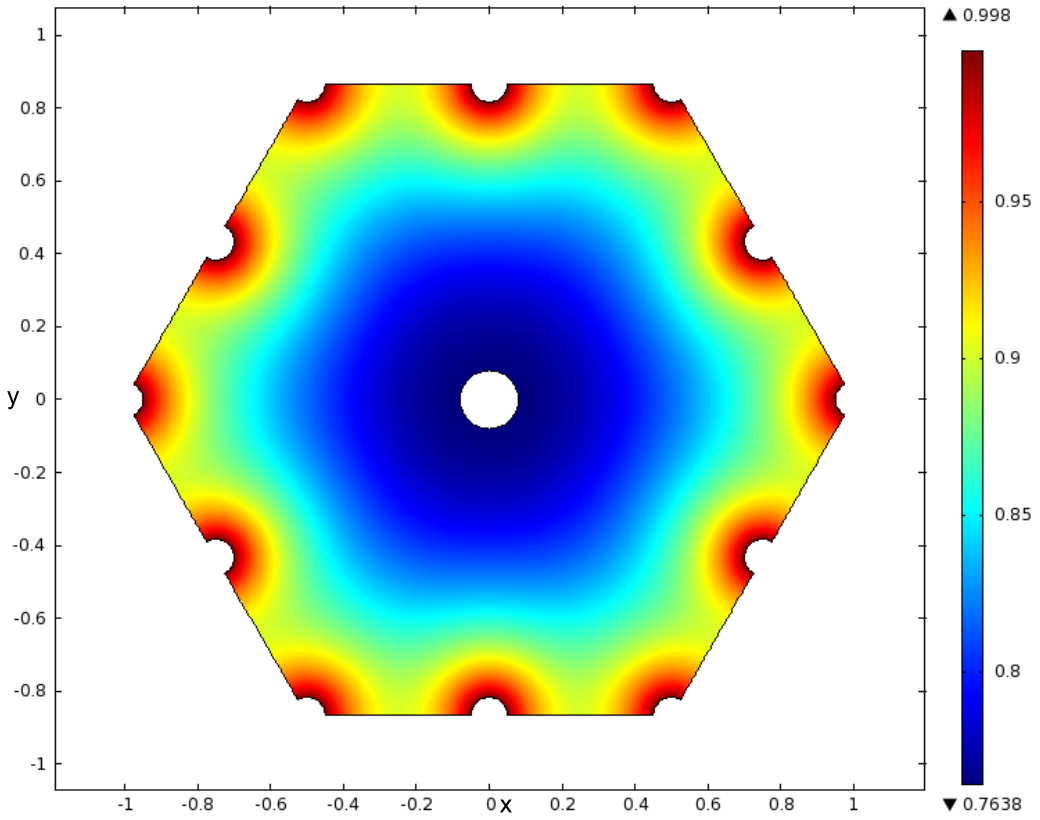

Figure 6.2.3: Interstitial oxygen concentration gradient (dimensionless) when $n = 5$.

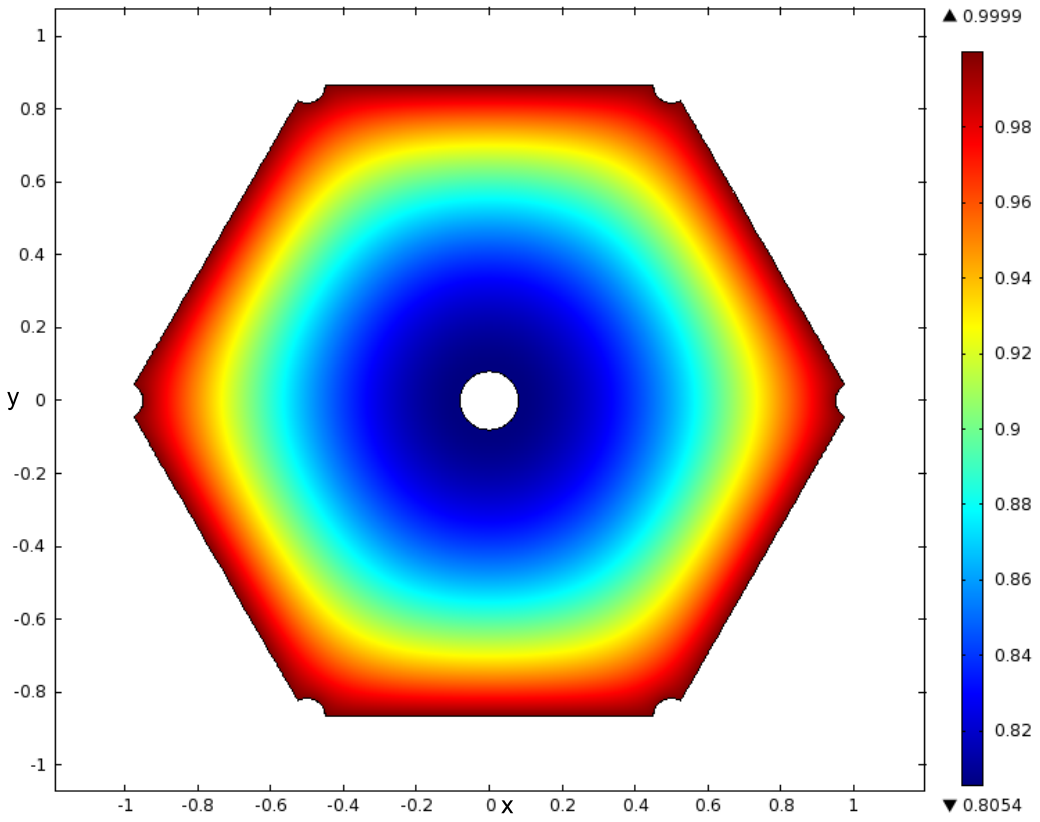

Figure 6.2.4: Interstitial oxygen concentration gradient (dimensionless) when applying vascular septa.

6.3 The effect of geometry on oxygen distribution in the lobule

Since the geometry of the lobule in the histological image is unclear, in this section, we study other possible geometries of the lobules as we aim to answer the question what is the optimal geometry of the lobule that give the optimal perfusion to cells. In this section, we compare the minimum oxygen concentration in the classical lobule to other lobules with different geometries.

6.3.1 Geometry description

To simplify the problem, we consider the geometries that can be tessellated as a regular and uniform lattice. Therefore, four regular geometries are chosen: hexagon, triangle, square, and rhombus with an angle of $\frac{\pi}{4}$ radian. In each case, the portal tracts are located at the vertices. The area of the lobule in each geometry is conserved with respect to the area of the hexagonal lobule. The size of the vessels is also similar in each geometry. Moreover, since the results in the previous section show that the vascular septa gives better oxygen distribution to the lobule; therefore, in this section, we include the vascular septa as the feeding vessels to each model. The relevant parameters used in the model are listed in table 6.4 and 6.5.

6.3.2 Governing equations

Similar to the previous section, we use the same governing equations for the flow and oxygen distribution in the sinusoids and the interstitial space: (5.1.1), (5.1.2), (5.1.10), and (5.1.11).

6.3.3 Boundary conditions

We assume that the total amount of flux flowing from the portal tracts and the vascular septa into the lobule is the same in each case, meaning that the flux per vessel is different in the each case. The total amount of flux used in each geometry is the same amount of flux used in the previous section. The pressure boundary condition P_{SCV} is also applied at the centrilobular vein.

6.3.4 Nondimensionalisation

All variables and parameters are nondimensionalised as done in chapter 5 except the lengths that are nondimensionalised with respect to the length of edges in each geometry. The dimensional and nondimensional parameter values are shown in table 6.4 and 6.5, respectively.

Table 6.4: Table of dimensional parameters used in section 6.3 and the minimum oxygen concentration ($[O_2]$) measured

Geometry of lobule	Length of edges (μm)	Flux per unit area of vessels (m/s)	Minimum $[O_2]$ (mol/m^3)
Hexagon	500	7.30×10^{-6}	0.169
Triangle	1228	0.91×10^{-6}	0.149
Square	800	2.41×10^{-6}	0.153
Rhombus	866	1.93×10^{-6}	0.154

Table 6.5: Table of nondimensionalized parameters used in section 6.3 and the minimum oxygen concentration ($[O_2]$) measured

Geometry of lobule	Flux per unit area of vessels	Minimum $[O_2]$
Hexagon	0.330	0.8054
Triangle	0.112	0.7001
Square	0.193	0.7244
Rhombus	0.167	0.7291

6.3.5 Numerical results

The governing equations with the boundary conditions are calculated numerically by using weak formulations as inputs in COMSOL Multiphysics software version 4.2. The results are shown in figure 6.3.1 - 6.3.4 and both dimensional and nondimensional minimum oxygen concentrations in each case are listed in table 6.4 and 6.5, respectively. The results show that the level of minimum oxygen concentration is highest in the hexagonal lobule and lowest in the triangular lobule. However, the differences between the minimum oxygen concentrations are small in different cases ($< 20\%$). This could explain why the shape of lobules in histological findings is irregular but tends to be arranged as approximately a hexagon.

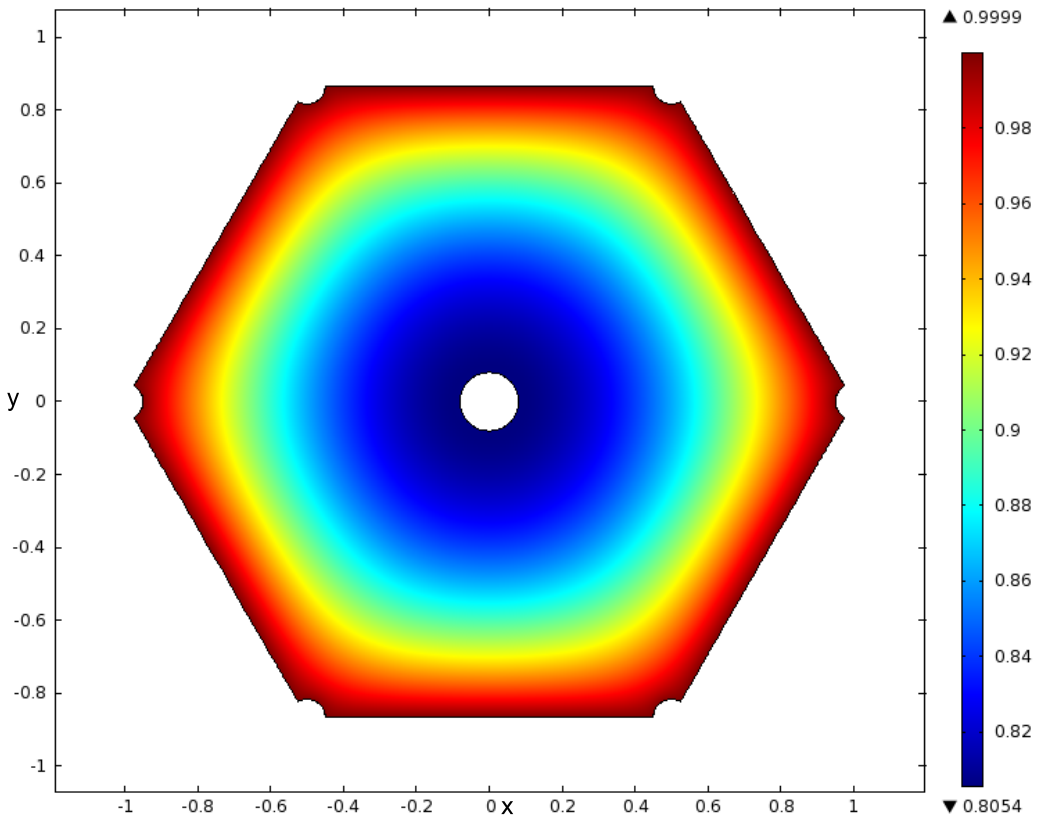

Figure 6.3.1: Interstitial oxygen concentration gradient (dimensionless) in hexagonal lobule.

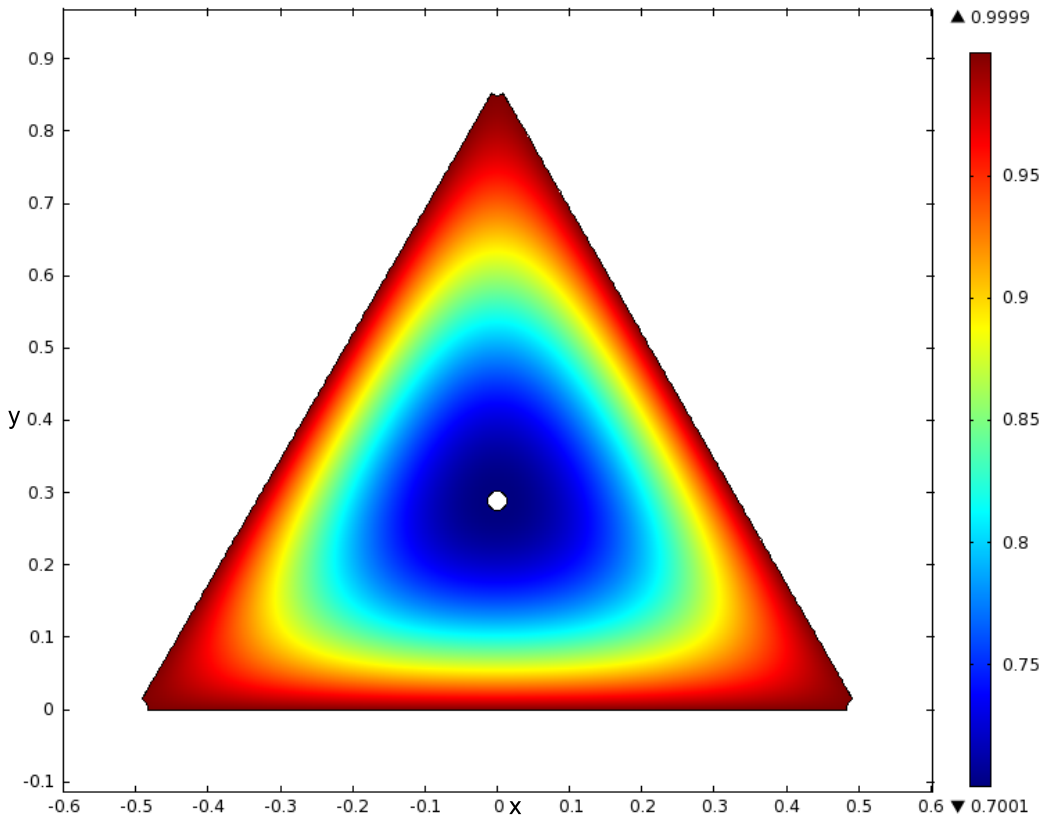

Figure 6.3.2: Interstitial oxygen concentration gradient (dimensionless) in triangular lobule.

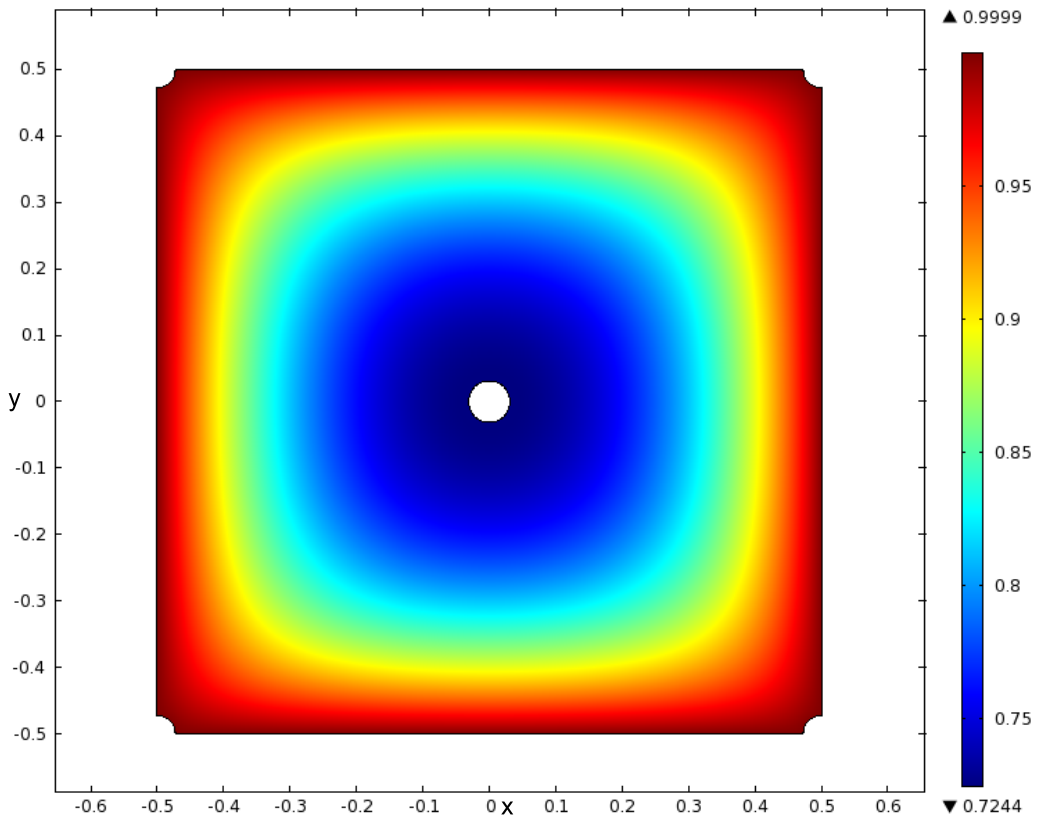

Figure 6.3.3: Interstitial oxygen concentration gradient (dimensionless) in square lobule.

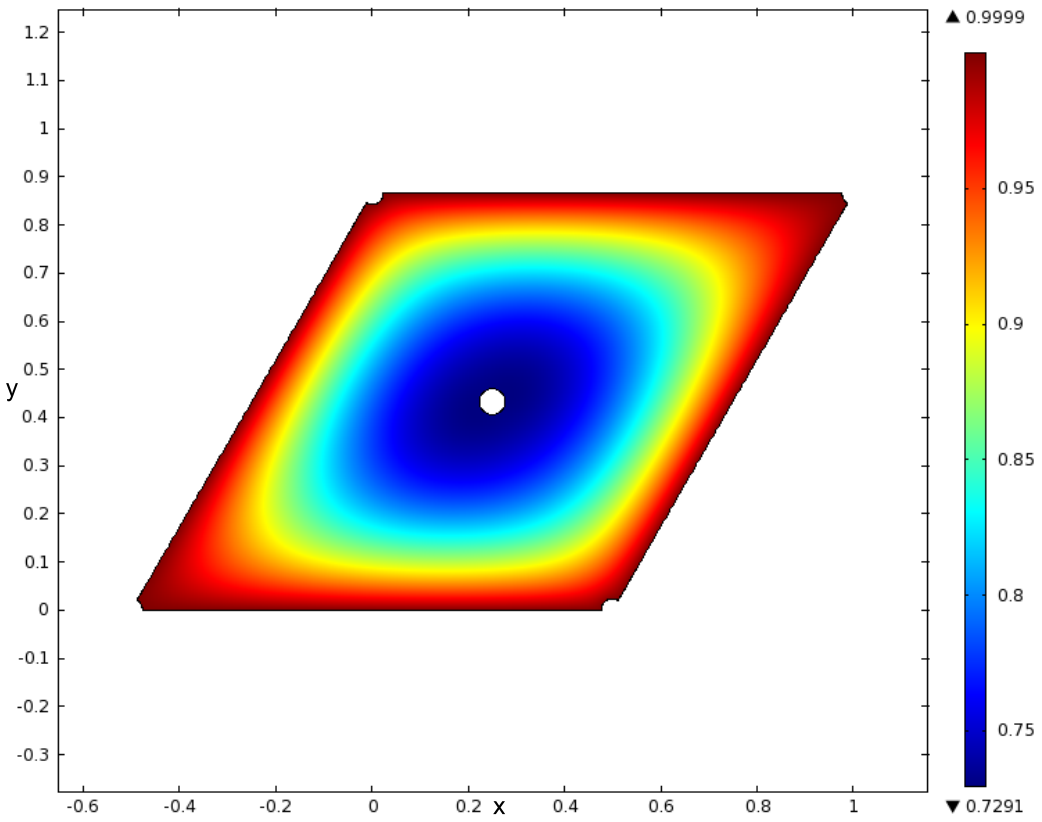

Figure 6.3.4: Interstitial oxygen concentration gradient (dimensionless) in rhomboid lobule.

6.4 Summary and discussion

In this chapter, we investigated blood flow and oxygen distribution in several geometries of the lobule with variation of the distribution of the vessels in order to find whether the classical hexagonal lobule is the optimal geometry for the model. The results show that the hexagon lobule with the vascular septa give the best perfusion compared to the other geometries with the vascular septa and also the hexagon lobule without the vascular septa.

Moreover, there is no difference of the homogeneity of blood distribution between the hexagon lobule with uniformly distributed vessels and with non-uniformly distributed vessels when the prescribed flux boundary condition is applied. On the other hand, in prescribed pressure boundary condition, the hexagon lobule with uniformly distributed vessels give better homogeneity of blood perfusion than the lobule with non-uniformly distributed vessels. However, the difference of blood distribution between the symmetrical hexagonal lobule and the others is small and can explain the irregular shape of the lobules in the histological findings of liver tissue.

In summary, the results suggest that the classical hexagonal lobule with the vascular septa is an appropriate model to represent the liver lobule in physiological modelling.

Chapter 7

Conclusion

Liver microcirculation is one of the most complex systems of the physiological flow in the human. In this thesis, we developed models of fluid microcirculation in the liver lobule by treating it as solid porous medium. The model was developed further from the model of Bonfiglio et al with several additional components, mainly the interstitial fluid pathways.

In the third chapter, we investigated the behaviour of the lobule including elastic properties of the tissue. We first treated the lobule as an elastic solid, assuming it has the simple geometry of a circular cylinder. We also assume that all lobules are packed together within a spherical liver. The dynamic process of the deformation was then investigated by applying pressure boundary condition at the surface of the liver. The results show that liver deforms linearly and slightly even under high pressure condition. The dynamic of the deformation over time was also analysed with the applied periodic

boundary condition.

In the next part of the chapter, the lobule was treated as a poroelastic circular cylinder, governed by the Biot formulation and the Darcy equation. The similar pressure boundary condition used in the elastic model was applied to the lobule for the deformation. The numerical result shows that the poroelastic model deforms more than the elastic model, suggesting that it might be significant under high pressure condition such as a small-for-size syndrome occurs afer a partial hepatectomy or after an implantation of a small size liver. The model was further studied by Bonfiglio et al to determine the relationship between pressure and flux in the hexagonal lobule. The result shows weakly non-linear relationship between pressure and flux, meaning that the permeability increases more than linearly when pressure increases.

In chapter 4, we incorporated the interstitial flow to the model using Darcy's equation same as in the sinusoidal space but with a different permeability. The interstitial space is connected with the sinusoids via the endothelial fenestrations. The interstitial fluid exits the liver via three pathways: through the lymphatic ducts, via the bare area, and across the lower surfaces of the liver via the Glisson's capsule, and in this chapter we included all pathways in the model.

In some pathological livers, the amount of fluid leaking from the lower surface of the liver increases, causing the fluid to collect in the abdominal cavity, leading to a condi-

tion called ascites. In order to investigate the fluid flow in this pathway, the lobules are considered to connect together as a lattice model, tessellating to form the whole liver. The amount of interstitial fluid exit in every pathway was calculated numerically and compared, with the majority of the interstitial fluid leaving the liver is via the lymphatic duct and the bare area combined together via the thoracic duct. When the flux boundary condition is applied, the calculated amount of the interstitial fluid leaving the liver via the thoracic duct is closer to the physiological value than prescribing the pressure boundary condition. However, both types of boundary condition give a good prediction on the amount of ascites production. Overall, our model shows the potential that it could be used as a model of microcirculation in the liver in order to predict the blood and interstitial flow within a single lobules and within the whole liver.

The importance of some parameters on the ascitic fluid production was also investigated. Our results show that the portal tract pressures, the permeabilities of sinusoids and interstitial spaces are the most important factors on the production of the ascites. Changing in these parameters can cause a dramatic change in the ascitic fluid production as occurs in some clinical conditions. This agrees with the experimental findings from Vanheule et al [83] and Mori et al [84] that the sinusoidal diameter decreases in some liver diseases, in which ascites usually produced, such as cirrhosis. The size of the liver is another factor that determines the amount of the fluid leakage. The liver with smaller volume produces more ascitic fluid relatively to the normal size liver. However, the small size liver with less surface area per volume will produce less amount of ascites.

This information could be used by surgeons to apply the surgical technique to reduce the liver surface per volume as much as possible in partial hepatectomy.

In the fifth chapter, we investigated the oxygen distribution within the lobule. The model is described by advection–diffusion equation for the distribution in the sinusoids, from the sinusoids to the interstitial space via the fenestrated membrane, and within the interstitial space. The Michaelis–Menten kinetics is used for the cellular uptake. The results show that about 1/3 of oxygen supply is consumed by the hepatocytes. The number is a good estimate compared to the results from the experiments of Matsumura et al [79], [80]. The level of oxygen in the sinusoids and in the interstitial space is also very close. This agrees with the model of Beard [81], in which the different gap of oxygen levels in the capillary and in the interstitial space is very narrow.

The effect of each parameter on the oxygen transport was also investigated. High portal tract pressure, high oxygen concentration, high permeability of the sinusoids, and low oxygen uptake rate give better oxygen distribution to the hepatocytes living in the lobule. In contrast, the permeabilities of the fenestrations and the interstitial space give unchange in the oxygen distribution. The results also suggest that oxygen is mainly delivered in the sinusoids by the advection process. On the other hand, the oxygen flowing across the endothelial wall and within the interstitial space is mainly transported by the diffusion process.

However, in our model, we assume that blood is a Newtonian fluid and only oxygen in the plasma is investigated. We neglect the effect of red blood cells which contains haemoglobin that function as a carrier of the majority of oxygen in blood. The effect of haemoglobin should be included in the future study to make the outcome more precise.

Finally, since real histological samples of liver tissue show that the arrangement of vessels and lobules is irregular and non-uniform, we investigated what effect a non-uniform arrangement has, and what is the optimal distribution of vessels to ensure good oxygen supply to the hepatocytes. Firstly, the comparison of the uniformly and non-uniformly distributed vessels were investigated by considering the total flux, and distribution of the magnitude of the velocity over the lobule. The results show that the uniformly distributed vessels give more consistent blood supply than the non-uniform model. In the second part, the effectiveness of perfusion in the different geometries of the lobule is investigated. Oxygen distribution in four simple geometries are compared: hexagon, triangle, square, and rhombus. The results show that the regular hexagonal lobule with vascular septa has the highest minimum oxygen concentration, meaning that it provides the optimal blood supply; however, with only small difference compared to the others. These findings can explain the irregular shape and arrangement of the liver lobule in the histological sections from the liver biopsy.

In summary, in this thesis, we developed a mathematical model of the microcirculation in the liver based on the classical liver lobule model of Kiernan. We investigated

the role of tissue elasticity, interstitial flow, oxygen distribution, and the spatial arrangement of the vessels. Our study gives us more understanding to the experimental and histological findings from the literature and; therefore, shed light on the dynamics of the liver microcirculation and point the way for future studies, in which pathological livers should be investigated.

Appendices

Appendix A

Approximation of the term $zK_0'(z)$ when $z \to 0$

We use the formulae (Abramovitz and Stegun)

$$K_0(z) = -\left(\ln(\frac{1}{2}z) + \gamma\right) I_0(z) + \frac{\frac{1}{4}z^2}{(1!)^2} + (1+\frac{1}{2})\frac{(\frac{1}{4}z^2)^2}{(2!)^2} + (1+\frac{1}{2}+\frac{1}{3})\frac{(\frac{1}{4}z^2)^3}{(3!)^2} + ... \quad \text{(A.0.1)}$$

and

$$I_0(z) = 1 + \frac{\frac{1}{4}z^2}{(1!)^2} + \frac{(\frac{1}{4}z^2)^2}{(2!)^2} + \frac{(\frac{1}{4}z^2)^3}{(3!)^2} + ... \quad \text{(A.0.2)}$$

Thus

$$I_0'(z) = \frac{\frac{1}{2}z^2}{(1!)^2} + \frac{\frac{1}{4}z^3}{(2!)^2} + \frac{\frac{3}{32}z^5}{(3!)^2} + ... \quad \text{(A.0.3)}$$

and

$$K_0'(z) = -\left(\ln(\frac{1}{2}z) + \gamma\right) I_0'(z) - \left(\frac{1}{z}\right) I_0(z) + \frac{\frac{1}{2}z^2}{(1!)^2} + \frac{\frac{1}{4}z^3}{(2!)^2} + \frac{\frac{3}{32}z^5}{(3!)^2} + ... \qquad \text{(A.0.4)}$$

meaning that

$$\begin{aligned} zK_0'(z) &= -\left(\ln(\frac{1}{2}z) + \gamma\right) zI_0'(z) - I_0(z) + \frac{\frac{1}{2}z^3}{(1!)^2} + \frac{\frac{1}{4}z^4}{(2!)^2} + \frac{\frac{3}{32}z^6}{(3!)^2} + ... \\ &= -I_0(z) + \left(1 - \ln(\frac{1}{2}z) + \gamma\right)\left(\frac{\frac{1}{2}z^3}{(1!)^2} + \frac{\frac{1}{4}z^4}{(2!)^2} + \frac{\frac{3}{32}z^6}{(3!)^2} + ...\right) \qquad \text{(A.0.5)} \end{aligned}$$

As $z \to 0$, the second term on the RHS of (A.0.5) tends to zero. Also, $I_0(z)$ tends to 1. Hence,

$$\lim_{z\to 0} zK_0'(z) \approx -1. \qquad \text{(A.0.6)}$$

Appendix B

Determination of the hepatic filtration coefficient

In equation (4.1.3), we defined the parameter β which is the measure of flux per unit length of sinusoidal vessel per unit pressure drop between the fluid in the sinusoids and in the interstitium. In this section, we estimate its value.

Greenway and Lautt (1970) measured the transsinusoidal fluid filtration in the cat liver experimentally. They found the value of hepatic filtration coefficient $F = 0.3\ ml/min/mmHg$ per 100 g of the liver [59]. In order to convert this to a value, we therefore require data on the spatial density of the sinusoids.

Dahmen et al (2007) measured the functional sinusoidal density, which is defined as the total length of sinusoids per unit cross-sectional area [40]. This was measured from

an image of rat liver in vivo near the surface of the liver by found it has an average value of 43 cm/cm^2 in normal livers. Assuming the sinusoids lie perpendicular to portal tracts and are uniformly distributed. Therefore, in a 1 cm^3 cube of liver tissue, the total sinusoidal length is $43 \times 43 \ = 1849\ cm$ (or equal $1.849 \times 10^7\ m/m^3$).

The relationship between β, and F is $\beta = \frac{\rho_{liver} F}{L_S}$ where ρ_{liver} is the density of liver tissue, which we take to be 1060 kg/m^3 and L_S is the length of sinusoids per unit volume of liver tissue.

We first convert F to SI units

$$\begin{aligned} F &= 0.3 \frac{ml}{min \cdot mmHg \cdot 100\ g} \times \frac{1}{60} \frac{min}{s} \times \frac{1}{10^6} \frac{m^3}{ml} \times 10^3 \frac{g}{kg} \\ &= 5 \times 10^{-8}\ m^3/s/kg/mmHg \end{aligned}$$

Hence $\beta = \frac{1000 \times 5 \times 10^{-8}}{1.849 \times 10^7} = 2.7 \times 10^{-12}\ m^2/s/mmHg$

Appendix C

Estimation of the permeability of the interstitial space

Due to lacking of experimental data of the permeability of the interstitial space in the liver, we here estimate the value using some related physical parameters by assuming that each sinusoid has a shape of circular cylinder surrounded by the space of Disse.

We use Kozeny-Carmen formula $K = \frac{1}{\mu}\frac{\phi^3}{cS^2}$ [34], where ϕ is porosity, S is wet surface area and c is a dimensionless constant, to relate the hydraulic conductivity of the interstitial space to that of the sinusoids:

$$K_I = \left(\frac{\mu_S}{\mu_I}\right)\left(\frac{S_S}{S_I}\right)^2\left(\frac{\phi_I}{\phi_S}\right)^3 K_S \tag{C.0.1}$$

Since the majority of the volume of the interstitium is in the space of Disse, and each sinusoid correspond to a space of Disse, we have

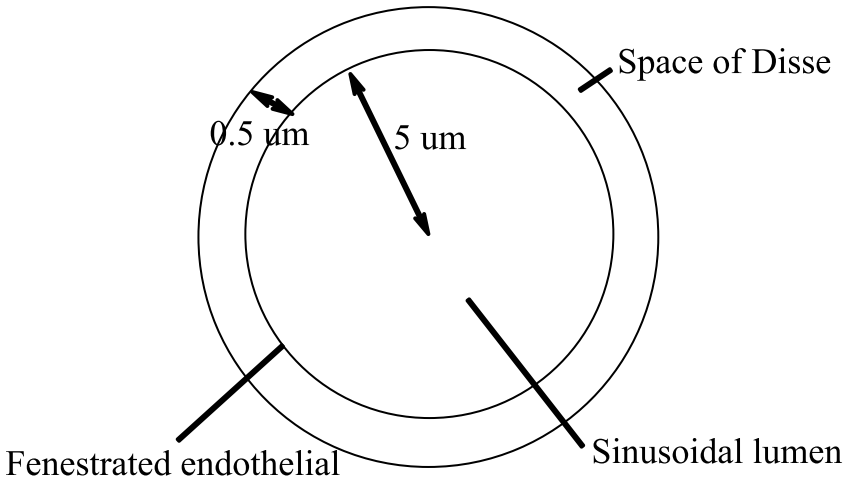

Figure C.0.1: Diagram for the estimation of the permeability of the interstitial space. The sinusoid (radius = $5\mu m$ [71] [72]) is assumed to be circular cylinders surrounded by the space of Disse (width = $0.5\mu m$ [73]).

$$\phi_I = \frac{A_I}{A_S}\phi_S \tag{C.0.2}$$

where A_S and A_I are the cross-sectional area of the sinusoid and the space of Disse, respectively. Then,

$$K_I = \left(\frac{\mu_S}{\mu_I}\right)\left(\frac{S_S}{S_I}\right)^2\left(\frac{A_I}{A_S}\right)^3 K_S \tag{C.0.3}$$

The cross-sectional areas are calculated as follows:

$A_S = \pi(5 \cdot 10^{-6})^2 = 25\pi \times 10^{-12}\ m^2$

$A_I = \pi(5.5 \cdot 10^{-6})^2 - \pi(5 \cdot 10^{-6})^2 = \frac{10.25}{4}\pi(10^{-6})^2 = 2.5625\pi \times 10^{-12}\ m^2$

Wet surface area of the interstitial space is estimated to be approximately twice that of the sinusoidal space since it covers around the sinusoids. Hence, $S_I = 2S_S$.

According to the Fahraeus-Linquist effect, the viscosity of blood in vessels whose diameters lie in the range of 6 to 9 μm) is given by the following empirical relationship [74]

$$\mu_{rel\ 0.45} = 220 \cdot e^{-1.3D} + 3.2 - 2.44 \cdot e^{-0.06D^{0.645}}, \tag{C.0.4}$$

where D is the vessel diameter.

From this relationship, viscosity of blood and plasma in the vessel of diameter $10\mu m$ is $\mu_{blood} \approx 1.3\ mPa \cdot s$ and $\mu_{plasma} = 1.16\ mPa \cdot s$

Substituting there parameter values into (C.0.3), we obtain the permeability of the interstitial space as

$$K_I = \left(\frac{1.3}{1.16}\right)\left(\frac{1}{2}\right)^2\left(\frac{2.5625\pi \times 10^{-12}}{25\pi \times 10^{-12}}\right)^3 K_S = 0.0003K_S. \tag{C.0.5}$$

It means that the permeability of the interstitial space is very small compare to the sinusoidal permeability.

Appendix D

Rescaling of the parameters

Several parameters appearing in the model are derived from experimental results in the literature. However, the measured values are not always in an appropriate form to be used directly in the model, and so in this section, we calculate some important parameter values.

- Hepatic filtration coefficient (F) [59]

$$\begin{aligned} F &= \frac{0.3\ ml}{min \cdot mmHg \cdot 100\ g.\ of\ tissue} \times \frac{min}{60\ s} \times \frac{m^3}{10^6\ ml} \times \frac{10^3\ g}{kg} \\ &= 5 \times 10^{-8} m^3 kg^{-1} mmHg^{-1} s^{-1} \end{aligned} \tag{D.0.1}$$

- Glissonian-Peritoneal membrane permeability (M_L) [61]

$$
\begin{aligned}
M_L &= 5.7 \times 10^{-3} \, \frac{ml}{h \cdot cmH_2O \cdot cm^2} \times \frac{1 \; h}{3600 \; s} \times \frac{m^3}{10^6 \; ml} \times \frac{1.36 \; cmH_2O}{1 \; mmHg} \times \frac{10^4 \; cm^2}{m^2} \\
&= 2.15 \times 10^{-8} \; m \cdot s^{-1} mmHg^{-1} \qquad \text{(D.0.2)}
\end{aligned}
$$

- Resistance of lymphatic ducts (R_l) [63]

Mongrel dog has an average liver/body weight ratio (g/kg) as 20.9 [75]; therefore,

$$
\begin{aligned}
R_l &= 0.056 \, \frac{cmH_2O \cdot 60s}{10^{-9} m^3} \times \frac{mmHg}{1.36 \; cmH_2O} \times 0.0209 \, \frac{kg}{kg} \times \frac{1}{1060} \, \frac{m^3}{kg} \times 25 \; kg \\
&= 1.22 \times 10^6 mmHg \cdot s \qquad \text{(D.0.3)}
\end{aligned}
$$

- Filtration coefficient of oxygen through the endothelial wall via diffusion process (G_W) [64] [76]

G_W can be calculated by dividing the oxygen diffusion coefficient by square of the endothelial thickness (175 nm) and multiplying the porosity of the fenestrations (0.034).

$$
\begin{aligned}
G_W &= 2 \times 10^{-9} \, \frac{m^2}{s} \times \frac{1}{(175 \times 10^{-9})^2} \, \frac{1}{m^2} \times 0.034 \\
&= 2220 s^{-1} \qquad \text{(D.0.4)}
\end{aligned}
$$

- Filtration coefficient of oxygen through the endothelial wall via advection process (F_W)

[59]

$$\begin{aligned} F_W &= \rho F \\ &= 1060\ \frac{kg}{m^3} \times 5 \times 10^{-8}\ \frac{m^3}{s \cdot kg \cdot mmHg} \\ &= 5.3 \times 10^{-5}\ mmHg^{-1}s^{-1} \end{aligned} \tag{D.0.5}$$

- Oxygen concentration at the portal tract (C_0) [62]

The amount of oxygen dissolves in plasma is about 2% of the total. The average weight of the human liver is about 1,650 g [77].

$$\begin{aligned} C_0 &= 0.3\ \frac{mlO_2}{min \cdot gliver} \times \frac{1}{1.78 \times 10^{-3}}\ \frac{min}{m^3} \times 1650\ gliver \times 0.02 \\ &= 5.56 \times 10^3\ \frac{mlO_2}{m^3} \end{aligned}$$

Moreover, the volume of oxygen can be converted into molar via the Henry's law of gas: $PV = nRT$. Therefore, at body temperature $37°C$ $(310K)$ and pressure 1 atm, we can find the concentration of oxygen dissolved in plasma as:

$$\begin{aligned} C_0 &= \frac{1 \times 5.56 \times 10^3}{10^3 \times 0.082 \times 310} \\ &= 0.21\ \frac{mol}{m^3} \end{aligned} \tag{D.0.6}$$

- Maximum oxygen uptake rate by hepatocytes (Q_m) [65]

From Ledezma paper [65], the maximum oxygen uptake rate (V_{max}) is 0.25 $nmol/s/10^6$ $cells$. The cells density is 10^5 $cells/cm^2$. We assume that the hepatocytes have a cuboid shape and the cells arrangement is uniform; therefore, the total number of cells in cubic centimetre is $10^{7.5}$ $cells/cm^3$. Q_m can be calculated as

$$\begin{aligned} Q_m &= 0.25 \times 10^{-9} \frac{mol}{s \cdot 10^6 \; cells} \times 10^{7.5} \frac{cells}{cm^3} \times 10^6 \frac{cm^3}{m^3} \\ &= 7.9 \times 10^{-3} \; mol/m^3/s \end{aligned} \tag{D.0.7}$$

- Michaelis-Menten constant (K_m) [65]

The Michaelis-Menten constant in partial pressure unit (5 $mmHg$) can be converted to molar concentration by using the solubility of oxygen in plasma ($\alpha = 0.03 \; l/m^3/mmHg$ [35]) and Henry's law of gas ($n = \frac{PV}{RT}$).

$$\begin{aligned} K_m &= 5 \; mmHg \times \alpha \times \frac{P}{RT} \\ &= 5 \; mmHg \times 0.03 \frac{l}{m^3 \cdot mmHg} \times 1 \; atm \times \frac{1}{0.082} \frac{mol}{atm \cdot l} \times \frac{1}{310 \; K} \\ &= 5.9 \times 10^{-3} \; mol/m^3 \end{aligned} \tag{D.0.8}$$

Appendix E

Michaelis-Menten theory

Michaelis-Menten kinetics can be derived from [78]

$$S + E \underset{k_{-1}}{\overset{k_1}{\rightleftharpoons}} SE \xrightarrow{k_2} P + E, \tag{E.0.1}$$

where S represents the substrate, E is the enzyme, SE is the intermediate complex, P is the product, and k_{-1}, k_1, and k_2 are the kinetic rates in the directions of the reaction.

From the reaction scheme above, we obtain ordinary differential equations governing each component:

$$\frac{ds}{dt} = -k_1 se + k_{-1} c, \tag{E.0.2}$$

$$\frac{de}{dt} = -k_1 se + (k_{-1} + k_2) c, \tag{E.0.3}$$

$$\frac{dc}{dt} = k_1 se - (k_{-1} + k_2)c, \tag{E.0.4}$$

$$\frac{dp}{dt} = k_2 c, \tag{E.0.5}$$

where s, e, c, p represent the concentrations of S, E, SE, and P, respectively.

Initial conditions We assume the initial concentrations for the substrate and enzyme are s_0 and e_0, respectively. There is neither intermediate complex nor product at $t = 0$. Thus,

$$s(0) = s_0, \quad e(0) = e_0, \quad c(0) = 0, \quad p(0) = 0. \tag{E.0.6}$$

Therefore, we can write

$$\frac{de}{dt} + \frac{dc}{dt} = 0; \tag{E.0.7}$$

then,

$$e(t) + c(t) = e_0. \tag{E.0.8}$$

Also,

$$\frac{ds}{dt} = -k_1 s e_0 + (k_1 s + k_{-1})c, \tag{E.0.9}$$

$$\frac{dc}{dt} = k_1 s e_0 - (k_1 s + k_{-1} + k_2)c. \tag{E.0.10}$$

We assume the enzyme is in plentiful supply, meaning that $\frac{de}{dt} \approx 0$, then $\frac{dc}{dt} \approx 0$; thus,

$$k_1 s e_0 - (k_1 s + k_{-1} + k_2)c \approx 0. \tag{E.0.11}$$

Then,

$$c = \frac{k_1 s e_0}{k_1 s + k_{-1} + k_2}. \tag{E.0.12}$$

Thus, we obtain

$$\frac{ds}{dt} \approx -k_2 c \approx \frac{-k_1 k_2 s e_0}{k_1 s + (k_{-1} + k_2)}. \tag{E.0.13}$$

Define

$$K_m = \frac{k_{-1} + k_2}{k_1}; \tag{E.0.14}$$

then,

$$\frac{ds}{dt} = \frac{-k_2 s e_0}{s + K_m}. \tag{E.0.15}$$

Define Q_m (Maximum oxygen uptake rate) as

$$Q_m = k_2 e_0; \tag{E.0.16}$$

thus,

$$\frac{ds}{dt} = -\frac{Q_m s}{s + K_m}. \tag{E.0.17}$$

Finally, we obtain the oxygen uptake rate term

$$\phi = -\frac{Q_m C_I}{C_I + K_m}. \tag{E.0.18}$$

Bibliography

[1] Gray H. *Gray's Anatomy*, The Classic Collectors Edition. New York: Gramercy Books, 1977: 1257

[2] Moore KL, Dalley AF, et al. *Clinical Oriented Anatomy*, 5th Edition, 2006: 289-300

[3] Thibodeau GA, Patton KT, et al. *Anatomy and Physiology*, 4th Edition, 1999: 751-755

[4] Launois B, Jamieson GG. "The importance of Glisson's capsule and its sheaths in the intrahepatic approach to resection of the liver." Surg Gynecol Obstet. 1992 Jan; 174(1): 7-10.

[5] Anne MR Agur, Arthur F Dalley. *Grant's Atlas of Anatomy*, 11th edition, 2003: 143

[6] Kiernan F. "The anatomy and physiology of the liver." Philossophical Transactions of the Royal Society of London, 1833; 123: 711-770.

[7] Mall FP. "A study of the structural unit of the liver." Am J of Anat 1906; 5: 227-308

[8] Rappaport AM, Borowy ZJ, Loughheed WM, Lotto WN. "Subdivision of hexagonal liver lobules into a structural and functional unit. Anat Rec 1954"; 119: 11-33.

[9] Teutsch HF, Schuerfeld D, Groezinger E. "Three-dimensional reconstruction of parenchymal units in the liver of the rat." Hepatology, 1999 Feb; 29(2): 494-505.

[10] Matsumoto T, Komori R, Magara T, Ui T, Kawakami M, Tokuda T, Takasaki S, et al. "A study on the normal structure of the human liver, with special reference to its angioarchitecture." Jikeikai Med J 1979; 26: 1-40

[11] Bonfiglio A, Leungchavaphongse K, Repetto R, Siggers JH. "Mathematical modeling of the circulation in the liver lobule." J Biomech Eng. 2010 Nov; 132(11): 111011.

[12] Martini, Frederic et al. *Anatomy and Physiology 2007 Ed.* 2007 Edition; p.537.

[13] Laine G.A., Hall J.T. "Transsinusoidal fluid dynamics in canine liver during venous hypertension" Circ Res. 1979 Sep; 45(3): 317-23.

[14] Osamu Ohtani, Yuko Ohtani. "Lymph Circulation in the Liver The Anatomical Record: Advances in Integrative Anatomy and Evolutionary Biology." Volume 291, Issue 6, pages 643652, June 2008.

[15] Michael Schnke, Erik Schulte, Udo Schumacher, Lawrence M. Ross, Edward D. Lamperti *Thieme Atlas of Anatomy. Neck an Internal Organs.* p.128-129.

[16] Kim S, Kim TU, Lee JW, Lee TH, Lee SH, Jeon TY, Kim KH. "The perihepatic space: comprehensive anatomy and CT features of pathologic conditions." Radiographics. 2007 Jan-Feb; 27(1): 129-43.

[17] Arroyo V. "Pathophysiology, diagnosis and treatment of ascites in cirrhosis." Ann Hepatol. 2002 Apr-Jun; 1(2): 72-9.

[18] Caro CG, Pedley TJ, Schroter RC, Seed WA *The Mechanics of the Circulation*

[19] Ku DN. "Blood flow in arteries." Annu Rev Fluid Mech 1997, 29: 399-434.

[20] Nicholas WW, O'Rourke MF. *McDonald's blood flow in arteries*

[21] Nick Jaensson "Experimental analysis of flow in a curved tube using particle image velocimetry" Internship report, November 2010, Eindhoven University of Technology, Department of Biomedical Engineering

[22] Albert L. Kunz, Norman A. Coulter, Jr. "Non-Newtonian Behavior of Blood in Oscillatory Flow." Biophys J. 1967 January; 7(1): 2536.

[23] C. Ross Ethier and C.A. Simmons *Introductory Biomechanics: From Cells to Organisms.* Cambridge University Press (2007)

[24] Otto, F. "Die Grundform des arteriellen Pulses", Zeitung fr Biologie 37 (1899) 483-586.

[25] Sagawa K, Lie RK, and Schaefer J. "Translation of Otto Frank's paper 'Die Grundform des Arteriellen Pulses'" Zeitschrift fur Biologie 37: 483526 (1899). J Mol Cell Cardiol 22: 253-277, 1990.

[26] Parker KH, Jones CJH. "Forward and backward running waves in the arteries: analysis using the method of characteristics." J Biomech Eng 112: 322-326, 1990.

[27] Parker KH. "An introduction to wave intensity analysis." Med Biol Eng Comput. 2009 Feb; 47(2): 175-88. Epub 2009 Feb 11.

[28] Bazigou E, Makinen T. "Flow control in our vessels: vascular valves make sure there is no way back." Cell Mol Life Sci. 2012 Aug 25.

[29] Khaled, Vafai. "The role of porous media in modeling flow and heat transfer in biological tissues." International Journal of Heat and Mass Transfer: 46 (2003), 4989-5003

[30] Schmid-Schonbein, H. "Conceptional proposition for a specific microcirculatory problem: maternal blood flow in hemochorial multivillous placentae as percolation of a 'porous medium'." Trophoblast Res. 3, 1738.

[31] Whang K, Goldstick TK, Healy KE. "A biodegradable polymer scaffold for delivery of osteotropic factors." Biomaterials. 2000 Dec; 21(24): 2545-51.

[32] Nicholson C. "Diffusion and related transport mechanism in brain tissue", Rep. Prog. Phys. 64 (2001) 815-884.

[33] Bear J. *Dynamics of fluids in porous media.* Dover Publications, 1972: 119–125

[34] Detournay E, Cheng A. "Fundamentals of poroelasticity" Comprehensive Rock Engineering. (J. Hudson, ed.), Vol. II, Pergamon Press, 1993: 113-169.

[35] Roland N. Pittman. “Regulation of Tissue Oxygenation.” Morgan and Claypool Life Sciences; 2011.

[36] Lautt WW. “Mechanism and role of intrinsic regulation of hepatic arterial blood flow: hepatic arterial buffer response.” Am J Physiol. 1985 Nov; 249(5 Pt 1): G549-56.

[37] Hector Daniel Gonzalez, Zi Wei Liu, Sophia Cashman, and Giuseppe K Fusai. “Small for size syndrome following living donor and split liver transplantation.” World J Gastrointest Surg. 2010 December 27; 2(12): 389-394.

[38] Tucker ON, Heaton N. “The ’small for size’ liver syndrome.” Curr Opin Crit Care. 2005 Apr.; 11(2): 150-5

[39] Gruttadauria S, Pagano D, Luca A, Gridelli B. “Small-for-size syndrome in adult-to-adult living-related liver transplantation.” World J Gastroenterol. 2010 October 16(40): 5011-5015.

[40] Dahmen U, Hall CA, Madrahimov N, Milekhin V, Dirsch O. “Regulation of hepatic microcirculation in stepwise liver resection.” Acta Gastro-Enterologica Belgica, 2007; 70: 345-351

[41] Condon RE, Chapman ND, Nyhus LM, Harkins HN. “Hepatic arterial and portal venous pressure-flow relationships in isolated, perfused liver.” The American Journal of Physiology, 1962; 202: 1090-1094

[42] Kawada N, Tran-Thi TA, Klein H, Decker K. "The contraction of hepatic stellate (Ito) cells stimulated with vasoactive substances." European Journal of Biochemistry, 1993; 213: 815-823

[43] McCuskey RS. "A dynamic and static study of hepatic arterioles and hepatic sphincters." The American Journal of Anatomy, 1966; 119: 455-478

[44] McCuskey RS. "Morphological mechanisms for regulating blood flow through hepatic sinusoids." Liver, 2000; 20: 3-7

[45] Zhang JX, Pegoli W, Clemens MG. "Endothelin-1 induces direct constriction of hepatic sinusoids." The American Journal of Physiology - Gastrointestical and Liver Physiology, 1994; 266: G624-G632

[46] Arroyo V. "Pathophysiology, diagnosis and treatment of ascites in cirrhosis." Ann Hepatol. 2002 Apr-Jun; 1(2): 72-9.

[47] Rani HP, Sheu T, Chang TM, Liang PC. "Numerical investigation of non-Newtonian microcirculatory blood flow in hepatic lobule." Journal of Biomechanics 2006; 39: 551-563

[48] van der Plaats A, 't Hart NA, Verkerke GJ, Leuvenink HG, Verdonck P, Ploeg RJ, Rakhorst G. "Numerical simulation of the hepatic circulation." Int J Artif Organs. 2004 Mar; 27(3): 222-30.

[49] Debbaut C, Monbaliu D, Casteleyn C, Cornillie P, Van Loo D, Masschaele B, Pirenne J, Simoens P, Van Hoorebeke L, Segers P. "From vascular corrosion cast to

electrical analog model for the study of human liver hemodynamics and perfusion." IEEE Trans Biomed Eng. 2011 Jan; 58(1): 25-35.

[50] Ricken T, Dahmen U, Dirsch O. "A biphasic model for sinusoidal liver perfusion remodeling after outflow obstruction." Biomech Model Mechanobiol. 2010 Aug; 9(4): 435–50.

[51] Burt, A. D., Portmann, B. C., and Ferrell, L. D., 2006, *MacSweens Pathology of the Liver*, 5th ed., Churchill Livingstone, Elsevier, Philadelphia, PA.

[52] Sakuma I, Chui C. "Methods in combined compression and elongation of liver tissue and their application in surgical simulation." Biomechanical Systems Technology: Cardiovascular Systems, 2007: 225-261

[53] K. Farahani, H. Bahai. "Hyper-elastic constitutive equations of conjugate stresses and strain tensors for the SethHill strain measures." International Journal of Engineering Science, Volume 42, Issue 1, January 2004, Pages 29-41

[54] Wang X. "The elastodynamic solution for a solid sphere and dynamic stress-focusing phenomenon." Applied Mathematics and Mechanics, vol.18, 1993 Aug; Issue 8, pp.777–785

[55] Wang X, Gong Y. "A theoretical solution for axially symmetric problems in elastodynamics." ACTA MECHANICA SINICA, vol.7, 1991 Aug; Issue 3, pp.275-282

[56] Annamma Paul *Anatomy Simplified for Nursing Paramedical Students*,2/e. BI Publications Pvt Ltd, 1 Jan 2003. pp.177

[57] Schiff ER, Maddrey WC, Sorrell MF *Schiff's Diseases of the Liver*

[58] Kotiluoto P, Auterinen I. "MCNP study for epithermal neutron irradiation of an isolated liver at the Finnish BNCT facility." Appl Radiat Isot. 2004 Nov; 61(5): 781-5.

[59] Greenway CV, Lautt WW "Effects of hepatic venous pressure on transsinusoidal Quid transfer in the liver of the anesthetized cat." Circ Res 26: 697-703

[60] Suzuki K, Epstein ML, Kohlbrenner R, Garg S, Hori M, Oto A, Baron RL. "Quantitative radiology: automated CT liver volumetry compared with interactive volumetry and manual volumetry." AJR Am J Roentgenol. 2011 Oct; 197(4): W706-12.

[61] Negrini D, Gonano C, Del Fabbro M, Miserocchi G. "Transperitoneal fluid dynamics in rabbit liver J Appl Physiol." 1990 Aug; 69(2): 625-9.

[62] Izamis ML "Meeting the oxygen requirements of an isolated perfused rat liver", DSpace@MIT: Massachusetts Institute of Technology. 2006 MSc Dissertation, Massachusetts Institute of Technology.

[63] Elk J.R., Laine G.A. "Lymphatic function in the liver after hepatic venous pressure elevation Am J Physiol." 1988 May;254(5 Pt 1):G748-52.

[64] Tannock IF "Oxygen diffusion and the distribution of cellular radiosensitivity in tumours." British Journal of Radiology (1972) 45, 515-524

[65] Ledezma GA, Folch A, Bhatia SN, Balis UJ, Yarmush ML, Toner M. "Numerical model of fluid flow and oxygen transport in a radial-flow microchannel containing hepatocytes." J Biomech Eng. 1999 Feb; 121(1): 58-64.

[66] Cunningham, Carol C.; van Horn, Cynthia G. "Energy Availability and Alcohol-Related Liver Pathology." Alcohol Research Health; 2003, Vol. 27 Issue 4, p291

[67] Nanji AA, Hiller-Sturmhfel S. "Apoptosis and necrosis: two types of cell death in alcoholic liver disease." Alcohol Health Res World. 1997; 21(4): 325-30.

[68] ROBERT D. ODZE, MD, FRCP(C), and JOHN R. GOLDBLUM, MD *Surgical Pathology of the GI Tract, Liver, Biliary Tract, and Pancreas (Second Edition)*

[69] Le Couteur DG, Fraser R, Hilmer S, Rivory LP, McLean AJ. "The hepatic sinusoid in aging and cirrhosis: effects on hepatic substrate disposition and drug clearance." Clin Pharmacokinet. 2005; 44(2): 187-200.

[70] Onori P, Morini S, Franchitto A, Sferra R, Alvaro D, Gaudio E. "Hepatic microvascular features in experimental cirrhosis: a structural and morphometrical study in CCl4-treated rats." J Hepatol. 2000 Oct; 33(4): 555-63.

[71] Cern V, Turek Z, Parzkov R. "In situ assessment of the liver microcirculation in mechanically ventilated rats using sidestream dark-field imaging." Physiol Res. 2009; 58(1): 49-55. Epub 2008 Jan 17.

[72] Shakado S, Sakisaka S, Noguchi K, Yoshitake M, Harada M, Mimura Y, Sata M, Tanikawa K. "Effects of extracellular matrices on tube formation of cultured rat hepatic sinusoidal endothelial cells." Hepatology. 1995 Sep;22(3):969-73.

[73] Wolfgang Kuhnel. *Color Atlas of Cytology, Histology, and Microscopic Anatomy.*: p.449

[74] Pries AR, Neuhaus D, Gaehtgens P. "Blood viscosity in tube flow: dependence on diameter and hematocrit." Am J Physiol. 1992 Dec; 263(6 Pt 2): H1770-8.

[75] Fittschen C, Bellamy JE. "Prednisone-induced morphologic and chemical changes in the liver of dogs." Vet Pathol. 1984 Jul; 21(4): 399-406.

[76] Cheluvappa R, Cogger VC, Kwun SY, OReilly JN, Le Couteur DG, Hilmer SN "Liver sinusoidal endothelial cells and acute non-oxidative hepatic injury induced by Pseudomonas aeruginosa pyocyanin." Int J Exp Pathol. 2008 December; 89(6): 410418.

[77] Obradovic D, Aleksic N, Mijatov-Ukropina L. "Standardization of liver dimensions for the local population." Med Pregl. 1991; 44(5-6): 266-8.

[78] Jeremy M Berg, John L Tymoczko, and Lubert Stryer. *Biochemistry*, 5th edition.

[79] Matsumura T, Thurman RG. "Predominance of glycolysis in pericentral regions of the liver lobule." Eur J Biochem. 1984 Apr 16; 140(2): 229-34.

[80] Matsumura T, Yoshihara H, Jeffs R, Takei Y, Nukina S, Hijioka T, Evans RK, Kauffman FC, Thurman RG. "Hormones increase oxygen uptake in periportal and

pericentral regions of the liver lobule." Am J Physiol. 1992 Apr; 262(4 Pt 1): G645-50.

[81] Beard DA. "Modeling of oxygen transport and cellular energetics explains observations on in vivo cardiac energy metabolism." PLoS Comput Biol. 2006 Sep 15; 2(9): e107. Epub 2006 Jul 10.

[82] Mueller S. Sandrin L. "Liver stiffness: a novel parameter for the diagnosis of liver disease." Dovepress. Hepatic Medicine: Evidence and Research 2010:2 4967

[83] Vanheule E, Geerts AM, Reynaert H, Van Vlierberghe H, Geerts A, De Vos M, Colle I. "Influence of somatostatin and octreotide on liver microcirculation in an experimental mouse model of cirrhosis studied by intravital fluorescence microscopy." Liver Int. 2008 Jan; 28(1): 107-16.

[84] Mori T, Okanoue T, Sawa Y, Hori N, Ohta M, Kagawa K. "Defenestration of the sinusoidal endothelial cell in a rat model of cirrhosis." Hepatology. 1993 May; 17(5): 891-7.

[85] Witte MH, Dumont AE, Clauss RH, Rader B, Levine N, Breed ES. "Lymph circulation in congestive heart failure: effect of external thoracic duct drainage." Circulation. 1969 Jun; 39(6): 723-33.

[86] Mobley WP, Kintner K, Witte CL, Witte MH. "Contribution of the liver to thoracic duct lymph flow in a motionless subject." Lymphology. 1989 Jun; 22(2): 81-4.